國立臺灣大學工學院機械工程學系

碩士論文

Department of Mechanical Engineering
College of Engineering
National Taiwan University

Master Thesis

# 以奈米壓痕試驗及雷射掃描式共軛焦顯微技術評估高分子系統的耐刮性

# Scratch Resistance Assessments of Polymeric Systems – Using Instrumented Indentation Testing and Laser Scanning Confocal Microscopy

黃宇欣
Yu-Hsin Huang

指導教授：馬劍清 博士
宋麗品 博士

Advisor: Chien-Ching Ma, Ph.D.
Li-Piin Sung, Ph.D.

中華民國 99 年 6 月

June, 2010

# 國立臺灣大學碩士學位論文
# 口試委員會審定書

以奈米壓痕試驗及雷射掃描式共軛焦顯微技術評估

高分子系統的耐刮性

Scratch Resistance Assessments of Polymeric Systems –

Using Instrumented Indentation Testing

and Laser Scanning Confocal Microscopy

本論文係黃宇欣君（R97522502）在國立臺灣大學機械工程學系完成之碩士學位論文，於民國 99 年 6 月 9 日承下列考試委員審查通過及口試及格，特此證明

口試委員：

馬劍清(指導教授) 馬劍清 （簽名）

宋麗品(共同指導) 宋麗品

張所鎧 張所鎧

盧中仁 盧中仁

系 主 任: 張所鎧 張所鎧 （簽名）

# 誌謝

本論文得以付梓所需要感謝的人很多。首先，要感謝恩師馬劍清老師。馬老師敦厚的待人處事態度一直是我學習的榜樣，感謝老師對人的細心關懷，不但非常注重學生的興趣、鼓勵學生多元發展，也一直為我們爭取最好的機會。在研究與求學期間，老師清晰的思慮與堅持的精神帶給我很多啟發與激勵。謝謝老師，用開放和寬厚的態度使我們學習成長。

於 NIST 研究期間，我非常感謝我的另一位指導教授兼 supervisor 宋麗品博士。宋博士亦師亦母的教導與照顧我，一方面培養我獨立思考、解決問題的能力，一方面在我疑惑時又給予我詳盡的指引，使我在學習之餘也能快速的適應環境。在與人相處方面，更加感激宋博士時常給我很多有用的建議，讓我無論是學習研究或者處事都能有所進步。

特別感謝兩位口試委員，張所鋐所長與盧中仁教授所提出的指正與建議使本論文更趨完整，並且讓我更進一步思考到研究中的細微之處。此外，非常謝謝張所長提供我這次到美國短期研究的寶貴機會。

在此感謝Dr. Jonathan W. Martin 和Dr. Joannie W. Chin 讓我能夠參與NIST的研究。感謝Polymer Surface/Interface (PSI) 成員提供了寶貴的實驗樣品供我試驗。感謝我的第二位supervisor Dr. Aaron M. Forster，教我使用儀器、分析data，並且總是很有耐心的為我解惑。

能夠順利的進行到美國的短期研究，感謝學長能凱與學姊柏伃的有用建議與鼓勵。除此之外，感謝同事巧奇在我初到美國之際的細心照料與打氣，教我使用 DMTA 與停車。感謝室友 Christina 對我的特別照顧和關心，以及借車子給

我讓我免於淋雨受凍。感謝 Allison 贈與我好多家具，讓我剛到美國時幾乎都不需要特別煩惱生活上的問題。謝謝同事 Kar Tean 常常提供我友善的幫助、替我解決了很多使用 DMTA 上的疑問，並且協助我校對 DMTA 的論文章節。感謝親切的 Melissa 幫我改正論文中的文法錯誤，是非常盡職的英文小老師。感謝 Debbie 幫我搬家，還有寫論文時的相互鼓勵。感謝 Yongyan 對口試內容的建議，使我獲益良多。感謝辦公室友 Julien 的陪伴，在我煩悶時偶爾會教我幾句實用的法語。 除此之外，也要特別感謝好友 Kenway 給我眾多的幫助與建議，在寫論文之餘，也不忘邀我出門看太陽調劑身心。謝謝好友 Catherine、芳瑜、遠哥和立凡帶給我的歡樂時光。非常感謝好友竣翔對本論文的不吝指正，解決我電腦與使用軟體上眾多的疑難雜症，也常常給我鼓勵和心靈支持。

在溫馨的實驗室中，要特別感謝國志哥亦師亦友的帶領我學習，一起旁聽課程，並且時常替我禱告。謝謝學長敬源在學業和電腦工具使用上的教導與啟發，還有常常說笑話使實驗室增添許多幽默時刻。謝謝學姊于琪在學業上的幫助，並且在我低潮時給我很大的鼓勵。謝謝學長世皓對實驗室的管理，讓我們能夠專心投入研究。謝謝學長恆增和亦莊時常和我交換心得，指引我轉化心情。也感謝學長育熙、宜賢、康哲，學姐依姿、善盈，還有凱蘭、Yoko 和黃博的照顧。另外，感謝可愛的學弟奇儒、榮樺、泓嶔和鈞凱，常幫忙買便當及製造笑料。感謝同學兆祥在修課時期的陪伴，還有替我處理了很多口試的事務。

另外，也謝謝一直在關心我的朋友們，讓我真的覺得很幸福。非常感謝同學宜沐自大學以來在課業上的指導。還有在我感到低潮的時刻，要特別感謝學姊怡潔與好友渝婷的關心和陪伴，讓我有力量的去面對困難。我相信我所學習及得到的確實是超出了我的所求所想。

最後，謹將這份完成學業的喜悅獻給我最愛也最愛我的家人。謝謝爸爸帶給我從來不放棄、不認輸的勇氣，還有正面處理事情，開心向上的力量。謝謝姊姊替我處理好多事情，總是用實際的行動來支持我，還有幫我在家裡侍奉爸媽。謝謝默默關心我的表哥建榮和表姊逸璇。感謝我最愛的媽媽，讓我懂得體貼和溫柔帶給別人的溫暖，鼓勵我追求夢想，並且總是讓我知道我的身後永遠有後援，可以盡情揮灑。

宇欣

2010　年暑

于破壞實驗室

# ABSTRACT

In this thesis, a combination of instrumented indentation technique (IIT) and laser scanning confocal microscopy (LSCM) was used to assess the scratch resistance of polymer systems. The effect of glass transition temperatures $T_g$ and nanoparticle additive polarities on the surface mechanical properties and scratch resistance of polymers were investigated. By the continuous stiffness measurement (CSM) method, the elastic modulus and hardness of polymer systems were measured using IIT. The scratch resistance assessment was based on measuring the damage deformation and analyzing the scratch data, such as the scratch depths, scratch width, recovery, and friction coefficient as a qualitative method to evaluate the durability of the polymer system. Two types of scratch test methods were used: the progressive force and constant force scratch tests. The onset force at which scratch damage changed from elastic (total recover, invisible) to plastic (visible) deformation was approximately estimated from the progressive force scratch test. From an array of constant force scratch test, the onset force was determined more accurately. The onset force of elastic-plastic deformation can be used as an indicator to rank scratch resistance of a polymer system. The scratch morphology including scratch depths, scratch width, pile-up height were measured using LSCM. The scratch morphological data were analyzed and also used to assess the scratch resistance of the system.

Two polymer systems were studied in this thesis: 1. Crosslinked epoxy (EP) systems with different glass transition temperatures; 2. Polyurethane (PU) thin films containing 2 % nanosilica ($SiO_2$) with dispersant/additive of different polarities. In the first case study, the effect of glass transition temperature on the scratch behavior was

evident. The higher glass transition temperature, the higher scratch resistance. In the second case study, two series of the PU-$SiO_2$ films were used due to different preparation conditions. Series 1 is thinner and has a higher glass transition temperature (~ 90 $^{o}$C), and series 2 is thicker and has a lower glass transition temperature (~ 55 $^{o}$C). In series 1, the control sample and reference group had similar mechanical data and scratch morphology so that the final ranking of scratch resistance is not clear. On the other hand, the control sample in the series 2 has the weakest scratch resistance and worst damage right after scratched. However, after 16 hours, the scratch damage of control sample (in series 2) recovered faster than that of the reference group. The scratch morphology of control sample (in series 2) became wider and shallower and less visible. Overall, the scratch damages were found to be more severe in the series with the lower glass transition temperature. Therefore, the testing results in both case studies indicated that the higher glass transition temperature had a stronger scratch resistance.

Keywords: Instrumented indentation technique, Laser scanning confocal microscopy, Nanoparticle silica, Glass transition temperature, Elastic modulus, Hardness, Scratch resistance

# 摘要

本論文結合了奈米壓痕試驗 (instrumented indentation technique) 及雷射共軛焦顯微技術 (laser scanning confocal microscopy) 來評估高分子系統的耐刮性 (scratch resistance)，並且研究不同玻璃轉移溫度與奈米添加物極性，對於高分子聚合物表面機械性質的影響。利用連續剛性量測技術 (continuous stiffness measurement method)，奈米材料的彈性模數與硬度可以由奈米壓痕試驗所測定。耐刮性研究主要是基於測量刮痕的損傷變形，佐以分析刮痕測試得到的深度、寬度、彈性回復指數、摩擦係數等資訊來定性評估材料的耐久性 (durability)。刮痕測試的施行，包括了連續增加負載與定量負載兩種方式。連續增加負載的刮痕測試提供了傷痕由無到有生成的完整資訊，並且可用來粗估代表了材料彈性至塑性變形的臨界破壞力 (onset force)；一系列定量負載的刮痕測試，則可用來精確評估材料的臨界破壞力，並藉此作為材料間傷痕肇始 (彈性至塑性變形) 相對於耐刮性比較的依據。本文中所有的刮痕形態，包括了刮痕深度、寬度和邊緣堆積高度，皆是使用雷射共軛焦顯微技術量測和分析，並且進一步用作耐刮性的評估。

實驗材料包括了兩個高分子系統： 1. 交聯結構的環氧樹脂 (epoxy) ，具有不同的玻璃轉移溫度 2. 聚胺甲酸酯 (polyurethane) 薄膜，添加了 2% 不同極性的奈米矽顆粒。在第一個研究個案中，玻璃轉移溫度對於刮痕測試的影響非常顯著，高的玻璃轉移溫度對應於高的耐刮性。第二個研究個案中，兩組含有奈米矽的聚胺甲酸酯薄膜按照不同的製備方式製成。第一組的材料較薄而且有著較高的玻璃轉移溫度 (~ 90 ℃)，第二組材料較厚而且有著較低的玻璃轉移溫度 (~ 55 ℃)。第一組的實驗試片 (control sample) 與對照組試片 (reference group)有著非常

近似的機械性質與刮痕形態，因此耐刮性的評估並不顯著。另一方面，第二組的實驗試片對於傷痕的抵抗力較弱，刮痕測試後得到的初始損傷深度是最嚴重的。然而，經過了 16 個小時，其復原的行為卻比其他對照組試片都快，傷痕變得寬而淺，可見度也降低了。依照整體來觀察，玻璃轉移溫度較低的聚胺甲酸酯組別，在刮痕試驗裡表現出了較嚴重的損傷變形。因此，由兩個高分子系統的研究中共同顯示，增加材料的玻璃轉移溫度可以使得抗刮性提升。

關鍵字: 奈米壓痕試驗、雷射共軛焦顯微技術、奈米碳、玻璃轉移溫度、彈性模數、硬度、耐刮性

# TABLE OF CONTENTS

# LIST OF FIGURES

# LIST OF TABLES

# Chapter 1 INTRODUCTION*

## 1-1 Research Motivation

In order to ensure a sustainable use of polymeric materials, the investigation of durability study can lead a significant increase of service life and reduce the waste of natural resources. Owing to the relatively soft and easily scratched features of polymeric materials, the enhancing of the scratch resistance is becoming more important. In recent years, many industrial companies attain the best quality of their products by improving the durability performance of coatings [1-2]. Also, some works indicated that the glass transition temperature $T_g$ plays a vital role in the mechanical properties of materials [3-4]. $T_g$ can be changed by adjusting the architecture of polymer network, and it can thus be related to the alteration of scratch resistance. On the other hand, the use of nanotechnology and its applications is becoming more multifarious and widespread. Incorporating metal-oxide nanoparticles such as nano-alumina and nano-silica into polymeric coatings to enhance the mechanical durability has become a trend in current anti-scratch technologies [5-6]. The results are promising, but current test methods for evaluating the mechanical properties and assessing the scratch resistance are still used traditional and field mechanical analysis. Traditional testing methods, such as dynamic mechanical thermal analysis and tensile tests, are not always suitable or sensitive to the local structural features impacted by network (cross-link) microstructures and the addition of the nanoparticle, which is much smaller compared to the area/volume of measurement.

* Certain instruments or materials are identified in this paper in order to adequately specify experimental details. In no case does it imply endorsement by NIST or imply that it is necessarily the best product for the experimental procedure.

It is important to use relevant techniques to measure the structure-property relationships at the appropriate length scale in order to understand the impact of the network microstructure and nanoparticle additives on materials and mechanical properties of polymer systems. This is the main objective of this study: to choose proper instrumentation and a well-designed testing method to investigate the impacts of network microstructure and nanoparticle additives on surface mechanical properties and scratch resistance of two polymeric systems.

For a long period of time, the scratch testing is used for studying the durability of materials. A study of scratch tests aims to understand the response and resistance to marring or scratching of a material. Typically, a mar is small and light damage on the sample surface. As for a scratch, it has a more severe damage than a mar and usually results in wider and deeper damage. Several scratch test methods are used to rank the durability of materials, such as the Taber test, field simulation test, ford test, and single probe test [7].

The Taber test utilizes an abrader wheel with an applied loading to test the abrasion resistance for a material. Before the test, the sample has to be weighed and the surface luster is recorded by gloss measurements. After a given number of rotations under the abrader wheel (spins and grinds), the sample has to be reweighed and measured the gloss value again. The ranking is made by percentage changes in the weight and gloss values due to the surface abrasion. The field simulation tests are in an attempt to simulate realistic damage conditions. Crockmeter test is one of the field simulation tests and uses the method of a laboratory scale car wash approximation. In this testing, some abrasive biodegradable cleansers are used to mimic naturally occurring dust and debris particles. After the sample is abraded by a probe/brush and washed with cold tap water and dried, the percentage of the gloss retention can be measured to rank the scratch

resistance.

The ford test is also known as the five finger test. This method using five probes, with each probe applied with a constant load to scratch the sample at a constant velocity. The scratch resistance is then evaluated in terms of the residual scratch depth. Unlike the Taber test and field simulation tests, this method has the ability to record the scratch morphology rather than relating the abrasion by gloss measurements using a commercial glossmeter. Specular gloss measurements have significant limitations relative to assessing scratch and mar damage. For example, a severe scratch or damage from multiple scratches on a coating surface results in a strong suppression of the specular gloss. A commercial glossmeter is only sensitive to the overall reduction in specular gloss and not the underlying scratch morphology that actually reduced the gloss value [5].

Single probe test is a similar method to the ford test, but only uses one probe to perform a test. This method is easier to control the scratch test conditions and can be used to relate the scratch damages to the materials properties of a sample. The instruments, such as atomic force microscope (AFM) and nanoindenter, are equipped with the basic abilities to carry out a single probe test. The results provide the values of applied lateral load forces and friction coefficients in the moments of initial loading and final unloading. The force range of AFM is usually smaller and hard to calibrate, and it is time-consuming to obtain the pre-scratch profile and past-scratch profiles. Using nanoindenter with proper test methods, it is easy to conduct a scratch test. The scratch resistance can be ranked by the onset of plastic deformation or crack formation from the residual scratch penetration curves. However, the scratch morphology is not provided from the test results, and the interpretation from penetration curves or friction coefficients can be complicated.

In addition to the scratch test tools, the assessment methods on the scratch damage are also a challenge to coating industry. Assessment methods such as gloss change in gray scale level or lightness have been created as useful adjuncts to visual inspection to help distinguish between two highly damaged surfaces. However, these methods often provide only a relative answer, such as whether the surface is scratched or not. Moreover, most studies do not include discussion of the relationships between scratch appearance and the material properties or surface characteristics (e.g., elastic modulus, frictional coefficient, and surface roughness). These issues are the major barriers to the development and acceptance of standard measurement techniques for determining scratch and mar resistance.

In order to successfully implement a scientifically based standardized test method for quantifying scratch resistance, it is vital to understand the relationships between material/mechanical properties, morphology, and appearance (optical properties) of surface and sub-surface deformation. A three-step methodology is developed by National Institute of Standards and Technology (NIST) to provide the information required and to draw conclusions about structure-property relationships that govern scratch resistance. A scratch is first generated in a material using a well-controlled scratch measurement protocol [8]. Second, an optical imaging technique is utilized to identify the “onset” of plastic deformation. At this point, the onset may be linked to the mechanical properties. Finally, the scratch damage is characterized with respect to the background signal from the undamaged surface by measuring both the specular and off-specular scattering intensities.

In this thesis, the first two steps are adopted from NIST methodology to investigate the impacts of network microstructure and nanoparticle additives on surface mechanical properties and scratch resistance of two polymeric systems. In the 1st step, a single

probe tester with depth-sensing technique such as nanoindenter is used. The control test variables include scratch depth, scratch velocity, applied loading, scratch length, and sensitivity of measurements. Scratch data can be recorded in three different procedures: pre-scan, scratch scan and post scan. The force and depth data can also be tracked during the complete scratching process. In the 2nd step, a high resolution optical imaging microscope is selected to measure the scratch morphology and identify onset of plastic deformation. This method will ensures the reliable and reproducible data and provide an objective way of durability analyses.

## 1-2 Literature Review

In this thesis, the assessments of the scratch resistances and the scratch behaviors are investigated in two polymeric systems: system 1- three epoxies of different glass tradition temperatures ($T_g$); system 2- polymer coatings containing nano-silica particle with different additive polarities. Therefore, recent research efforts related to $T_g$, nanoparticle additives, and scratch tests will be discussed in this section.

### 1-2.1 Introduce to Glass Transition Temperature

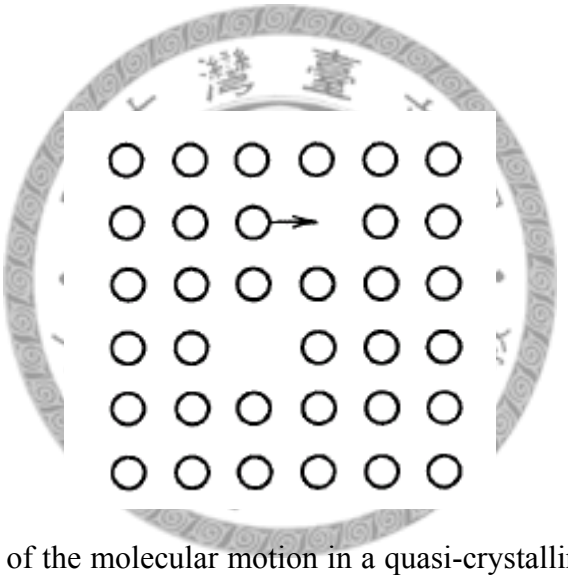

Figure 1.1 Schematic of the molecular motion in a quasi-crystalline lattice for the free-volume theory [9]

In 1936, Eyring first introduced the free-volume theory for describing the phenomenon of glass transition temperature [10]. Figure 1.1 shows the schematic of the molecular motion in a quasi-crystalline lattice. In this theory, the molecular motion is owing to the presence of holes. As a leading molecule moves into a hole, the other molecules exchange the places consequently. Later, Fox and Flory studied the glass transition correlation with molecular weight and relaxation time for polystyrene [11].

Gibbs and DiMarzio provided a series of experiments and pointed out that the glass transition temperature is increasing as enhancing the chain stiffness and decreasing when more free volumes exist [12]. Also, Wolfgardt et al determine the entropy close to the glass transition in a computer simulation and compared the results with the Gibbs-DiMarzio theory [13].

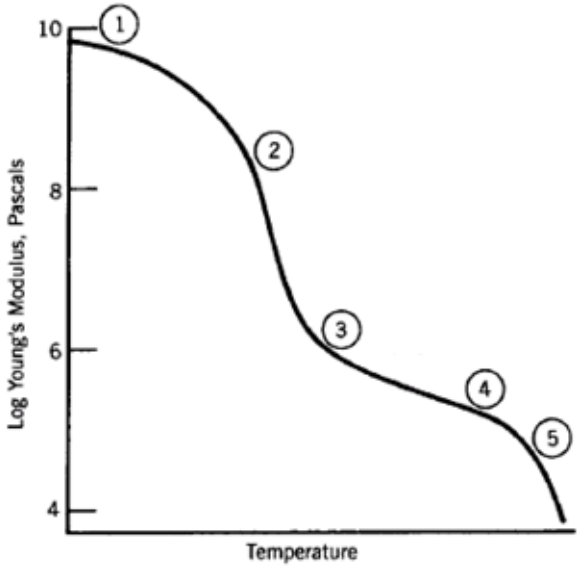


Figure 1.2 The Young's modulus as a function of temperature for an amorphous polymer [9].

The glass transition temperature $T_g$ is the phase transformation from a hard and brittle glassy type to a soft and elastic rubbery state. Figure 1.2 shows the Young's modulus-temperature behavior of an amorphous polymer. In region 1, only a few vibrational motions are taken place, and the polymer is hard and glassy. Region 2 is the glass transition region. In this region, polymers become soften, the modulus drops very fast so that the material becomes rubbery. Region 3, 4, and 5 represent the rubbery plateau, rubbery flow, and viscous flow regions, respectively. Two different materials

can be compared at the same point relative to their respective glass transition temperatures. In addition, $T_g$ is a reliable basis of choosing the suitable working region for a material.

### 1-2.2 Introduce to Nanoparticle Additives

Recent advances in nanoparticles are used as the functional additives to enhance the mechanical surface properties of polymers. Adding nanoparticles to a coating adjusts many characteristics of materials [5]. For example, the flexibility or toughness can be strengthened, the resistance to heat or corrosion can be improved, and the recovery feature under loading or scratching can also be changed. Generally, the final property of a nanocomposite is affected in many ways, such as the aspect ratio of additives, the dispersion condition, and the surface conditions (density, oligomer length, etc.). It is also regarded as the reflection of the three phases of a nanocomposite: inorganic core, bulk polymer and interphase. As the name implies, a nanocomposite coating is in the order of 100 nm or smaller. Owing to such a small size, the surface to volume ratio for nanoparticles is larger than conventional and macroscopic materials. Under this circumstance, the interaction between a polymeric host matrix and nanoparticle additives is mostly higher than other cases.

Nanoparticle additives can be designed to facilitate dispersion into a coating and carry the functional agent. The surface modified method is a way to tune the functional properties and results in the increment of exceptional thermal, mechanical and barrier properties of nanocomposites. Figure 1.3 shows the different surface modified methods of nanoparticles. By the addition of short and long organics chains, the physical properties, such as the glass transition temperature, storage and loss modulus, and

flexibility, can be amended and adapted to the experimental request. The alteration of high and low surface density can help the dispersion of additions to organic materials. Since the solubility is important for nanoparticles, the choosing of surface groups can lead to a judiciously adjustment of solubility. Moreover, the crosslink structures, which are generated by additional reactive groups, can improve the stability and durability of nanoparticle additives.

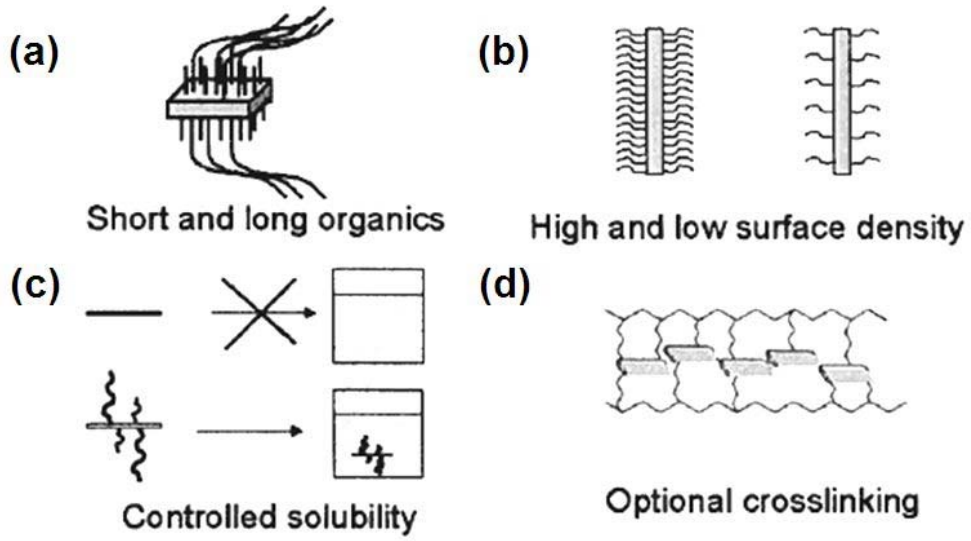


Figure 1.3 Schematic of different surface modified methods of nanoparticles [5].

### 1-2.3 Introduce to Scratch Testing

In order to have a better understanding of the surface mechanical properties of polymers, the scratch testing is helpful in detecting the surface behaviors under various experimental conditions and thus improves the contact and tribological performances [14]. Morel and Jardret investigated the scratch resistance and indentation properties as a function of temperature, and compared the compression and tensile properties to the scratch results for studying of the material's behavior [15]. Figure 1.4 illustrates the

stress distribution in a typical scratch test. Along the tip moving forward, a compression zone is generated in the front of the indenter. The compression zone is caused by the pressing effect of the tip and it usually accompanies the pile-up responses of materials. Oppositely, the zone behind the tip is termed a tensile zone. As the indenter slides away, a material bears the tensile forces in this area and some cracks created as a result.

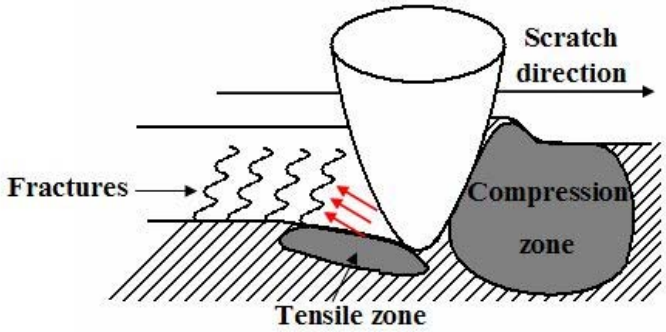


Figure 1.4 Schematic of the stress distribution in scratch testing [15].

Since the scratch testing is regarded as a tangential indentation, the scratch tail can not only map the tip shape at the end of the scratch test, but also be used to explore the recovery features for polymers. Gauthier et al presented the investigation of elastic recovery features of polymethyl-methacrylate (PMMA) by analyzing the geometry of scratch tails [16-17]. The shape and area of a scratch tail can be used to predict an elastic or elastic-plastic deformation, and the recovery behavior can be assessed. Figure 1.5 shows the rear and front portions of a scratch tail image. Here, $a_f$ is the length of the front contact, $a_r$ is the length of the rear contact, and $\omega_a$ is the angle characterizing the rear contact. Equation (1.1) is the formula for elastic-plastic contact. Where, the c is the yield stress ratio under a compression condition to the scratch hardness (c=2 for polymer), $\varepsilon$ is the strain of contact, $\varepsilon_e$ is the greatest possible strain of the contact of the

elastic sliding, $\varepsilon_p$ is the lowest possible strain of the plastic contact, and Y is the yield stress. The rear contact area is generated by the plastic deformation of the polymer and it is identical to the front area if the contact is approaching to a perfectly elastic deformation, i.e., under a completely elastic contact, the ratio $a_f$ / $a_r$ should equal to 1. The formula for the plastic contact is shown in Equation (1.2). Thus, by comparing the front and rear area, the plastic and elastic-plastic contact on a material surface can be associated.

$$\frac{a_r}{a_f} = 1 - \left[1 - \sqrt{\frac{2cY}{E_r}\tan\alpha}\right]\frac{\varepsilon - \varepsilon_e}{\varepsilon - \varepsilon_p} \tag{1.1}$$

$$\frac{a_r}{a_f} = \left[1 - \sqrt{\frac{2cY}{E_r}\tan\alpha}\right] \tag{1.2}$$

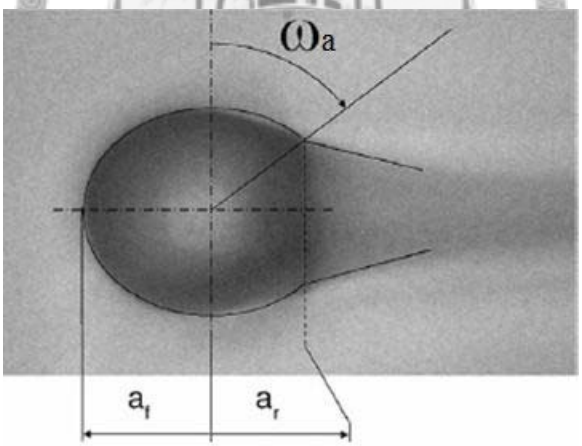


Figure 1.5 An image of the scratch tail with a front and a rear part [17].

In addition to a connection between the scratch tail and the elastic recovery behavior of polymers, the damage type in the middle portion of a scratch can be associated to the different material categories: ductile, brittle and tough. Gu et al demonstrated the surface microstructure and morphology changes due to the ultraviolet

(UV) exposure effect, and three different materials with dissimilar scratch deformations are adopted to characterize the nanomechanical properties [18]. Figure 1.6 shows the scratch damages under three material categories. The damage type of a ductile material is formed as an irregular fractured pattern (a drop shape). It is because the ultimate strength of the ductile material is relatively high and it won't crack easily. The damage type of the brittle material is found to be a concave deformation because the cracks occur rapidly once the loading reaching the fracture point. Similarly, the tough material has a convex deformation due to its compliant feature.

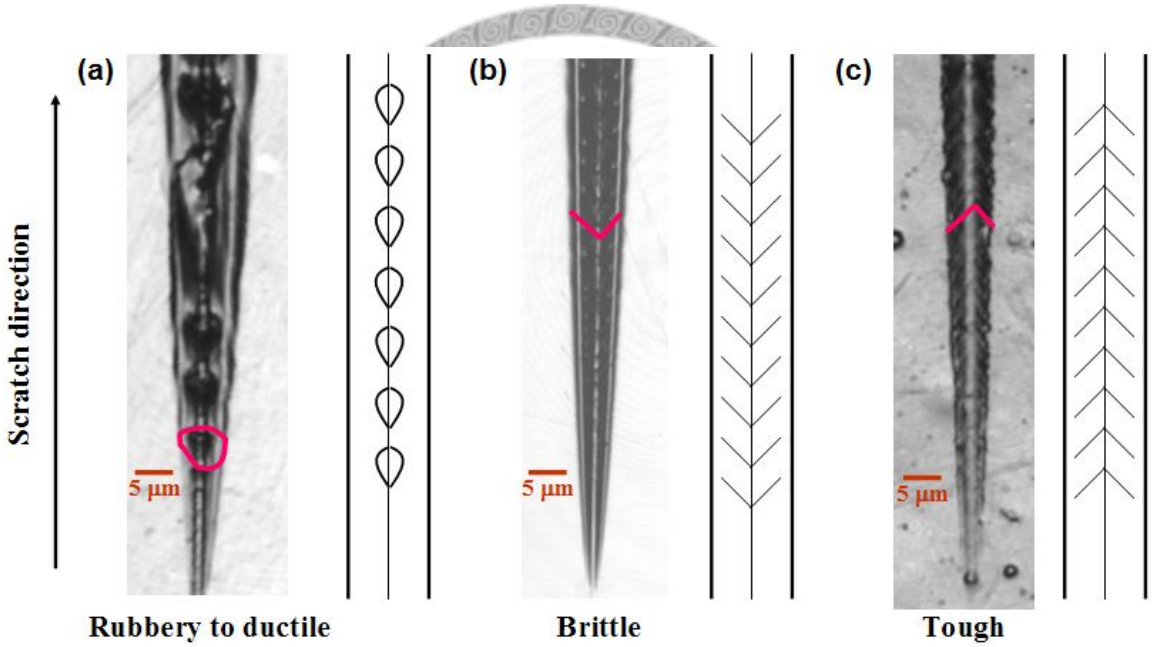


Figure 1.6 Schematic of the scratch damages under different material categories: (a) rubbery to ductile material (b) brittle material (c) tough material [18].

In order to expand the understanding of scratch deformation, Briscoe et al carried out many experiments under varying scratch conditions using rigid conical indenters [19-20]. The changing of scratch conditions includes the alteration of tip angles, temperatures, scratch velocities, and applied forces. Figure 1.7 shows related damage

deformation for a polycarbonate resin under various cone angles. Also, Figure 1.8 shows the scratch deformation map under various scratch conditions.

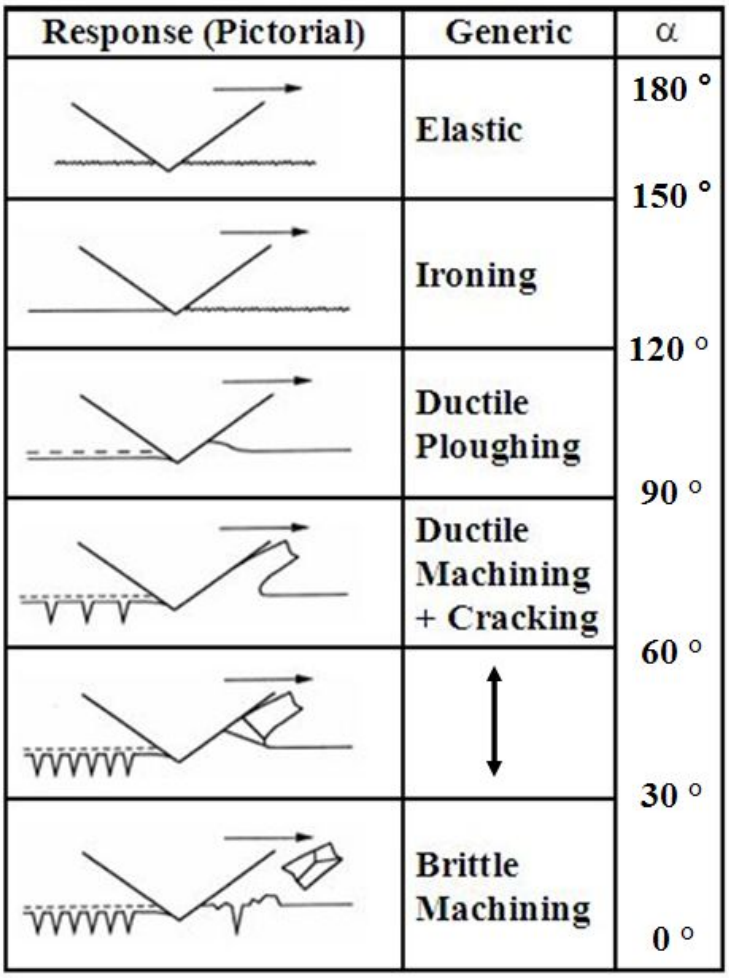


Figure 1.7 The damage types under scratch tests with various face angles [19].

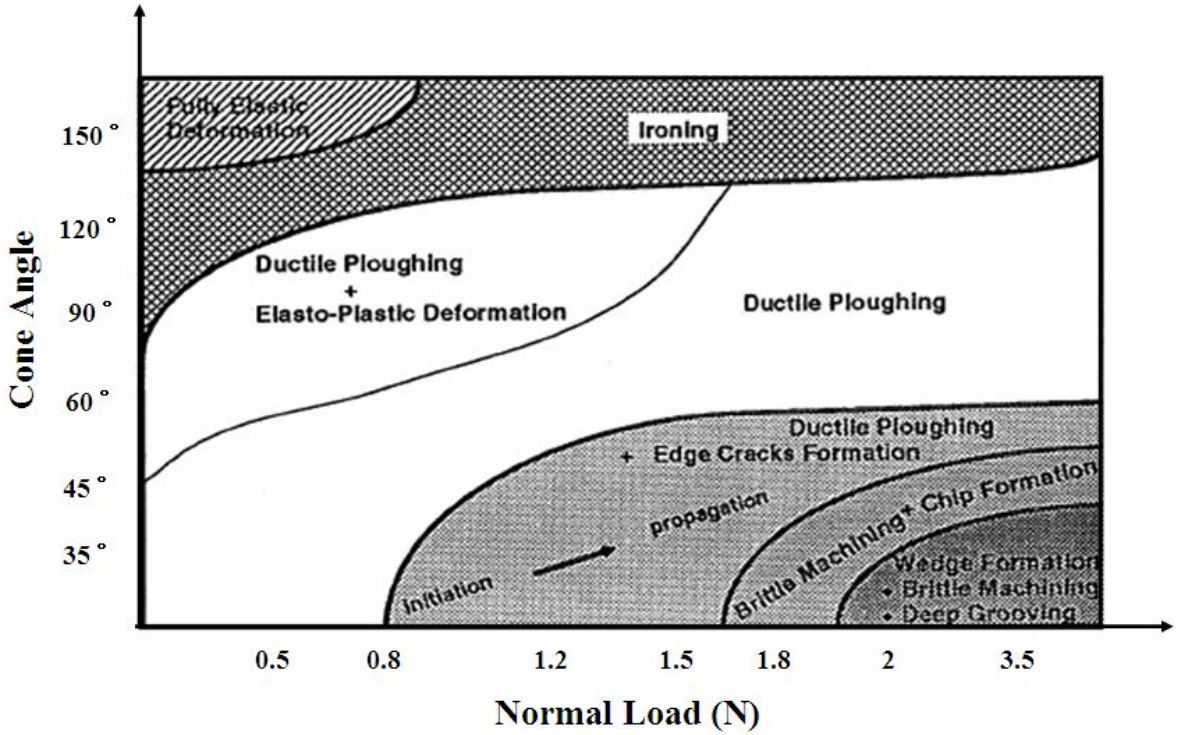


Figure 1.8 Schematic of the scratch deformation map under different cone angles and normal forces for a polycarbonate resin. The scratch tests were performed at room temperature and with a velocity of 2.6 mm/s [20].

Further researches and simulation works are reported to investigate the scratch behaviors. Misra and coworkers studied the scratch deformation parameters and local crystallinity characteristics of polymers using atomic force microscopy [21]. Sue and coworkers evaluated the scratch resistance under the effect of scratch loading and speeds for talc-filled polypropylene materials using three-dimensional finite element method (FEM) [22-23]. The characterizing of the scratch resistance from experimental scratch visibility and simulation shows a good qualitative correlation. In addition, they demonstrated a series of scratch behavior analyses based on FEM model for four categories of polymers: (1) ductile and strong, (2) ductile and weak, (3) brittle and weak, (4) brittle and strong [24].

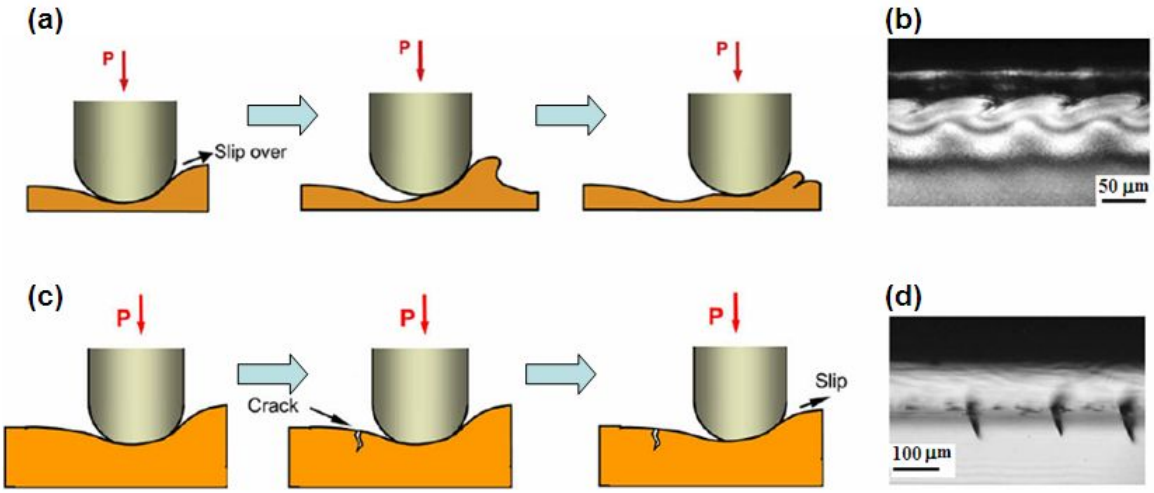


Figure 1.9 Schematic of (a) the formation of fish-scale damage (b) the fish-scale image (c) the formation of parabolic crack damage (d) the parabolic crack image [24].

Figure 1.9 (a) is the formation of the fish-scale damage. This kind of stick-slip step usually occurs on the ductile and weak polymers, in which the ironing effect and plastic deformation occur frequently. As the normal force increases and the frictional coefficient rises successively, the tip drags the material along with it during the scratch. If the exerted tensile is not over the ultimate strength of the material, the scratch tip will keep dragging the material and finally slip over the edge of the pile-up region. Figure 1.9 (b) shows the image of a series of the fish-scale damages. Figure 1.9 (c) is the formation of the parabolic crack damage, and it usually takes place on the brittle and strong polymers. As the tip moves forward with the strain energy accumulating, the crack of the brittle material occurs when the strain finally crosses the level of the ultimate strength. Figure 1.9 (d) shows the image of a series of the parabolic crack damages. For all of the scratch test, the damage feature will be triggered by a particular force level and repeat continuously after the force being high enough to start the next damage mode.

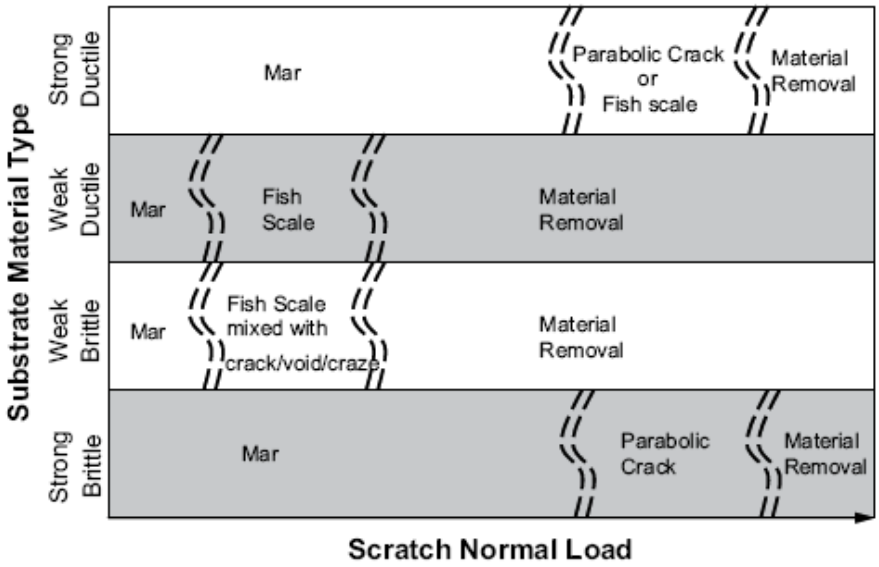


Figure 1.10 A evolution map of scratch damages for different categories of polymeric materals [24].

Figure 1.10 shows the evolution map of scratch damages for different categories of polymers. The formation of a scratch damage is dominated by many variables, such as the adhesive forces between the sample and the indenter, the indenter shape (see Appendix A), scratch speed, the value of the normal force, and the material categories.

## 1-3 Thesis Organization

This thesis is divided into five chapters. Chapter 1 introduces the research motivation and is followed by the reviews of literatures. Chapter 2 presents the experiment procedure and introduces the materials which are studied in this thesis. Chapter 3 describes the principles of instruments and uses few examples to present its applications. Chapter 4 is the results and discussion which includes the experimental results, data analyzing, and scratch resistance assessments. Finally, Chapter 5 contains the conclusions of this thesis and the recommendation for future works.

# Chapter 2 EXPERIMENTAL PROCEDURE AND MATERIALS

## 2-1 Experimental Procedure

This section introduces the experimental procedure for quantitatively characterizing the scratch and mar resistance of a polymer coating. This procedure adopts the protocol of NIST Polymer Surface/Interface (PSI) scratch test method [8], see Appendix B.

### 2-1.1 Introduction

This procedure is used to perform scratch testing by a single-probe scratch tester via instrumented nanoindention and characterize the scratch morphology by laser scanning confocal microscopy. Two types of scratch testing are carried out in this protocol: a progressive force scratch test and a constant force scratch test. The scratch resistance can thus be quantified by the magnitude of the applied normal load necessary to impart the visible scratch damage. Also, the resultant scratch morphology can be related to appearance attributes of the coating. Both the scratch resistance and scratch morphology are characteristics depending upon unique mechanical properties of the coatings and the specific parameters under which scratch tests are performed.

A typical scratch test includes three steps, as shown in Figure 2.1. In the beginning of a test, a pre-scan will be run with an applied normal force of 0.1 mN and the pre-scan result provides the original surface profile of the test sample. After the pre-

scan, an actual scratch scan is held. The applied normal load gradually varies from a minimum force to a maximum force through this scan. In the constant force scratch test, the minimum force equals to the maximum force. By comparing the pre-scan and the scratch scan data, the effect due to the uncontrollable surface conditions can be excluded. Subsequently, a post scan pursues the same path with a 0.1 mN normal load, and it helps to establish the recording of residual scratch data.

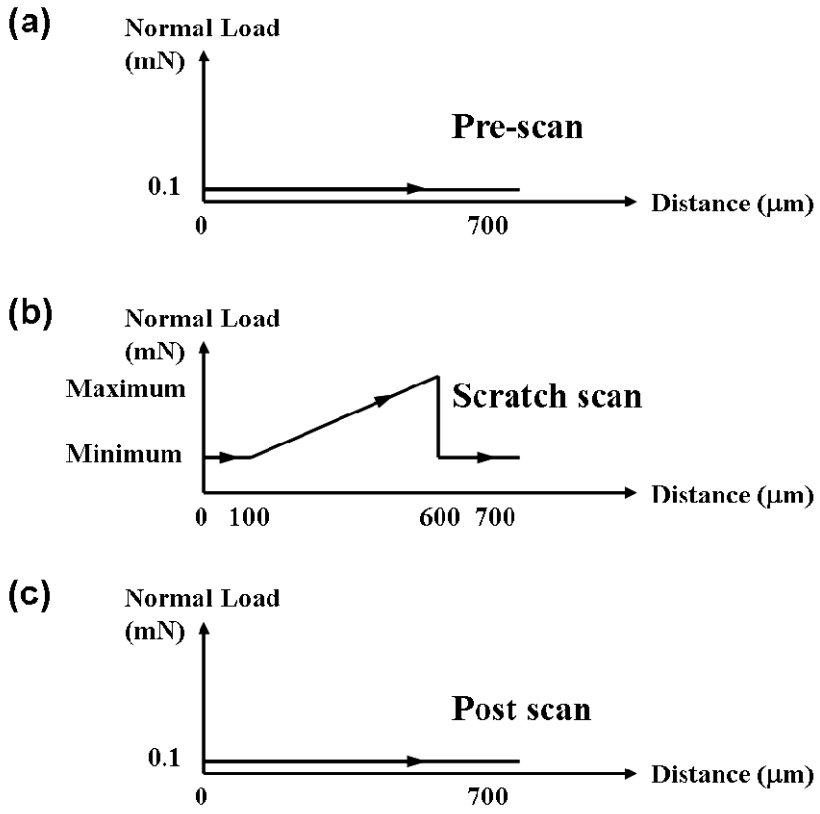


Figure 2.1 Schematic of the three steps of a scratch test.

Test samples should be prepared as specified by the provider, so as to reflect the state of the samples as they would be used in service. The scratch test is conducted on the smooth flat surface of a coating on a hard substrate. Detailed of sample specification including sample size, thickness and related material properties should be recorded. In each test, the testing condition should be controlled at a room temperature of 23 °C ±

2 °C and a relative humidity of 50 % ± 5 %. The allowable drift rate is selected to be 2.0 nm/s, the scratch velocity sets at 10 μm/s, the surface approach sensitivity is 30 % and surface approach velocity is 10 nm/s, the surface approach distance is 3000 nm. However, for samples with a rougher surface it may be necessary to adjust the distance to 5000 nm.

There are two primary apparatuses applied so as to implement the scratch protocol: a single-probe scratch tester and a high resolution reflection optical microscope. The details of the instruments are described in the next chapter, and the basic requirements of the apparatuses are described here:

*Single-probe scratch tester*

Instrumented nanoindenter or other kind of a single-probe scratch tester can be used. The instrument is adopted to perform the constant and progressive force scratches and keep track of the force-feedback data. The maximum applied normal load capability should be at least 50 mN and a minimum force of 20 μN. Note that all scratch tests in this report were conducted using a nominal 10 μm 90 diamond tip, which has a sphere head and the semi-apical angle of the cone is around 45° (see Appendix A). The tip should be cleared with ethanol before the task. The scratch velocity is set at 10 μm/s. The scratch length varying from 500 μm to 1000 μm depends on test samples. Scratch data, such as the initial and residual penetration depths, friction coefficients, and friction forces along the scratch, should be recorded.

*High resolution reflection optical microscope*

Laser scanning confocal microscope or other high resolution optical microscope can be used in this test method. Laser scanning confocal microscopy (LSCM) is a

noninvasive technique for measuring the surface morphology and subsurface microstructure without contacting sample surface directly. The scratch morphology and damage patterns can be assessed and observed clearly using LSCM. For consistency, all of the samples will be measured at 16 hours after scratch tests were performed. Magnification can be achieved between 5x and 150x using different lenses of 5x, 10x, 50x, 100x and 150x. A two-dimensional (2D) projection and the subsequent 3D profile analysis of a selected region should be recorded and used for measuring the scratch profile.

### 2-1.2 Protocol

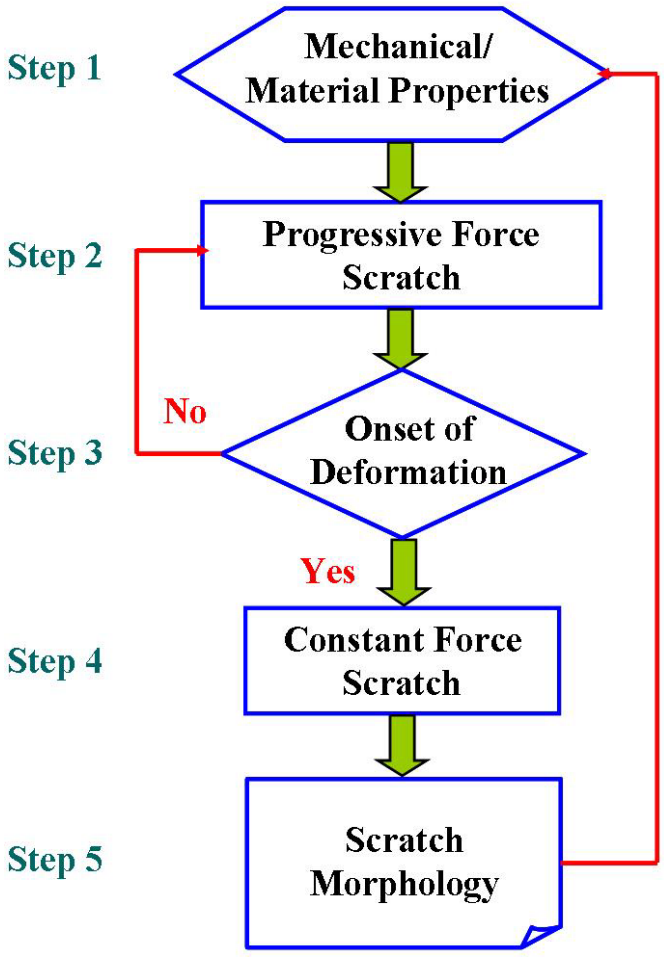


Figure 2.2 The flowchart of experimental protocol for scratch testing.

Figure 2.2 shows the experimental protocol for the revised PSI scratch test method (this protocol doesn't include the optical scattering section in the original PSI test method), the steps are as follow:

*Step 1. Mechanical and material properties*

Mechanical and materials properties can strongly influence the results of scratch tests. Therefore, it is important to record these properties and any alternations in the sample conditions (such as annealing, polishing) prior to tests. These properties include: material composition, mechanical modulus and hardness (bulk and surface), glass transition temperature, surface morphology, subsurface or microstructure (including cystallinity and filler dispersion), and other remarks on materials if necessary. In this study, the surface and bulk mechanical properties (modulus and hardness), and glass transition temperature were investigated using instrumented nanoindention and dynamic mechanical thermal analysis (see Appendix C).

*Step 2. Progressive force scratch*

Initially, a progressive force scratch (PS) test is used to estimate an approximate range of scratch damage and the onset force of elastic-plastic deformation. Figure 2.3 shows a set of three progressive force scratches in the range of 0 mN to 30 mN. Since the onset force is a quantity to rank the scratch resistance, it is important to measure the accurate value of onset force. If the force range of a PS test is not suitable, for example, no elastic-plastic deformation is observed, that a new set of force will be chosen, and the PS test will be repeated to determine onset force. The details of the onset force will be introduced in the next step.

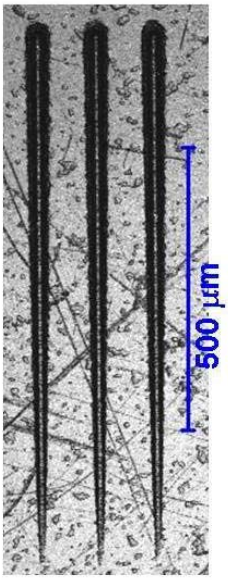


Figure 2.3 LSCM images of three progressive force scratches: the force range: 0 mN to 30 mN, with a scratch length of 1000 μm.

In this report, the minimum scratch load should be set at 0 mN, and the maximum scratch load should be set at 30 mN or 50 mN. The scratch length should be set to be 500 μm or 1000 μm.

*Step 3.* *Onset of deformation*

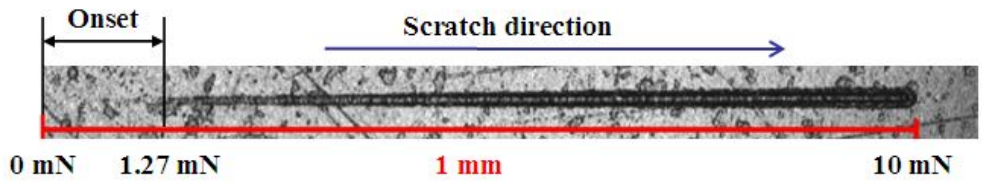


Figure 2.4 LSCM image of the onset force under a PS with loads ranging from 0 mN to 10 mN.

The onset force is defined as the force at which the scratch damage changes from elastic (fully recovered) to plastic deformation. The onset force value is determined from the LSCM image at 5x or 10x magnification, Figure 2.4 shows a LSCM image of a PS at the force range from 0 mN to 10 mN. The onset force at which the scratch damage becomes visible can be obtained by converting the damage position to the applied force. If the onset force is properly identified or estimated, the protocol moves to Step 4 – "Constant force scratch" for more precise determination of the onset force. If not, the protocol returns to Sept 2 – to repeat "Progressive force scratch" with a more appropriate force range.

*Step 4. Constant Force Scratch*

From a PS test, one can estimate the onset force using LSCM images at low magnifications. To get a more precise measurement of the onset force, an array of constant force scratch (CS) tests is needed. Typically, an entire array is consisting of five (or more) pairs of constant force scratches with corresponding forces determined from PS tests, as shown in Figure 2.5. Where, $F_{onset}$ is the onset force determined from PS.

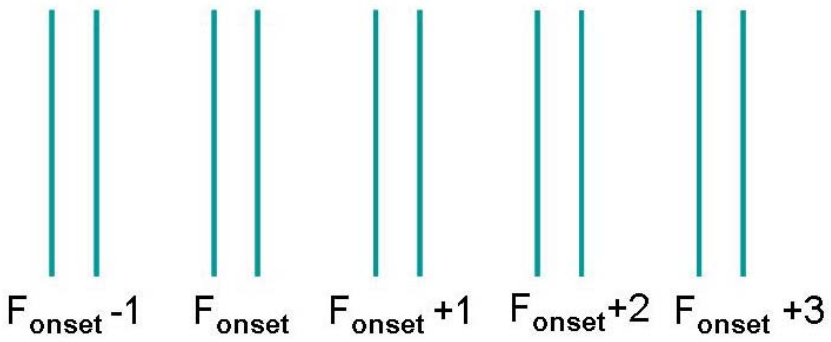


Figure 2.5 Schematic of an array of CS tests consisting of 5 pair scratches.

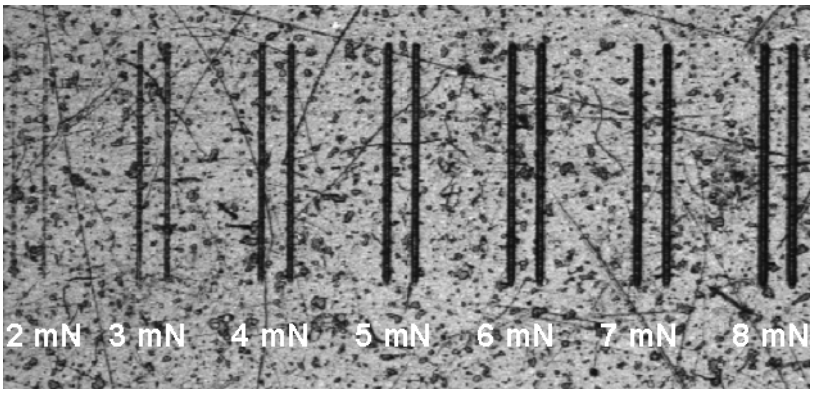


Figure 2.6 An array of constant force scratches of different scratch loads, as indicated in the graph.

Figure 2.6 shows the CS array of various constant scratch forces: 2 mN, 3 mN, 4 mN, 5 mN, 6 mN, 7mN, and 8 mN. As shown in the figure, the scratches of 2 mN scratch load are almost invisible. Thus, the actual onset force is assessed to be 3 mN.

*Step 5. Scratch morphology*

The scratch morphology including scratch width, depth, pile-up and damage patterns can be characterized using LSCM at the high magnifications. The images measured by 150x magnification are used in this study. Figure 2.7 shows a cross profile of a CS at 30mN. Here, $W_p$ is defined as the peak-to-peak scratch width, $D_f$ is the full penetration depth, and $h_b$ is the pile-up height. Figure 2.8 shows a scratch profile (tail) at the end of a CS at 30 mN with the measuring of the front contact length $a_f$, the rear contact length $a_r$ and the rear contact angle $\omega_a$. $\omega_{average}$ is the average value of the two contact angles from the rear tail portion.

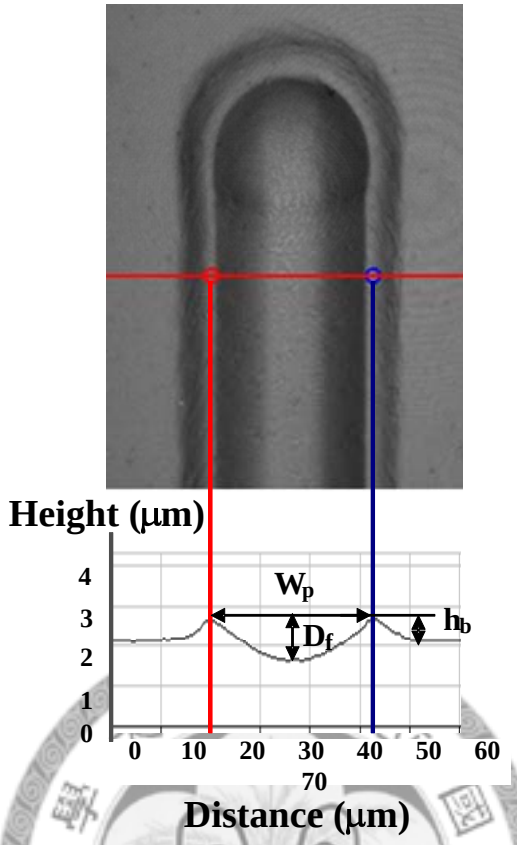


Figure 2.7 Schematic of a scratch cross profile of a CS at 30 mN. The symbol is defined in the text.

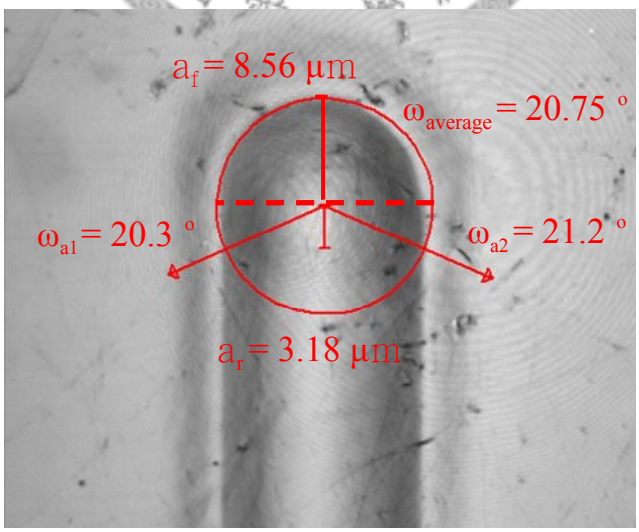


Figure 2.8 Schematic of a scratch tail with the measuring of the front contact length $a_f$, rear contact length $a_r$ and the rear contact angle $\omega_a$ under a CS at 30mN.

### 2-1.3 Report

Several experimental parameters must be recorded form pre-scan, scratch scan and post scan procedures, such as the applied load on sample, displacement curves, penetration depth, friction coefficient, residual roughness, and residual morphology. For example, Figure 2.9 shows the typical recorded data obtained from the instrumented nanoindentation. The percentage of recovery can be calculated by Equation (2.1).

$$R_p = \frac{D_i - D_r}{D_i} \times 100 \tag{2.1}$$

Where, $R_p$ is the percentage of recovery, $D_i$ is the initial penetration depth, and $D_r$ is the residual penetration depth. $D_i$ and $D_r$ were obtained from the instrumented indentation scratch test.

Also, the residual roughness level indicates the damage degree of the scratch, and it is attained from the post scan.

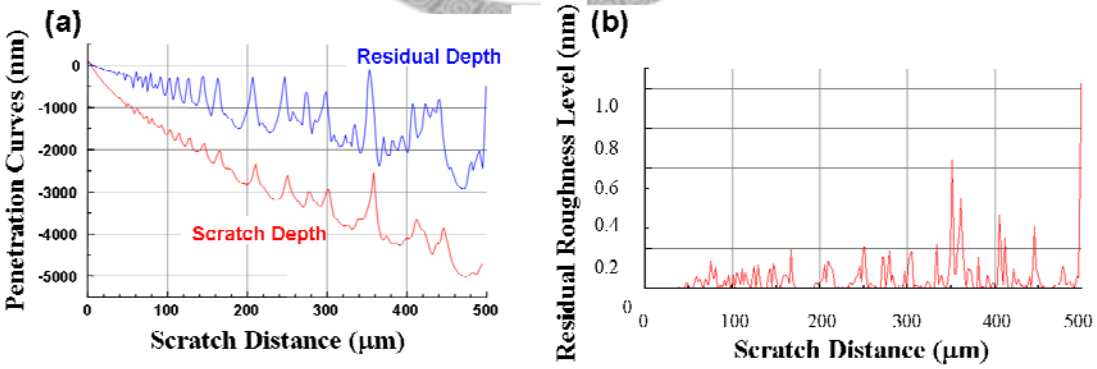


Figure 2.9 The results under a progressive scratch test: (a) the penetration curves (b) the residual roughness level.

The following information should be reported for a scratch test:

1. Type of coating and the material (chemical and physical) and mechanical properties.
2. The progressive force scratch: force range and scratch conditions.
3. Onset force of deformation determined by PS using LSCM.
4. The constant force scratch: force range and scratch conditions
5. Onset force of deformation determined by constant force scratch using LSCM.
6. Characterization of scratch damage modes using LSCM, including the parameters from scratch tails and cross profiles.
7. Penetration depths, recovery, and friction coefficient data for both PS and CS tests recording by instrumented nanoindenter.

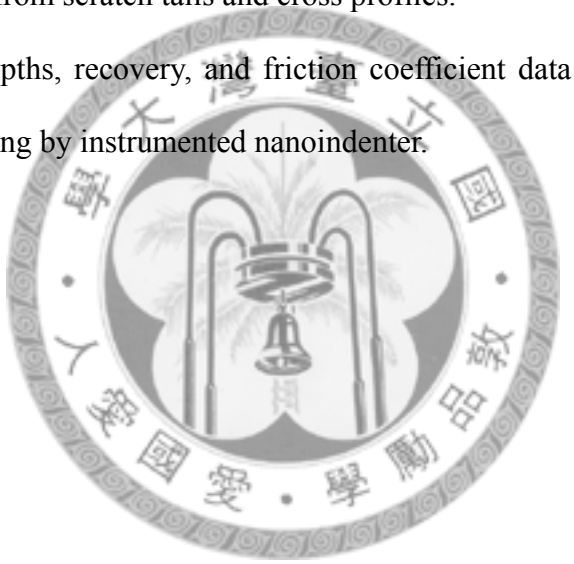

## 2-2 Materials

### 2-2.1 Epoxy

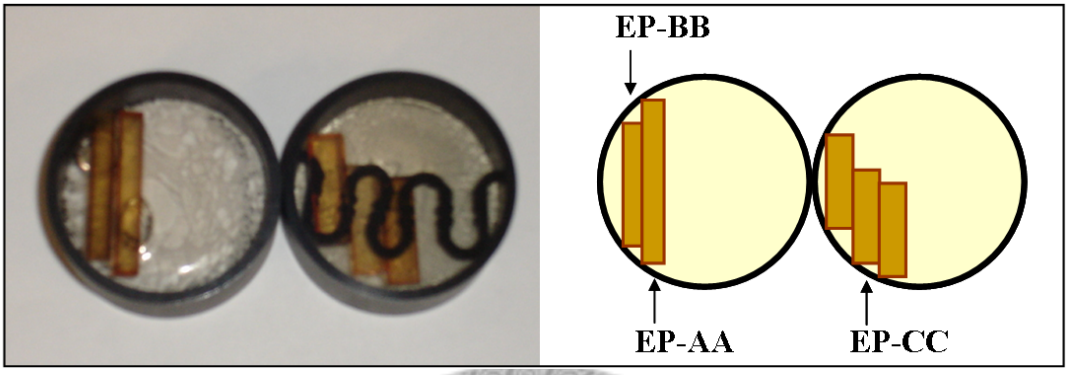


Figure 2.10 Photo and schematic of thermoset epoxy samples.

Three amine-cured bisphenol A epoxies were supplied by Dow Chemical, Figure 2.10 shows the photo and schematic of epoxy samples. The samples were mounted in epoxy mold and polished to provide a smooth surface for the indentation and scratch test. These samples are classified as thermoset polymers and have crosslinked network structures. The molecular weight $M_c$ between the crosslinks is varied by increasing the number of repeat units in the amine crosslinker. As a result, the glass transition temperature $T_g$ decreases when increasing the molecular weight. Table 2.1 shows the molecular weight and glass transition temperature information of three samples.

Table 2.1 $M_c$ and $T_g$ information of three epoxy samples provided by Dow Chemical.

| Sample Name | molecular weight $M_c$ (g/mol) | Glass transition temperature $T_g$ (°C) |
|---|---|---|
| EP-AA | 630 | 117 |
| EP-BB | 920 | 88 |
| EP-CC | 5290 | 71 |

## 2-2.2 Polyurethane – Nanosilica Coatings

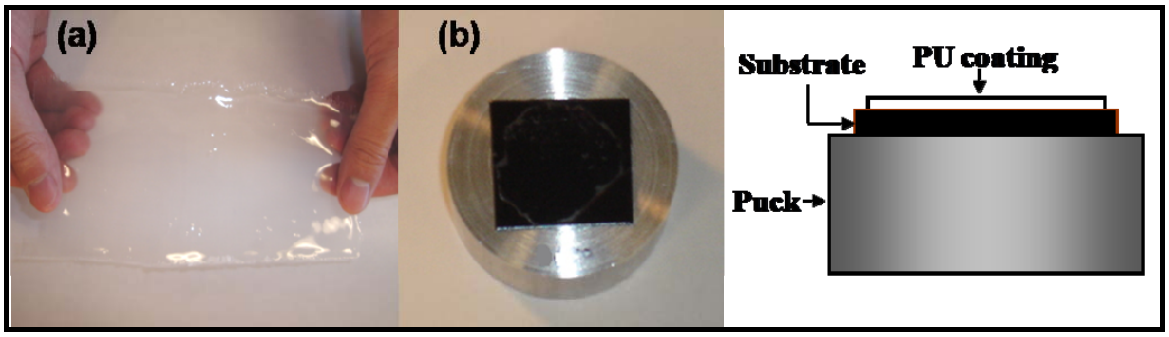


Figure 2.11 (a) The photo of a polyurethane free film, (b) the photo (top view) and schematic (side view) of a PU coating glued on a black substrate and mounted the metal puck.

Table 2.2 The formulation of the 2K-polyurethane part A is the acrylic component and part B is the crosslinker.

| Part A | wt(%) |
|---|---|
| Acrylic Polyol (68%) | 49.5 |
| MAK (Methyl Amyl Ketone) | 15.14 |
| EEP (Ethyl 3-Ethoxypropionate) | 8.59 |
| Butyl acetate | 2.54 |
| Cellulose Acetobutyrate (40 %) | 5.07 |
| UV Stabilizer 1 | 0.33 |
| UV Stabilizer 2 | 0.49 |
| Polysiloxane wetting agent | 0.16 |
| Total part A | 81.82 |
| Part B | wt(%) |
| Desmodur N-75 (75%) | 18.18 |
| Total | 100 |

Figure 2.11 shows (a) photo of a polyurethane (PU) films prepared by a draw-down technique; (b) the photo and schematic of a PU coating glued on a black substrate

and mounted the metal puck for scratch test. Two series of polyurethane automotive refinish coatings samples provided by BYK-USA were used in this study. Each series contains one control sample: pure PU with no nanoparticle, and three polyurethane–nanosilica (PU-$SiO_2$) coatings containing 2 % nanosilcia with different dispersants. The polyurethane are 2K (two-component) coatings consisting of acrylic part (Acrylic Polyol, Joncryl 909) and crosslinker part (Desmodur N-75, a curing agent). The detailed formulation of PU is listed in Table 2.2.

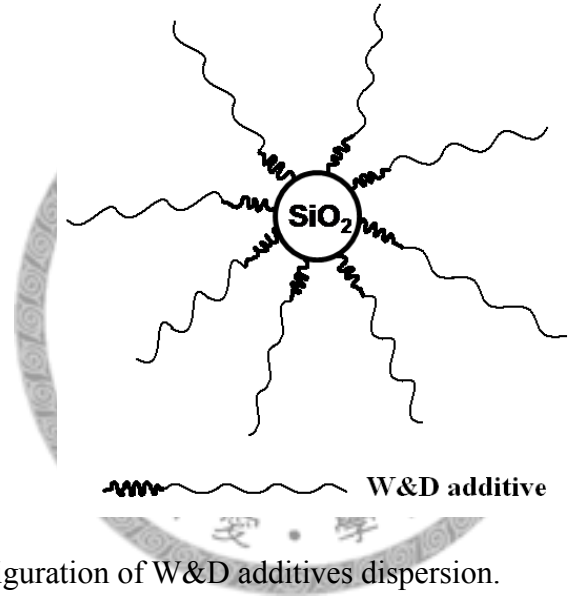


Figure 2.12 The configuration of W&D additives dispersion.

The nanosilica particles (sizes ≈ 20 nm) have been pre-dispersed in solvent-borne suspensions using different wetting and dispersing (W&D) additives (copolymers of different polarities). Figure 2.12 shows the illustration of W&D additives dispersion configuration, the additives can be linear or branched. Due to different architectures of W&D additives, the surface properties of $SiO_2$ exhibit different polarities. The pre-dispersed nanoparticles were added into part A (stir for 2 minutes, 600 rpm) and then part B was added into the mixture (stir for 10 minutes, 600 rpm). The final PU coatings were prepared by a draw-down application, dried in the air for 2 hours and cured in an

oven at 120 °C (248 °F) for 30 minutes. Series 2 films was prepared almost 6 months later after the preparation of series 1 films. Note: The formulation and preparation processes are the similar, but $T_g$ are different (series 1 ≈ 90 °C, series 2 ≈ 55 °C). It would due to slightly differences in the PU chemistries or solvent curing conditions. The final dry film thicknesses are also different: series 1 ≈ 0.06 mm and series 2 ≈ 0.12 mm.

Table 2.3 Lists of two series of polyurethane-nanosilica samples with 2 % $SiO_2$ nanoparticles of different W&D additives and polarities.

| Series | Sample Name | Nano Silica | W&D Additive |
|---|---|---|---|
| 1 | PU-CTRL1 | No | - |
| | PU-A1 | 2 % | linear copolymer; low polarity |
| | PU-B1 | 2 % | linear copolymer; medium polarity |
| | PU-C1 | 2 % | branched copolymer; high polarity |
| 2 | PU-CTRL2 | No | - |
| | PU-A2 | 2 % | linear copolymer; low polarity |
| | PU-B2 | 2 % | linear copolymer; medium polarity |
| | PU-C2 | 2 % | branched copolymer; high polarity |

# Chapter 3 INSTRUMENTATION AND ITS APPLICATIONS

## 3-1 Laser Scanning Confocal Microscopy (LSCM)

The objective of this section is to understand the principle of laser scanning confocal microscopy (LSCM) and its measurement capabilities. Many material properties, such as surface roughness, metallic flake orientation, particle dispersion in the coating, can be obtained by analyzing LSCM images. The scratch morphology, including scratch width, depth, length, and damage patterns, can also be characterized using LSCM. Several examples will be used to demonstrate the applications of LSCM in this section.

### 3-1.1 Basic Principle of Laser Scanning Confocal Microscopy

A Zeiss model LSM510 reflection laser scanning confocal microscope was used to characterize surface properties, subsurface microstructures, and scratch profiles of polymeric coatings. A helium/neon laser having a wavelength of 543 nm was used, and the analyses of the raw data were processed using the software provided by Carl Zeiss Co. [25].

Figure 3.1 shows the schematic of optical layout of the LSCM system. It is called confocal because the laser lights are cohered and collected in the same light path [26]. The effect of the pinhole is to filter the light that doesn't come from the single focal plane. Compared to the regular compound microscope, the focal plane of LSCM is

much smaller. The depth resolution in the axial direction (z direction) is commonly defined as the distance between half-power points (3-dB points) of the intensity response. It is determined by the wavelength, numerical aperture of the objective, and the size of the pinhole, as shown in Equation (3.1).

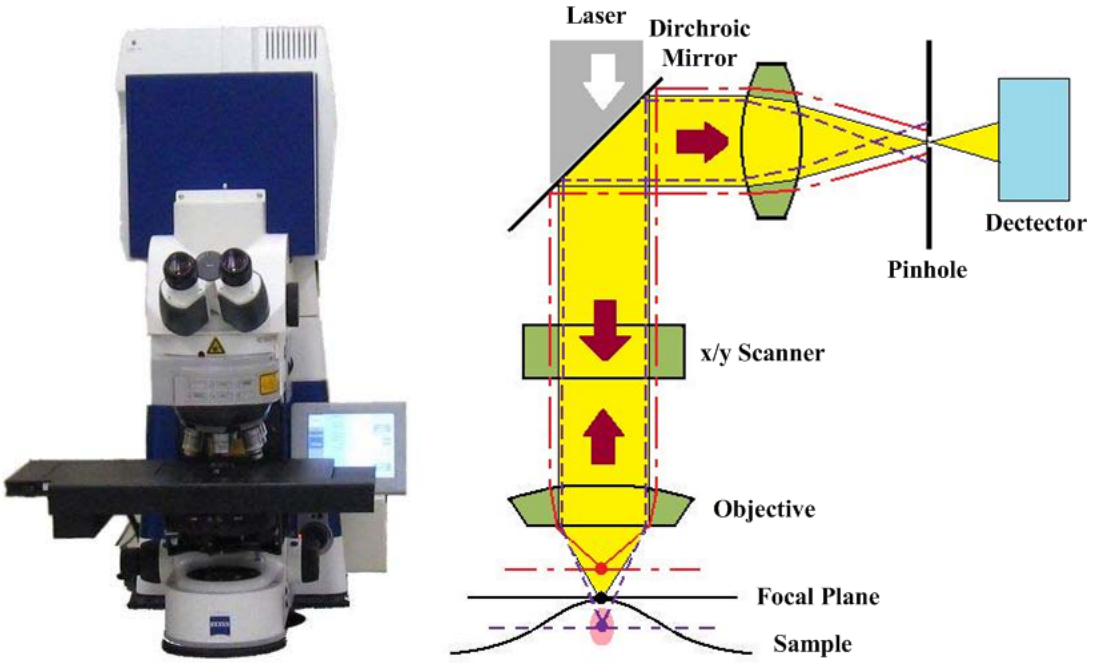


Figure 3.1 The photo (left) and schematic of optical layout (right) of LSCM system.

$$D_Z(3dB) = \frac{0.89\lambda}{(NA)^2} \tag{3.1}$$

Where λ is the wavelength and NA is the numerical aperture. The 3-dB depth resolution for a lens with NA = 0.95, measuring in the air, of various wavelengths, is shown in Table 3.1.

Table 3.1 Depth resolutions for NA = 0.95 [26].

| Wavelength λ | Depth resolution $D_z$ (3dB) |
|---|---|
| 633 nm | 414 nm |
| 546 nm | 357 nm |
| 436 nm | 285 nm |
| 365 nm | 238 nm |
| 248 nm | 162 nm |

The numerical aperture, NA, characterizes the range of angles over the sample (see Figure 3.2). The definition of NA is shown as Equation (3.2). Here, $\theta^{NA}$ is the half-angle of the maximum cone of light that can transit the lens, and n is the refractive index of the medium in which the lens is present.

$$NA = n \sin \theta^{NA} \tag{3.2}$$

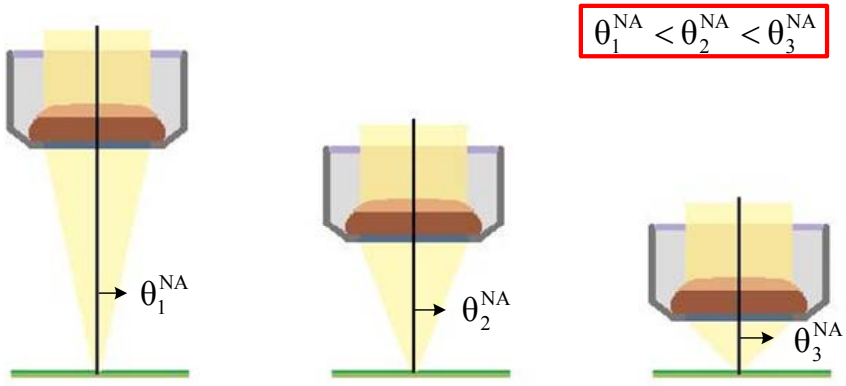


Figure 3.2 Schematic of the effect of the numerical aperture on the light collected through a lens.

It is indicated that a lens with a larger NA has a higher resolution and brighter images than one with a smaller NA. The effect of NA under the same magnification is illustrated in Figure 3.2.

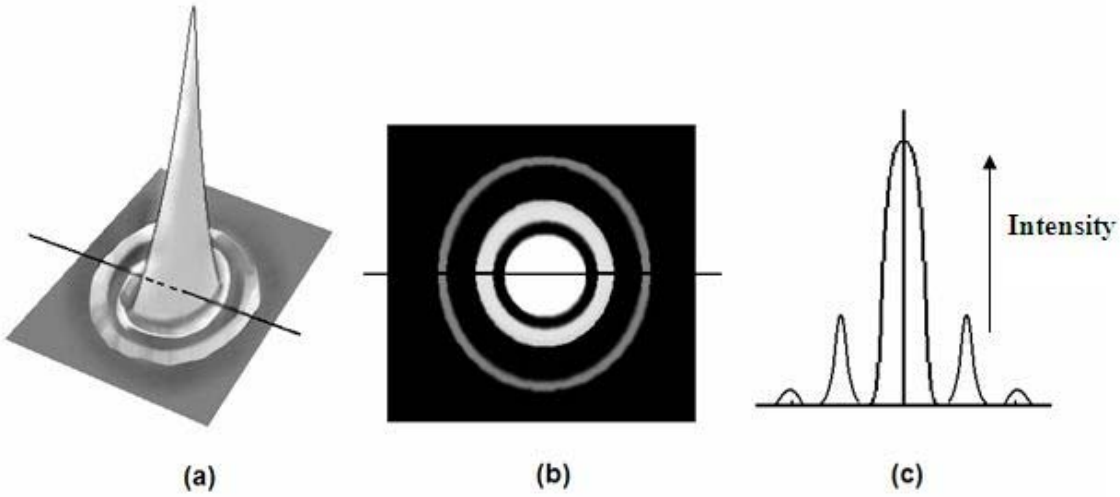


Figure 3.3 (a) 3D image of the sample surface (b) Intensity distribution of plane image (c) Intensity from the profile of the airy disk.

The intensity is directly proportional to the fourth power of NA, and inversely proportional to the square of the magnification. Figure 3.3 shows that the light strength in each spot is obtained by weighing the intensity distribution of the plane image. The intensity distribution is varied with the height to the real sample surface. For example, the darker the area in an intensity distribution plane means it is farther away from the objective. Hence, the distance from objective to every single point in the field can thereby be determined.

By traditional methods via optical microscope, it doesn't have the capability of scanning entirely sample in z direction automatically in sub-micron precision. As a result, only a few of discontinuous slices are obtained and information between slices is often missing. However, LSCM scans the sample plane with an overlapping stack of z-scan in succession, as shown in Figure 3.4. Therefore, the whole depth information with a series of optical slices can be obtained by LSCM.

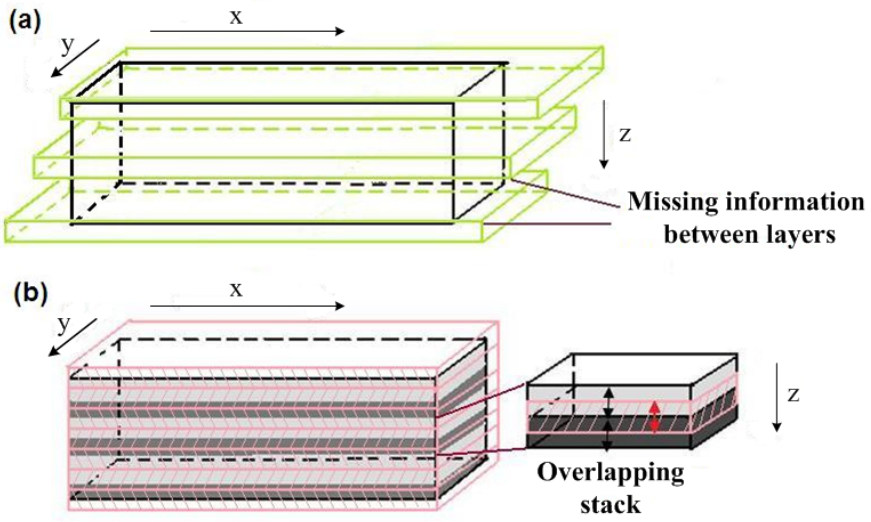


Figure 3.4 (a) Missing z-scan images information between layers by traditional microscope (b) Overlapping stack of z-scan images by LSCM.

LSCM can measure a wide range of area by altering the objective from 5x to 150x. The measure area can be as large as 1.68 mm × 1.68 mm down to as small as 56.3 μm × 56.3 μm without digital magnification. Each image is consisted of 512 × 512 pixels. The z-step size used to scan is 1 μm for an objective of 5x, 0.5 μm for an objective of 10x, and 0.1 μm for objectives of 50x, 100x and 150x, respectively.

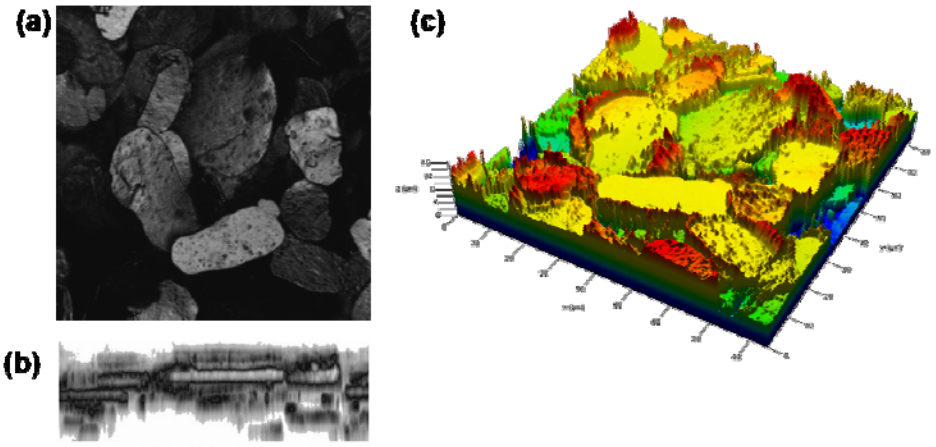


Figure 3.5 (a) 2D projection (x-y plane) (b) Z projection (side view) (c) 3D topography.

LSCM images can be presented in two-dimensional (2D) projection and 3D topography, as shown in Figure 3.5. Projection images are stacked through all the slices of the same direction into a single plane. Usually called 2D projection (Figure 3.5a), an image constructed in the x-y plane can be obtained by stacking images in the z direction. The side view projection (Figure 3.5b) stacks through the y direction and is constructed in the x-z plane.

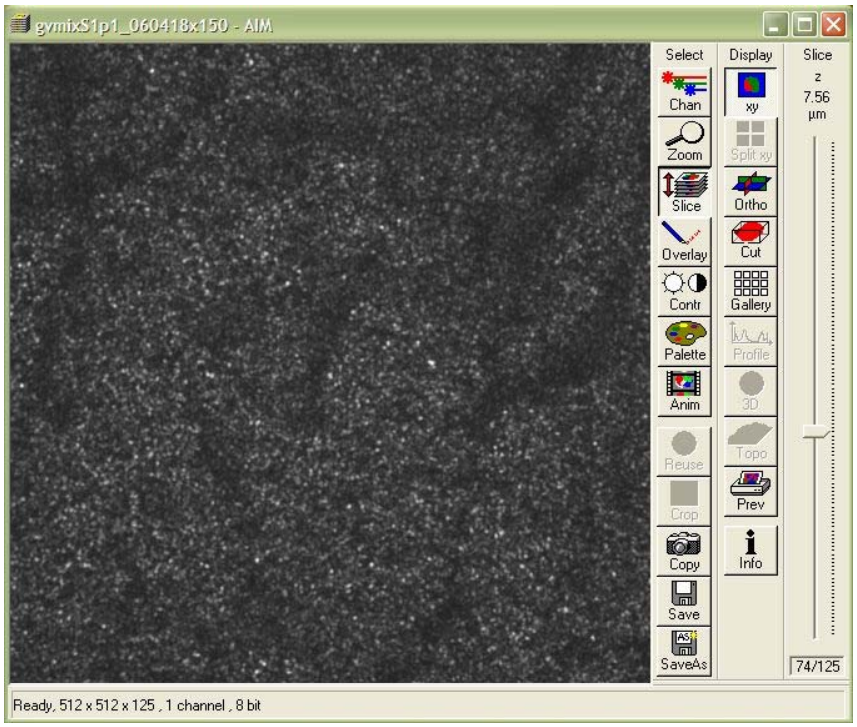


Figure 3.6 The single slice/layer image of the subsurface.

In addition to the projection image, a single slice/layer image from a particular z position can be measured and stored separately. A single slice image can also be selected from a stack of LSCM images using the "Slice" function (right-hand-side indicator of Figure 3.6). This type of single slice image often provides a unique feature describing subsurface microstructure, which can be different from surface microstructure. Time-dependent measurements can also be obtained by scanning a single slice image at the same location for a period of time. This type of measurement is

very useful for recording creep behavior of a sample under stress/strain or the recovery of scratch damage as a function of time.

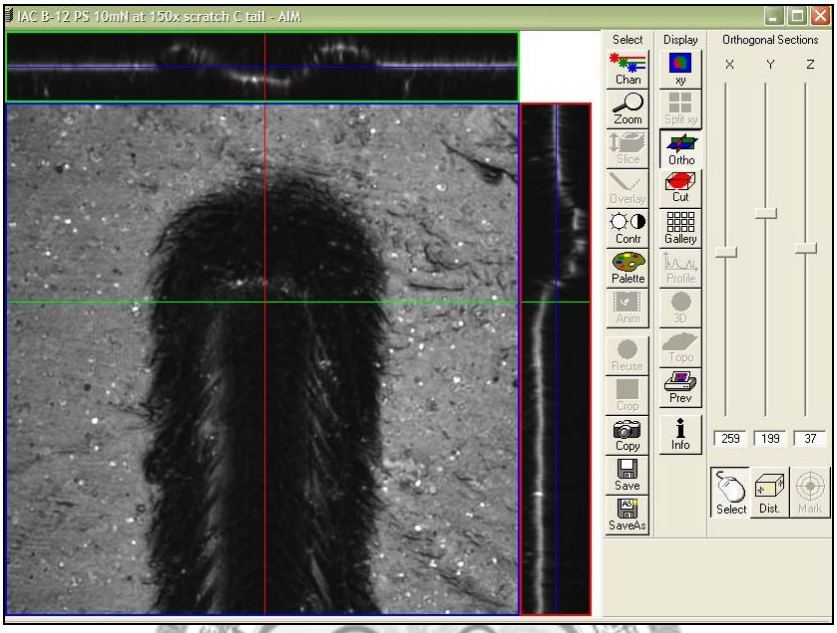


Figure 3.7 The image of an orthogonal presentation.

Figure 3.7 shows the "ortho" function. The red line in the vertical direction indicates the different x positions of the y-z plane. By changing the x position, the profile of y-z plane can be altered and shown on the rectangular area in the right side of the screen. Similarly, changing the y position using the green line in the horizontal direction can alter the profile of the x-z plane which is shown on the rectangular area in the top of the screen. Therefore, the profile in any location of the sample can be revealed.

The other important feature of the LSM image browser program is the "Topo" function. In this function, the 3D topographic map, height information in a specific location, line profile at x-z plane, and roughness value of a surface or a single line can be determined. For example, Figure 3.8 shows the line profile and the height information of a scratched sample.

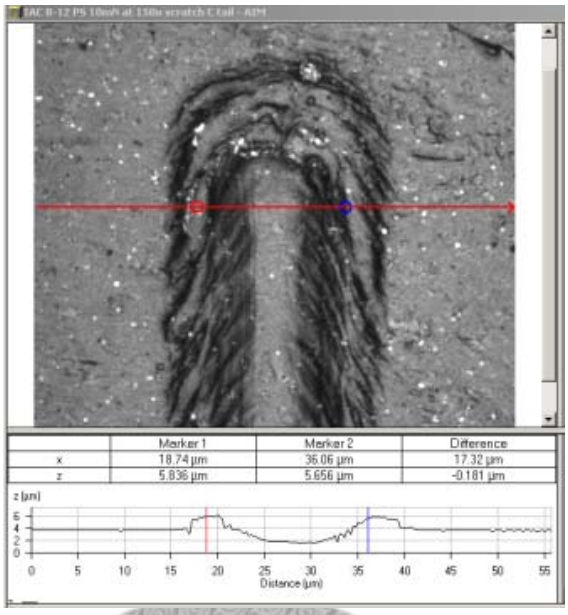


Figure 3.8 The line profile and height information of an scratched sample.

### 3-1.2 Examples of LSCM Application

*1. Surface roughness and metallic flake orientation characterization*

Surface roughness is a measure of the texture of a sample surface, and is quantified by the vertical deviations associated to the ideal surface. The higher deviation means the greater degree of surface roughness, and the smaller value of surface roughness means smoother surface. Roughness is associated with the friction and wear of materials. A surface with a large surface roughness value results in higher friction [27]. Surface roughness can be also used to monitor and correlate the physical and optical changes during UV degradation of coatings [28]. I.e. surface roughness can be an indicator for degree of degradation. As exposure time increasing, the surface roughness values increased and gloss values decreased (surface became dull).

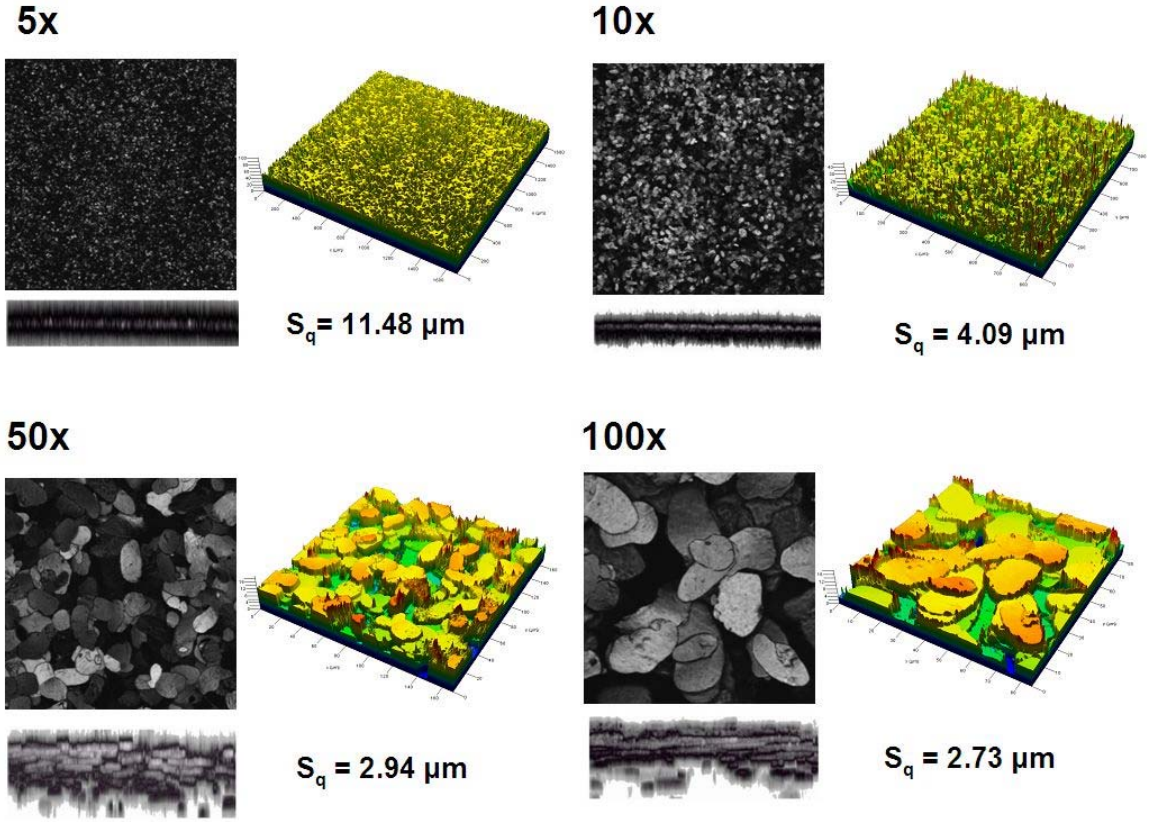


Figure 3.9 2D projection, z projection and 3D topography at different magnifications.

The surface roughness values are also used to characterize orientation of the metallic flakes in a coating. Figure 3.9 shows the 2D projection, side view and 3D topography of a coating containing metallic flakes at different magnifications. The root mean square (RMS) surface roughness $S_q$ is defined as Equation (3.3) and Equation (3.4).

$$S_q = \sqrt{\frac{1}{N_x \cdot N_y} \cdot \sum_{i=1}^{N_x} \sum_{j=1}^{N_y} \cdot [z(x_i, y_j) - S_c]^2} \tag{3.3}$$

$$S_c = \frac{1}{N_x \cdot N_y} \cdot \sum_{i=1}^{N_x} \sum_{j=1}^{N_y} \cdot z(x_i, y_j) \tag{3.4}$$

Here, $z(x_i, y_j)$ is the surface height at position $(x_i, y_j)$, and $N_x$ and $N_y$ are the number of pixels in the x and y direction, respectively. The roughness values are different at

different measurement sizes. The RMS is smaller for high magnification at smaller measurement area. Therefore it is very important to compare the RMS values at the same measurement size.

The metallic flake orientation can also be observed through the 3D and side images. In the 3D view, the shape and the direction of each metallic flake show distinctly. The distribution, such as gap and overlap among the metallic flakes, is presented in the side images. To characterize the orientation of the individual metallic flake is often time-consuming, so that collected surface roughness values can be used as a measure for the orientation of all metallic flakes in the total measured area, which is directly influence the appearance of the coatings, Using surface roughness value to quantify the metallic flake orientation has been adopted as a QC tool in the coating industry and provides a new scientific-based approach to characterize metallic coatings [29].

## 2. *Particle dispersion characterization*

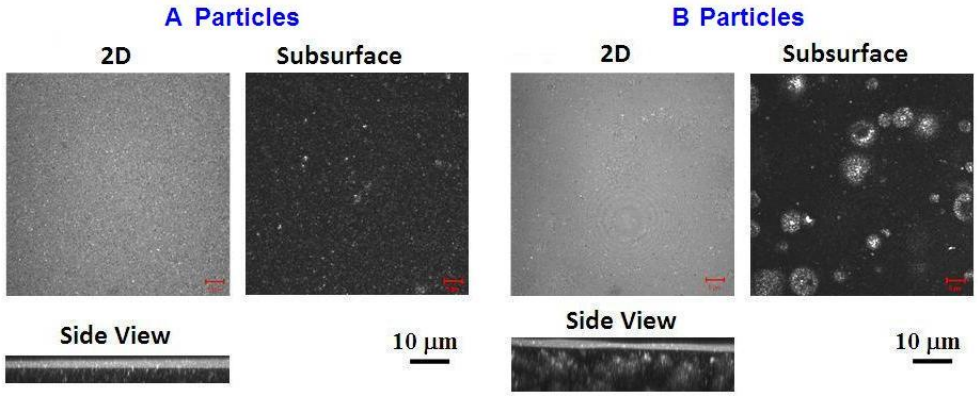


Figure 3.10 2D projection, a single- layer subsurface, and the side view images for coating systems containing two particles [30].

The addition of nanoparticle into polymeric coatings influences performance (appearance, service life, and mechanical properties) of polymer nanocomposites. Poor

dispersion of nanoparticles often results poor appearance and durability. It is important to measure the particle dispersion in the coatings and correlate the dispersion to performance properties such as appearance and mechanical properties. The surface morphology and nanoparticle dispersion can be measured using LSCM. Figure 3.10 shows the different nanoparticle dispersion results in a 2D projection, a single-layer subsurface image, and the side view projection images.

As shown in the figure, the z-depth is different for particle A system and particle B system at the side view. The A particles are distributed uniformly and tightly near the surface. Oppositely, the B particles are loosely packed so that the gap between the particles is larger. In such a case, the penetration depth for particle B system is about twice of the A particle system due to the laser penetrating deeper into the coating through the gaps.

### 3. *Scratch morphology characterization*

The scratch damage is often used to assess scratch resistance of the coatings [31-32]. LSCM can be used to characterize scratch morphology. Figure 3.11 shows a set of three progressive force scratches, which were generated using scratch force 0 mN to 30 mN at a total initial scratch length of 1000 μm. By measuring the final residual scratch length, we can calculate the onset force of elastic-to-plastic transition from the LSCM image. The onset force is defined as Equation (3.5). For example, in this case the residual scratch length $L_r$ = 850.71 μm, so that the onset force is 4.48 mN. Where, $F_{max}$ is the maximum progressive load, $L_i$ is the initial scratch length, and $L_r$ is the residual scratch length.

$$F_{onset} = F_{max} \times \frac{(L_i - L_r)}{L_i} \tag{3.5}$$

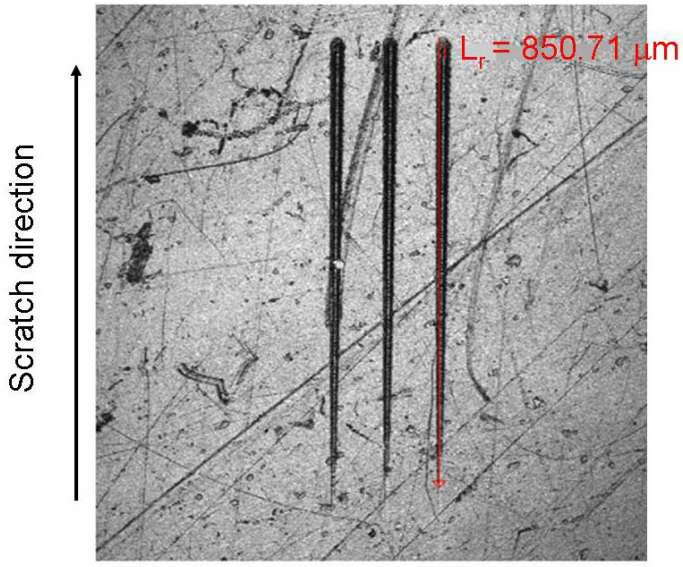


Figure 3.11 LSCM image of three progressive-force scratches in 2D projection presentation.

This onset force is a "quantity" we can use to rank the scratch resistance. The higher onset force indicates a higher scratch resistance. Also, from the scratch morphology at a high magnification, the overall scratch morphology, such as scratch width, depth, and damage patterns, can be determined. These quantities can also be used to rank scratch resistance, i.e. a wider scratch width a deeper scratch depth has a worse scratch resistance.

It is also important to monitor the recovery of the scratch damage as a function of time. Figure 3.12 shows the scratch width, depth and cross profile near the end force (~ 30 mN) at three times (8 hours, 7.5 weeks, and 4 months) after scratched. The shape changed dramatically at 7.5 weeks (purple line) from 8 hours (blue line). It shows that the scratch damages recovered, in some degree, in terms of the scratch depth. The surface shows the indication of materials reflowed so that the scratch profile is very different from regular scratch profiles like that one after 8 hours, even more, after 4 months (green), the profile becomes flatter, it is hard to compare to original profile.

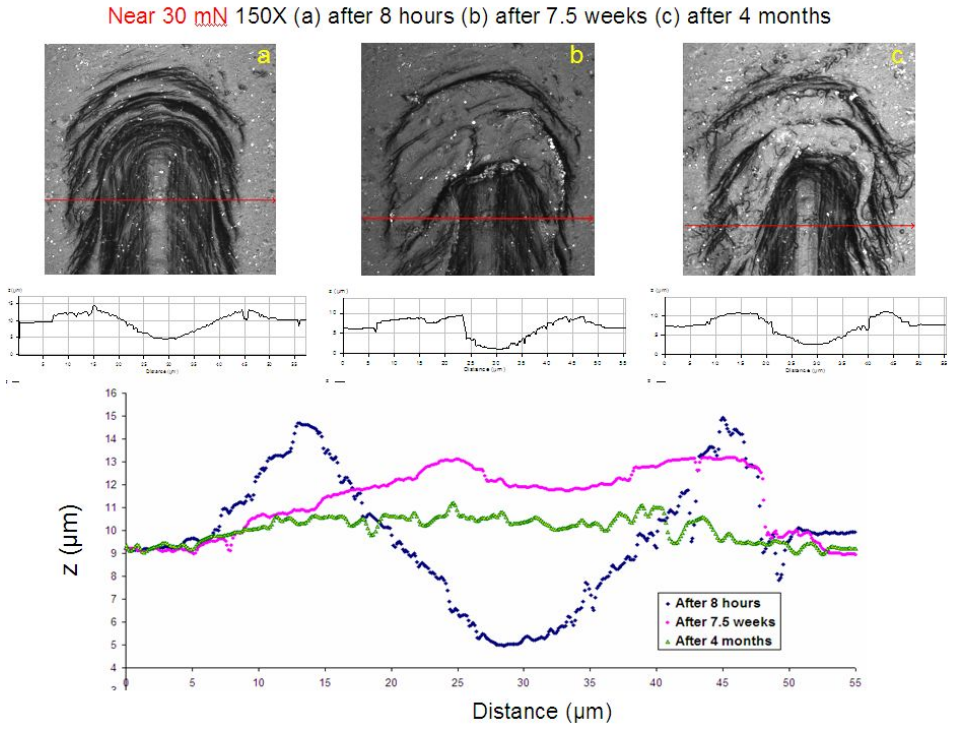


Figure 3.12 Cross profile of scratch tails (at the end force 30 mN) at three times scratches.

## 3-2 Instrumented Indentation Testing (IIT)

The purpose of this section is to introduce the theory and the basic principle of instrumented indentation testing (IIT). The load and displacement data measured from IIT are useful in deducing the modulus of elasticity, hardness, and contact harmonic stiffness. In addition, investigating the indentation testing results could help us to establish a comprehensive understanding of the surface properties of materials. The various testing conditions, such as tip geometry (shape and size), strain rate, velocity of contact, and maximum loading, could impact on the indentation and scratch results.

### 3-2.1 Basic Principle of Instrumented Indentation Testing

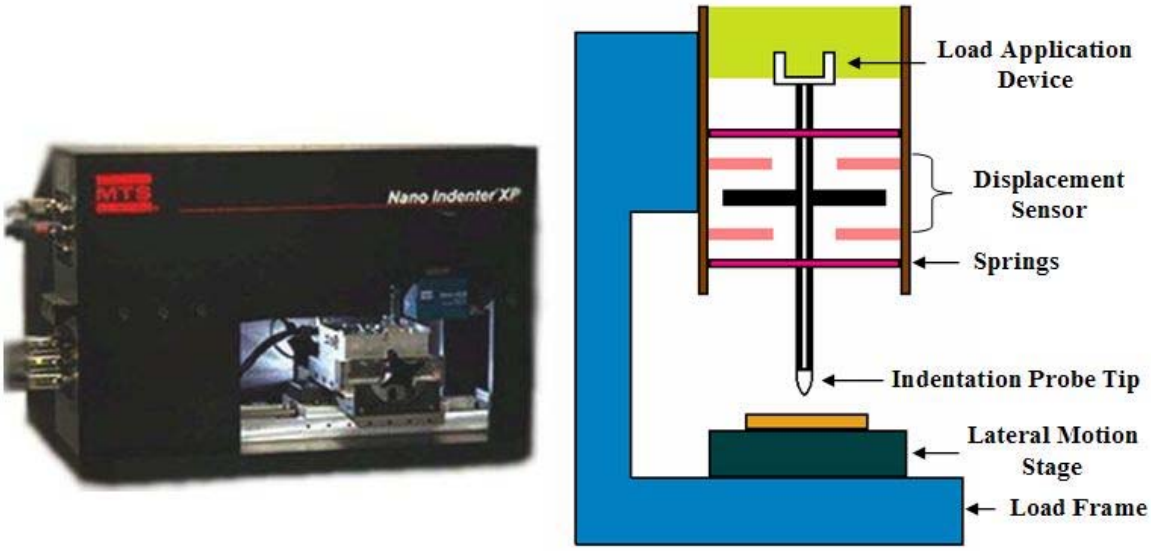


Figure 3.13 Photo and schematic of the Nano Indenter® XP system.

The instrumented indentation techniques have been developed over several decades [33], and are also known as depth sensing indentation (DSI). The techniques are commonly used in measuring the elastic modulus of thin films and small volumes. Oliver and Pharr introduced a method for measuring hardness and elastic modulus by

IIT [34-35]. The basic assumption of this method was analyzed by Sneddon [36]. He demonstrated the indentation testing of an elastic half space by a flat and a cylindrical punch so that the contact area between the indenter and the specimen can be approximated. Recently, studies on instrumented indentation techniques have resulted in improving the quasi-static force sensitivity and the maturation of continuous stiffness measurement (CSM) method [37].

The indentation measurements and scratch testing were performed using a Nano Indenter® XP system in this study, as shown in Figure 3.13. The load application device is composed of a coil and a circular magnet. Since the force is directly proportional to the current, by which a magnetic field is generated, and the force can be varied by changing the currents. After the operator sets the loading value, a current will be imposed on to the indenter and transformed to a loading. The resolution of the load is reported to be 50 nN. The displacement sensor is made up of three capacitive circular plates. The one fixed to the central indenter is limited by the others in the vertical direction. By observing the differences in current, the variations of the voltage and the gap due to the distance changes among the parallel plates can be correlated. The resolution of the displacement is reported to be 0.04 nm. In order to make sure the shaft slides smoothly along the perpendicular side rather than moving sideways, two special springs for the purpose of support are applied. The spring is designed to have very high stiffness in the horizontal direction and very low stiffness in the vertical direction so as to assist the axial motion of the shaft. In order to measure the friction force and the scratch profile, the sample is fixed on a lateral motion stage which provides an option to perform scratch testing.

The side views with a cone indenter present the indentation and scratch testing in Figure 3.14. Here, $\phi$ is the attack angle between the sample surface and the slope of the

cone. Indentation testing is performed by an axial load with a constant force and it comes down perpendicularly to the sample. Similarly, scratch testing is also carried out by an axial load with a constant or progressive force. The difference between the two tests is that the indenter in the scratch testing parallels to the sample instead of moving perpendicularly. The horizontal motion at a constant velocity in the scratch testing generates a slender scratch with special damage features.

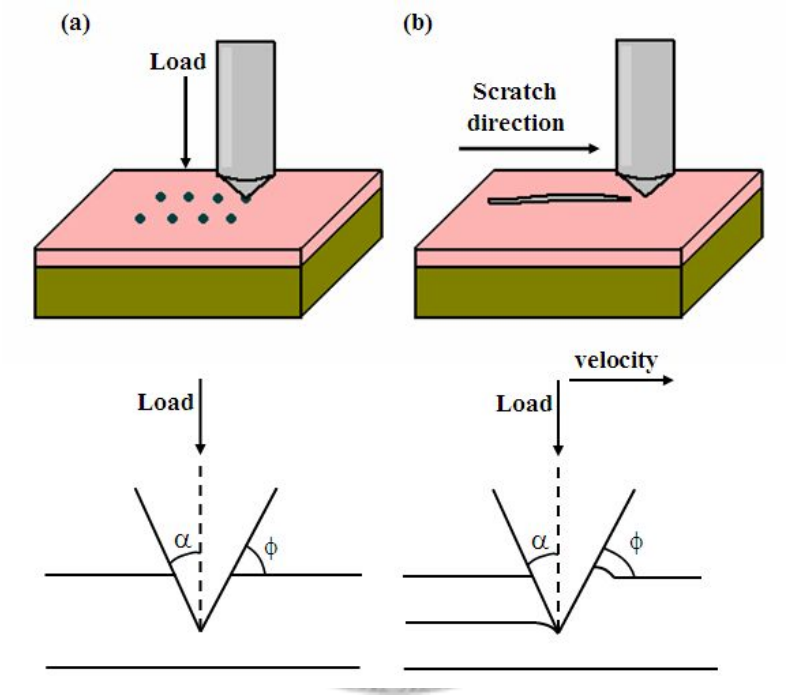


Figure 3.14 Schematic of (a) the indentation testing with a constant load (b) the scratch testing sliding with a constant (or progressive) load and a constant velocity [19].

The loading and unloading relationship for any punch (a solid of revolution of a smooth function) is defined as Equation (3.6).

$$P = \rho(h - h_f)^m \tag{3.6}$$

Where P is the indenter load, h is the indentation depth, $h_f$ is the residual depth after unloading, ρ and m are constant. The value of m relies on the punch geometries, such as m = 1 for flat cylinders, m = 1.5 for paraboloids of revolution and in the limit of

small displacements for the spheres, and m = 2 for cones. The load-displacement curve for an indentation testing is shown in Figure 3.15. Here, $h_{max}$ is the peak indentation depth, $P_{max}$ is the peak indentation load, and S is the contact stiffness.

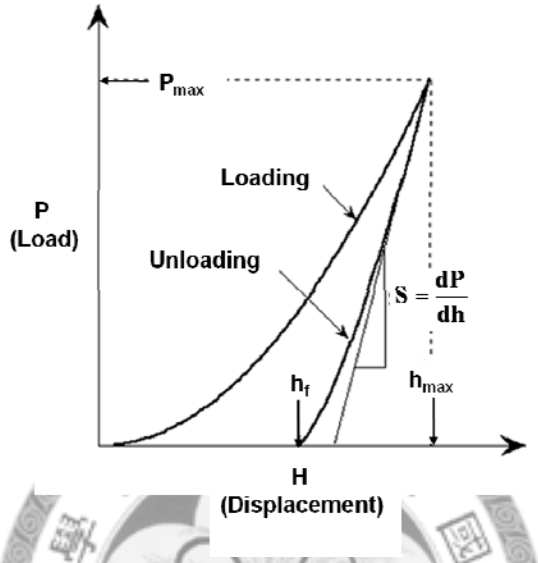


Figure 3.15 A typical load-displacement curve for an indentation testing [35].

Figure 3.16 illustrates the cross section of an indentation testing. Where $h_c$ is the contact depth, and $h_s$ is the displacement at the edge of the contact surface. The sum of those two parameters equals to the indentation depth, as shown in Equation (3.7).

$$h = h_c + h_s \tag{3.7}$$

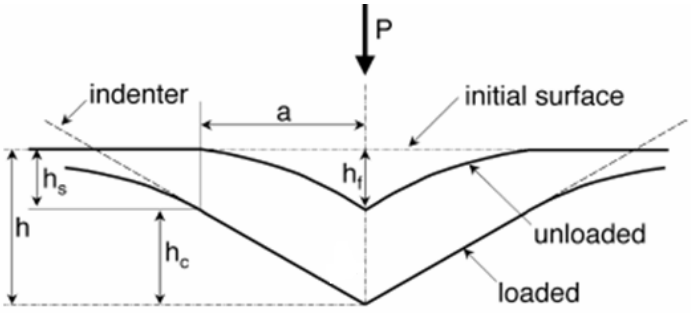


Figure 3.16 Schematic of a section through an indentation testing [35].

The contact stiffness S is also referred to elastic stiffness. It can be obtained directly from the slope of the unloading curve, as defined in Equation (3.8).

$$S = \frac{dP}{dh} = \rho m(h - h_f)^{m-1} = \frac{2}{\sqrt{\pi}} E_r \sqrt{A} \tag{3.8}$$

Here, A is the projected contact area and $E_r$ is the reduced modulus. The definition of $E_r$ is described as Equation (3.9).

$$\frac{1}{E_r} = \frac{(1-\nu^2)}{E} + \frac{(1-\nu_i^{\,2})}{E_i} \tag{3.9}$$

Where, E is the elastic modulus for the specimen, $\nu$ is the Poisson's ratio for the specimen, $E_i$ is the elastic modulus for the indenter, and $\nu_i$ is the Poisson's ratio for the indenter.

The contact depth $h_c$ is estimated using Equation (3.10) and Equation (3.11).

$$h_s = \kappa \frac{P_{max}}{S} \tag{3.10}$$

$$h_c = h_{max} - h_s = h_{max} - \kappa \frac{P_{max}}{S} \tag{3.11}$$

Where, $\kappa$ is a constant and depends on the indenter geometry. For example, $\kappa = 0.72$ for a conical punch, $\kappa = 0.75$ for a paraboloid of revolution, and $\kappa = 1.00$ for a flat punch.

The hardness, H, is defined in Equation (3.12).

$$H = \frac{P_{max}}{A} \tag{3.12}$$

Since the displacement value measured from the indentation testing is the amount of the displacements in the specimen and the load frame, the load frame compliance must be known with precision. The compliance relationship between the specimen and the load frame can be expressed by Equation (3.13).

$$C = C_s + C_f \tag{3.13}$$

Where C is the total compliance, $C_s$ is the compliance of the specimen, and $C_f$ is the

compliance of the load frame.

Because the compliance is defined as the inverse of the contact stiffness S, Equation (3.8) and Equation (3.13) can combine to yield Equation (3.14). Thus, a formula which comprises compliance and projected contact area can be obtained.

$$C = C_f + \frac{\sqrt{\pi}}{2E_r}\frac{1}{\sqrt{A}} \tag{3.14}$$

By rewriting Equation (3.14), the projected contact area can be defined as a function of compliance, as shown in Equation (3.15).

$$A = \frac{\pi}{4}\frac{1}{E_r^2}\frac{1}{(C - C_f)^2} \tag{3.15}$$

Once the contact depth is determined, the contact area can then be computed as a function of contact depth, as shown in Equation (3.16) and Equation (3.17).

$$A = F(h_c) \tag{3.16}$$

$$A(h_c) = C_0 h_c^2 + C_1 h_c^1 + C_2 h_c^{\frac{1}{2}} + C_3 h_c^{\frac{1}{4}} + ..... + C_8 h_c^{\frac{1}{128}} \tag{3.17}$$

$C_0$ through $C_8$ are constants, which can be established by the method of curve fitting from many experimental data. In this study, the work of the tip shape function calibration is determined by performing the ideal indentation testing on a fused silica sample. Thus, the reduced modulus can be determined using Equation (3.8) and the modulus and the hardness can be obtained by Equation (3.9) and Equation (3.12), respectively.

The continuous stiffness measurement (CSM) method can be used for acquiring the stiffness information continuously through an indentation testing. The idea of this method is to apply a small amplitude oscillation at a relatively high frequency on to the test force signal, so that the stiffness value is recounted incessantly during the loading cycle. The models of CSM systems are shown below. Figure 3.17 (a) displays the basic

dynamic mechanical model and Figure 3.17 (b) illustrates a dynamic mechanical model consisting of the load frame and the tip compliances.

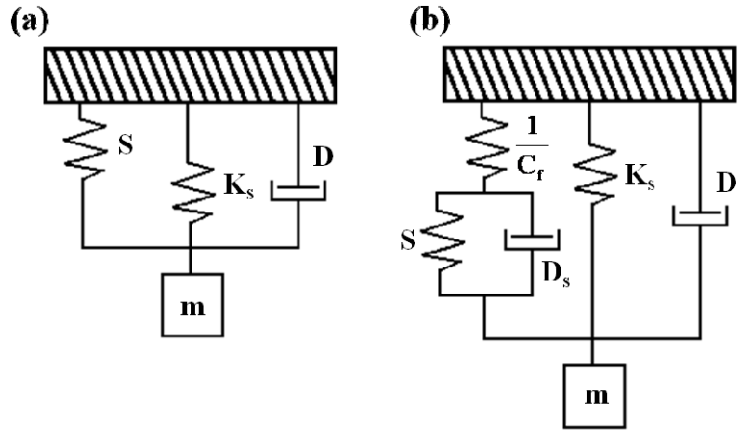


Figure 3.17 Schematic of a Dynamic mechanical model of a nanoindentation instrument: (a) a simple model (b) a model of the relation with compliance of the load frame and the tip [38].

The contact stiffness can be computed by Equation (3.18) and Equation (3.19).

$$\left|\frac{P_{os}}{h(\omega)}\right| = \sqrt{\left\{\left(S^{-1}+C_f\right)^{-1}+K_s-m\omega^2\right\}^2+\omega^2D^2} \tag{3.18}$$

$$\tan(\phi) = \frac{\omega D}{(S^{-1}+C_f)^{-1}+K_s-m\omega^2} \tag{3.19}$$

Where the $k_s$ is the stiffness of the support spring, D is the damping coefficient, $D_s$ is the damping coefficient of the contact, ω is the frequency, $P_{os}$ is the magnitude of the force oscillation, φ is the phase difference, and m is the mass of the indenter and shaft.

### 3-2.2 Examples of IIT Application

*1. Cluster distribution and modulus correlation characterization*

The effect of agglomeration and dispersion of the nanoparticle additives on material properties such as surface modulus can be studied by using IIT. In this example, the measured moduli were different at different locations due to the encounter of nanoparticles spreading over the sample. In order to correlate the particle dispersion to the changes in material properties (surface mechanical properties in this case), the nanoindentation experiments were carried out in an array (4x5) using a Berkovich pyramidal tip with an indention depth of 3 μm [30]. Figure 3.18ab shows the residual indents on the surface of two $TiO_2$-AU coatings: (a) particle A system; (b) particle B system. The particle A system has a better particle dispersion than that in particle B system, as shown in the subsurface image (3 μm below polymer-air surface – in the middle graph). In particle A system, particles disperse more uniformly in the coatings, as a result the shapes of all indents appear similar and symmetrical. The corresponding modulus-displacement curves (in the right-hand-side graph) are overlapped upon each other and the modulus values are the same for all intents in the whole penetration range (0 μm - 3 μm). The particle B system has a poor particle dispersion (Figure 3.18 b), and the result shows that the size and location of particle clusters influence the shape of the residual indents and the surface elastic modulus. For the first indent, it is affected by the cluster apparently from the beginning of the indentation. Thus, the modulus is greater than other indents. Similarly, the tip hits the clusters during the indentation testing for indents number 3 and number 8. The modulus value increases gradually as indenter tip approaching the particle clusters. For those indents (such as # 13) do not encounter larger clusters, the modulus-displacement curves is similar to that in Figure 3.18 (a).

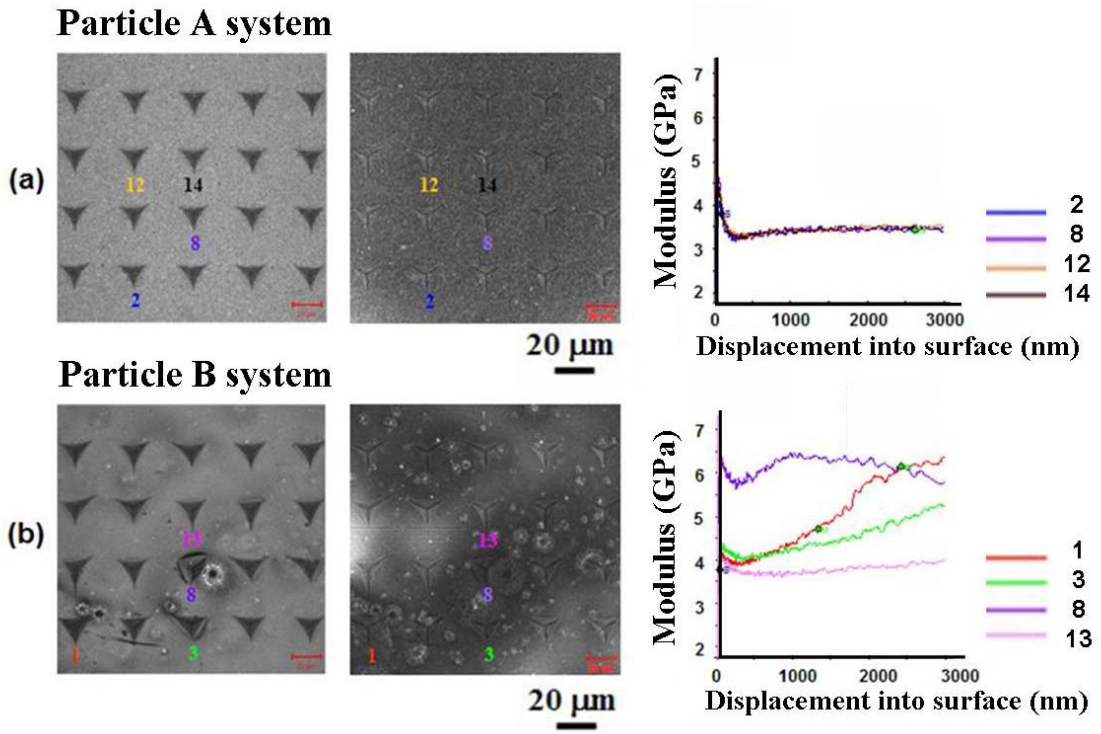


Figure 3.18 2D LSCM projection images (left column), the single-layer subsurface images (middle column, 3 μm below the polymer-air surface), and the corresponding modulus-displacement curves (right column) of a pyramidal tip for two $TiO_2$-AU coatings: (a) particle A system, (b) particle B system [30].

## 2. *Scratch behavior characterization*

The addition of nanoparticles into polymer coatings is expected to reduce the scratch damage or increase the ability of recovery. In reality, the adding of nanoparticles does not always lead to the improvement of scratch resistance. Many results indicate that there are really intricate effects of nanoparticle additives on the scratch behavior of polymers [39]. For example, the scratch visibility is dramatically reduced but the onset of the elastic-plastic transition occurs earlier as increasing the additive concentrations.

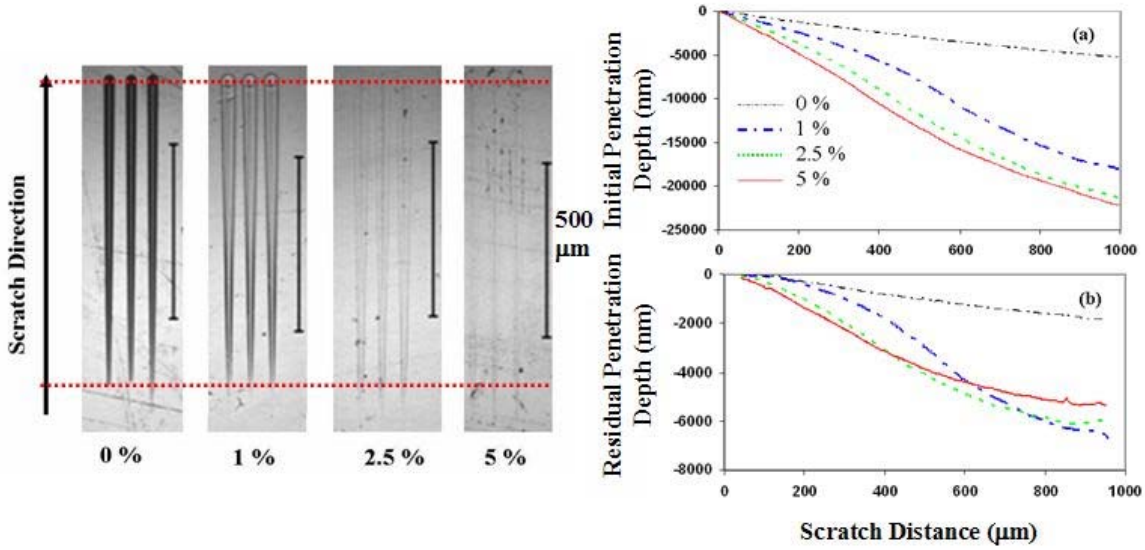


Figure 3.19 LSCM images, initial penetration curves, and residual penetration curves under progressive force scratches (0 mN to 50 mN) for a nano-alumina (particle size ≈ 40 nm) polymer coatings in different concentration of nanoparticle additives (0 %, 1 %, 2.5 %, and 5 %) [39].

Figure 3.19 shows the LSCM images, initial penetration curves and residual penetration curves of progressive force scratch test (0 mN ~ 50 mN) for $Al_2O_3$ nanoparticles of different additive concentrations: 0 %, 1 %, 2.5 %, and 5 % (mass fraction). The LSCM images, which were taken a few hours after the scratch tests, show that as the nanoparticle concentration increases, the scratch damage is less visible. However, it is found that the onset force moves to a lower load with increasing the additive concentrations. This result indicates that the elastic-plastic transition occurs at a lower scratch load in the higher additive concentration. If we use the onset force to rank the scratch resistance, then the scratch resistance becomes lower as increasing additive concentration. This result is not desirable. However, it is noticeable that at higher scratch loads that the scratch damage is not visible for higher additive concentration (5 %), and the damage profile/shape is very different to the 0% system. To examine the

data carefully, we plot the initial penetration and residual penetration curves (right graph of Figure 3.19), which were recorded from IIT during the testing and right after scratched, respectively. As the initial penetration curves show, the increase in the nanoparticle concentration results in a deeper damage just when the scratch generated. It is interesting to compare the change of residual penetration curves to initial penetration curves. The recovery for higher additive concentration system is faster than that of the lower additive concentration system. For example, the residual penetration depth for the 5 % system is less than these of the 1 % and 2.5 % systems after the scratch distance near 650 μm, while the initial penetration depth is greater than these of the 1 % and 2.5 % systems. Therefore, it is important to take into account at what force range the scratch tests are performed when discussing and comparing the impact of nanoparticles on the polymer coatings.

# Chapter 4 RESULTS AND DISCUSSION

## 4-1 Epoxy

### 4-1.1 Indentation Data

The surface modulus and hardness results obtained from the instrumented indentation testing are listed in Table 4.1. These results are averaged from 15 indents using a nominal 10 μm 90 diamond tip (see Appendix A) and indented into 2000 nm with a strain rate of 0.05 1/s. Reported values of modulus and hardness for each indent were averaged over a depth range from 1000 nm to 1500 nm without a drift correction. Figures 4.1-4.3 display surface elastic modulus (E), hardness (H), and the ratio of hardness to modulus (H/E) for three epoxies. The surface elastic modulus increases slightly as $T_g$ decreases. EP-BB has the greatest hardness value and EP-CC is the lowest. To relate mechanical properties to wear and scratch resistance, the ratio of hardness to modulus (H/E) is often used as an indicator [40-41]. For example, for materials of similar modulus, the material having a higher hardness has a higher scratch resistance. On the other hand, the material of similar hardness value, the lower modulus the higher scratch resistance. In this case, EP-AA has the highest $T_g$ and H/E ratio. EP-CC has the lowest $T_g$ which is corresponding to the lowest H/E ratio. It is expected that EP-AA (higher $T_g$ and higher H/E ratio) has a higher scratch resistance. The effect of $T_g$ on scratch behavior will be discussed in the next section.

Table 4.1 Glass transition temperature ($T_g$), elastic modulus (E), hardness (H), and ratio of H/E of three epoxy samples. The error bar represents one standard deviation from the averaged value of 15 indentations.

| Sample | $T_g$ (°C) | Modulus, E (GPa) | Hardness, H (GPa) | H/E |
|---|---|---|---|---|
| EP-AA | 117 | 3.301 ± 0.038 | 0.290 ± 0.006 | 0.088 |
| EP-BB | 88 | 3.589 ± 0.029 | 0.307 ± 0.004 | 0.086 |
| EP-CC | 71 | 3.765 ± 0.022 | 0.271 ± 0.003 | 0.072 |

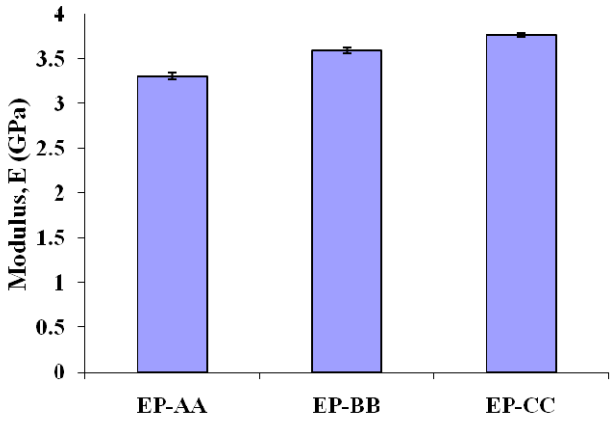


Figure 4.1 Surface modulus (E) data for three epoxy samples.

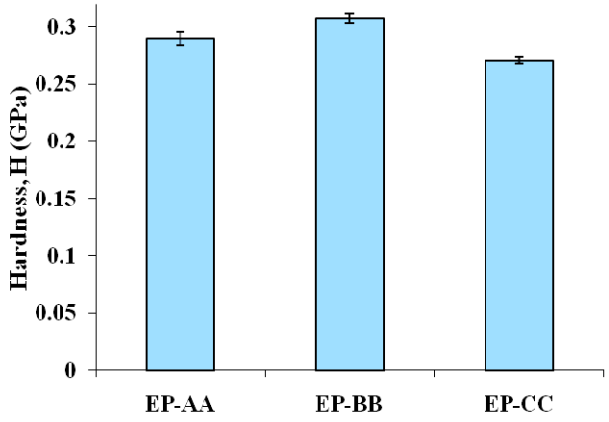


Figure 4.2 Surface Hardness (H) data for three epoxy samples.

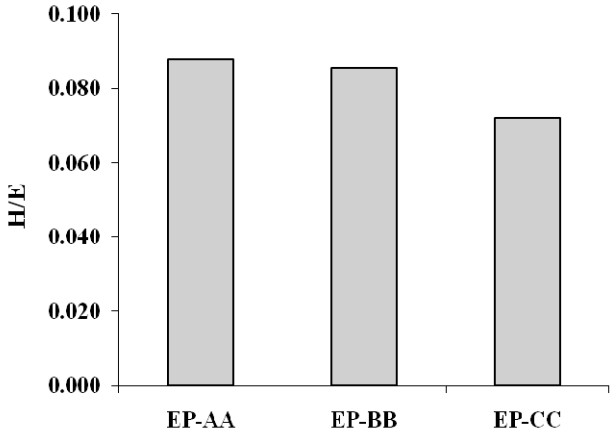


Figure 4.3 Hardness to modulus (H/E) ratio for three epoxy samples.

### 4-1.2 PS Data

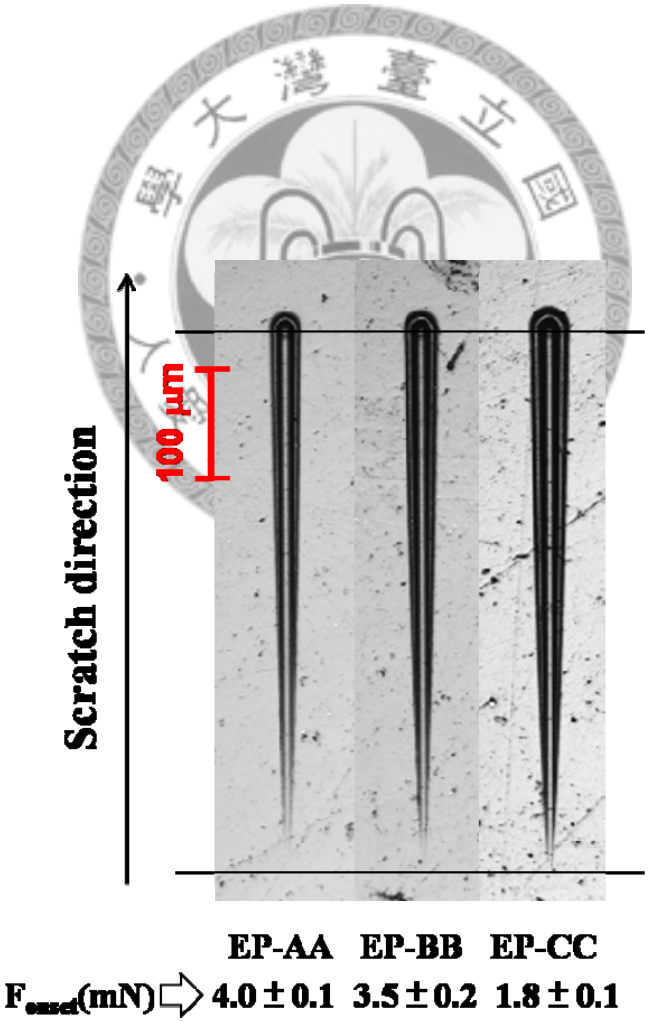


Figure 4.4 LSCM images and onset forces obtained from PS tests (0 mN to 50 mN, scratch length = 500 μm, scratch speed = 10 μm/s) of three epoxy samples.

Figure 4.4 shows the results of onset forces and LSCM images obtained from the PS tests. The scratch force range is from 0 mN to 50 mN, and the scratch length is 500 μm with a scratch speed of 10 μm/s. Two scratches were performed on each sample and the onset force presented here is the averaged value of the two. Note that the onset force is defined as the force at which the elastic-plastic deformation occurs. A lower onset force, a lower scratch resistance. As figure shows, EP-AA and EP-BB have similar onset forces (in the order of 3-4 mN, EP-AA has a slightly higher value), which are greater than the onset force of EP-CC. This result is consistent with the H/E ratio, i.e., EP-CC has a lowest $T_g$ and H/E ratio, and a lowest onset force. The EP-CC sample has a lowest scratch resistance ranked by onset force.

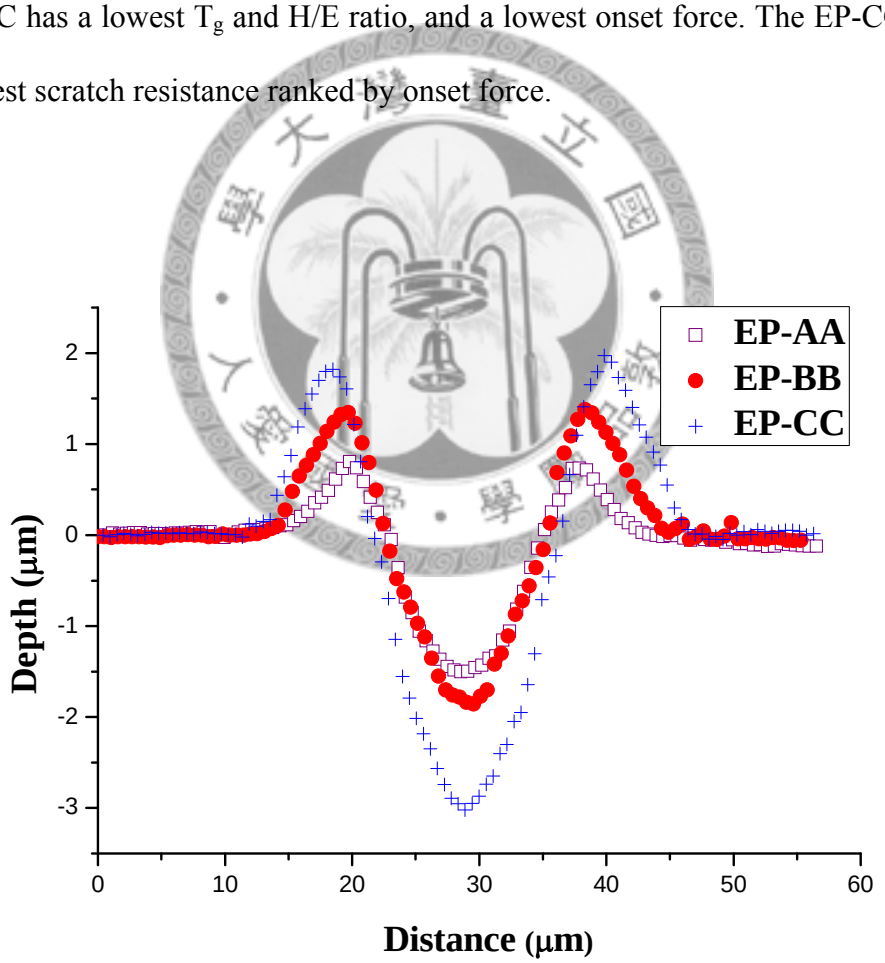


Figure 4.5 Cross profiles of three epoxies obtained from PS tests near 50 mN.

Figure 4.5 plots the cross profiles of three epoxies at the force near 50 mN (the tail). It is also observed that the scratch profiles near the tail of PS (Figure 4.5) are very different. The scratches of EP-AA and EP-BB appear similar, but EP-CC definitely has a much border scratch width. The difference in scratch width is not as large as that in the scratch depth. Overall, EP-CC has the largest scratch width and depth, and EP-AA has the smallest scratch width and depth. In terms of scratch damage, the EP-CC has the most severe damage. EP-CC has a lowest $T_g$ and H/E ratio, and EP-CC sample has a lowest scratch resistance ranked by scratch damages.

Table 4.2 lists the detailed cross profile information including peak-to-peak scratch width, $W_p$, full penetration depth, $D_f$, pile-up height, $h_b$, and the ratio of $W_p/D_f$ and $W_p/h_b$. The values of $W_p$, $D_p$ and $h_b$ all increase from EP-AA to EP-BB and then to EP-CC. The ratio of $W_p/D_f$ and $W_p/h_b$ can be used to rank the scratch resistance. A shallower and wider scratch (higher $W_p/D_f$ value) is less visible than a deep and narrower one. Thus, the ratios of $W_p/D_f$ and $W_p/h_b$ characterize the shape of a scratch and the visibility of a scratch which is highly depending on the scratch geometry. A larger ratio of $W_p/D_f$ represents a shallower scratch and less visible, i.e., the scratch appears less damage [5]. The $W_p/h_b$ ratio is also an important parameter for assessing scratch visibility. Similar to the $W_p/D_f$ ratio, the larger $W_p/h_b$ ratio, the less visible a scratch. EP-AA has the greatest ratios and EP-CC has the lowest, i.e., EP-AA has the strongest scratch resistance and EP-CC has the weakest. This result is consistent with previous results, which obtained from H/E ratio and onset force by PS tests.

Table 4.2 The detailed peak-to-peak scratch width, $W_p$, full penetration depth, $D_f$, pile-up height, $h_b$, and the ratio of $W_p/D_f$ and $W_p/h_b$ of three epoxies obtained from PS near the tail at the force near 50 mN. The definition of these quantities is defined and illustrated in the insert graph. The error bar represents one standard deviation from two scratches.

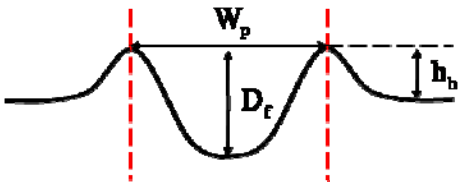


| Sample | $W_p$ (μm) | $D_f$ (μm) | $h_b$ (μm) | $W_p/D_f$ | $W_p/h_b$ |
|---|---|---|---|---|---|
| EP-AA | 17.8 ± 0.2 | 2.3 ± 0.2 | 0.9 ± 0.1 | 7.7 | 19.8 |
| EP-BB | 19.0 ± 0.2 | 3.3 ± 0.2 | 1.4 ± 0.1 | 5.8 | 13.6 |
| EP-CC | 21.5 ± 0.2 | 5.0 ± 0.3 | 2.0 ± 0.1 | 4.3 | 10.8 |

Table 4.3 The front contact length, $a_f$, rear contact length, $a_r$, average rear contact angle, $\omega_{average}$, and $a_r/a_f$ ratio of three epoxies obtained from PS near 50 mN. The definition of these quantities is defined and illustrated in the insert graph. The error bar represents one standard deviation from two scratches.

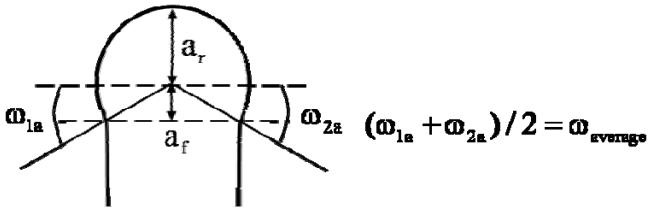


| Sample | $a_r$ (μm) | $a_f$ (μm) | $a_r/a_f$ ratio | $\omega_{average}$ (°) |
|---|---|---|---|---|
| EP-AA | 3.3 ± 0.3 | 9.2 ± 0.2 | 0.4 | 21.0 ± 2.6 |
| EP-BB | 3.8 ± 0.2 | 9.6 ± 0.3 | 0.4 | 21.9 ± 1.5 |
| EP-CC | 3.6 ± 0.2 | 10.7 ± 0.3 | 0.3 | 19.5 ± 1.7 |

The front contact length, $a_f$, rear contact length, $a_r$, average rear contact angle, $\omega_{average}$, and $a_r$ to $a_f$ ratio are shown in Table 4.3. As mentioned in chapter 2, the $a_r/a_f$ ratio indicates the degree of elastic to plastic deformation. In the case of a pure elastic deformation, the $a_r/a_f$ ratio approaches to 1. All three $a_r/a_f$ ratios are less than 0.5, and this result implies all three epoxies are under plastic deformation. EP-CC has a smallest $a_r/a_f$ ratio and the worst scratch damage. The values of $\omega_{average}$ are close for all epoxies with EP-CC slightly smaller. It is expected since we predicted that EP-CC has the weakest scratch resistance from $W_p/D_f$ and $W_p/h_b$ ratios. A poor scratch resistance causes a severe damage with a high degree of plastic deformation.

In addition to the scratch morphology measured by LSCM, there are important scratch data can be obtained from IIT directly. These data include initial, residual penetration depths, friction coefficients, and the friction forces along scratches. Figures 4.6 and 4.7 display the initial and residual penetration curves of three epoxies. In both plots, EP-CC has the larger initial and residual penetration depths and EP-AA has the lowest ones. The depth differences between three samples are larger in the residual than the initial curves. This result implies that EP-CC has a lower recovery right after the scratch, and it is also plotted in Figure 4.8. The recovery is defined as $(D_i - D_r)/D_i \times 100$, (as defined in Equation (2.1) in Chapter 2) and the quantity reflects viscoelastic response of the material. EP-AA has a highest recovery among three epoxies. For scratch force larger than 20 mN (at scratch distance = 200 μm), the recovery of EP-CC reaches a value around 50 %, while EP-BB is at 65 % and EP-AA at 70 % level. Clearly, EP-AA has the highest recovery and best scratch resistance among three epoxies, and EP-CC has lowest recovery and worst scratch resistance.

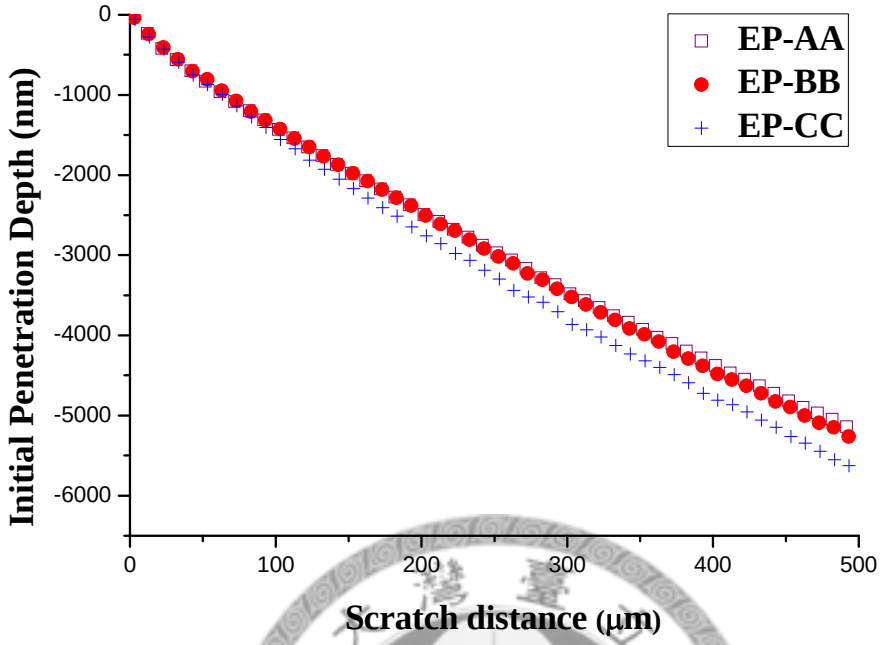


Figure 4.6 The initial penetration curves of three epoxies obtained from PS tests.

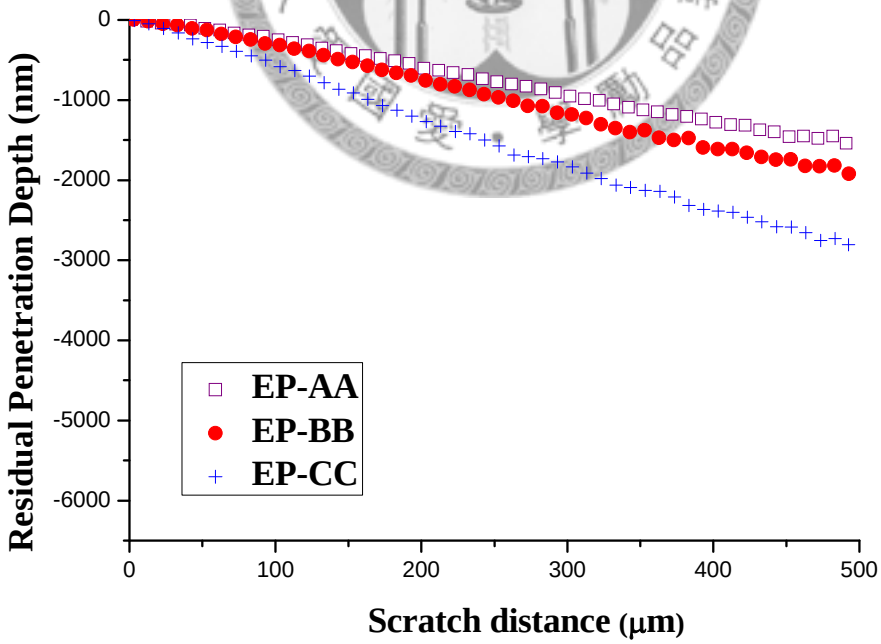


Figure 4.7 The residual penetration curves of three epoxies obtained from PS tests.

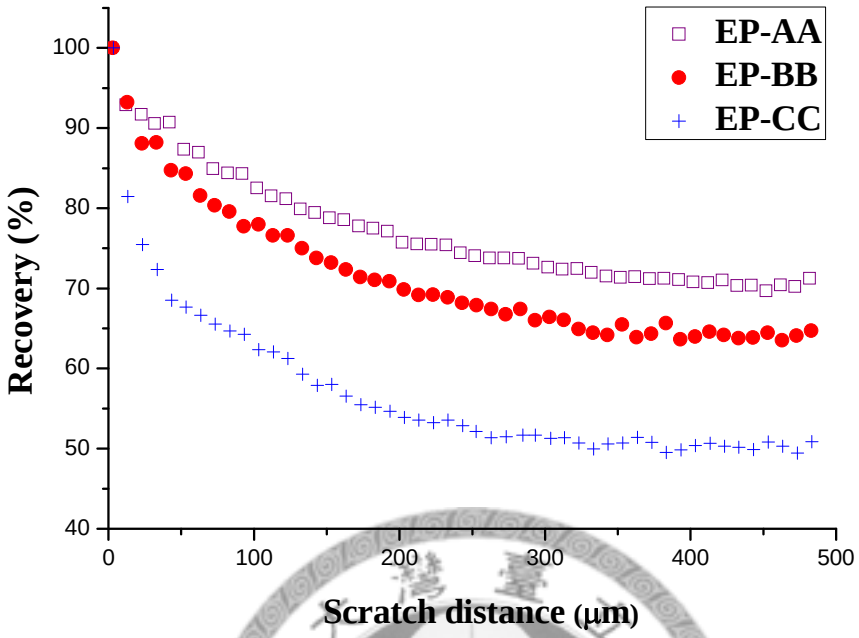


Figure 4.8 The recovery of three epoxies obtained from PS tests.

Figure 4.9 plots the friction forces along scratches as a function of scratch distance for three epoxies. For scratch force less than 12 mN (scratch distance less than 120 μm), the friction forces increase slowly and the curves of three samples are almost overlapped. After that, the friction forces start to increase significantly. The friction force of EP-CC increases faster than these of the other two, which are still very close to each other. The friction coefficients of three epoxies are also plotted in Figure 4.10. Note that the friction coefficient is the ratio of friction force to the normal scratch force. Typically, the friction coefficient values start with a very small value in the static friction region, increase linearly with response to the increasing scratch force, and finally reach a plateau after the scratch force reaches to the kinetic friction region. However, the friction coefficients curves of epoxies do not follow a liner trend in the beginning, and the transition between a static and kinetic friction region is not obvious.

Another interest point is that the curves are overlapped together around the scratch distance before 120 μm (the static friction region), and the static friction coefficients are similar for three epoxies. After the 120 μm, EP-CC has the highest friction coefficient, i.e., the "kinetic" friction coefficient is higher for EP-CC. This finding indicates that the friction behavior of EP-CC is quite different from EP-BB and EP-AA. Note that the crosslink molecular weight of EP-CC is 5,290 g/mol at least 6 times larger than that of EP-AA and EP-BB (EP-AA: 630 g/mol and EP: 920 g/mol). The crosslink network microstructure of EP-CC may be very different from the other two EPs, especially deep inside samples when the penetration depth is great. Detailed study on the crosslink network microstructure of epoxies may provide some answers. However, the study is quite complex.

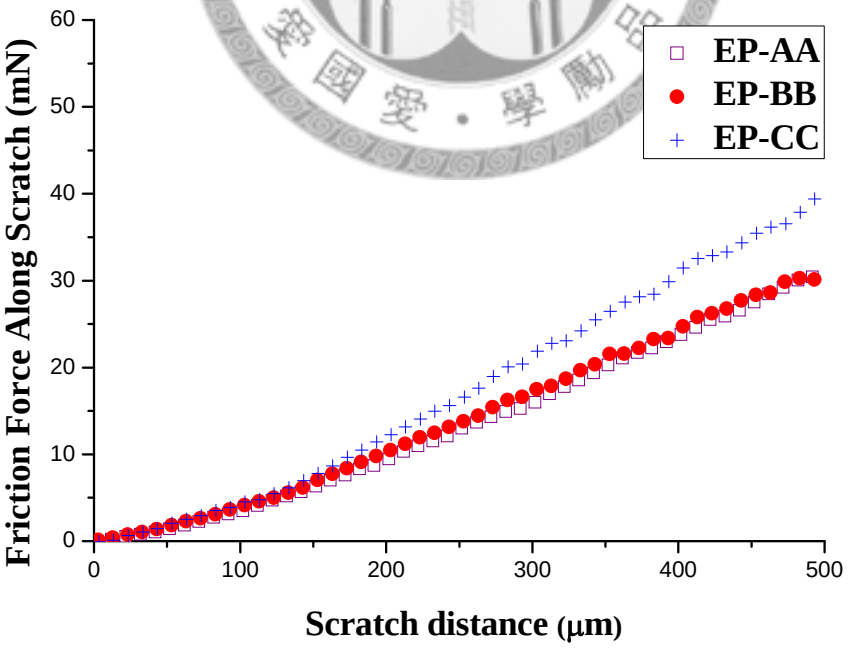


Figure 4.9 The friction forces along scratches of three epoxies obtained from PS tests.

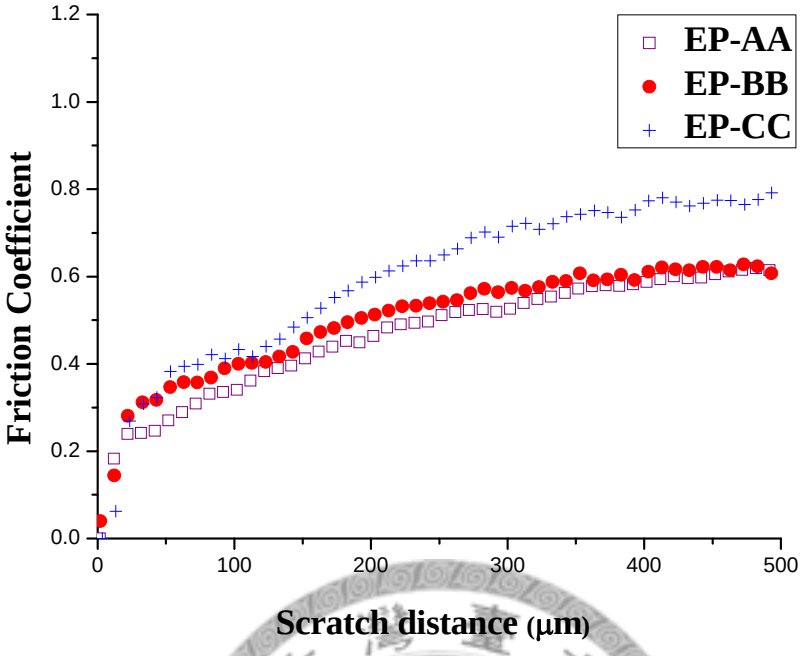


Figure 4.10 The friction coefficients of three epoxies obtained from PS tests.

### 4-1.3 CS Data

Figure 4.11 shows the LSCM images of CS array and the onset forces obtained from both PS and CS tests. The CS scratch forces include 1 mN, 2 mN, 3 mN, 4 mN, 5 mN, 6 mN, as shown in the figure. Two scratches are generated at each force and the scratch length is 500 μm. The CS onset forces match with the results obtained from PS. EP-AA and EP-BB still have similar scratch appearance even in the small force range, and the onset forces are between 3 mN to 4 mN determined by CS. The onset force of EP-CC is around 2 mN and the damages are quite severe compare to others. At higher scratch force (6 mN) in the scratch array, the scratch damages become noticeably more severe from EP-AA to EP-CC. From both PS and CS tests, the results in terms of onset force determination and the scratch behaviors in terms of scratch damages at low scratch forces are consistent. The EP-AA has the best scratch resistance and the EP-CC has the worst.

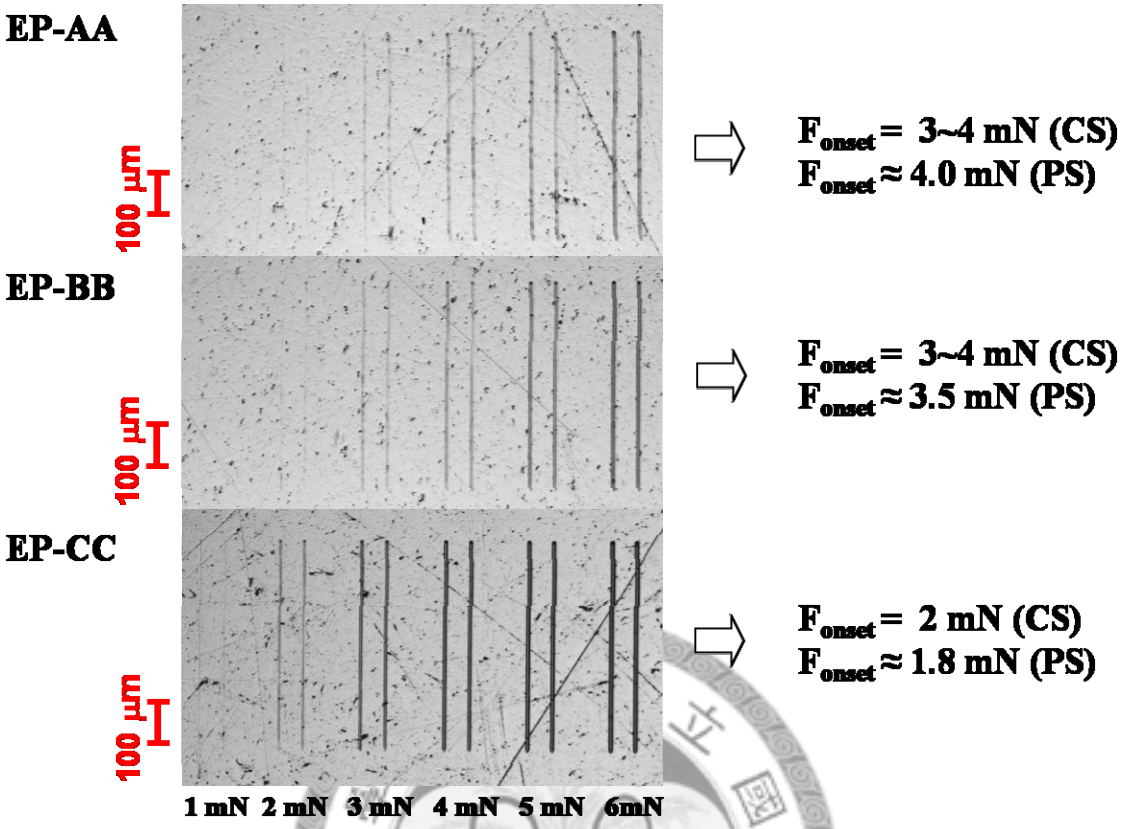


Figure 4.11 LSCM images from CS array and onset forces of three epoxy samples.

After the assessment of onset force, another series of CS tests were carried out to measure the scratch damages and further assess the scratch resistance of three epoxies. Same test conditions were applied but the force magnitudes are different for the new CS tests. Figure 4.12 shows the tail images from the new CS tests (10 mN, 20 mN, 30 mN, 40 mN, and 50 mN) of three epoxy samples. A pair of scratches with the length of 500 μm is generated in each force. The tail images show a significant difference in scratch profile in three epoxies at different forces. In the same force, EP-AA always has the less damage, and EP-CC is the worst. As the force increasing, the scratch profile becomes wider and more visible (increasing optical contrast). The tail sizes (width) of EP-AA and EP-BB are similar, and noticeably smaller than that of EP-CC.

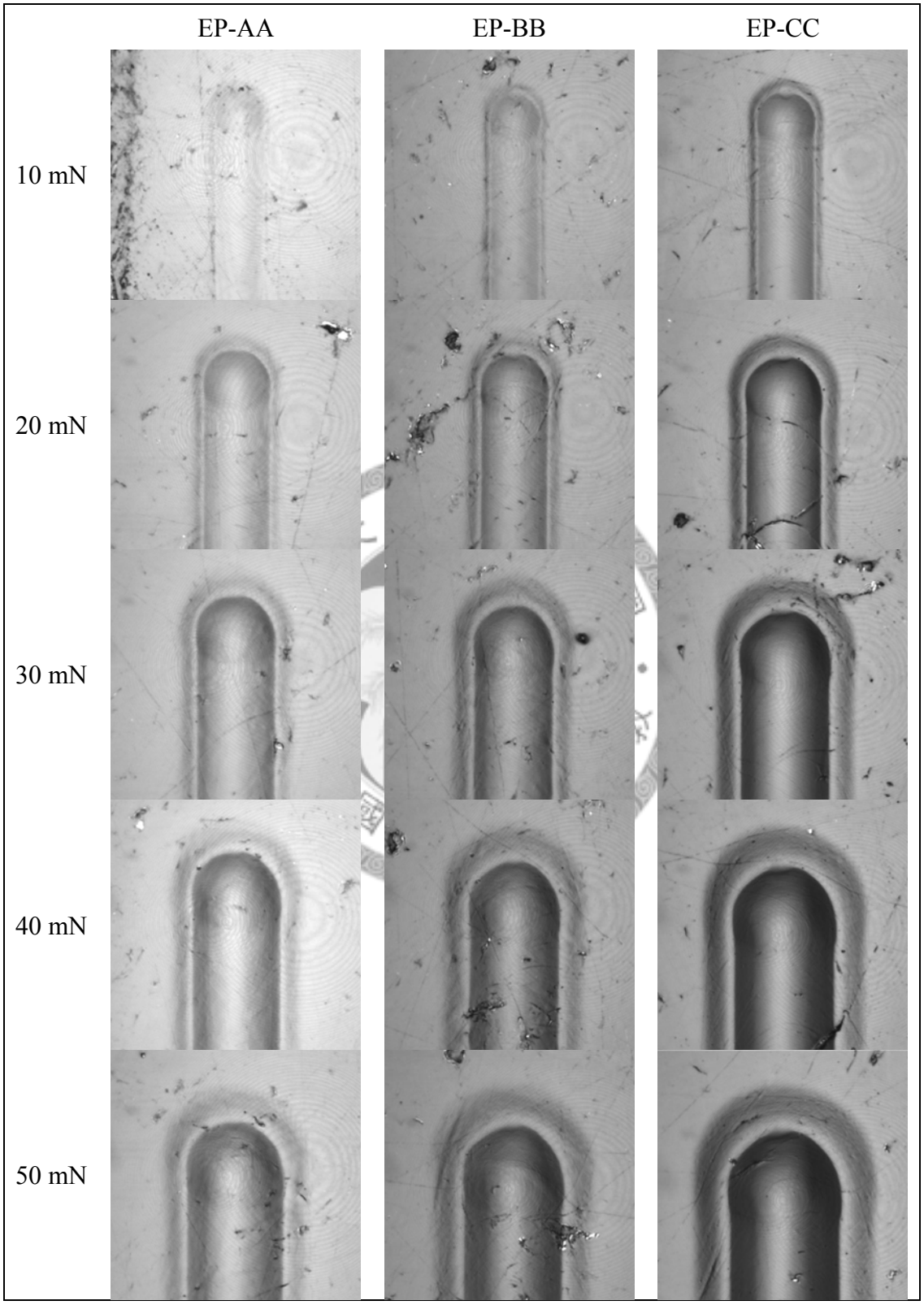


Figure 4.12 Tail images from CS (10 mN, 20 mN, 30 mN, 40 mN, and 50 mN) of three epoxy samples.

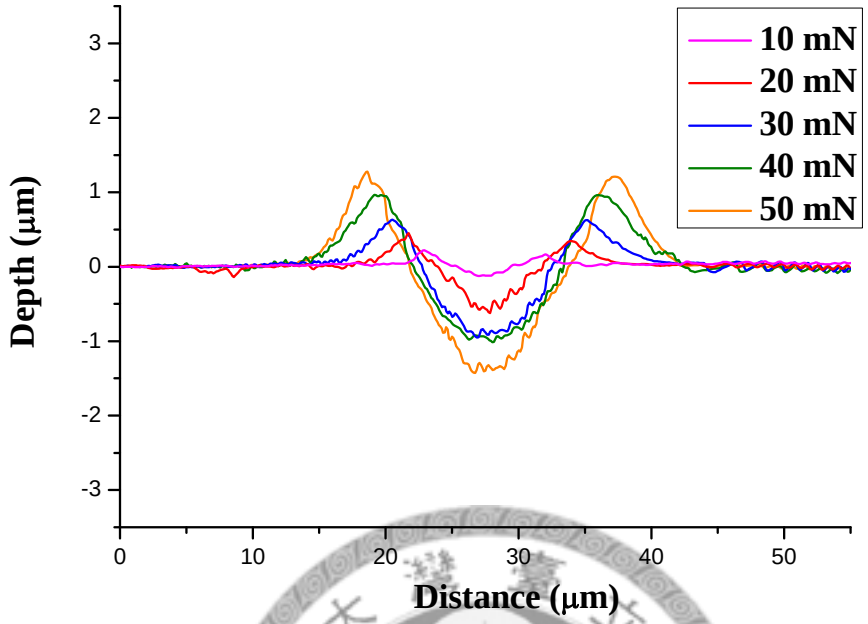


Figure 4.13 Cross profiles of EP-AA scratches for different CS forces (10 mN, 20 mN, 30 mN, 40 mN, 50 mN).

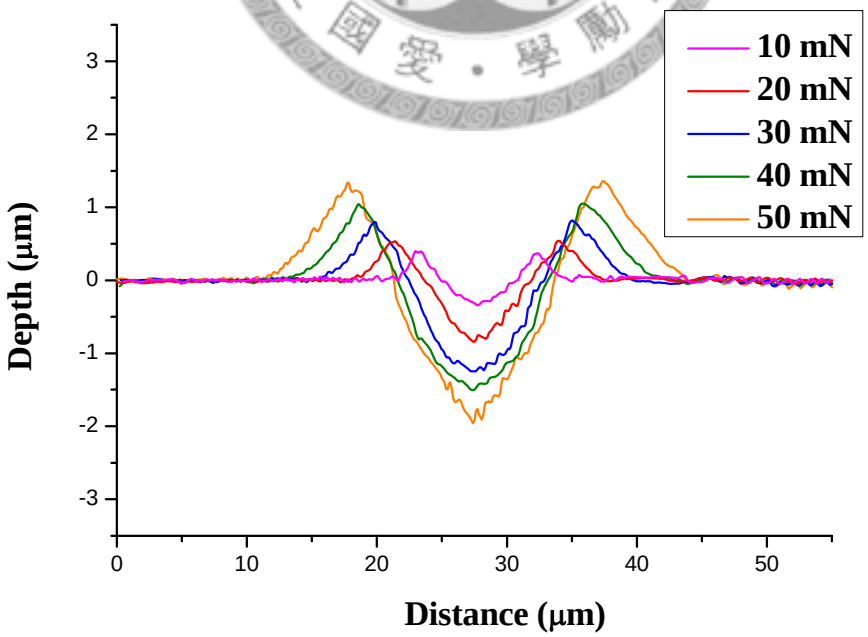


Figure 4.14 Cross profiles of EP-BB scratches for different CS forces (10 mN, 20 mN, 30 mN, 40 mN, and 50 mN).

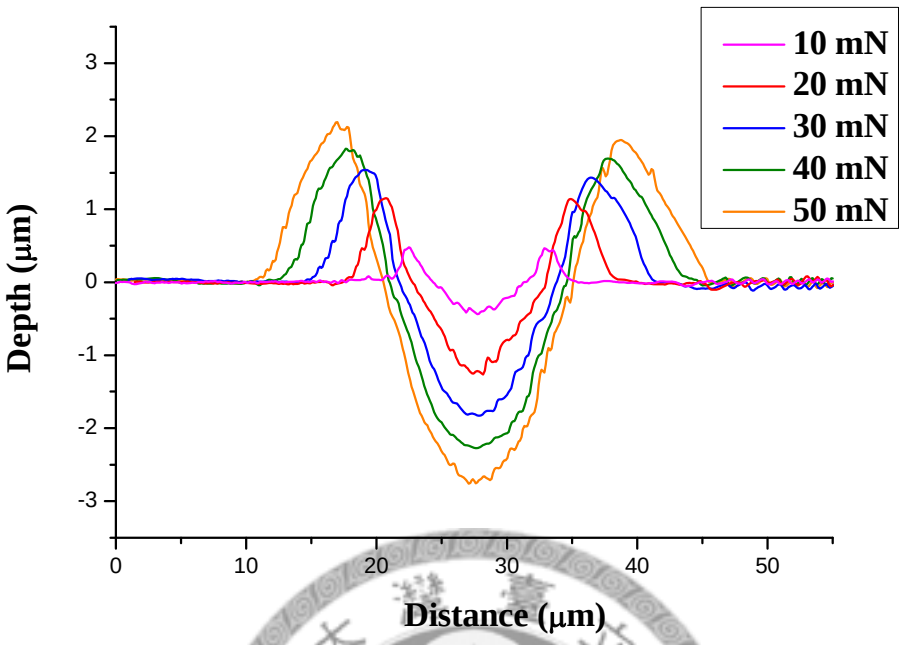


Figure 4.15 Cross profiles of EP-CC scratches for different CS forces (10 mN, 20 mN, 30 mN, 40 mN, and 50 mN).

Figures 4.13, 4.14 and 4.15 shows the cross profiles of EP-AA, EP-BB, and EP-CC in the various CS forces: 10 mN, 20 mN, 30 mN, 40 mN, and 50 mN. For the constant force test, the cross profiles should be the same along the entire scratch. The data presented in figures are from the middle sections of scratches. As a result, peak-to-peak scratch width, $W_p$, becomes larger as well as $D_f$ and $h_b$ with increasing scratch force. Again, EP-CC also has the most severe damages among three epoxies. Figure 4.16 and Figure 4.17 also shows the penetration depths obtained from IIT from different CS tests. The CS results (symbols) are overlapped with the previous PS results (lines), which were converted as a function of scratch forces. The results are consistent between PS and CS tests. The penetration depth values of EP-AA and EP-BB are very close, and EP-CC has the largest initial and penetration depths in each force.

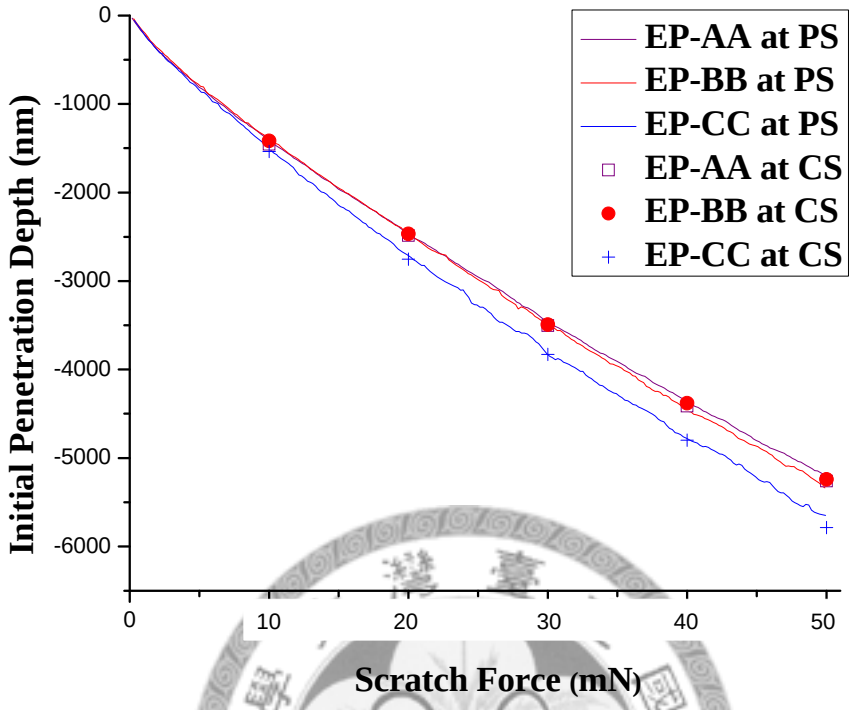


Figure 4.16 The initial penetration depths from CS (symbols) and PS (lines).

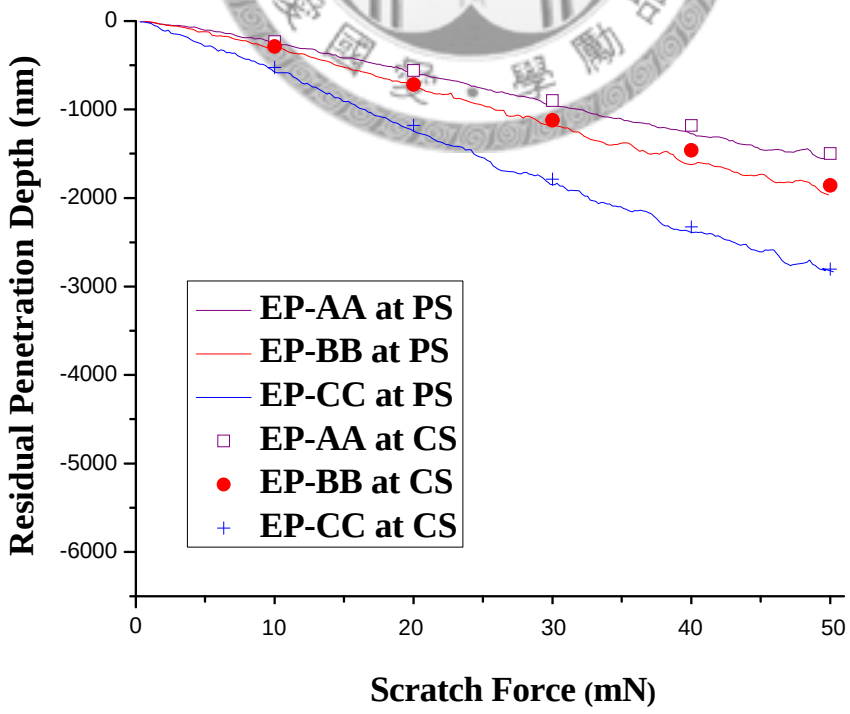


Figure 4.17 The residual penetration depths from CS (symbols) and PS (lines).

Table 4.4 The detailed cross profile information ($W_p$, $D_p$, $h_b$, ratio of $W_p/D_f$ and $W_p/h_b$) of three epoxies obtained from CS tests (10 mN, 20 mN, 30 mN, 40 mN, and 50 mN). The error bar represents one standard deviation from two scratches.

| Force (mN) | Sample | $W_p$ (μm) | $D_f$ (μm) | $h_b$ (μm) | $W_p/D_f$ | $W_p/h_b$ |
|---|---|---|---|---|---|---|
| 10 | EP-AA | 9.1 ± 0.2 | 0.3 ± 0.1 | 0.1 ± 0.1 | 30.3 | 91.0 |
| | EP-BB | 8.9 ± 0.2 | 0.7 ± 0.1 | 0.3 ± 0.1 | 12.7 | 29.7 |
| | EP-CC | 10.7 ± 0.2 | 1.1 ± 0.1 | 0.6 ± 0.1 | 9.7 | 17.8 |
| Force (mN) | Sample | $W_p$ (μm) | $D_f$ (μm) | $h_b$ (μm) | $W_p/D_f$ | $W_p/h_b$ |
| 20 | EP-AA | 12.2 ± 0.2 | 1.0 ± 0.1 | 0.4 ± 0.1 | 12.2 | 30.5 |
| | EP-BB | 12.7 ± 0.2 | 1.3 ± 0.1 | 0.6 ± 0.1 | 9.8 | 21.2 |
| | EP-CC | 14.5 ± 0.2 | 2.6 ± 0.2 | 1.1 ± 0.1 | 5.6 | 13.2 |
| Force (mN) | Sample | $W_p$ (μm) | $D_f$ (μm) | $h_b$ (μm) | $W_p/D_f$ | $W_p/h_b$ |
| 30 | EP-AA | 14.9 ± 0.2 | 1.0 ± 0.1 | 0.4 ± 0.1 | 14.9 | 37.3 |
| | EP-BB | 15.4 ± 0.4 | 2.0 ± 0.2 | 0.8 ± 0.1 | 7.7 | 19.3 |
| | EP-CC | 17.4 ± 0.3 | 3.4 ± 0.2 | 1.6 ± 0.1 | 5.1 | 10.9 |
| Force (mN) | Sample | $W_p$ (μm) | $D_f$ (μm) | $h_b$ (μm) | $W_p/D_f$ | $W_p/h_b$ |
| 40 | EP-AA | 16.4 ± 0.3 | 2.0 ± 0.1 | 0.9 ± 0.1 | 8.2 | 18.2 |
| | EP-BB | 17.2 ± 0.5 | 2.4 ± 0.2 | 1.1 ± 0.1 | 7.2 | 15.6 |
| | EP-CC | 19.3 ± 0.5 | 4.1 ± 0.2 | 1.8 ± 0.1 | 4.7 | 10.7 |
| Force (mN) | Sample | $W_p$ (μm) | $D_f$ (μm) | $h_b$ (μm) | $W_p/D_f$ | $W_p/h_b$ |
| 50 | EP-AA | 18.5 ± 0.3 | 2.6 ± 0.1 | 1.3 ± 0.1 | 7.1 | 14.2 |
| | EP-BB | 19.4 ± 0.3 | 3.3 ± 0.2 | 1.3 ± 0.1 | 5.9 | 14.9 |
| | EP-CC | 22.1 ± 0.6 | 5.1 ± 0.3 | 2.2 ± 0.2 | 4.3 | 10.0 |

Table 4.4 summarizes the detailed cross profile information ($W_p$, $D_p$, $h_b$, ratio of $W_p/D_f$ and $W_p/h_b$). In each force, EP-AA has the greatest $W_p/D_f$ and $W_p/h_b$ ratios, and EP-CC has the lowest. The corresponding relationships of $W_p/D_f$ and $W_p/h_b$ ratio are illustrated in Figure 4.18 and Figure 4.19. According to the denominators of two ratios are the same, and both numerators are the depth parameters obtained from the same

scratch cross profile, the $W_p/D_f$ and $W_p/h_b$ ratios should be similar. The ratios decrease as the force increases except for EP-AA at force = 30 mN. Note that the values of $D_p$ and $h_b$ do not change (all within measurement uncertainty) as faster as the $W_p$ values when the force increases from 20 mN to 40 mN. As mentioned before, a less damaged scratch is expected to be wide and shallow. By comparing the ratios of $W_p/D_f$ or $W_p/h_b$ based on different forces (Figures 4.18-4.19), EP-AA has the greatest and EP-CC has worst scratch resistance. The results are consistent with the result only using the $W_p/D_f$ and $W_p/h_b$ ratio to rank scratch resistance at particular force between 10 mN to 50 mN.

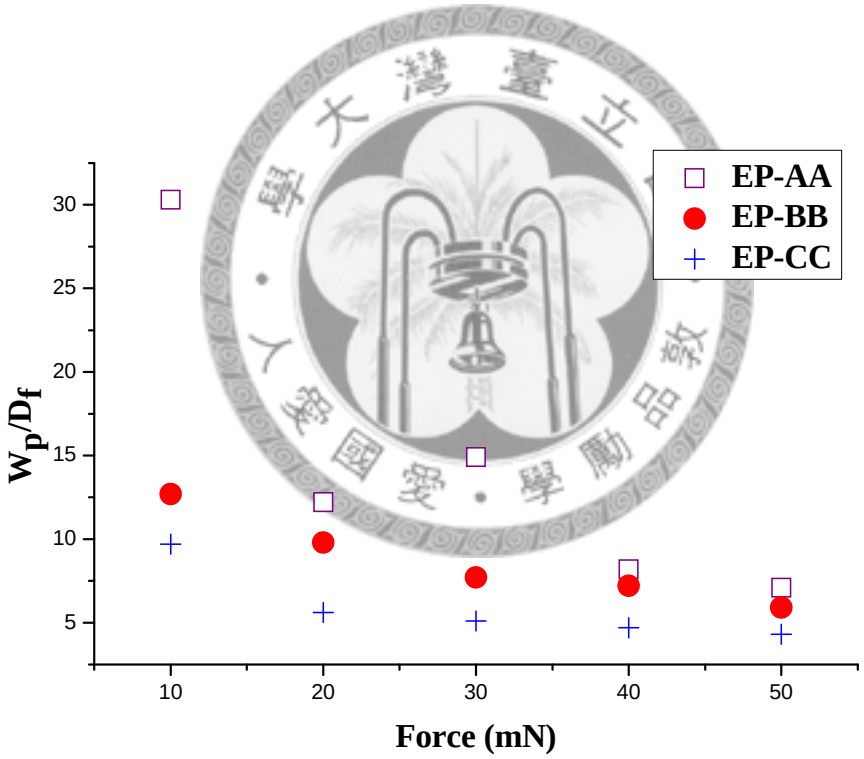


Figure 4.18 The $W_p/D_f$ ratio for three epoxies in different CS tests (10 mN, 20 mN, 30 mN, 40 mN and 50 mN).

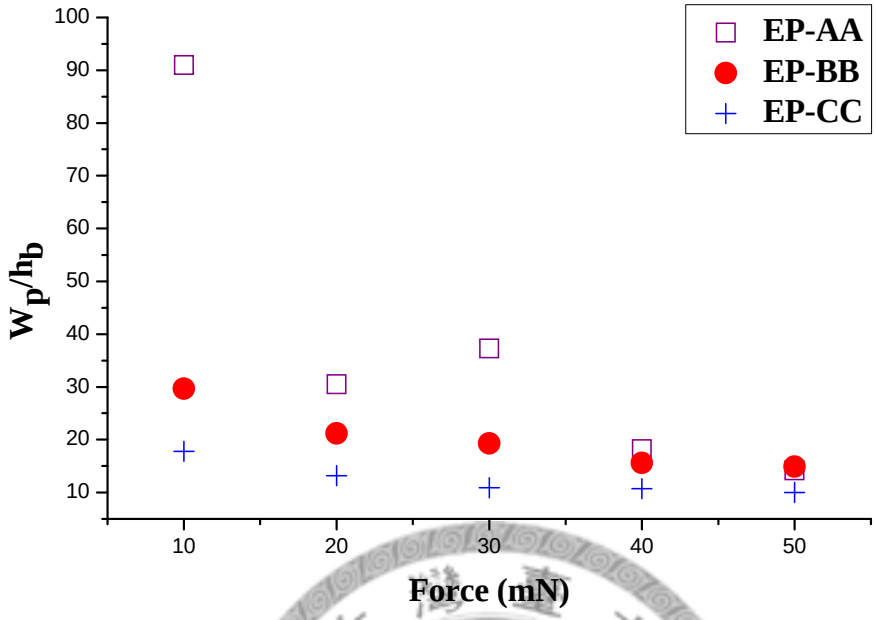


Figure 4.19 The $W_p/h_b$ ratio for three epoxies in different CS tests (10 mN, 20 mN, 30 mN, 40 mN and 50 mN).

Table 4.5 summarizes of detailed scratch tail information ($a_r$, $a_f$, $a_r/a_f$ ratio, and $\omega_{average}$). The $a_r/a_f$ ratio and $\omega_{average}$ are similar for three samples for each force, but decrease as increasing CS force. This result indicates that damage increases as increasing scratch forces. However, these quantities listed in Table 4.5 are not as easy to use to rank the scratch resistance of the materials.

Table 4.5 The detailed tail information ($a_r$, $a_f$, $a_r/a_f$ ratio, and $\omega_{average}$) of three epoxies obtained from CS tests (10 mN, 20 mN, 30 mN, 40 mN, and 50 mN) The error bar represents one standard deviation from two scratches.

| Force (mN) | Sample | $a_f$ (μm) | $a_r$ (μm) | $a_r/a_f$ ratio | $\omega_{average}$ (°) |
|---|---|---|---|---|---|
| 10 | EP-AA | 4.5 ± 0.2 | 2.5 ± 0.3 | 0.6 | 34.3 ± 1.1 |
| | EP-BB | 4.8 ± 0.2 | 2.2 ± 0.2 | 0.5 | 28.2 ± 2.1 |
| | EP-CC | 5.5 ± 0.3 | 2.4 ± 0.2 | 0.4 | 23.6 ± 1.7 |
| Force (mN) | Sample | $a_f$ (μm) | $a_r$ (μm) | $a_r/a_f$ ratio | $\omega_{average}$ (°) |
| 20 | EP-AA | 6.5 ± 0.2 | 2.6 ± 0.2 | 0.4 | 26.1 ± 2.0 |
| | EP-BB | 6.6 ± 0.2 | 2.7 ± 0.3 | 0.4 | 26.7 ± 3.3 |
| | EP-CC | 7.4 ± 0.2 | 2.7 ± 0.3 | 0.4 | 22.1 ± 1.1 |
| Force (mN) | Sample | $a_f$ (μm) | $a_r$ (μm) | $a_r/a_f$ ratio | $\omega_{average}$ (°) |
| 30 | EP-AA | 7.6 ± 0.2 | 2.9 ± 0.2 | 0.4 | 24.4 ± 1.1 |
| | EP-BB | 7.8 ± 0.3 | 3.2 ± 0.2 | 0.4 | 23.6 ± 0.6 |
| | EP-CC | 8.9 ± 0.2 | 3.3 ± 0.2 | 0.4 | 22.0 ± 1.7 |
| Force (mN) | Sample | $a_f$ (μm) | $a_r$ (μm) | $a_r/a_f$ ratio | $\omega_{average}$ (°) |
| 40 | EP-AA | 8.4 ± 0.2 | 3.1 ± 0.3 | 0.4 | 21.6± 2.2 |
| | EP-BB | 8.9 ± 0.3 | 3.6 ± 0.2 | 0.4 | 23.2 ± 1.3 |
| | EP-CC | 9.9 ± 0.2 | 3.6 ± 0.2 | 0.4 | 20.5 ± 2.3 |
| Force (mN) | Sample | $a_f$ (μm) | $a_r$ (μm) | $a_r/a_f$ ratio | $\omega_{average}$ (°) |
| 50 | EP-AA | 9.3 ± 0.2 | 3.2 ± 0.2 | 0.3 | 20.8 ± 0.8 |
| | EP-BB | 9.9 ± 0.3 | 4.0 ± 0.2 | 0.4 | 22.8 ± 1.6 |
| | EP-CC | 11.3 ± 0.2 | 3.7 ± 0.2 | 0.3 | 20.1 ± 2.5 |

### 4-1.4 Summary

In this study, five different methods are used to investigate the scratch behaviors and rank the scratch resistances of epoxy samples:

1. H/E ratio from IIT.
2. The onset force obtained from PS and CS tests.
3. The cross profile width to depth ratios: $W_p/D_f$ and $W_p/h_{b.}$
4. The recovery after scratched.
5. The scratch tail parameters: $a_r/a_f$ ratio, and $\omega_{average}$.

The H/E ratio is often used to rank the scratch and wear resistance in coating industry. In this study, using the H/E ratio, we conclude that EP-AA and EP-BB have the similar scratch resistance, and EP-CC has the weakest resistance. It is interesting because the modulus and hardness values are both higher in EP-BB than EP-AA. However, due to the correlation of these two quantities like the resistance to the scratch and recovery ability, the damage degree in EP-AA and EP-BB turns out to be close. The onset forces results confirm this point. From PS tests, the onset force values for two epoxies are close. Furthermore, the precise onset forces are acquired from an array of CS test at lower forces. The onset forces obtained from both tests are consistent. The scratch morphology and damage profile from an array of CS test at higher forces are also consistent with the observation from the tail image of PS results near 50 mN. The degree of damage can be distinguished clearly from the cross profiles of CS scratches at different CS forces. Although the scratch profiles appear similar for EP-AA and EP-BB (Figures 4.13-4.15), the detailed cross profile data provide a comprehensive understanding of the overall scratch behavior of three materials. The corresponding width to depth ratios such as $W_p/D_f$ and $W_p/h_b$ are suitable for ranking the scratch

resistance in the same force for different materials.

The recovery right after scratch can also be used to rank the scratch resistance. The recovery indicates the elasticity of the materials, which is the ability of recovery after being damage rather than to resist the damage. In this case study, the result is clear that EP-CC has a lowest recovery and worst scratch resistance at the range of force between 0 mN to 50 mN. Finally, the $a_r/a_f$ ratio and $\omega_{average}$ data from the scratch tail images can provide a general idea how much the materials is under the elastic deformation. In this case study, using $a_r/a_f$ ratio, and $\omega_{average}$ to rank scratch damage yields consistent results as using other methods. However, it is not robust to use the $a_r/a_f$ ratio, and $\omega_{average}$ as a good indicator to rank the scratch resistance because these two parameters are not as sensitive as other indicators.

Table 4.6 Summary of normalized indicators (ratio to EP-AA) for three epoxy samples.

| | EP-AA | EP-BB | EP-CC |
|---|---|---|---|
| $T_g$ (°C) | 117 | 88 | 71 |
| $T_g$ -$T_r$ (°) | 94 | 65 | 48 |
| H/E ratio | 1.000 | 0.977 | 0.818 |
| onset force | 1.0 | 0.9 | 0.5 |
| $W_p/D_f$ ratio | 1.0 | 0.8 | 0.6 |
| $W_p/h_b$ ratio | 1.0 | 0.7 | 0.5 |
| Recovery | 1.0 | 0.9 | 0.7 |
| $a_r/a_f$ ratio | 1.0 | 1.0 | 0.8 |
| $\omega_{average}$ | 1.0 | 1.0 | 0.9 |

Table 4.6 and Figure 4.20 summarize the pre-mentioned indicators to rank the scratch resistance for three epoxy samples, all the numbers are normalized by dividing the values from EP-AA. The H/E ratios come from IIT. The onset forces, $W_p/D_f$, $W_p/h_b$,

$a_r/a_f$ ratios, $\omega_{average}$ and recovery are obtained from PS tests. The $W_p/D_f$, $W_p/h_b$ ratios and recovery are acquired at the force near 50 mN. $T_r$ is the room temperature at 23 °C. Clearly, the indicators: onset force, $W_p/D_f$, and $W_p/h_b$ are better than other indicators. The $a_r/a_f$ ratio and $\omega_{average}$ are the worse indicators.

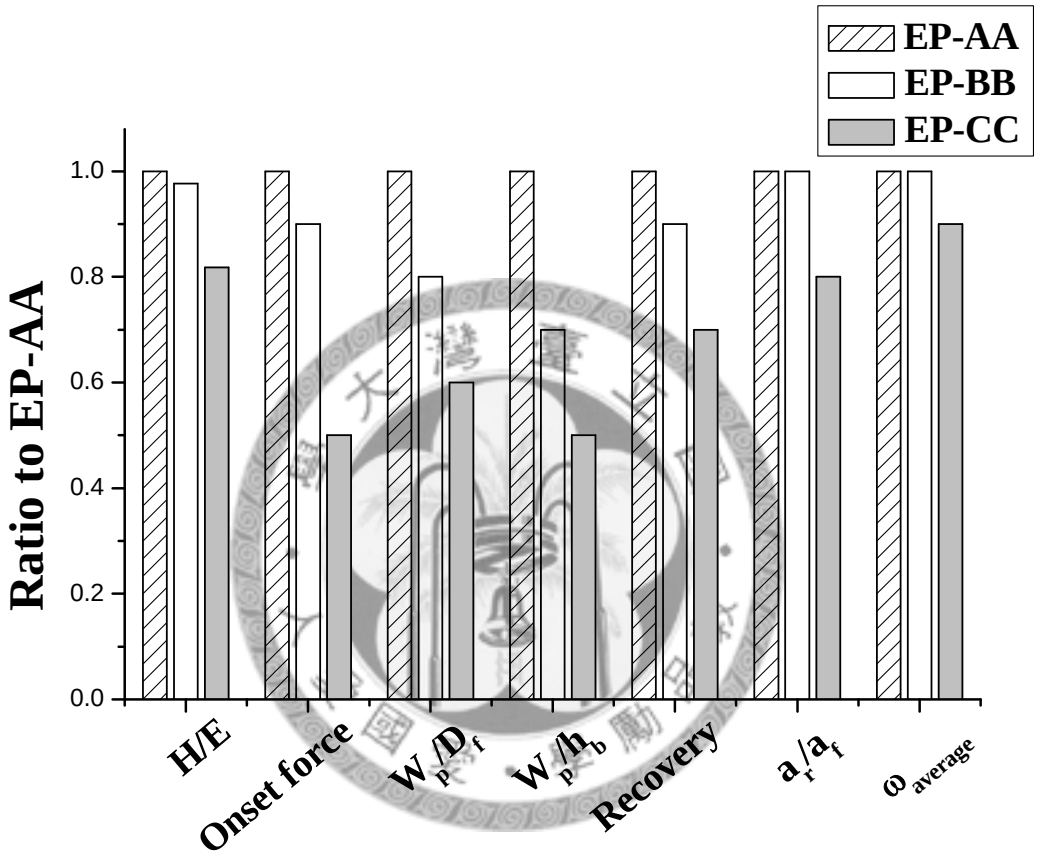


Figure 4.20 The diagrammatic summary of three epoxy samples presented in the normalized indicators (ratio to EP-AA).

In summary, EP-AA has a highest glass transition temperature $T_g$ and best scratch resistance among the three epoxies, and EP-CC has a lowest $T_g$ and worst scratch resistance.

## 4-2 Polyurethane Series 1

### 4-2.1 Indentation Data

The elastic modulus and hardness results obtained from the instrumented indentation tests are summarized in Table 4.7. These results are averaged from 5 indents. A nominal 10 μm 90 diamond tip was applied and indented into 1000 nm with a strain rate of 0.05 1/s. Reported values of modulus and hardness for each indent were averaged over a depth range from 500 nm to 900 nm without a drift correction. Figure 4.21 to Figure 4.23 plot modulus, hardness, and H/E ratio for four PU samples from series 1. The modulus data are almost the same, within measurement uncertainties. For four samples, similar results for the hardness values except a slightly low value for PU-B1. The difference in H values reflects on the H/E ratios as shown in Figure 4.23. The PU-B1 has a slight low H/E ratio compared to the rest of the samples.

Table 4.7 Surface mechanical properties of four PU samples from series 1, which are determined by indentation testing using a conical indenter. The error bar represents one standard deviation from the averaged value of 5 indentations.

| Sample | Modulus, E (GPa) | Hardness, H (GPa) | H/E |
|---|---|---|---|
| PU-CTRL1 | 3.123 ± 0.02 | 0.234 ± 0.002 | 0.075 |
| PU-A1 | 3.057 ± 0.079 | 0.239 ± 0.013 | 0.078 |
| PU-B1 | 3.092± 0.013 | 0.216 ± 0.003 | 0.070 |
| PU-C1 | 3.138 ± 0.014 | 0.239 ± 0.005 | 0.076 |

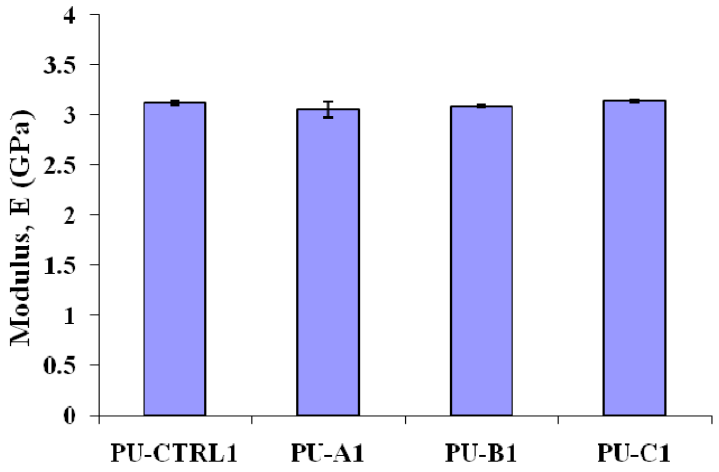


Figure 4.21 Modulus value for series 1 four PU samples.

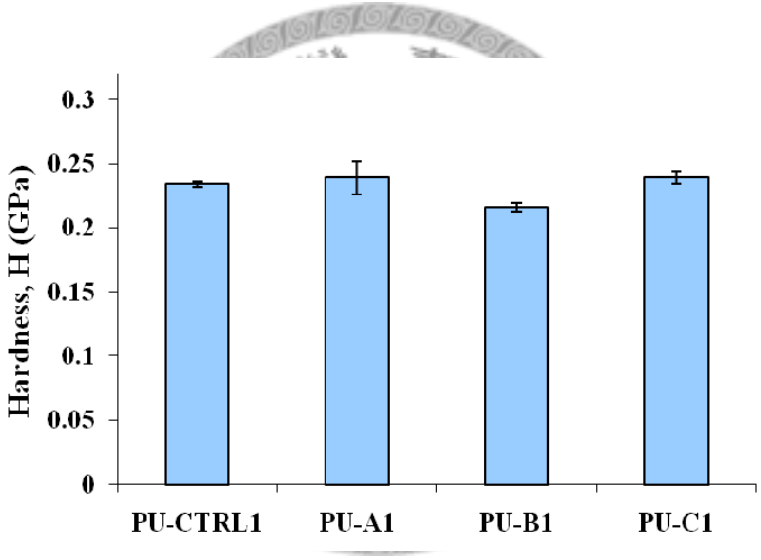


Figure 4.22 Hardness value for series 1 four PU samples.

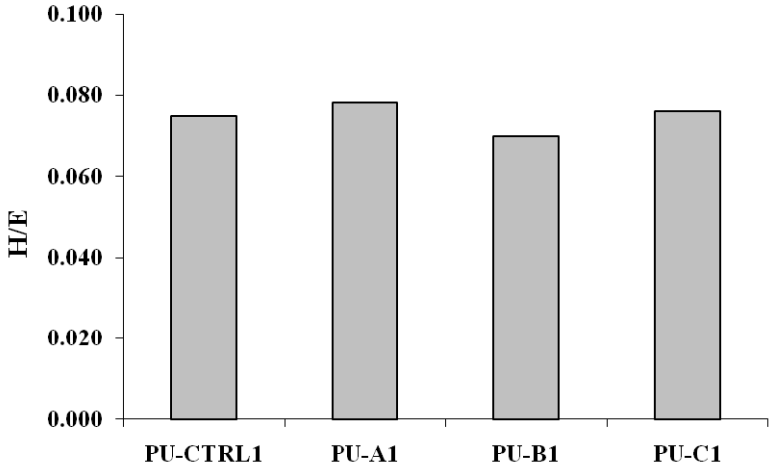


Figure 4.23 Hardness to modulus ratio for series 1 four PU samples.

The effect of different strain rates plays a vital role in the indentation testing [42]. In order to study the PU samples thoroughly, the various strain rates (0.01 1/s, 0.05 1/s, 0.1 1/s, 0.5 1/s, and 1 1/s) are also applied to perform the indentation tests in succession. 5 indents are carried out in each strain rate and the indent depth is 1000 nm. Figure 4.24 and Figure 4.25 plot modulus for four samples under different strain rates using a 10 μm radius conical tip and a Berkovich tip, respectively. The modulus values are almost the same for all four samples (within measurement uncertainties) and the results are consistent by two different indenters. Also, the modulus decreases while increasing the strain rate in both cases (using two different indenters). The hardness as a function of strain rate is plotted in Figure 4.26 and Figure 4.27 for a conical tip, and a Berkovich tip, respectively. On the contrary, the hardness increases as increasing the strain rate. Again, the trends in the data are consistent using two different indenters. The data of modulus and hardness under different strain rates for four samples are summarized in Table 4.8 to Table 4.11. Clearly, the modulus and hardness values depend strongly on the applied strain rates and the indenter tip geometry. It is important to keep the test condition constant before comparison.

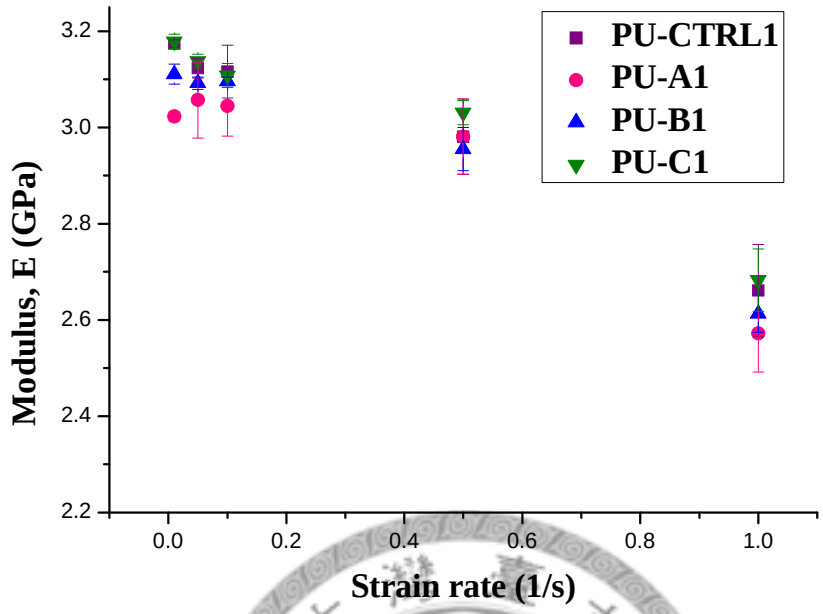


Figure 4.24 Modulus of four PU samples (series 1) under different strain rates using a 10 μm radius conical indenter.

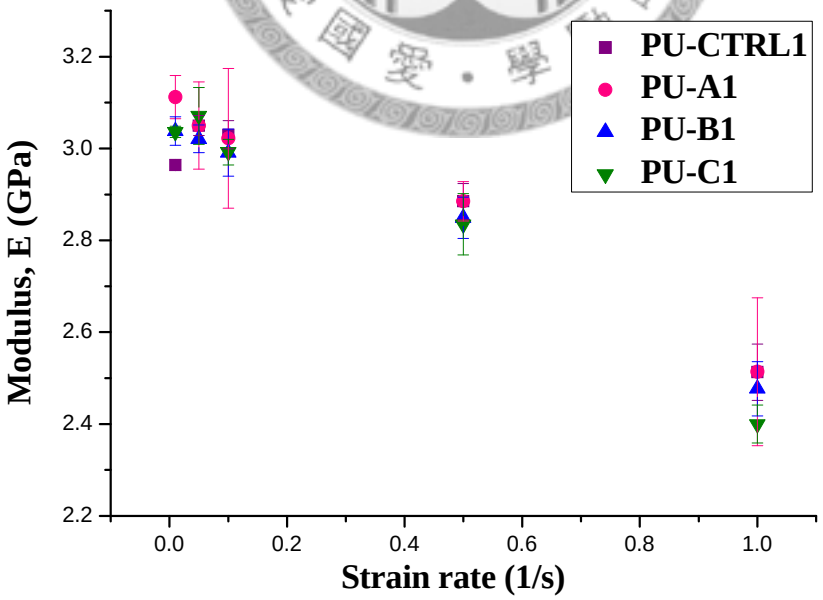


Figure 4.25 Modulus of four PU samples (series 1) under different strain rates using a Berkovich indenter.

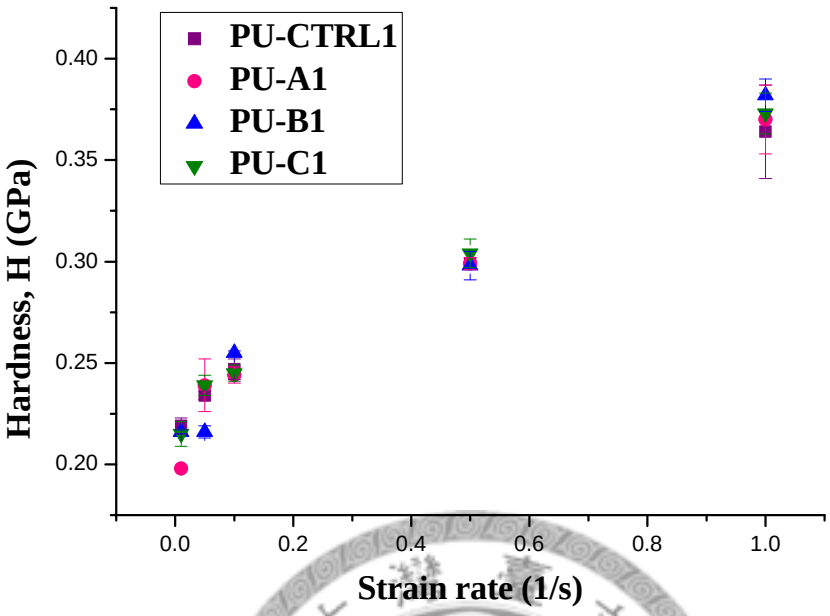


Figure 4.26 Hardness of four PU samples (series 1) under different strain rates using a 10 μm radius conical indenter.

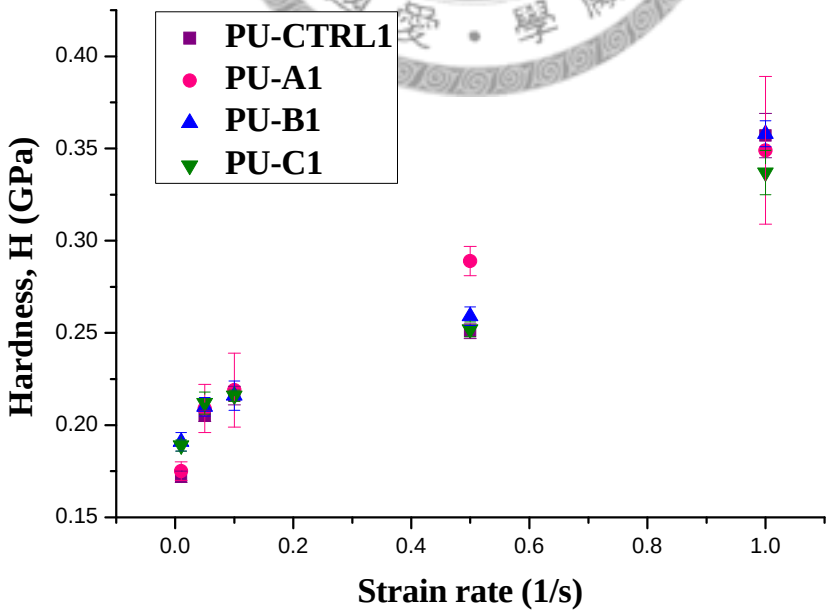


Figure 4.27 Hardness of four PU samples (series 1) under different strain rates using a Berkovich indenter.

Table 4.8 The modulus values of four PU samples (series 1) under different strain rates using a 10 μm radius conical indenter. The error bar represents one standard deviation from the averaged value of 5 indentations.

| Strain rate (1/s) | Modulus, E (GPa) | | | |
|---|---|---|---|---|
| | PU-CTRL1 | PU-A1 | PU-B1 | PU-C1 |
| 0.01 | 3.174 ± 0.008 | 3.023 ± 0.009 | 3.111 ± 0.021 | 3.179 ± 0.015 |
| 0.05 | 3.123 ± 0.020 | 3.057 ± 0.079 | 3.092 ± 0.013 | 3.138 ± 0.014 |
| 0.1 | 3.116 ± 0.055 | 3.045 ± 0.063 | 3.096 ± 0.009 | 3.108 ± 0.025 |
| 0.5 | 2.981 ± 0.078 | 2.981 ± 0.078 | 2.955 ± 0.045 | 3.031 ± 0.025 |
| 1 | 2.661 ± 0.096 | 2.572 ± 0.080 | 2.613 ± 0.039 | 2.683 ± 0.065 |

Table 4.9 The modulus values of four PU samples (series 1) under different strain rates using a Berkovich indenter. The error bar represents one standard deviation from the averaged value of 5 indentations.

| Strain rate (1/s) | Modulus, E (GPa) | | | |
|---|---|---|---|---|
| | PU-CTRL1 | PU-A1 | PU-B1 | PU-C1 |
| 0.01 | 2.964 ± 0.012 | 3.112 ± 0.047 | 3.038 ± 0.031 | 3.036 ± 0.012 |
| 0.05 | 3.050 ± 0.022 | 3.050 ± 0.095 | 3.021 ± 0.030 | 3.071 ± 0.062 |
| 0.1 | 3.030 ± 0.031 | 3.022 ± 0.152 | 2.991 ± 0.051 | 2.992 ± 0.028 |
| 0.5 | 2.885 ± 0.039 | 2.885 ± 0.043 | 2.849 ± 0.045 | 2.835 ± 0.067 |
| 1 | 2.513 ± 0.061 | 2.514 ± 0.161 | 2.477 ± 0.059 | 2.400 ± 0.041 |

Table 4.10 The hardness values of four PU samples (series 1) under different strain rates using a 10 μm radius conical indenter. The error bar represents one standard deviation from the averaged value of 5 indentations.

| Strain rate (1/s) | Hardness, H (GPa) | | | |
|---|---|---|---|---|
| | PU-CTRL1 | PU-A1 | PU-B1 | PU-C1 |
| 0.01 | 0.219 ± 0.004 | 0.198 ± 0.001 | 0.216 ± 0.001 | 0.215 ± 0.006 |
| 0.05 | 0.234 ± 0.002 | 0.239 ± 0.0013 | 0.216 ± 0.003 | 0.239 ± 0.005 |
| 0.1 | 0.247 ± 0.005 | 0.244 ± 0.004 | 0.255 ± 0.001 | 0.245 ± 0.004 |
| 0.5 | 0.299 ± 0.003 | 0.299 ± 0.003 | 0.298 ± 0.007 | 0.304 ± 0.007 |
| 1 | 0.364 ± 0.0023 | 0.37 ± 0.017 | 0.382 ± 0.008 | 0.373 ± 0.010 |

Table 4.11 The hardness values of four PU samples (series 1) under different strain rates using a Berkovich indenter. The error bar represents one standard deviation from the averaged value of 5 indentations.

| Strain rate (1/s) | Hardness, H (GPa) | | | |
|---|---|---|---|---|
| | PU-CTRL1 | PU-A1 | PU-B1 | PU-C1 |
| 0.01 | 0.172 ± 0.003 | 0.175 ± 0.005 | 0.191 ± 0.005 | 0.189 ± 0.003 |
| 0.05 | 0.205 ± 0.003 | 0.209 ± 0.013 | 0.210 ± 0.005 | 0.212 ± 0.006 |
| 0.1 | 0.216 ± 0.005 | 0.219 ± 0.020 | 0.216 ± 0.008 | 0.216 ± 0.003 |
| 0.5 | 0.251 ± 0.004 | 0.289 ± 0.008 | 0.259 ± 0.005 | 0.252 ± 0.004 |
| 1 | 0.357 ± 0.012 | 0.349 ± 0.040 | 0.358 ± 0.007 | 0.337 ± 0.012 |

### 4-2.2 PS Data

Figure 4.28 shows the results of onset forces and LSCM images obtained from the PS tests. Three scratches are generated for each sample. The scratch force range is from 0 mN to 30 mN, and the scratch length is 1000 μm with a speed of 10 μm/s. The onset force is smallest for PU-A1 ($F_{onset}$ = 3.9 mN ± 0.1 mN) and largest for PU-C1 ($F_{onset}$ =

4.8 mN ± 0.2 mN). Comparing to the result from H/E ratios, PU-B1 has the lowest H/E ratio but it does not show the smallest onset force. Instead, PU-A1 has the highest H/E ratio but the smallest onset force, i.e., the weakest scratch resistance. The inconsistency of two testing results is understandable because the H/E ratios are almost the same within measurement uncertainties. The onset force is a better indicator for ranking scratch resistance in this case.


Figure 4.28 LSCM images and onset forces obtained from PS tests (0 mN to 30 mN, scratch length= 1000 μm) of four PU samples (series 1).

Figure 4.29 shows the tail images of four PU samples (series 1) obtained from PS tests near 30 mN. As the images show, all the scratch damages appear similar in the

tail portions of scratches. Figure 4.30 shows the cross profiles of four PU samples (series 1) obtained from PS tests at the force near 30 mN. All profiles appear similar except PU-B1 is slight different with a higher pile-up. Table 4.12 summarizes the detailed cross profile information, including $W_p$, $D_p$, $h_b$, ratio of $W_p/D_f$ and $W_p/h_b$ for four PU samples (series 1) near 30 mN in PS tests. The values of $W_p$, $D_f$, and $h_b$ are the same (within the experimental uncertainties) for all 4 samples. PU-B1 has the slightly smallest $W_p/D_f$ ratio, but still within experimental uncertainties compared to the other three samples. No clear conclusion can be made here. The corresponding tail information includes $a_f$, $a_r$, $\omega_{average}$, and $a_r$ to $a_f$ ratio are listed in Table 4.13. The $a_r/a_f$ ratio and $\omega_{average}$ are almost the same for four samples.

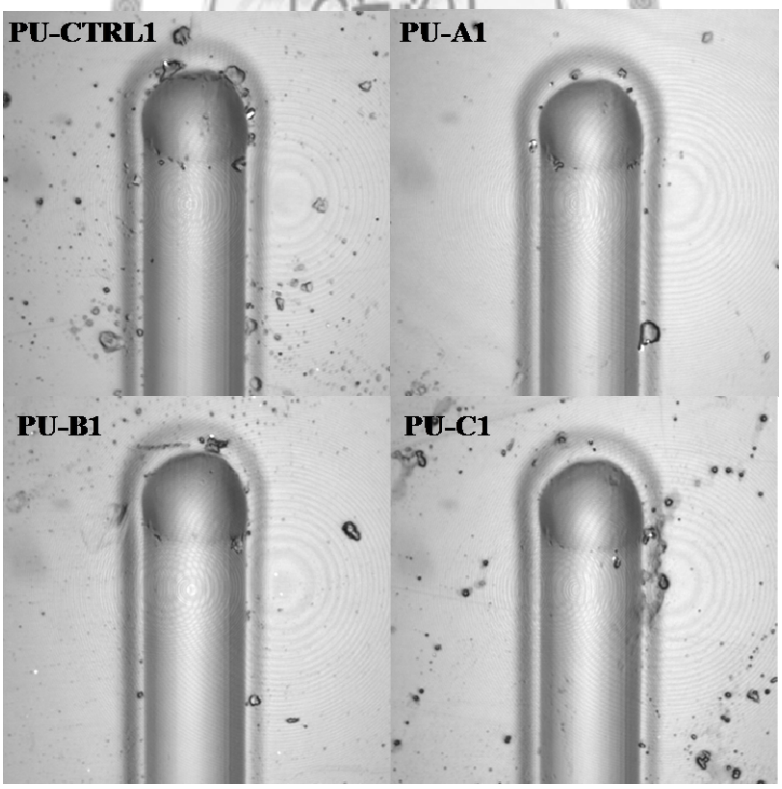


Figure 4.29 The tail images of four PU samples (series 1) obtained from PS tests near 30 mN.

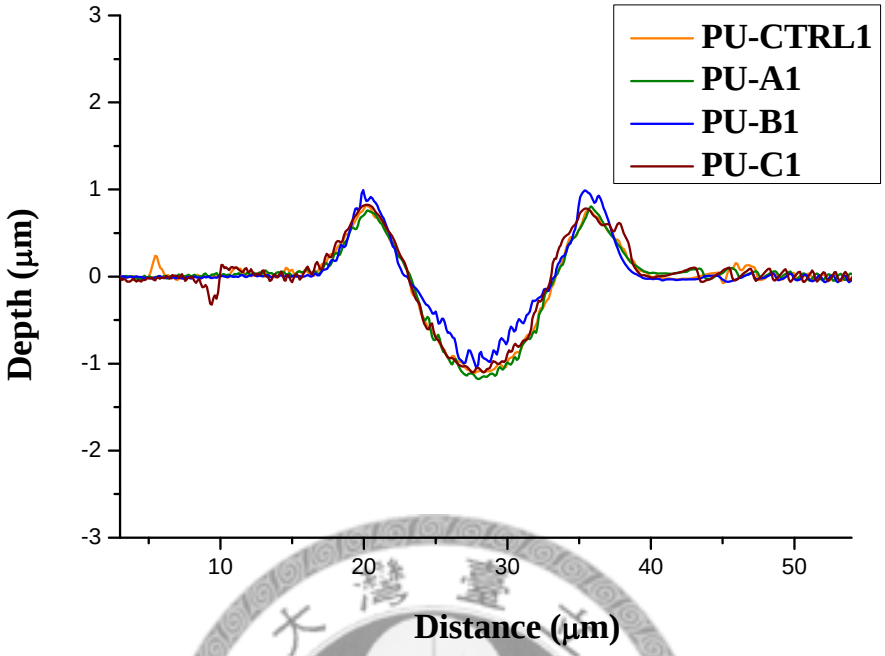


Figure 4.30 The cross profiles of four PU samples (series 1) obtained from PS tests near 30 mN.

Table 4.12 The detailed cross profile information ($W_p$, $D_p$, $h_b$, ratio of $W_p/D_f$ and $W_p/h_b$) of four PU samples (series 1) obtained from PS tests (0 mN to 30 mN, scratch length= 1000 μm) at the force near 30 mN. The error bar represents one standard deviation from two scratches.

| Sample | $W_p$ (μm) | $D_f$ (μm) | $h_b$ (μm) | $W_p/D_f$ | $W_p/h_b$ |
|---|---|---|---|---|---|
| PU-CNTL1 | 15.4 ± 0.2 | 1.9 ± 0.1 | 0.8 ± 0.1 | 8.1 | 19.3 |
| PU-A1 | 15.4 ± 0.4 | 1.9 ± 0.1 | 0.8 ± 0.1 | 8.1 | 19.1 |
| PU-B1 | 15.4 ± 0.2 | 2.0 ± 0.2 | 1.0 ± 0.1 | 7.6 | 15.2 |
| PU-C1 | 15.4 ± 0.4 | 1.9 ± 0.1 | 1.0 ± 0.2 | 8.1 | 15.4 |

Table 4.13 The detailed scratch tail information ($a_r$, $a_f$, $a_r/a_f$ ratio, and $\omega_{average}$) of four PU samples (series 1) obtained from PS tests. The error bar represents one standard deviation from two scratches.

| Sample | $a_r$ (μm) | $a_f$ (μm) | $a_r/a_f$ ratio | $\omega_{average}$ (°) |
|---|---|---|---|---|
| PU-CNTL1 | 3.5 ± 0.2 | 8.2 ± 0.1 | 0.4 | 24.3 ± 1.1 |
| PU-A1 | 3.0 ± 0.1 | 8.0 ± 0.1 | 0.4 | 24.0 ± 2.5 |
| PU-B1 | 3.1 ± 0.1 | 8.0 ± 0.1 | 0.4 | 24.5 ± 1.3 |
| PU-C1 | 3.2 ± 0.1 | 8.0 ± 0.1 | 0.4 | 24.2 ± 2.8 |

Figure 4.31 and Figure 4.32 display the initial and residual penetration curves of four PU samples (series 1) obtained from PS tests, respectively. All of the curves are overlapped to each other. The same as the recovery results, as shown in Figure 4.33. So far, no significant difference is observed in the scratch morphology, penetration curves, and recovery for all PU samples (series 1). Interestingly, the friction forces are different for four samples. As shown in Figure 4.34, PU-C1 has highest friction force, and PU-CTRL1 has the lowest one, after scratch distance greater than 400 μm. The friction force curves of PU-A1 and PU-B1 are similar. The friction coefficient curve reflects the same trend as the friction force curves (see Figure 4.35). PU-C1 has the highest friction coefficient values, PU-B1 is the second, PU-A1 is the third, and PU-CTRL1 has the lowest. The difference shown in the friction behavior is intriguing. From 4.1 epoxy section, we observed that a higher friction force/coefficient (EP-CC) implies a lower scratch resistance. If the PU systems have the same friction behavior, PU-C1 has a worst scratch resistance. However, it is inclusive to make this judgment because it is no significant difference observed in other scratch data from PS tests.

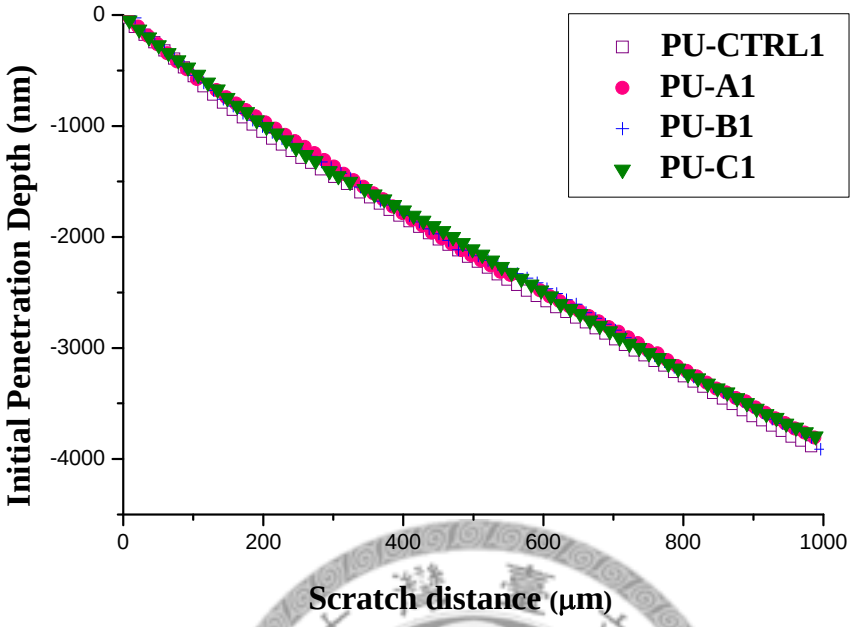


Figure 4.31 The initial penetration curves of four PU samples (series 1) obtained from PS tests.

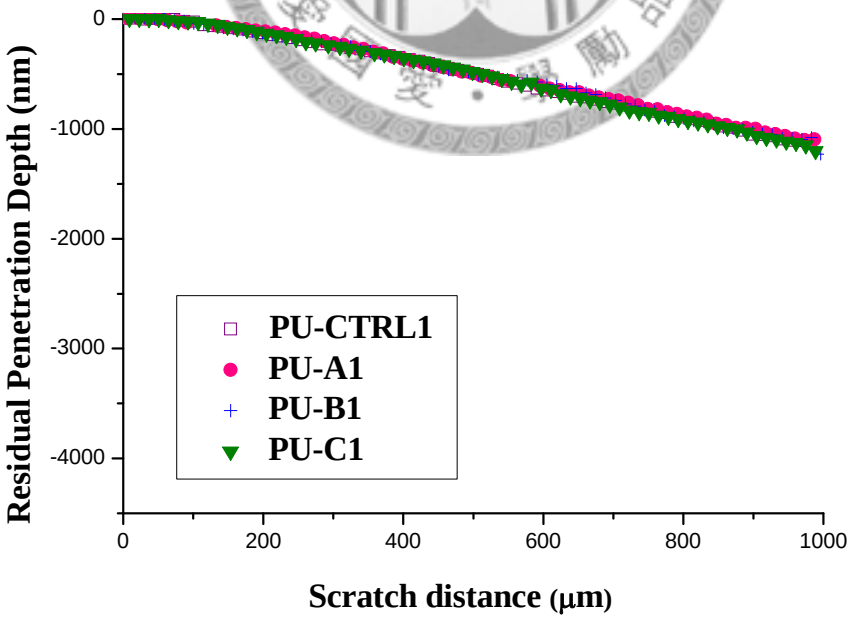


Figure 4.32 The residual penetration curves of four PU samples (series 1) obtained from PS tests.

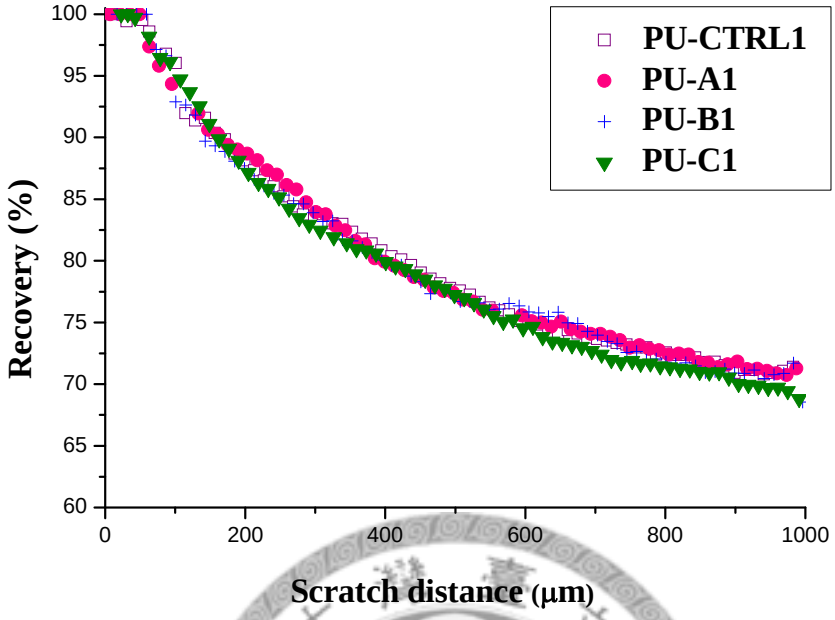


Figure 4.33 The recovery of four PU samples (series 1) obtained from PS tests.

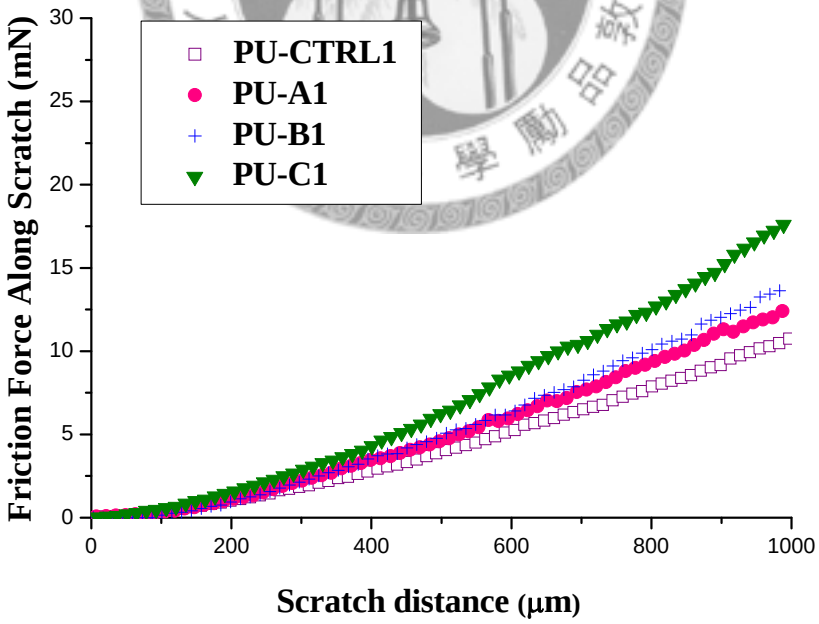


Figure 4.34 The friction forces along scratches of four PU samples (series 1) obtained from PS tests.

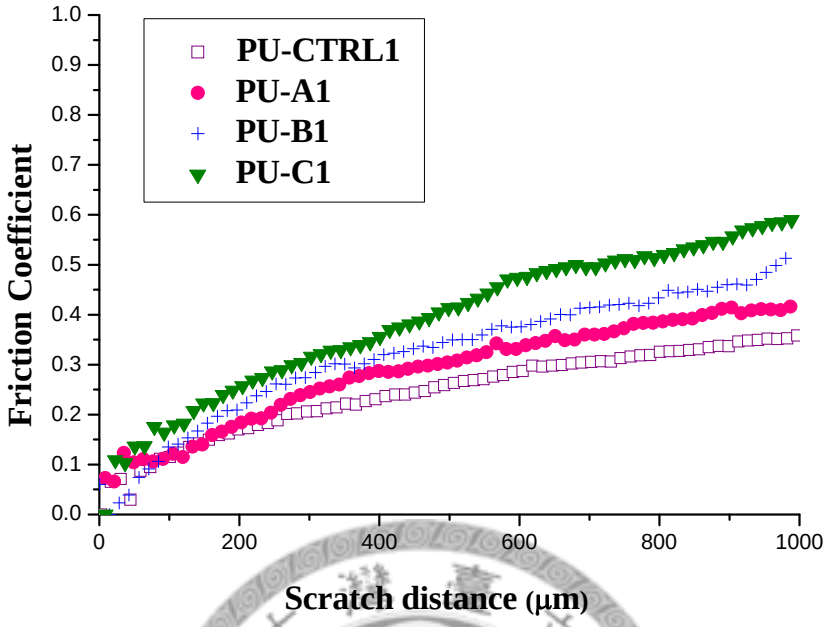


Figure 4.35 The friction coefficients of four PU samples (series 1) obtained from PS tests.

### 4-2.3 CS Data

A series of CS tests were carried out to assess the accurate onset forces of four PU samples (series 1). The CS scratch forces include: 3 mN, 4 mN, 5 mN, 6mN, and 7 mN. The scratch length is 500 μm, and two scratches are generated for each force. Figure 4.36 shows the CS array images and the onset forces obtained from PS and CS tests. The onset force values are close between PS and CS tests. PU-A1 has the smallest onset force in both tests. Also, the CS arrays appear similar between PU-CTRL1 and PU-B1. The results of PU-C1 are more interesting. Although PU-C1 has the highest onset force in the PS tests, the scratches in CS test are even more severe in the low forces (3 mN and 4 mN) comparing to PU-CTRL1 and PU-B1. As the picture shows, a long scratch line (in the left-hand-side low corner) crosses the scratch array in PU-C1. Below the

line, the scratches are almost invisible; above the line, the scratch damages become visible. This line is found to divide two regions with different responses to the scratch. The result might be due to the poor dispersion of nanoparticles or a rough surface in PU-C1.

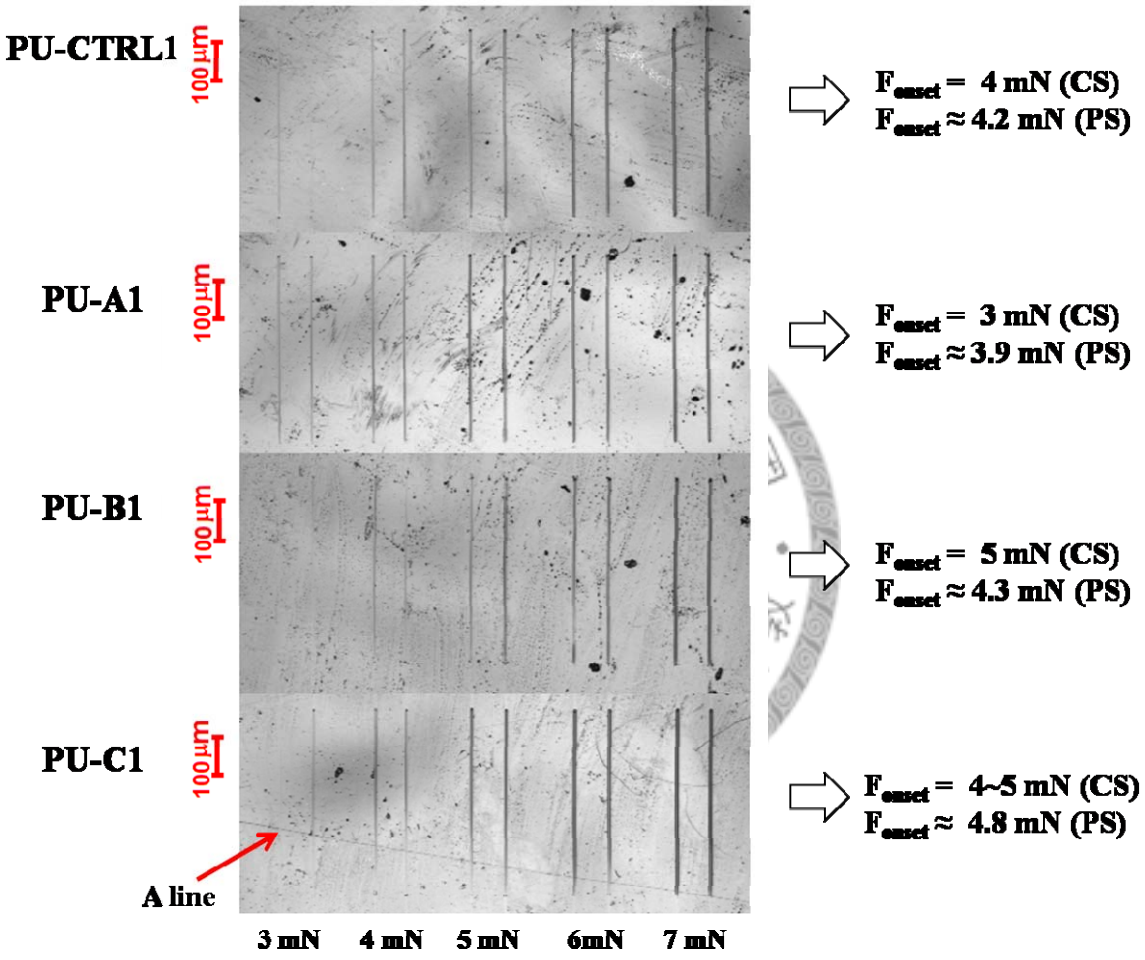


Figure 4.36 CS array (3 mN, 4 mN, 5 mN, 6mN, and 7 mN) and onset forces of four polyurethane samples (series 1).

### 4-2.4 Summary

Table 4.14 The normalized indicators (ratio to PU-CTRL1) for four PU samples (series 1). The H/E ratios come from IIT. The onset forces, $W_p/D_f$, $W_p/h_b$, $a_r/a_f$ ratios, $\omega_{average}$ and recovery are obtained from PS tests. The $W_p/D_f$, $W_p/h_b$ ratios and recovery are acquired at the force near 30 mN.

| | PU-CTRL1 | PU-A1 | PU-B1 | PU-C1 |
|---|---|---|---|---|
| H/E | 1.000 | 1.040 | 0.933 | 1.013 |
| Onset force | 1.0 | 0.9 | 1.0 | 1.1 |
| $W_p/D_f$ | 1.0 | 1.0 | 0.9 | 1.0 |
| $W_p/h_b$ | 1.0 | 1.0 | 0.8 | 0.8 |
| Recovery | 1.0 | 1.0 | 1.0 | 1.0 |
| $a_r/a_f$ ratio | 1.0 | 1.0 | 1.0 | 1.0 |
| $\omega_{average}$ | 1.0 | 1.0 | 1.0 | 1.0 |

Similar to section 4.1, many indicators are used to rank the scratch resistances of polyurethane samples (series 1). These indicators include H/E ratio, onset force obtained from PS and CS tests, $W_p/D_f$, $W_p/h_b$, $a_r/a_f$ ratio, $\omega_{average}$, and the recovery. The H/E ratio does not show any significant difference among all four samples. In the case of using onset force as an indicator: PU-A1 has the weakest scratch resistance (lowest onset force), and both PU-CTRL1 and PU-B1 are similar in scratch ranking in both PS and CS test. PU-C1 has the highest onset force thus the strongest scratch resistance in the PS tests. However, the onset force depends on the region of sample, as shown in Figure 4.36. The poor nanoparticle dispersion within the coating or surface roughness may affect the scratch test results. Similar cause might contribute the reason why the friction force and coefficient are different when the initial and residual penetration curves are almost identical for four PU samples. The other indicators also show that the

scratch resistances are almost the same for four samples. Table 4.14 and Figure 4.37 summarize the ranking from all normalized indicators mentioned in the text for four PU samples (series 1). Overall, the investigation from all indicators provides the same conclusion. The onset force is slightly different from four samples, but no other significant changes are observed. Hence, the scratch behaviors are found to be similar in this polyurethane series.

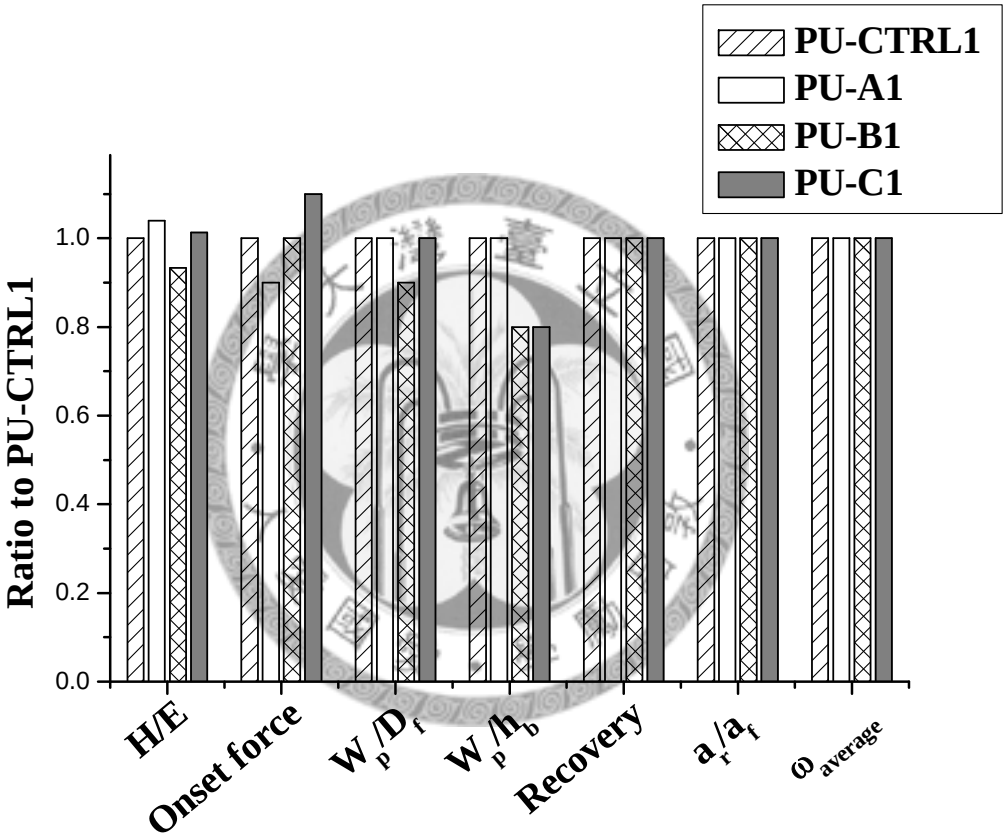


Figure 4.37 The diagrammatic summary of four polyurethane samples (series 1) presented in the normalized indicators (ratio to PU-CTRL1).

## 4-3 Polyurethane Series 2

### 4-3.1 Indentation Data

The elastic modulus and hardness results of PU series 2 samples obtained from the instrumented indentation tests are shown in Table 4.15. The same conical indenter with the 10 μm radius was applied. These results are averaged from 5 indents, and the indent depth is 1000 nm with a strain rate of 0.05 1/s. Reported values of modulus and hardness for each indent were averaged over a depth range from 500 nm to 900 nm without a drift correction. Figure 4.38 to Figure 4.40 plot modulus, hardness, and H/E ratio for four PU (series 2) samples. As mentioned in the material chapter, the polarities of nanosilica additives are different between samples. PU-CTRL2 has no nanoparticle and dispersant, and the additive polarities for PU-A2 to PU-C2 are from low to high. Unlike the series 1 samples, a trend is observed in all three plots of series 2 samples. The PU-CTRL has the lowest modulus, hardness, and H/E ratio, and those quantities increase in the reference group as increasing the additives polarities. PU-C2 has the highest modulus, hardness and H/E ratio than other samples. The E and H values of PU-A2 and PU-B2 are similar with slightly higher values in PU-B2. A noteworthy fact is that the additive structures in PU-A2 and PU-B2 are both linear copolymers, and PU-C2 has a more complicated branched copolymer structures.

Table 4.15 Surface mechanical properties of four PU samples (series 2), determined by indentation testing using a conical indenter. The error bar represents one standard deviation from the averaged value of 5 indentations.

| Sample | Modulus, E (GPa) | Hardness, H (GPa) | H/E |
|---|---|---|---|
| PU-CTRL2 | 1.826 ± 0.014 | 0.075 ± 0.001 | 0.041 |
| PU-A2 | 1.906 ± 0.009 | 0.088 ± 0.001 | 0.046 |
| PU-B2 | 1.937 ± 0.004 | 0.091 ± 0.001 | 0.047 |
| PU-C2 | 2.340 ± 0.011 | 0.128 ± 0.001 | 0.055 |

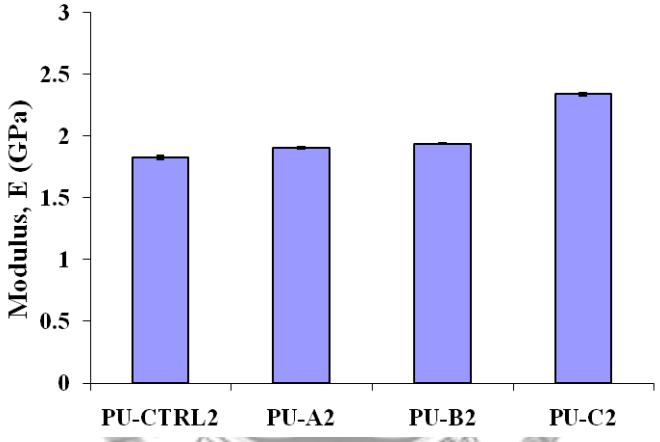


Figure 4.38 Modulus value for four PU samples (series 2).

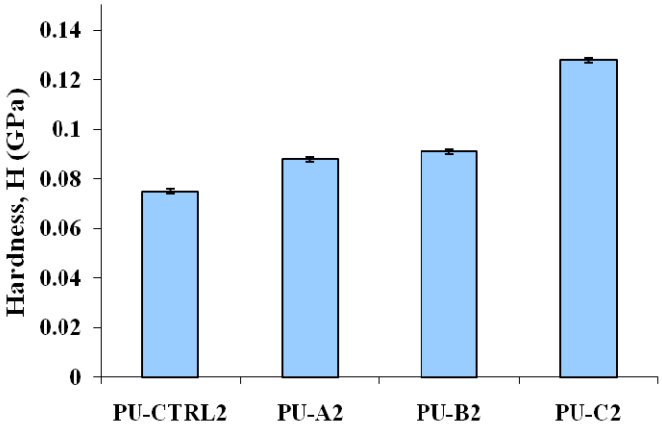


Figure 4.39 Hardness value for four PU samples (series 2).

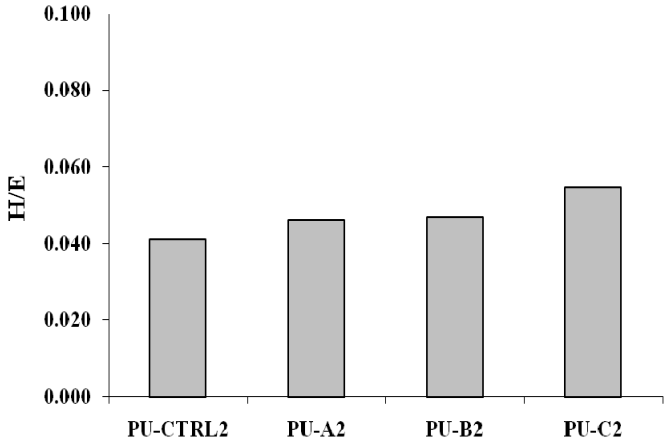


Figure 4.40 Hardness to modulus ratio for four PU samples (series 2).

The modulus, hardness and H/E ratio are smaller for this series of samples than series 1. The result is reasonable owing to a material with lower $T_g$ is usually easily to deform under the loading. The effect of different strain rates is also examined in this series of samples. The strain rates include: 0.01 1/s, 0.05 1/s, 0.1 1/s, 0.5 1/s, and 1 1/s. The experimental conditions are the same as in series 1. In each strain rate, 5 indents are carried out and the indent depth is 1000 nm. Figure 4.41 and Figure 4.42 plot modulus for four samples under different strain rates using a 10 μm radius conical tip and a Berkovich indenter. A clear trend is observed from two plots. The modulus increases as increasing the strain rate at first, and then decreases at the strain rate of 0.5 1/s and 1 1/s. The increasing of modulus in the low strain rate is not observed in series 1. In addition, the results are consistent by using two different tips. PU-C2 still has the highest modulus at all strain rates studied here than other samples. This result matches with the H/E ratio. Also, Figures 4.43- 4.44 plot hardness as a function of strain rate using a conical tip, and a Berkovich tip, respectively. PU-CTRL2 still has the lowest hardness values and PU-C2 has the highest at all stain rates. The trend in the hardness data versus the strain rate is consistent with series 1. The results of modulus and hardness under different strain rates for series 2 samples are summarized in Table 4.16 to Table 4.19.

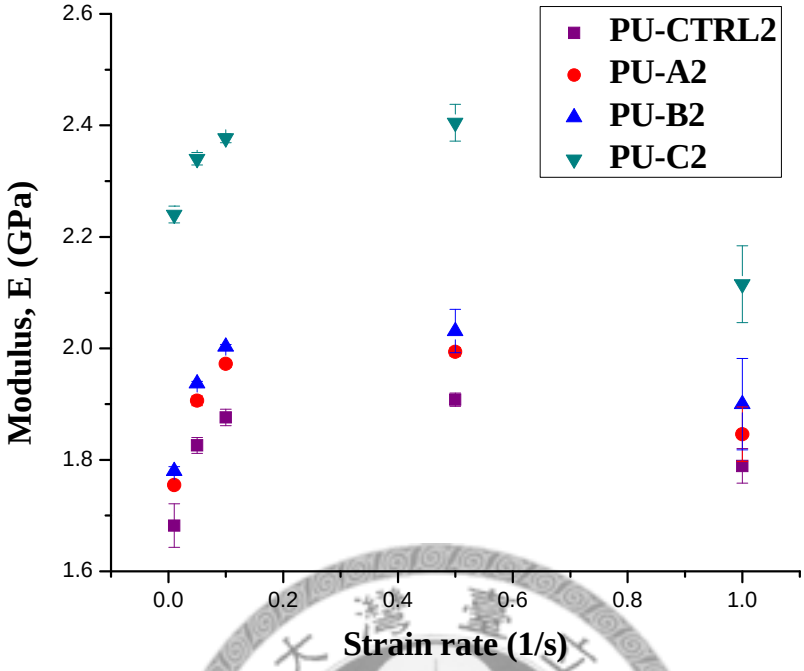


Figure 4.41 Modulus of four PU samples (series 2) under different strain rates using a 10 μm radius conical indenter.

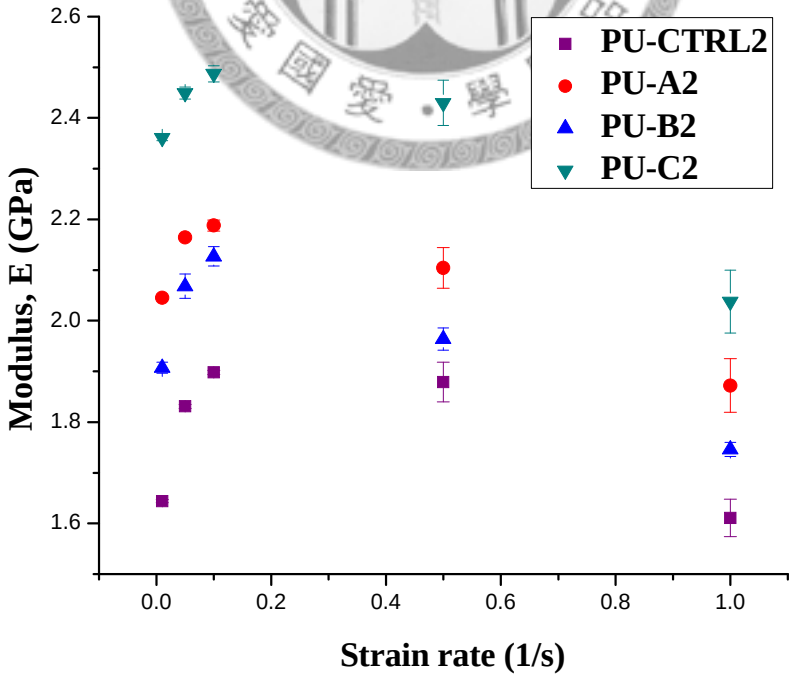


Figure 4.42 Modulus of four PU samples (series 2) under different strain rates using a Berkovich indenter.

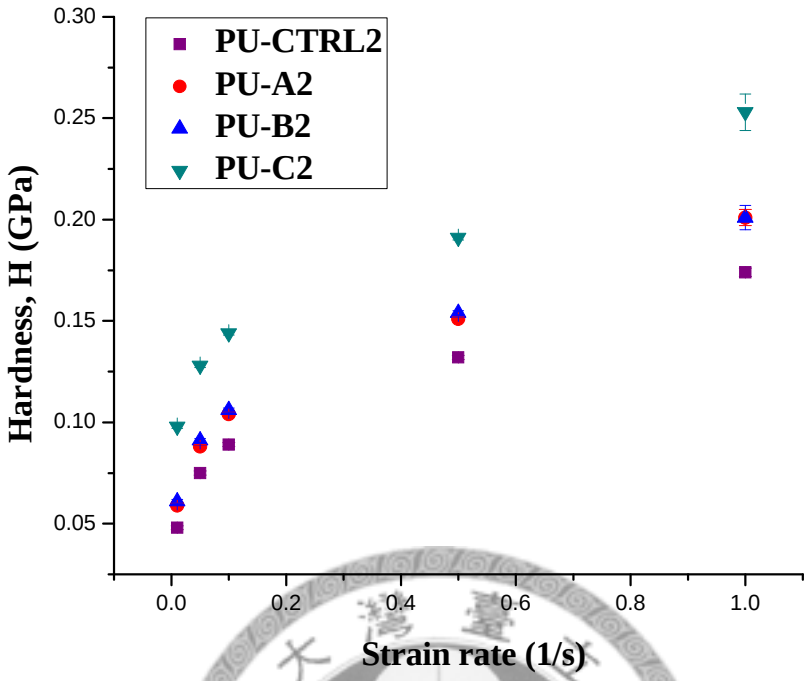


Figure 4.43 Hardness of four PU samples (series 2) under different strain rates using a 10 μm radius conical indenter.

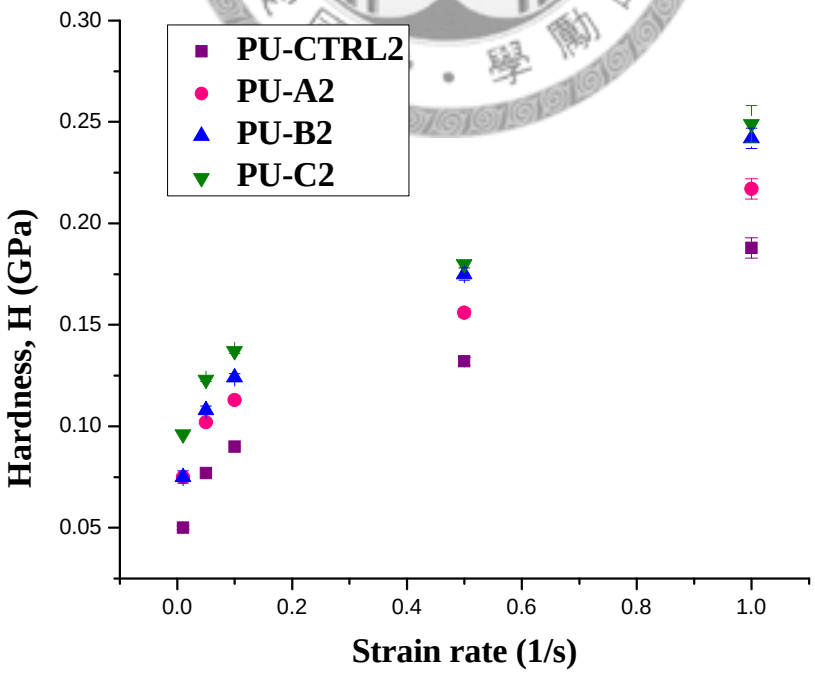


Figure 4.44 Hardness of four PU samples (series 2) under different strain rates using a Berkovich indenter.

Table 4.16 Modulus values of four PU samples (series 2) under different strain rates using a 10 μm radius conical indenter. The error bar represents one standard deviation from the averaged value of 5 indentations.

| Strain rate (1/s) | Modulus, E (GPa) | | | |
|---|---|---|---|---|
| | PU-CTRL2 | PU-A2 | PU-B2 | PU-C2 |
| 0.01 | 1.682 ± 0.039 | 1.755 ± 0.005 | 1.780 ± 0.008 | 2.240 ± 0.015 |
| 0.05 | 1.826 ± 0.014 | 1.906 ± 0.009 | 1.937 ± 0.004 | 2.340 ± 0.011 |
| 0.1 | 1.876 ± 0.015 | 1.972 ± 0.006 | 2.003 ± 0.004 | 2.377 ± 0.008 |
| 0.5 | 1.908 ± 0.012 | 1.994 ± 0.008 | 2.031 ± 0.039 | 2.405 ± 0.033 |
| 1 | 1.789 ± 0.031 | 1.846 ± 0.049 | 1.900 ± 0.082 | 2.115 ± 0.069 |

Table 4.17 Modulus values of four PU samples (series 2) under different strain rates using a Berkovich indenter. The error bar represents one standard deviation from the averaged value of 5 indentations.

| Strain rate (1/s) | Modulus, E (GPa) | | | |
|---|---|---|---|---|
| | PU-CTRL2 | PU-A2 | PU-B2 | PU-C2 |
| 0.01 | 1.644 ± 0.003 | 2.045 ± 0.003 | 1.907 ± 0.011 | 2.361 ± 0.006 |
| 0.05 | 1.831 ± 0.004 | 2.164 ± 0.004 | 2.068 ± 0.024 | 2.449 ± 0.012 |
| 0.1 | 1.898 ± 0.004 | 2.188 ± 0.011 | 2.127 ± 0.019 | 2.487 ± 0.016 |
| 0.5 | 1.879 ± 0.039 | 2.104 ± 0.004 | 1.964 ± 0.022 | 2.430 ± 0.045 |
| 1 | 1.611 ± 0.037 | 1.872 ± 0.053 | 1.746 ± 0.014 | 2.038 ± 0.062 |

Table 4.18 Hardness values of four PU samples (series 2) under different strain rates using a 10 μm radius conical indenter. The error bar represents one standard deviation from the averaged value of 5 indentations.

| Strain rate (1/s) | Hardness, H (GPa) | | | |
|---|---|---|---|---|
| | PU-CTRL2 | PU-A2 | PU-B2 | PU-C2 |
| 0.01 | 0.048 ± 0.001 | 0.059 ± 0.001 | 0.061 ± 0.001 | 0.098 ± 0.001 |
| 0.05 | 0.075 ± 0.001 | 0.088 ± 0.001 | 0.091 ± 0.001 | 0.128 ± 0.001 |
| 0.1 | 0.089 ± 0.001 | 0.104 ± 0.001 | 0.106 ± 0.001 | 0.144 ± 0.001 |
| 0.5 | 0.132 ± 0.001 | 0.151 ± 0.001 | 0.154 ± 0.001 | 0.191 ± 0.001 |
| 1 | 0.174 ± 0.002 | 0.201 ± 0.004 | 0.201 ± 0.006 | 0.253 ± 0.009 |

Table 4.19 Hardness values of four PU samples (series 2) under different strain rates using a Berkovich indenter. The error bar represents one standard deviation from the averaged value of 5 indentations.

| Strain rate (1/s) | Hardness, H (GPa) | | | |
|---|---|---|---|---|
| | PU-CTRL2 | PU-A2 | PU-B2 | PU-C2 |
| 0.01 | 0.050 ± 0.001 | 0.075 ± 0.001 | 0.075 ± 0.003 | 0.096 ± 0.001 |
| 0.05 | 0.077 ± 0.001 | 0.102 ± 0.001 | 0.108 ± 0.002 | 0.123 ± 0.001 |
| 0.1 | 0.090 ± 0.001 | 0.113 ± 0.001 | 0.124 ± 0.002 | 0.137 ± 0.001 |
| 0.5 | 0.132 ± 0.002 | 0.156 ± 0.002 | 0.175 ± 0.003 | 0.180 ± 0.001 |
| 1 | 0.188 ± 0.005 | 0.217 ± 0.005 | 0.242 ± 0.005 | 0.249 ± 0.009 |

### 4-3.2 PS Data

Figure 4.45 shows the results of onset forces and LSCM images obtained from the PS tests on four PU (series 2) samples. Three scratches are generated for each sample. The scratch force range is from 0 mN to 30 mN, and the scratch length is 1000 μm with a scratch speed of 10 μm/s. PU-B2 has the greatest onset force and PU-CTRL2 has the

lowest. All the reference samples seem having a better scratch resistance than the PU-CTRL2 according to the onset force. At the smaller force range (near the onset force), the damage appears lighter (optical contrast is lower) for PU-CTRL2 than in other reference samples.

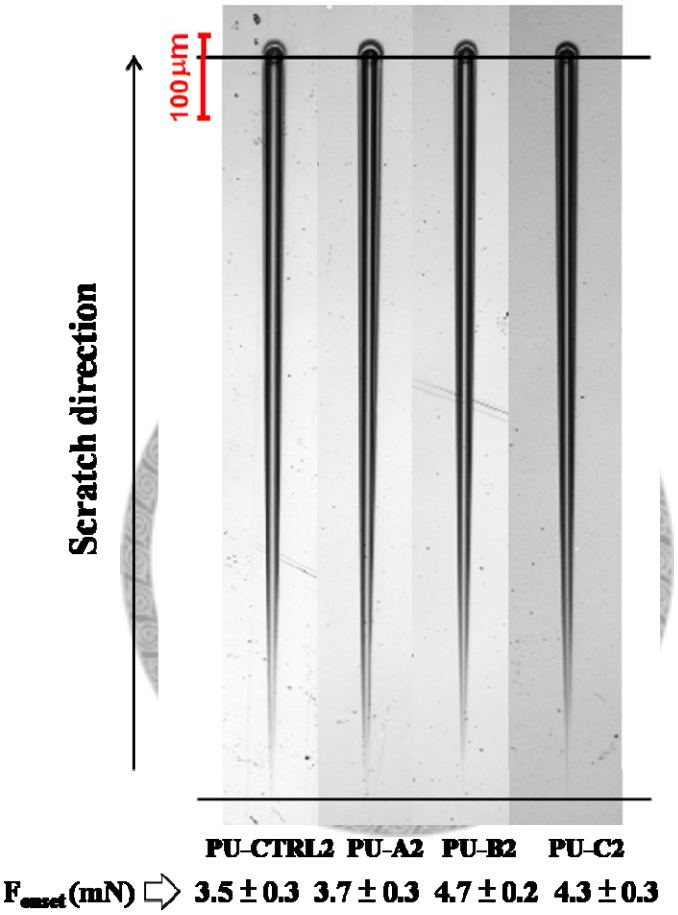


Figure 4.45 LSCM images and onset forces obtained from PS tests (0 mN to 30 mN, scratch length= 1000 µm) of four PU samples (series 2).

At the larger force range, the damage (see in Figure 4.46, the tail images near 30 mN) of PU-CTRL2 is larger than others from the reference group. Also, the tail images from this series are obviously larger than series 1. The cross profiles for four PU samples (series 2) around 30mN are also plotted in Figure 4.47. Noticeably, the PU-CTRL2 has a larger scratch width and smaller scratch depth and pile-up, PU-C2 has the

smallest scratch width and the largest scratch depth. In this case the ratios of $W_p/D_f$ and $W_p/h_b$ are important because these parameters describe the scratch shape and further indicate the visibility of the scratch.

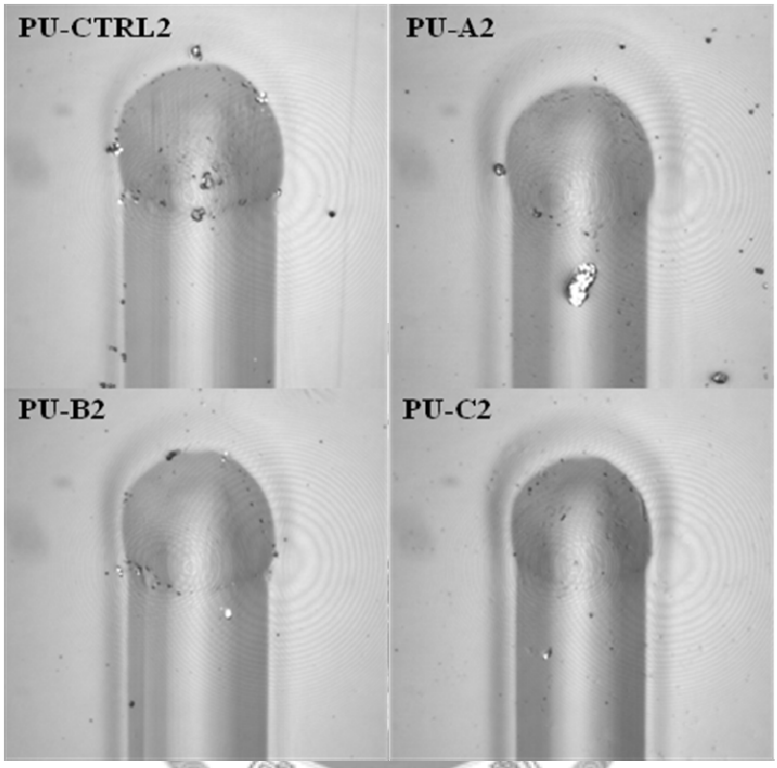


Figure 4.46 The tail images of four polyurethane samples (series 2) obtained from PS tests near 30 mN.

Table 4.20 summarizes the detailed cross profile information ($W_p$, $D_p$, $h_b$, ratio of $W_p/D_f$ and $W_p/h_b$) of four PU samples (series 2). PU-CTRL2 has the greatest $W_p$ value and $W_p$ decreases as increases the additive polarities of reference group. However, from $W_p/D_f$ and $W_p/h_b$ ratios, it is reasonable to rank that PU-CTRL2 has the greatest scratch resistance, and PU-C2 is the weakest one. This result is in contradiction to the conclusion from the H/E ratio. The corresponding tail information includes $a_f$, $a_r$, $\omega_{average}$, and $a_r$ to $a_f$ ratio are also listed in Table 4.21. The values of $\omega_{average}$ are almost the same

for four samples. Although the front contact length $a_f$ is bigger in PU-CTRL2, its rear contact length $a_r$ is also greater so that the $a_r/a_f$ ratio is similar to other samples. Thus, no significant difference is observed in this case.

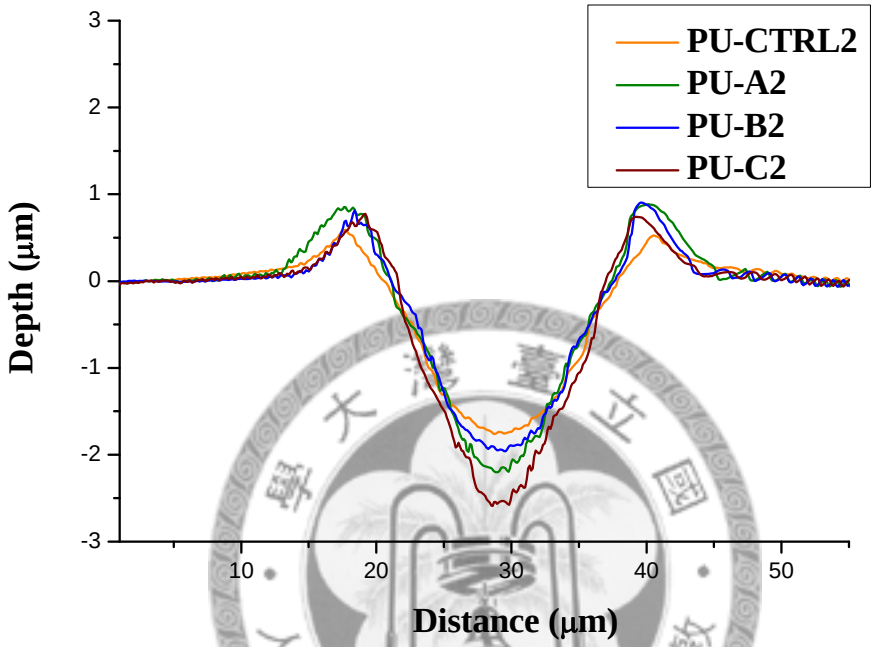


Figure 4.47 The cross profiles of four polyurethane samples (series 2) obtained from PS tests near 30 mN.

Table 4.20 The detailed cross profile information ($W_p$, $D_p$, $h_b$, ratio of $W_p/D_f$ and $W_p/h_b$) of four PU samples (series 2) obtained from PS tests (0 mN to 30 mN, scratch length= 1000 μm) at the force near 30 mN. The error bar represents one standard deviation from two scratches.

| Sample | $W_p$ (μm) | $D_f$ (μm) | $h_b$ (μm) | $W_p/D_f$ | $W_p/h_b$ |
|---|---|---|---|---|---|
| PU-CNTL2 | 22.9 ± 0.2 | 2.5 ± 0.2 | 0.6 ± 0.1 | 9.2 | 38.2 |
| PU-A2 | 21.1 ± 0.4 | 2.4 ± 0.2 | 0.7 ± 0.1 | 8.8 | 30.1 |
| PU-B2 | 20.8 ± 0.2 | 2.4 ± 0.2 | 0.9 ± 0.1 | 8.7 | 23.1 |
| PU-C2 | 19.6 ± 0.2 | 2.6 ± 0.2 | 0.9 ± 0.1 | 7.5 | 21.8 |

Table 4.21 The detailed scratch tail information ($a_r$, $a_f$, $a_r/a_f$ ratio, and $\omega_{average}$) of four polyurethane samples (series 2) obtained from PS tests. The error bar represents one standard deviation from two scratches.

| Sample | $a_r$ (μm) | $a_f$ (μm) | $a_r/a_f$ ratio | $\omega_{average}$ (°) |
|---|---|---|---|---|
| PU-CNTL2 | 6.2 ± 0.3 | 12.8 ± 0.1 | 0.5 | 24.3 ± 0.8 |
| PU-A2 | 5.4 ± 0.1 | 11.3 ± 0.1 | 0.5 | 24.0 ± 0.5 |
| PU-B2 | 5.4 ± 0.1 | 11.6 ± 0.1 | 0.5 | 24.5 ± 0.6 |
| PU-C2 | 4.7 ± 0.3 | 10.8 ± 0.1 | 0.4 | 24.2 ± 1.6 |

Figure 4.48 and Figure 4.49 show the initial and residual penetration curves of four PU samples (series 2) obtained from PS tests. PU-CTRL2 has the deepest initial and residual penetration depth in the tests. The recovery is obtained by comparing the initial and residual penetration depths, as shown in Figure 4.50. The recovery indicates the recovery ability right after being scratched. The recovery is similar for four samples with PU-C2 slightly higher and PU-CTRL2 slightly lower. However, the order of residual penetration depths in series 2 PU samples is opposed to the order in scratch depth of the cross profile results, which are acquired by LSCM at 16 hours later after scratched. A dramatic recovery behavior is found to take place within the 16 hours. The PU-CTRL2 sample somehow recovers and becomes shallower and broader compare to the others. Figure 4.51 and Figure 4.52 plot the friction forces and friction coefficients of four PU samples (series 2) as a function of scratch distance. PU-A2 has the great friction force values and coefficients. PU-CTRL1 and PU-B1 have very similar values, which are the lowest. The relationship between the friction forces and scratch resistance is intriguing and need to study more.

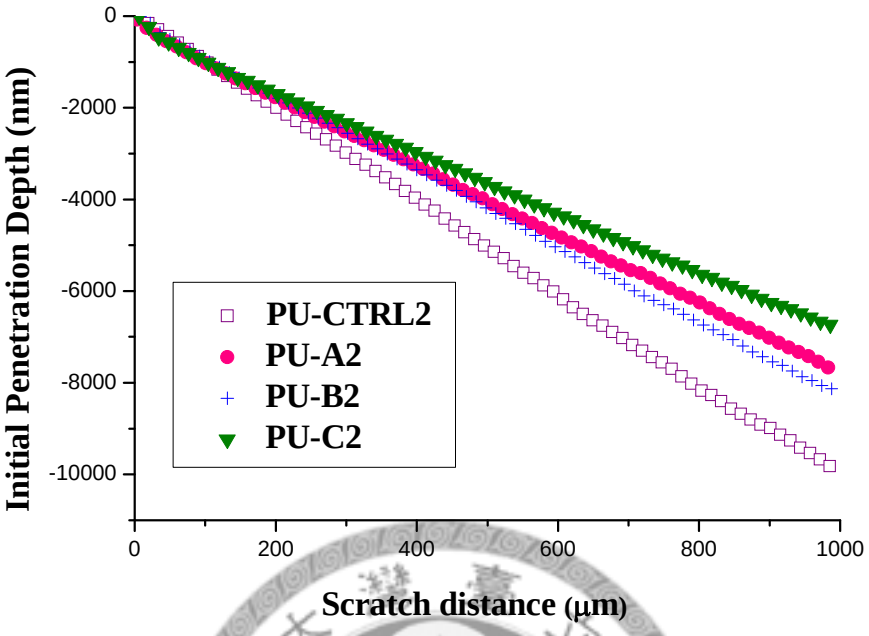


Figure 4.48 The initial penetration curves of four polyurethane samples (series 2) obtained from PS tests.

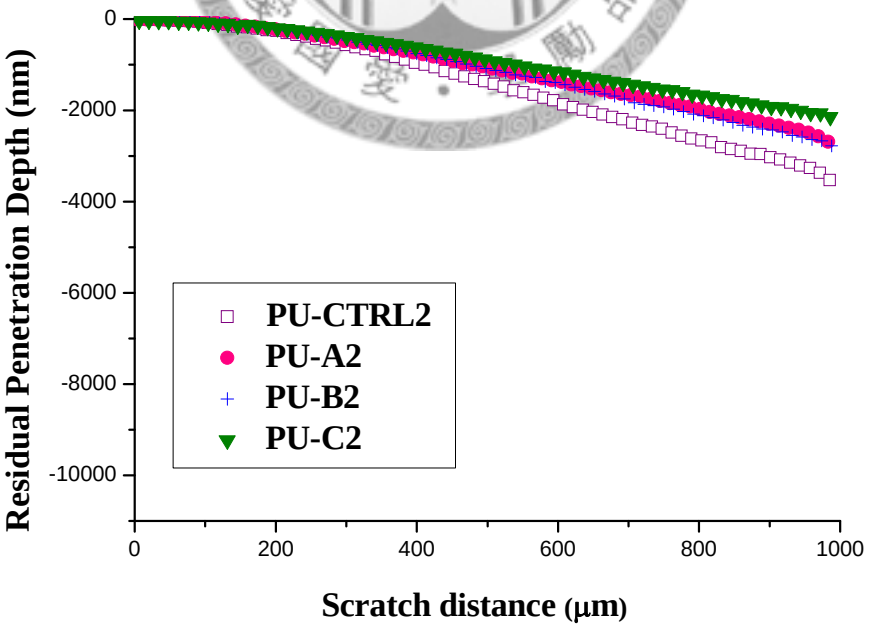


Figure 4.49 The residual penetration curves of four polyurethane samples (series 2) obtained from PS tests.

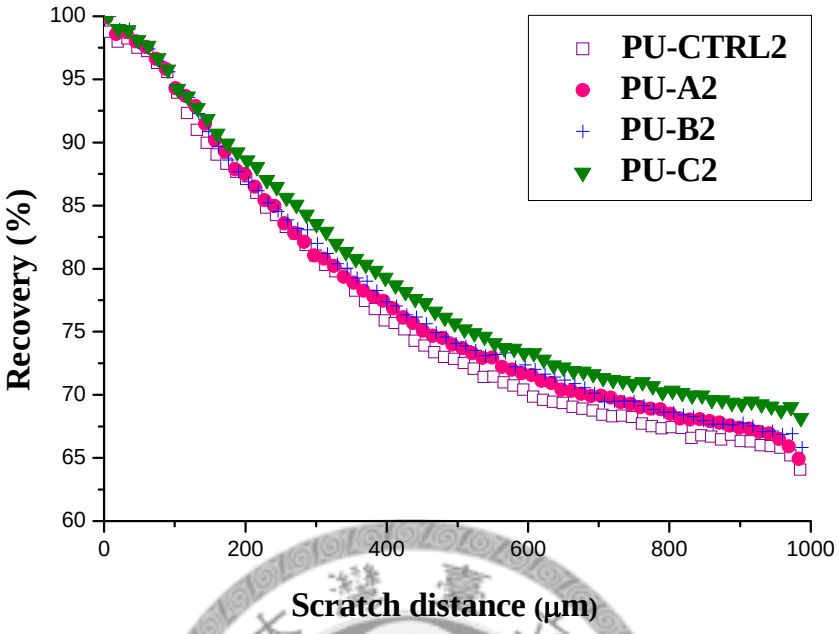


Figure 4.50 The recovery of four polyurethane samples (series 2) obtained from PS tests.

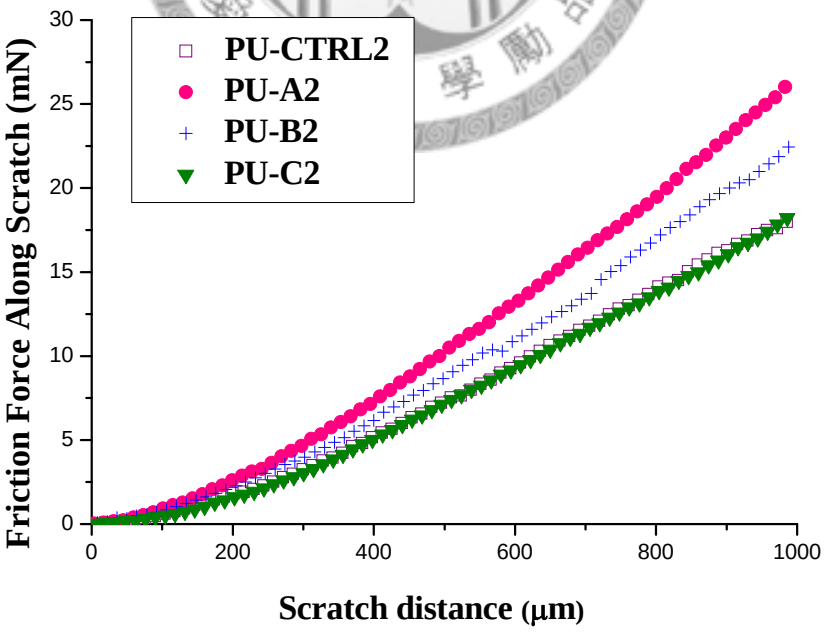


Figure 4.51 The friction forces along scratches of four polyurethane samples (series 2) obtained from PS tests.

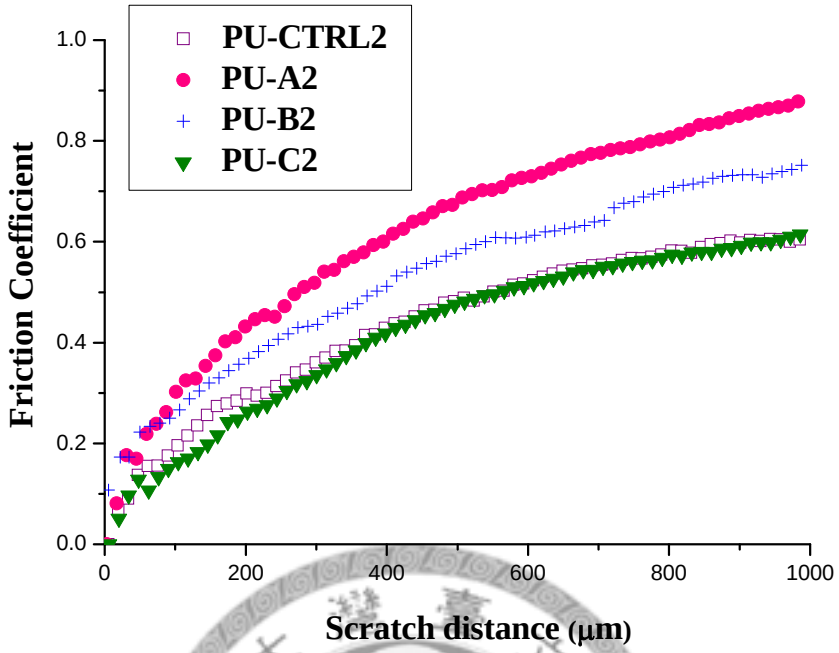


Figure 4.52 The friction coefficients of four polyurethane samples (series 2) obtained from PS tests.

### 4-3.3 CS Data

Finally, a new series of CS tests were carried out on four PU samples (series 2). The CS scratch forces include: 4 mN, 5 mN, 6mN, 7 mN, 8 mN, and 9 mN. The scratch length is 500 μm, and two scratches are generated at each force. Figure 4.53 shows the CS array images and the onset forces obtained from PS and CS tests. Although the onset force values are not very close between PS and CS tests, the order in the degree of damage from PS and CS tests for the reference group is similar. PU-A2 and PU-C2 have similar onset forces, PU-B2 have a higher onset force than the other two. The CS test results is inconsistent to the PS result for PU-CTRL2, which has the lowest onset force estimated from PS tests. As mentioned before, the damage appears lighter (optical contrast is lower) for PU-CTRL2 than in other reference samples near the onset force,

i.e., the scratch damage generate earlier but is less severe. Also, a strong time-dependent behavior in scratch morphology is observed in this series of samples. The pervious works indicate that PU-CTRL2 has the largest recovery rate at 16 hours after scratch. As a result, we cannot conclude that PU-CTRL2 has a higher scratch resistance than the reference group in spite of the CS array scratches in the force range from 4 mN to 6 mN are almost invisible.

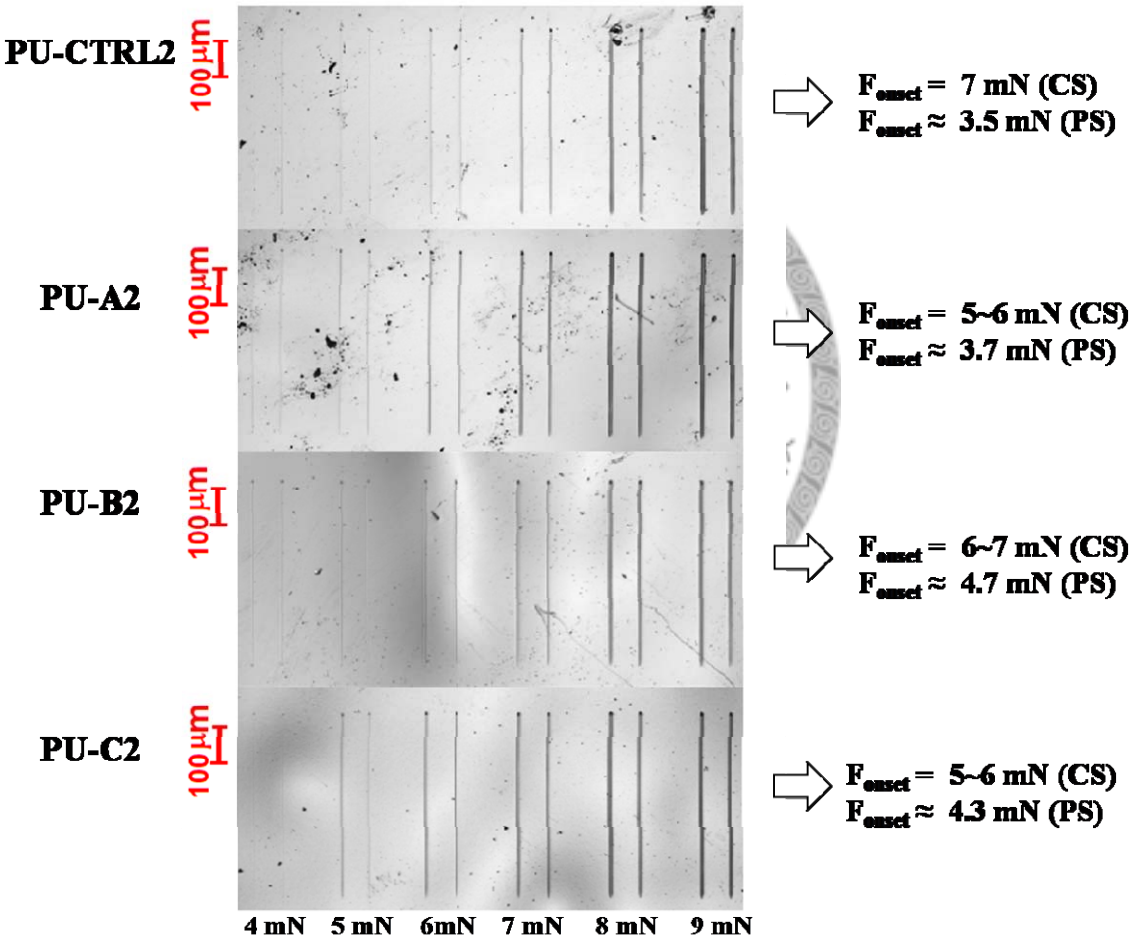


Figure 4.53 CS array (4 mN, 5 mN, 6mN, 7 mN, 8 mN, and 9 mN) and onset forces of four polyurethane samples (series 2).

### 4-3.4 Summary

The scratch behaviors are really complicated in this series (series 2). The H/E ratios are consistent with the onset force results from PS tests. All the reference group samples have a better scratch resistance than PU-CTRL2. From the penetration curves, PU-CTRL2 has the largest scratch and residual penetration depth, which reflect the weakest scratch resistance. On the other hand, PU-C2 has the smallest penetration depth and assumedly has the stronger scratch resistance. However, after comparing the LSCM images and cross profiles taken after 16 hours, the scratch damage of PU-CTRL2 recovered, the scratch profile becomes shallower. From the $W_p/D_f$ and $W_p/h_b$ ratios, the PU-CTRL2 sample reflects a stronger scratch resistance. The $a_r/a_f$ ratio, $\omega_{average}$, and recovery right after being scratched do not provide enough data to distinguish the difference in the scratch behavior, thus it is not useful for ranking the scratch resistance in this case.

Nevertheless, the degree of damages is much worse in series 2 than series 1 by comparing the tail images at 30 mN in the PS tests. The result using the H/E ratios as indicator is consistent with this finding. The series 1 samples have greater H/E ratios than those of the series 2, and the scratch damages are less in series 1. On the contrary, the onset forces from the CS tests provide different rankings. Moreover, the $T_g$ is quite different for these two series. Series 1 samples have a high $T_g$, so the scratch resistance should be better. Also, a lower $T_g$ is in series 2 so that the reflow and recovery behaviors are found to be more prominent. Therefore, the higher onset forces from CS tests in this series can be a misunderstanding due to the fast recovery rate.

Table 4.22 The normalized indicators (ratio to PU-CTRL2) for four PU samples (series 1). The H/E ratios come from IIT. The onset forces, $W_p/D_f$, $W_p/h_b$, $a_r/a_f$ ratios, $\omega_{average}$ and recovery are obtained from PS tests. The $W_p/D_f$, $W_p/h_b$ ratios and recovery are acquired at the force near 30 mN.

| | PU-CTRL2 | PU-A2 | PU-B2 | PU-C2 |
|---|---|---|---|---|
| H/E | 1.000 | 1.122 | 1.146 | 1.341 |
| Onset force | 1.0 | 1.1 | 1.3 | 1.2 |
| $W_p/D_f$ | 1.0 | 1.0 | 0.9 | 0.8 |
| $W_p/h_b$ | 1.0 | 0.8 | 0.6 | 0.6 |
| Recovery | 1.0 | 1.0 | 1.0 | 1.1 |
| $a_r/a_f$ ratio | 1.0 | 1.0 | 1.0 | 0.8 |
| $\omega_{average}$ | 1.0 | 1.0 | 1.0 | 1.0 |

Table 4.22 and Figure 4.54 summarize the ranking by using different indicators for four PU samples (series 2), all the numbers are normalized by dividing the values from PU-CTRL2. The indicators such as $a_r/a_f$ ratios, $\omega_{average}$ and recovery are not sensitive. However, the results from (H/E ratio and onset force) provide the opposite results from $W_p/D_f$ and $W_p/h_b$. This case study is difficult due to the two system has different $T_g$ and the time-dependent of the recovery behavior is complicated.

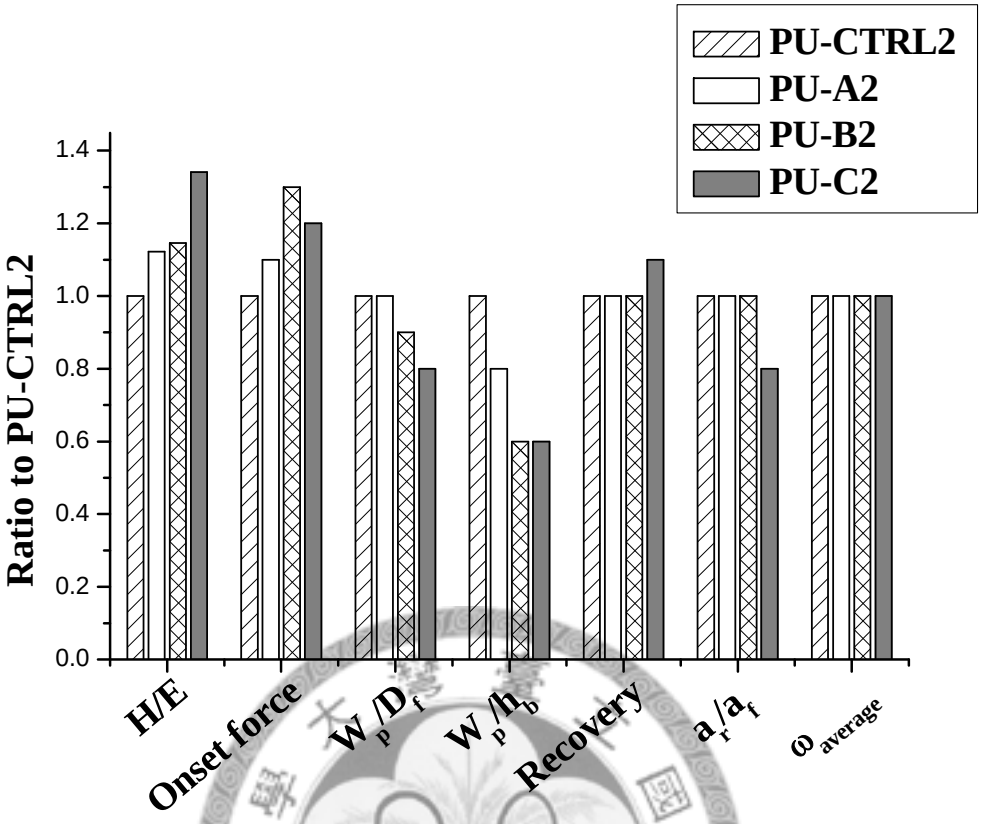


Figure 4.54 The diagrammatic summary of four polyurethane samples (series 2) presented in the normalized indicators (ratio to PU-CTRL2).

# Chapter 5 CONCLUSIONS AND FUTURE WORKS

In this thesis, the scratch resistance or "durability" of two polymeric systems were studied and assessed. The polymer systems are: 1. Three crosslinked epoxy (EP) samples with different glass transition temperatures, and 2. Two series (different $T_g$) of polyurethane (PU) thin films containing 2 % nanosilica ($SiO_2$) with dispersant/additive of different polarities. The experimental procedure adopts the protocol of NIST Polymer Surface/Interface scratch test method, which is used for quantitatively characterizing the scratch and mar resistance. Instrumented indentation technique (IIT) was used to perform the tests, and the scratch images were measured and analyzed by using laser scanning confocal microscopy (LSCM). Instrumented indentation testing, progressive and constant force scratch tests were conducted on all samples.

In the epoxy (EP) system, EP-AA has the highest $T_g$, EP-BB is the second, and EP-CC has the lowest. The H/E ratio indicates that EP-AA and EP-BB have the similar scratch resistance, and EP-CC has the weakest resistance. This result using H/E as indicator is consistent with the onset forces obtained from both PS and CS tests. Also, the ratios of $W_p/D_f$ and $W_p/h_b$ confirmed the same results. To conclude, EP-AA has a highest glass transition temperature and best scratch resistance among the three epoxies, and EP-CC has a lowest $T_g$ and worst scratch resistance.

In the polyurethane (PU) system, no significant difference is observed in series 1 samples. On the contrary, the scratch behaviors are really complicated for series 2. H/E ratios are consistent with the onset force results from PS tests in series 2. These evidences indicate that the reference group samples have a better scratch resistance than PU-CTRL2. However, after comparing the cross profile images taken by LSCM after 16 hours, a strong time-dependent behavior in scratch morphology is observed. It is found

that PU-CTRL2 has the largest recovery rate, and its damage becomes shallower and broader. Hence, PU-CTRL2 sample reflects a stronger scratch resistance observed from the $W_p/D_f$ and $W_p/h_b$ ratios. On the other hand, the degrees of damages are much worse in PU series 2 than series 1 by comparing the scratch tail images. Also, series 1 samples have greater H/E ratios than those of the series 2. These results are expected due to that series 1 has a higher $T_g$ (~ 90 $^oC$) and series 2 has a lower $T_g$ (~ 55 $^oC$).

Overall, a higher glass transition temperature corresponding to a stronger scratch resistance in this study. The H/E, onset force, $W_p/D_f$, and $W_p/h_b$ are better than other indicators in the scratch resistance assessment. The $a_r/a_f$ ratio and $\omega_{average}$ do not provide enough data to distinguish the differences to assess the scratch resistance in two polymer systems. The recovery is not suitable for ranking the scratch resistance in PU system. In addition, the relationship between the friction forces and scratch resistance is intriguing and needed for further investigations. The time-dependent behavior of scratch morphology for the sample is also important. So as to understand the scratch behavior thoroughly, the recovery rate of samples need to study more and be monitored in different time intervals.

# Appendix A: Introduce to Tip Geometries

Since the scratch deformations of indentation tests and scratch tests are dominated by indenter shapes, the investigation of tip shapes is helpful for choosing the suitable indenter based on the test requirements. Typically, the experimental results are clearly differentiated between the selecting of sharp or blunt tips. The sharp tip usually brings about the permanent damage of samples, i.e., the recovery is not complete or only a few percentages of damage depth is cured after unloading. In contrast, the elastic deformation happens frequently for using a blunt tip. A scratch which is caused by a blunt tip often results in a smooth and continuous damage type. Sharp and blunt are only the generally categories of tips, furthermore, the variations in tip geometries can also give rise to various damage behaviors and affect the damage appearances severely. Figure A.1 shows the common tip geometries, such as pyramids, cones, cylinders, and spheres. Where, r is the indenter radius, $\alpha$ is the semi-angle, a is the radius of the circle of contact, and $h_p$ is penetration depth. $\theta$ is the half angle, i.e., the face angles (semi-angle) with the central axis of the pyramidal indenter. $\theta_1$ and $\theta_2$ is the half angle of the Knoop indenter in two different sides.

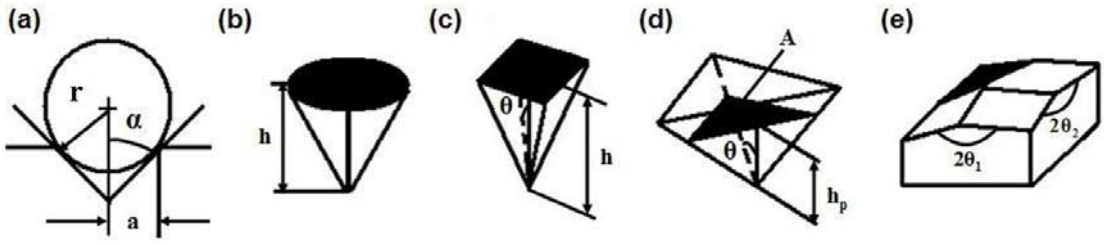


Figure A.1 Schematic of different tip geometries (a) spherical (b) cone (c) Vickers (d) Berkovich (e) Knoop [38].

The spherical indenter provides a smoother transition from the elastic to the plastic deformation, so it is suitable for a soft material or the damage profile requested to be smoothly. The cone indenter and pyramid indenter are termed sharp comparing to the spherical indenter. The magnitude of stress distribution increases owing to the angle reduction at the point of contact. Since the three edges of the pyramid are simply constructed to meet at a single point, the small-scale indentation analyses have commonly applied the Berkovich indenter instead of the four-sided Vickers pyramid. In order to compare the data obtained from Vickers hardness tests to nanoindentation tests by the Berkovich tip without difficulty, the face angle of the Berkovich tip is designed to be 65.3˚. It gives exactly the same actual surface area to depth ratio as a Vickers indenter. On the other hand, the indentation tests for the anisotropy material are often carried out by the Knoop indenter, which is a four-sided pyramidal indenter with two different half angles.

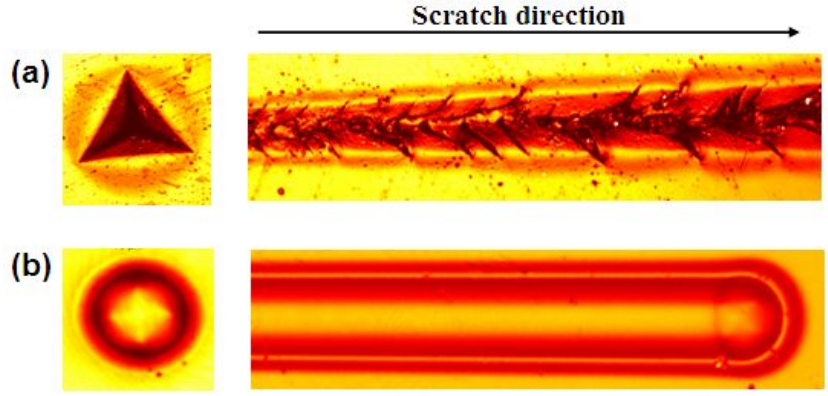


Figure A.2 The damages under an indentation test and a scratch test (a) using a standard Berkovich tip (b) using a concial tip with the radius of 10 μm.

Figure A.2 shows the indents and the scratch damages using a Berkovich and a conical indenter with the radius of 10 μm. By using the Berkovich tip, the scratch damage bursts during the test and the indent becomes sharp and deep. Oppositely, the indenter head of a cone with 10 μm is relatively big in the nanoscale tests, the damage type is smooth and the edge of this damage is in a particularly continuous and round form. Moreover, the indent (or scratch) penetration depths and surface damage types strongly depend on the size of the indenter head. The effort of investigating the variation of indenter size is reported by Wong and coworkers [43].

Table A.1 The formulae of counting the projected area, semi angle and effective cone angle of six types of indenters [38]. The effective cone angle is referred to as an axial-symmetric cone with the same area to depth ratio as the actual non-symmetric pyramidal indenter.

| Indenter type | Projected area | Semi-angle (deg) | Effective cone angle (deg) |
|---|---|---|---|
| **Sphere** | $A = 3\sqrt{3}h_p^2 \tan^2\theta$ | N/A | N/A |
| **Berkovich** | $A = 3\sqrt{3}h_p^2 \tan^2\theta$ | 65.3° | 70.2996° |
| **Vickers** | $A = 4h_p^2 \tan^2\theta$ | 68° | 70.32° |
| **Knoop** | $A = 2h_p^2 \tan\theta_1 \tan\theta_2$ | $\theta_1 = 86.25°$<br>$\theta_2 = 65°$ | 77.64° |
| **Cube Corner** | $A = 3\sqrt{3}h_p^2 \tan^2\theta$ | 35.26° | 42.28° |
| **Cone** | $A = \pi h_p^2 \tan^2\alpha$ | $\alpha$ | $\alpha$ |

In order to obtain the elastic modulus and the hardness of materials, the projected contact area A of the elastic contact plays a vital role in estimating those parameters.

Table A.1 shows the basic formulae of counting the projected area, semi angle and effective cone angle of six types of indenters.

Owing to the non-idealistic geometry of the indenter tip (due to the manufacture defect), the contact area of the indentation test is underestimated when the indentation penetration depth is not deep enough and it causes inaccuracy as computing the modulus and hardness. Figure A.3 (a) shows the comparison of contact areas between the ideal and the actual indenters using a conical indenter. Figure A.3 (b) shows the A/Ai ratio as a function of penetration depth hp using a standard Berkovich tip. It indicates that the actual indenter approaches the ideal indenter as the penetration depth increases. Figure A.3 (c) shows the scratch tail under a 30mN constant force scratch test and presents the non-ideal geometry of a conical tip with a radius of 10 μm.

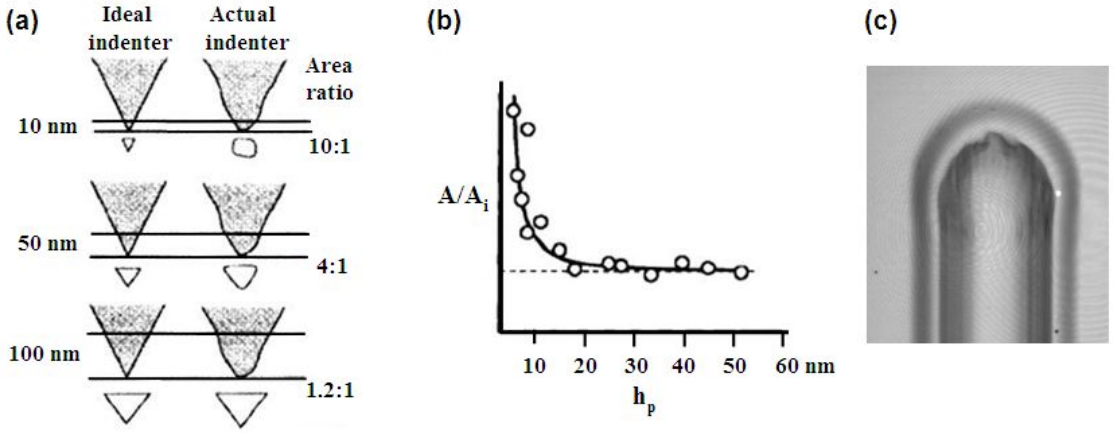


Figure A.3 (a) Schematic of the comparison of contact areas between the ideal and the actual indenters using a conical tip (b) Schematic of the A/Ai ratio as a function of penetration depth hp using a standard Berkovich tip (c) The non-ideal geometry of a conical tip under a 30 mN constant force scratch test [38].

Indentation size effect is another important topic due to the material properties. It is occurs using both the blunt and sharp indenter [44-45]. For a sharp tip like the pyramidal indenter, the penetration depth decrease in crystalline materials usually follows an increase in hardness. As for a blunt tip like the spherical indenter, hardness is affected by the radius of tip rather than penetration depth. In such a case, hardness rises when reducing the tip radius. This effect is caused by the dislocation and work-hardening conditions of materials.

Figure A.4 shows the size and detailed information of the diamond conical tip with a radius around 10 μm, and the semi-apical angle of this cone is around 45°. This conical tip was used to perform all of the scratch tests in this study.

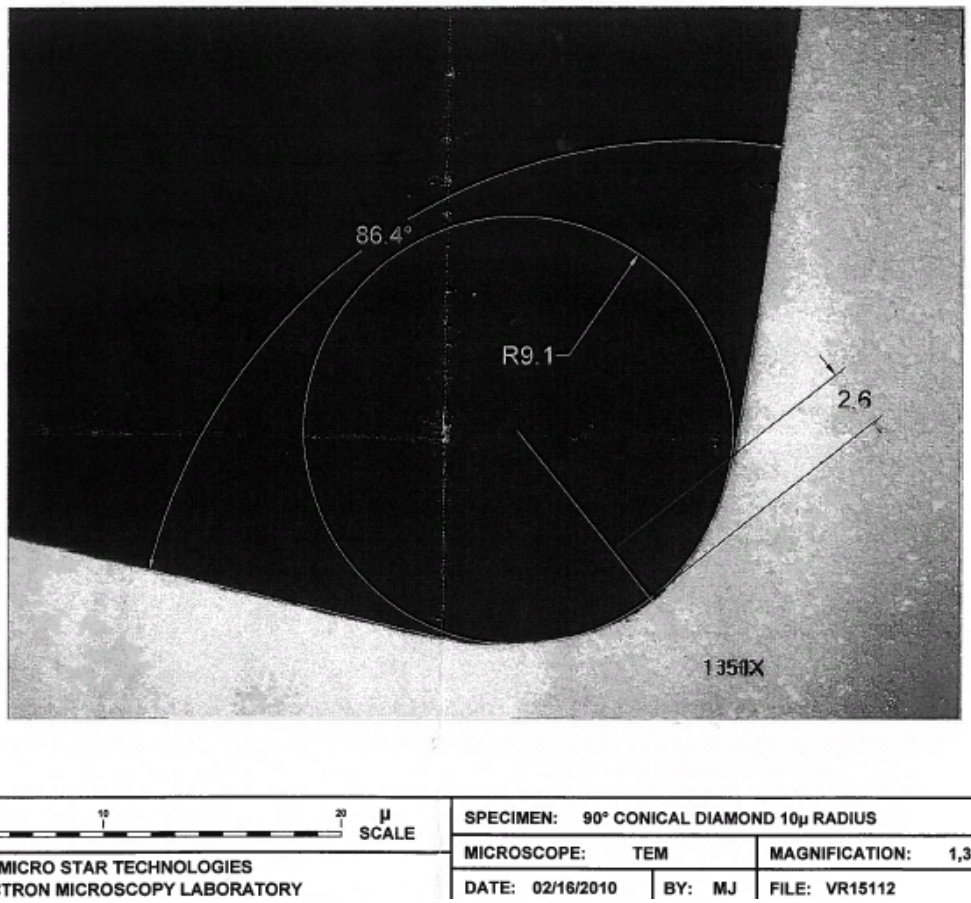


Figure A.4 Tip information of the nominal 10 μm90 conical tip used in this thesis.

# Appendix B: PIC Scratch Test Method- January 2007

## Test Method for Measuring Scratch/Mar Resistance of Coatings by Nanoscratching and Optical Scattering

### B-1 Scope

This test method outlines the procedure for performance scratch testing using instrumented nanoindention, characterizing scratch morphology, and evaluating the scratch resistance by assessing scratch visibility using optical scattering of polymer coatings applied to smooth flat surfaces. Scratch and mar resistance is quantified by the magnitude of the applied normal load necessary to impart visible scratch damage, as seen by the naked eye and through optical scattering methods. Both the scratch resistance and scratch morphology are characteristics dependent upon unique mechanical properties of the coatings and the specific parameters under which testing takes place. The visibility assessment using optical scattering methods provides an objective mean to rank the scratch and mar resistance.

### B-2 Referenced Documents

- D609 Practice for Preparation of Cold-Rolled Steel Panels for Testing Paint, Varnish, Conversion Coatings, and Related Coating Products
- D823 Practices for Producing Films of Uniform Thickness of Paint, Varnish and Related Products on Test Panels
- DXXX for terminology for appearance, reflectance measurments

## B-3 Summary of Test Method

This test method utilizes a single-probe scratch tester, via instrumented nanoindenter, to scratch polymer coatings with both a progressive increasing normal load and a constant normal load. The resultant scratch morphology can be qualitatively related to appearance attributes of the coating, while the scratch data can be used to quantitatively evaluate the coating's resistance to scratching and marring.

## B-4 Significance and Use

This test method provides a quantitative assessment of a coating's resistance to scratch and mar along with an outline of the analysis of scratch deformation patterns and visibility assessment. The test allows for manufacturers of paints and other coatings to predict the service life and durability of their products while also studying the response of the coatings to applied loads under specific testing conditions. Such variables as asperity dimensions, scratch velocity, and applied load allow for a range of results relative to situations occurred throughout the service life of the product. While this test method is best suited for films applied to laboratory test panels, it can also be carried out on solid, uncoated polymer samples.

## B-5 Apparatus

*1. Single-probe scratch tester:*

Instrumented nanoindenter or other kind of a single-probe scratch tester can be used. The instrument is required to be capable of implementing both constant and variable force scratches and allowing for the collection of force-feedback data. The

maximum applied normal load capability of the instrument should be at least 50 mN while a minimum force of 20 μN is necessary for pre and post scratch profiling. The indentation tip should be a diamond with a radius ranging between 1 μm and 10 μm and an asperity slope angle between 60˚ and 90˚. Compatible scratch analysis software should provide initial and residual penetration depths, as well as friction coefficients for both constant and progressive force scratches. In this report, a MTS nanoindenter is used for the scratch tester.

*2. High resolution reflection optical microscope*

Laser scanning confocal microscope (LSCM) or other high resolution optical microscope can be used for visual assessment of scratch morphology and damage patterns. The levels of magnification should reach between 5x and 150x with lenses capable of scanning at 5x, 10x, and 50x. Compatible software should allow for a 2D topographical projection of the surface and subsequent profile analysis of a selected region. The analysis should provide measurements of distances along the XY plane as well as depths in the Z axis direction. In this report, a Zeiss LSM 510 laser scanning confocal microscope is used for the characterization.

*3. Surface optical scattering instrument*

An optical scattering instrument equipped with various light sources, goniometric sample stage, and a detector. Scattering measurements can be performed in the reflection configuration with multi-angle, specular and off-specular measurement capability. Scattering results such as scattered intensity can be analyzed in terms of

angular distribution and separated into specular and off-specular contribution as needed. In this report, a NIST custom-made optical scattering instrument is used. This instrument is equipped with a laser and scanning wavelength illumination system, a five-axis goniometric sample stage, and a two-dimensional (2D) detector mounted in a concentric ring around the sample stage.

## B-6 Test Specimens

Coatings should be applied with a uniform film thickness to a substrate that is rigid and flat. Panels such as those specified in D609 or other substrates relevant to the coating's application should be coated according the specifications present in D823. Samples should be cut for testing on the nanoindenter using a shear for panels or a band saw for plastic materials into 20 mm square pieces. To add rigidity to the sample and reduce the risk of damaging the sample upon removal from the nanoindeter, each 20 mm square sample should be glued onto a 20 mm square piece of 1/16" sheet metal. Samples may be wiped of any dirt and debris using a kimwipe and a small amount of ethanol so long as the coating will not undergo physical or chemical change as a result of contact with ethanol. The sample may then be blown with air to remove any remaining dust or debris particles.

## B-7 Conditioning

Test samples should be cured as specified by the provider, so as to reflect the state of the samples as they would be used in service. Condition and test the test specimen at room temperature (23 $^{o}$C ± 2 $^{o}$C), a relative humidity of 50 % ± 5 % for at least 24 hours,

unless the providers/purchasers/sellers agree on more suitable test characteristics, as specified in the Atomoshpere of Test Method D 3924.

## B-8 Procedure

Mechanical and material properties are required and recorded for all samples before the testing. These properties include: material composition, mechanical modulus and hardness (bulk and surface), glass transition temperature, surface morphology, subsurface or microstructure (including cystallinity of the coating), other remarks on materials if necessary.

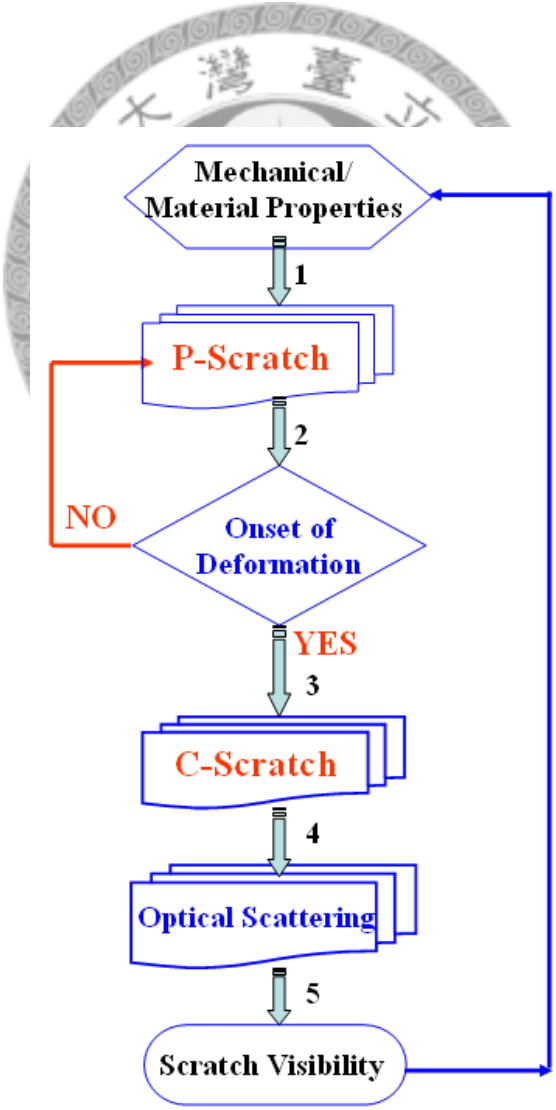


Figure B.1 Overall flowchart of PIC measurement protocol for scratch testing

### B-8.1 Progressive Scratch (P-scratch)

Secure the sample to the indenter puck using the minimum amount of adhesive necessary to hold the sample securely in place during the scratch test. Load the puck into the indenter tray such that vertical scratches will run parallel to the sample's edge and place tray into the indenter. Mark the upper left corner of the sample using a permanent marker and select all scratch locations relative to this position. This will make it much easier to locate scratches on the LSCM.

For each progressive scratch test, a pre-scratch profile and a post-scratch profile will be run with an applied normal load of 0.1 mN. A 10 μm 90° diamond cone (MTS Systems) is used as the scratch probe, where the spherical tip has a diameter of 10 μm and the semi-apical angle of the cone is 45°. Select the appropriate test method for a progressive scratch test and modify the parameters such that the allowable drift rate is 2.0 nm/s and the surface approach sensitivity and surface approach velocity are 50 % and 100 nm/s, respectively. The surface approach distance should be set at 3000 nm however for samples with a rougher surface it may be necessary to adjust the distance to 5000 nm.

The scratch length should be set at 1000 μm and the scratch velocity set at 10 μm/s. The initial scratch load should be set at 0 mN and the maximum scratch load set at 30 mN. For materials with particularly good scratch resistance characteristics, the max scratch load may be set to 50 mN. A location of known distance from the marked upper left corner should be designated for the progressive scratch array which is composed of 3 x 1 scratches separated by a distance of 65 μm in the x direction. LSCM analysis of the progressive scratch tests includes imaging the entire array in one frame at 10x magnification and 0.8 zoom (labeled as 10x0.8), along with taking segmented images over the entire length of the scratches at 50x magnification.

In procedure1, P-scratch results including parameter, shown in Figure B.2 should be recorded.

## B-8.2 Onset of Deformation

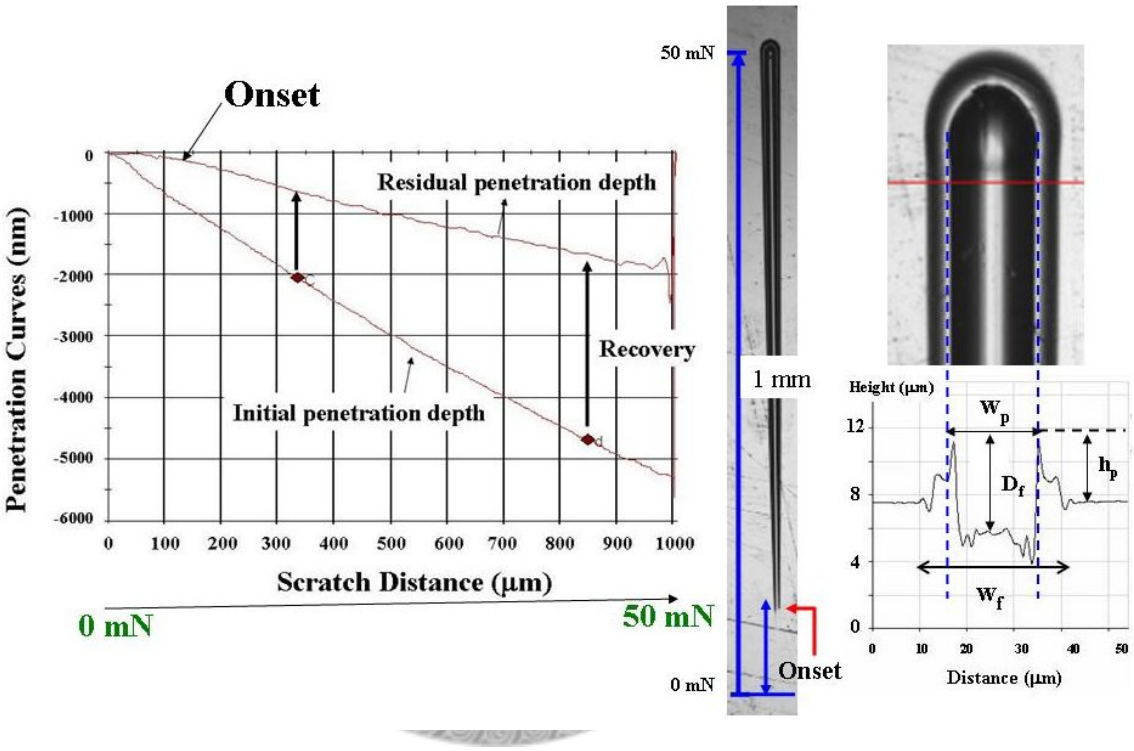


**(a)** **(b)** **(c)**

Figure B.2 (a) Penetration curves obtained from a P-scratch testing on a typical automotive clear coating with loads ranging from 0 mN to 50 mN, (b) LSCM image of scratch, and (c) a high magnification LSCM image of the scratch profile near 50 mN. Here, $w_f$ is the full scratch width; $w_p$: peak-to peak scratch width; $D_f$: full depth, and $h_p$: pile-up height.

The onset for elastic (almost 100 % recovery) to plastic deformation is determined from the LSCM image at 10x0.8 magnification, as indicated in Figure B.2. If the range of applied scratch load does not provide a good resolution for onset determination, a new scratch load range should be applied accordingly and procedure 8.1 should be repeated to determine the onset. In this procedure, the estimated onset load value from LSCM at 10x0.8 and 50x should be recorded. The operator should also compare his/her visual inspection of the scratch visibility to the onset selected from LSCM images at 10x0.8 magnification.

### B-8.3 Constant Scratch (C-scratch)

The sample should be secured to the puck and placed in the indenter tray in the same manner as described for the progressive scratch test. Just as in the progressive scratch tests, constant scratch data acquisition requires that both a pre and post scratch profile be taken with an applied force of 0.1 mN. The indenter tip, drift rate, surface approach sensitivity, surface approach velocity, and surface approach distance should all be set to the same values as were used for the progressive scratch test. The scratch length should be set to 500 μm while keeping the scratch velocity set at 10 μm/s. For each set of constant scratch tests the initial and maximum loads should be equal to one another.

The constant scratch array consists of 2 parallel scratches separated by a distance of 100 μm. For subsequent constant scratch tests of different applied loads, a distance of 400 μm separates each array of scratches. A complete set of constant scratch tests for a single sample will consist of an array of 10 sets of 2 constant scratches, with each set of 2 scratches having a different applied load. The applied loads for the constant scratch

tests are determined from the onset load estimated from the progressive scratch results, as defined in the calculations section below. For better practice, scratch load ranges from (Onset-5) mN to (Onset + 4) mN). This approach will allow us to obtain more precise onset of the deformation.

LSCM analysis of the constant scratch tests includes imaging the entire array in two images with each image containing 5 sets of 2 scratches each at 5x magnification, as shown in Figure B.3. A high magnification (50x or higher) of the scratch will provide accurate measurement of scratch width and profile for optical modeling. In this procedure, the operator should also compare his/her visual inspection on the scratch visibility to the onset selected from LSCM images at 5x magnification.

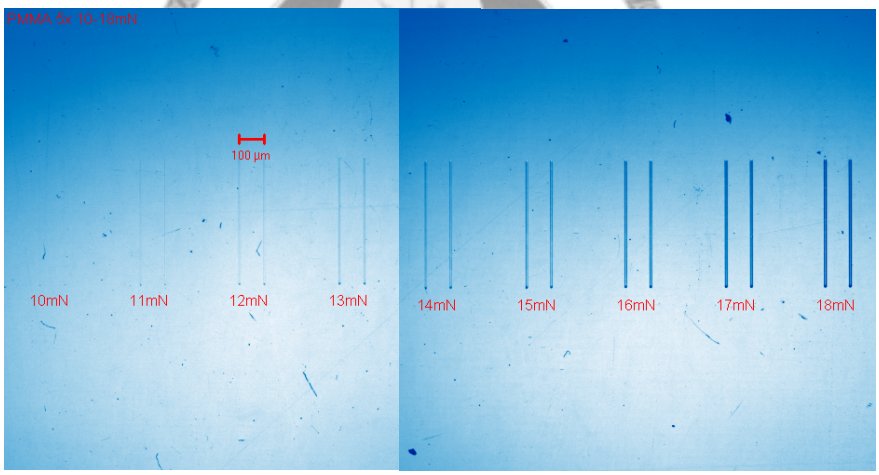


Figure B.3 Example of LSCM images of C-Scratch.

## B-8.4 Optical Scattering of a Scratch

*1. Sample for optical scattering:*

To prepare a sample for optical scattering experiments (using a laser beam), a 50 mm x 50 mm square piece of the sample must be cut in the same manner as described in the scratch test specimens section above. The sample should then be

scratched with two 5 x 1 constant force scratch arrays and one progressive force scratch, as shown in Figure B.4. The first constant force scratch array should be placed 10 mm to the left and 10 mm down from the top left corner of the sample. The force range for both constant scratch arrays is the same and is based upon the visual onset force determined from C-scratch. The constant scratch forces range from (Onset -1) mN to (Onset +3) mN in increments of 1 mN for a total of five scratch forces per array. The scratch length is 3 mm at 10 μm/s scratch velocity. The second constant scratch array is created using scratch velocity of 1 μm/s. The relative location and distance is described in Figure B.4. In addition to two C-scratch arrays, a progressive force scratch for the laser light scattering samples is conducted at 10 μm/s with scratch load ranging from (Onset -3) mN to (Onset +4) mN, and a total scratch length 5 mm.

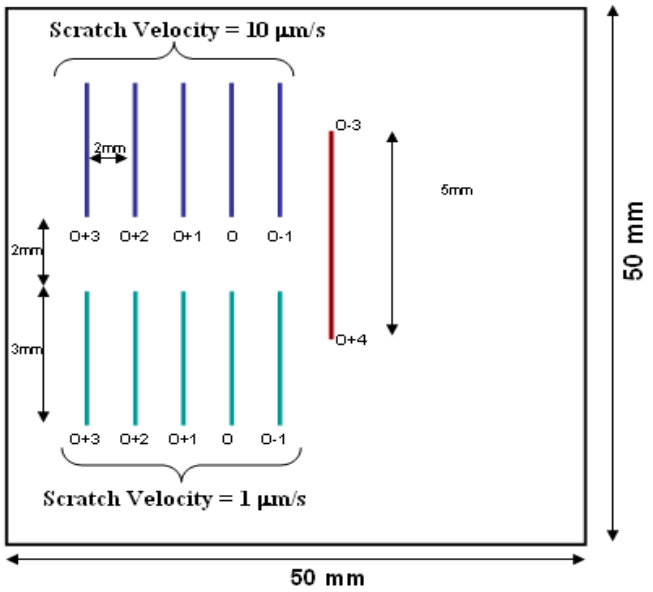


Figure B.4 Schematic of a sample prepared for optical scattering experiments. Scratch tests consist of two constant force scratch arrays at different scratch velocities and one-5 mm progressive scratch. The scratch load is described as O+1: (Onset force + 1) mN Schematic is not to scale.

## 2. *Optical scattering experiment*

To perform a robust and accurate measurement, the operator should follow the recommend procedures:

1) The scattering sample should be mounted securely onto the sample holder, and the top surface of samples should be located at optical plane of the instrument.
2) Move sample stage to home position of the reflection mode and align the sample surface to be exactly perpendicular to the laser beam (i.e. the reflected laser spot is symmetrically located on pinhole of the existing lens). Record the new zero position of the sample.
3) Locate the first scratch, rotate the sample position to incident angle of 20 degree ($\theta_I$ = 20 $^o$) and detector to 40 $^o$ ($\theta_s$ = 20 $^o$). (See Figure B.5 for optical geometry and definition of the notation).
4) Measure the scattering intensity for three aspecular angles ($\theta_{as}$) (0 $^o$, 3 $^o$, and 5 $^o$) – i.e. detector located at 40$^o$, 43$^o$, and 45$^o$.
5) Repeat the measurement for incident angles of 30 $^o$, 45 $^o$, 60 $^o$. Record the scattered intensity in two-dimensional (2D) profile (see example in Figure B.5) for each incident angles. Data information includes all optical geometrical parameters and the exposure time of detection.
6) Repeat (c)-(d) for each scratch and non-scratch area for reference.

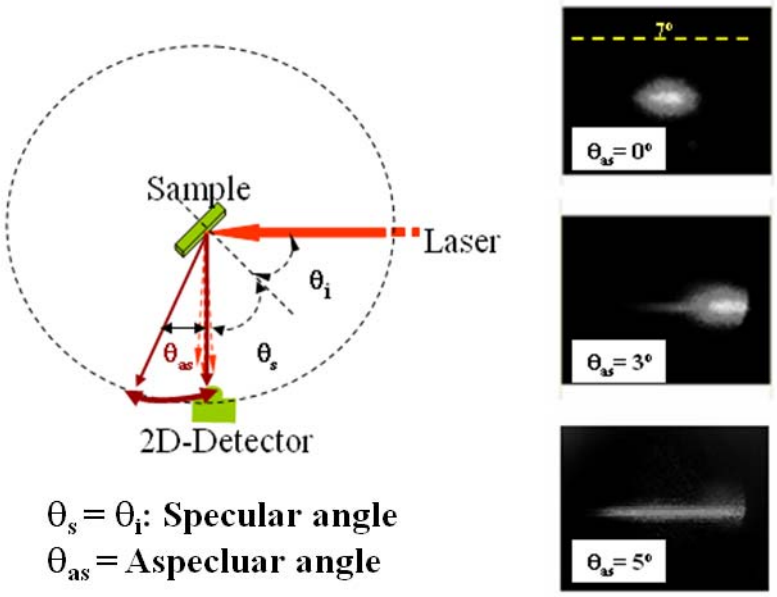


Figure B.5 Optical geometry of the scattering experiment and the 2D scattering profile obtained from a scratch at $\theta_{as}$ = 0 °, 3 °, and 5 °. Here $\theta_i$ is the incident angle, $\theta_s$ is the specular angle, and $\theta_{as}$ is the angle measured from the specular direction.

## B-9 Calculations

### B-9.1 Onset Force Determined by Progressive Scratch

An estimate of the onset force (the force required to produce visible scratch deformation) is made from the 10x 0.8 image of the progressive scratch array. The visible region of each of the three scratch lengths is measured in mm-scale and averaged as well as the length of a scaled measurement line generated by the LSCM software. A ratio is created between the length of the measured visible progressive scratch and its actual length and set equal to a ratio of the scaled measurement line compared to its representative length. This allows for determination of the visible scratch length.

The onset force is then found by creating a ratio between the maximum load applied and the total scratch length and set equal to a ratio between the instantaneous force and the length before visible scratch deformation. This allows for the calculation of the onset force determined by progressive scratch test method.

## B-9.2 Progressive Scratch Data Tabulation

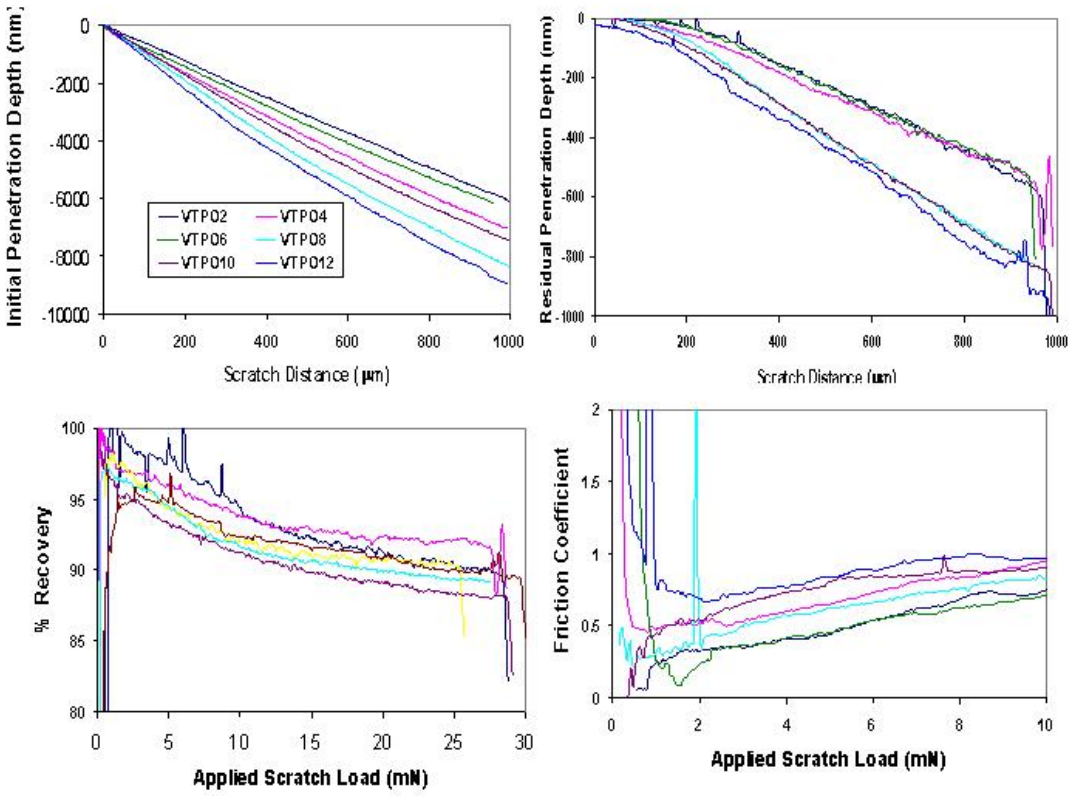


Figure B.6 Example of data needed to be recorded and plotted for a set of test samples in the P-Scratch test.

The progressive scratch data is exported from the indentation software to Microsoft Excel. The values for the initial penetration depths, residual penetration depths, friction coefficients and percent recovery are averaged for the three scratches (As shown in

Figure B.2). The percent recovery is calculated by subtracting the residual penetration depth from the initial penetration depth and dividing by the initial penetration depth. Plots are then constructed of each of the four values versus scratch length. Plots for subsequent samples can then be compared to determine differences in the response of materials to applied load, see an example in Figure B.6.

### B-9.3 Onset Force Determined by Constant Scratch

For each sample, an array of 10 sets of 2 constant scratches in made. The force range for the array is determined from the results of the progressive scratch determined onset force. Once the onset force is estimated using the results of the progressive scratch test, constant scratches are made at forces ranging from (Onset-5) mN to (Onset + 4) mN) in increments of 1mN. This produces a range of 10 forces for constant scratch tests. The onset force determined by constant scratch method is found by assessing the 5x LSCM images of the scratch array (as shown in Figure B.3). The onset force is the force of the last visible constant scratches in the array.

### B-9.4 Visual Onset Force from Constant Scratch

The constant scratch visual onset force is determined by visually assessing the constant scratch array. The lowest force constant scratch that can be seen with the naked eye is representative of the constant scratch visual onset force.

### B-9.5 Scratch Width Determination

The scratch width is determined using the 50x images taken with the LSCM. A profile line is drawn across the scratch in the LSCM program, making sure that the line is perpendicular to the scratch. The damage width is determined by measuring the distance across the scratch which includes all visible damage. The peak to peak width is then measured as the distance between the largest innermost peaks for samples exhibiting pile-up or the distance between the 2 largest peaks bracketing the center of the scratch for samples not exhibiting pile-up (see Figure B.2). The peak to peak width becomes irrelevant for samples which have a 50x surface roughness that exceeds the height of the scratch features. This tends to become the case in scratch forces very near to the onset force.

### B-9.6 Constant Scratch Data Tabulation

The constant scratch data is exported from the indentation software to Microsoft Excel. The average initial penetration depths, average residual penetration depths, percent recovery, friction coefficient, and pile up heights are calculated by averaging the results for both scratches in each constant scratch test. The results are then plotted versus scratch force. The results for scratch damage width, peak to peak width, and theoretical width are also plotted versus applied force.

### B-9.7 Optical Scattering Data Analysis

The scattering profiles in 2D presentation are recoded as illustrated in Figure B.5 for all incident and scattering angles. The scattering profile can be analyzed into three different scattering sections: specular, off-specular, and background, as illustrated in

Figure B.7 for the scattering profiles obtained from non-scratched and scratched surface (containing only one scratch) at an aspecular angle of 3 $^{o}$. The specular region covers the angular range ± 0.9 $^{o}$ around the specular angle. The intensity of the off-specular region mainly comes from the scratch on the smooth surface. As surface becomes rougher, the off-specular intensity increases noticeably and distributes symmetrically around the sepeuclar reflection (see Figure B.5). When the contribution from a scratch is relatively weak, the analysis of the scattering profile at aspecular angle of 5 $^{o}$ is needed. The background scattering is often a result of a heterogeneous microstructure of a coating surface.

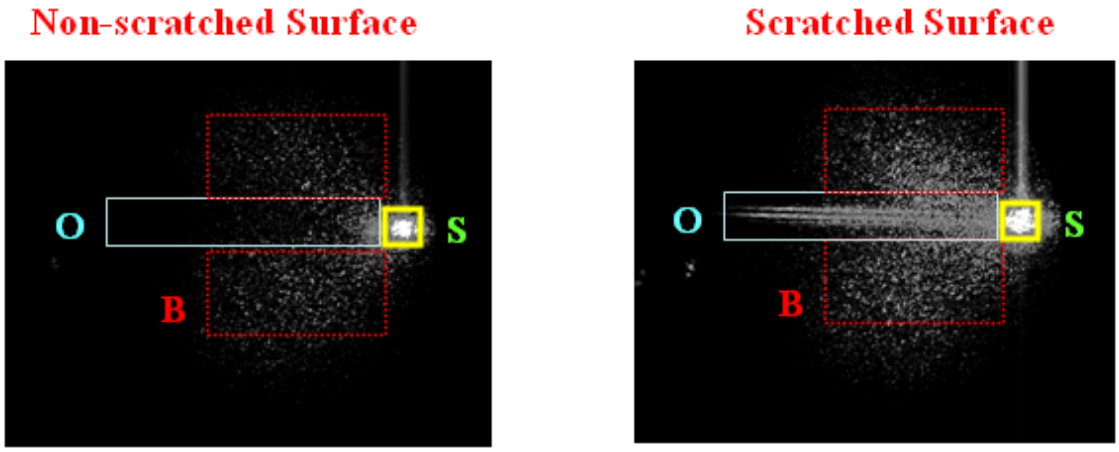


Figure B.7. The 2D scattering profiles obtained from non-scratched and scratched surfaces at an aspecular angle of 3 $^{o}$ are defined into three different scattering regions: specular (S), off-specular (O), background (B).

## B-10 Report

The following information should be reported:

a. Type of coating, materials (chemical, physical, and mechanical) properties

b. Onset force determined by progressive scratch.

c. Onset force determined by constant scratch using LSCM

d. Visual onset force determined from constant scratch

e. Characterization of scratch damage modes

f. Penetration depths, percent recovery, and friction coefficient data for both progressive and constant force scratch tests.

g. Optical scattering data, 2D scattering profile at aspecular angle 0 $^{o}$, 3 $^{o}$, and 5 $^{o}$.

h. Specular, off-specular and background scattered intensities for each scratch at all measured scattering angles. Plot of these quantities and their ratios.

i. Correlation between optical scattering results to visual onset determination.

# Appendix C: Dynamic Mechanical Thermal Analysis and Results

The objective of this section is to introduce the principle of dynamic mechanical thermal analysis (DMTA) and demonstrate the experimental results. This technique is used to study and characterize the mechanical properties of materials, such as modulus, viscosity and damping factor. It also aims to understand the temperature influence on the viscoelastic behavior of polymers. In order to find out the glass transition temperature and the modulus as a function of temperature and time, dynamic temperature ramp testing is applied to detect the behavior of materials. In addition, by the application of time-temperature superposition (TTS) principle, the long-term properties, under a variety of temperature and time conditions, can be approximated for materials. Finally, the experimental results of two PU systems were mentioned below.

## C-1 Basic principle of dynamic mechanical thermal analysis

Figure C.1 Photo of a Rheometrics system analyzer.

Dynamic mechanical analysis (DMA) or dynamic mechanical thermal analysis (DMTA) is used for performing the dynamic testing for different materials under a wide temperature, strain, or frequency ranges. It is also one of the best techniques for approaching the mechanical behavior under a particular temperature. In this study, the tests are carried out by Rheometrics system analyzer (RSA III, see photo in Figure C.1), and the TA Orchestrator 7.0 software is applied to control the instruments and analyze the data.

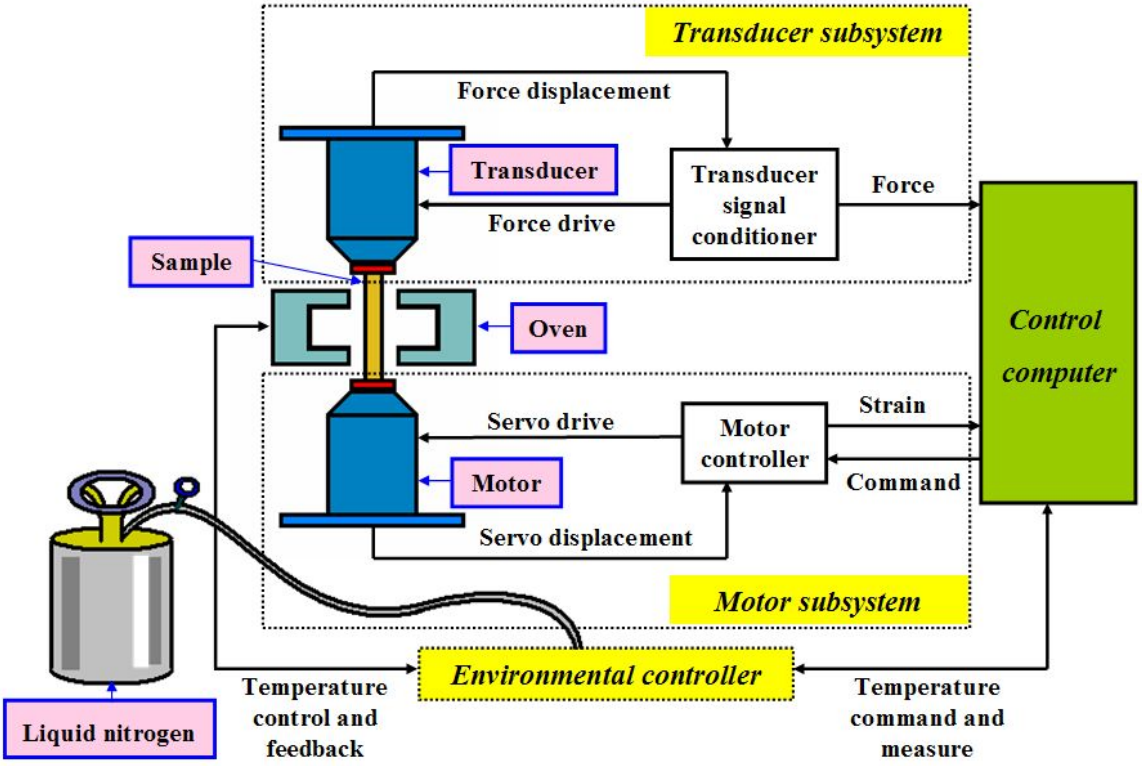


Figure C.2 Schematic of RSA Ⅲ system.

Figure C.2 shows the schematic of RSA Ⅲ system. RSA III system uses a servo drive linear motor to apply the oscillatory displacement and a force-rebalance transducer to measure force. The actuator imposes a sinusoidal stress upon the sample

and a sinusoidal strain is therefore generated. The phase delay (phase angle δ) can be calculated by comparing the stress and strain sinusoidal curves. The magnitude changes from the peak of sinusoid can also be obtained in the meantime, as shown in Figure C.3.

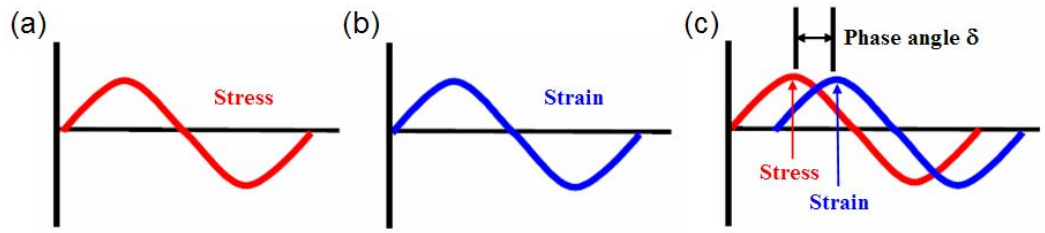


Figure C.3 Schematic of (a) a sinusoidal stress applied to the sample (b) a sinusoidal response in the form of strain (c) the phase angle δ between two signals.

The commanded maximum deformation of the motor is reported to be 1.5 mm; the force range of the transducer can vary from 0.001 N to 35 N, and the force resolution is reported to be 0.0001 N. Two transducers can be selected in the testing: transducer 1 operates under the loading of 350 g and transducer 2 operates under the loading of 3500 g. During the testing, the sample is surrounded by an oven, which is connected to a liquid nitrogen cooling system and can control the operation temperature from -150 °C to 600 °C. The isothermal stability of the oven is reported to be ± 0.1 ˚C.

There are several parameters commonly used as the indicators of mechanical performances of a material, such as complex modulus $E^*$, damping factor tan δ, storage modulus $E'$, and loss modulus $E''$. Figure C.4 shows the relationship between complex modulus and damping factor as related to storage modulus and loss modulus in the triangle geometry. The complex modulus is not exactly the same as Young's modulus, which is the elastics modulus for small deformation. It is a value used to indicate the

overall resistance to the deformation of a certain material. On the other hand, the complex modulus is calculated under vibratory conditions and it can be obtained from the material response to the sine wave loading by DMTA. The storage modulus, also called the elastic modulus, is equal to the value of the complex modulus multiplied by cos δ. It is noted that the storage modulus is always greater for elastic materials so as to be flexible under a loading and to recover to the original shape after unloading. It is also said that a material with a high storage modulus tends to store more energy. Likewise, the loss modulus is also known as the viscous modulus or the imaginary modulus. This value equals to the complex modulus multiplied by sin δ. A great loss modulus for a material has the tendency to dissipate energy like heat or power. Also, tan δ is the damping factor obtained from the measurement of material damping such as vibration or sound. It equals the value of the loss modulus divided by the storage modulus.

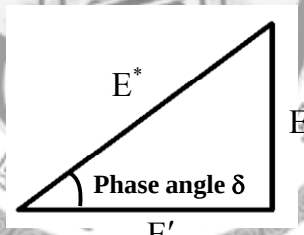


Figure C.4 Relationship between modulus ($E^*$) and damping factor (δ), as related to storage modulus ($E'$), and loss modulus($E''$), in the triangle geometry.

In a linearly viscoelastic material, stress and strain can be defined as Equation (C.1) and Equation (C.2), respectively.

$$\varepsilon(t) = \varepsilon_{max} \sin \omega t \qquad (C.1)$$

$$\sigma(t) = \sigma_{max} \sin(\omega t + \delta) \qquad (C.2)$$

Where $\varepsilon(t)$ is the dynamic strain, $\varepsilon_{max}$ is the maximum strain, $\sigma(t)$ is the dynamic stress, and $\sigma_{max}$ is the maximum stress. Equation (C.2) can be rewritten as Equation (C.3).

$$\begin{aligned}\sigma(t) &= \sigma_{max}(\sin\omega t \cdot \cos\delta + \cos\omega t \cdot \sin\delta) \\ &= \varepsilon_{max}\left(\frac{\sigma_{max}}{\varepsilon_{max}}\cos\delta \cdot \sin\omega t + \frac{\sigma_{max}}{\varepsilon_{max}}\sin\delta \cdot \cos\omega t\right)\end{aligned} \tag{C.3}$$

After being simplified, Equation (C.4) can be obtained.

$$\sigma(t) = E'\varepsilon_{max}\sin\omega t + E''\varepsilon_{max}\cos\omega t \tag{C.4}$$

Here, the storage modulus $E' = \frac{\sigma_{max}}{\varepsilon_{max}}\cos\delta$, and the loss modulus $E'' = \frac{\sigma_{max}}{\varepsilon_{max}}\sin\delta$.

According to Equation (C.4), the $\delta = 0$ when the sample is an elastic material. Thus, the dynamic stress response can be written as Equation (C.5).

$$\sigma(t) = E'\varepsilon_{max}\sin\omega t \tag{C.5}$$

In addition, the $\delta = \pi / 2$ if the sample is a viscous fluid material. The dynamic stress response can be written as Equation (C.6).

$$\sigma(t) = \eta\dot{\varepsilon} = \eta\varepsilon_{max}\omega\cos\omega t = E''\varepsilon_{max}\cos\omega t \tag{C.6}$$

Where, $\eta$ is the viscosity coefficient, and $\dot{\varepsilon}$ is the strain rate (or velocity gradient).

Figure C.5 shows the response of a purely elastic material and a purely viscous material (Newtonian liquid) under the dynamic mechanical testing.

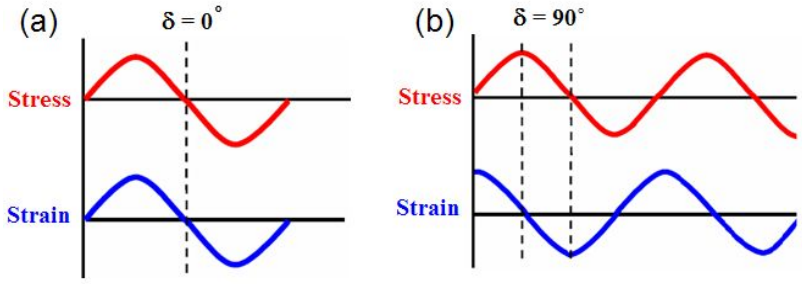


Figure C.5 Schematic of (a) no phase lag for a purely elastic response (b) 90° phase lag for a purely viscous response.

Equation (C.1) and Equation (C.2) can also be expressed as the complex form of Equation (C.7) and Equation (C.8), respectively.

$$\varepsilon(t) = \varepsilon_{max} e^{i\omega t} \tag{C.7}$$

$$\sigma(t) = \sigma_{max} e^{i(\omega t+\delta)} \tag{C.8}$$

Equation (C.9), the complex modulus, can be yielded by Equation (C.7) divided Equation (C.8).

$$E^* = \frac{\sigma(t)}{\varepsilon(t)} = \frac{\sigma_{max}}{\varepsilon_{max}} e^{i\delta} = \frac{\sigma_{max}}{\varepsilon_{max}} (\cos\delta + i\sin\delta) = E' + iE'' \tag{C.9}$$

As mentioned before, the damping factor tan δ is defined as Equation (C.10).

$$\tan\delta = \frac{E''}{E'} \tag{C.10}$$

Up to now, all the moduli and damping factor can be generated by connecting the experimental results to its theories.

## C.2 Examples of DMTA application

*1. Viscoelastic behavior characterization*

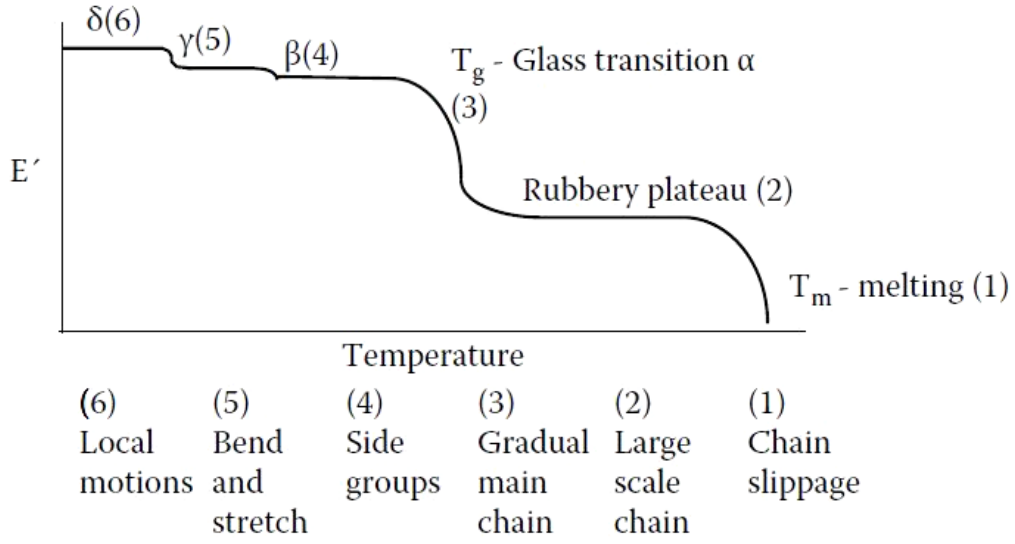


Figure C.6 Schematic of the effort of various molecular relaxations to polymers [46].

There are several dynamic tests that can be performed by DMTA, such as dynamic frequency sweep testing, dynamic strain sweep testing, dynamic temperature ramp testing, and frequency/temperature sweep testing. In order to detect the viscoelastic behavior for a polymer, the dynamic temperature ramp testing must be applied. This testing is operated over a range of temperatures and it is useful to find out the characteristics in each phase transformation for a material. Since there are six transformation zones which have usually been studied in a polymer, Figure C.6 presents the effort of molecular relaxations to those zones in a plot of storage modulus against temperature. The lowest temperature condition of the zone (6) is a state where no chain or side group can move. As the temperature increases, the storage modulus goes down

and the links between the atomic bonds gradually become looser. In the end, the whole chains can slip easily and the temperature rises to the highest temperature condition zone (1).

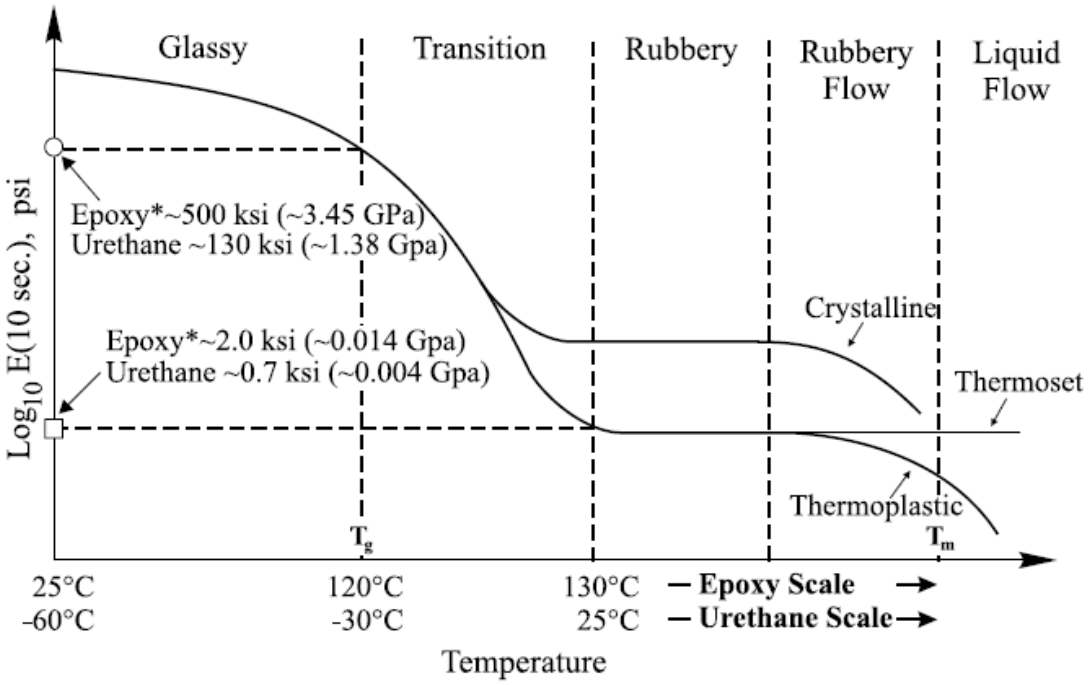


Figure C.7 Schematic of the viscoelastic behaviors for crystalline, themoset and thermoplastic polymers [47].

Figure C.7 presents the viscoelastic behaviors for crystalline, thermoset and thermoplastic polymers. There are five regions of viscoelastic behaviors: glassy state, transition state, rubbery state, rubbery flow state, and liquid flow state. Typically, the thermoset polymers only show the first three states. Thermoset materials have a stronger feature than thermoplastic materials because of the covalent bonds between chains, and are more suitable for high-temperature applications.

## 2. *Time- temperature superposition principle characterization*

The principle of time-temperature superposition (TTS) is used to study the interrelation of temperature and modulus changes of a polymeric material. This principle is suitable for amorphous polymers or materials with thermo-rheological features. Polymers have both temperature and time (frequency) dependents like creep or stress relaxation under a loading. For example, when a constant load and various temperatures are applied to a polymer, it endures the molecular rearrangement and tries to minimize the localized stress. Under this circumstance, the modulus and hardness can change depending on time. As a result, it is important to test the material under an overall temperature and time condition. By using the TTS method, we can avoid the inefficiency of measuring the behavior of a polymer over long periods of time at one particular temperature. In 1943, Leaderman systematized the general reviews of TTS method and he named a single creep curve extending over a wide time (frequency) range as a master curve [48]. After that, Tobolsky carried out further studies and demonstrated that the viscoelastic behavior at one temperature can be obtained by superimposing and shifting the data from different temperatures [49]. As the method reported, the stress relaxation curves are measured between time (frequency) and temperature in the beginning. Then, the relaxation data can be shifted separately along the horizontal axis (time or frequency) on a logarithmic time scale. Finally, it should be refined to a single master curve for a wide range of times (frequencies). Since the behavior of a polymer presents the same at a higher temperature or a shorter time, long-term properties can be accurately associated.

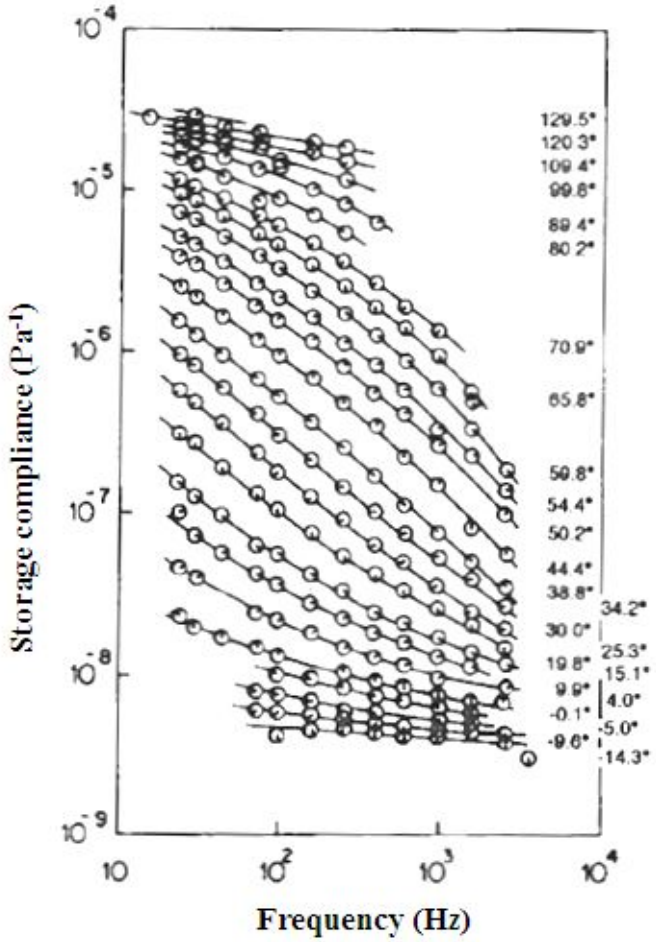


Figure C.8 Relaxation curves obtained from the experimental data of poly-n-octyl methacrylate as a function of frequency under 24 different temperatures [50].

Figure C.8 shows the relaxation curves obtained from the experimental data of poly-n-octyl methacrylate as a function of frequency under 24 different temperatures. At high temperature, there is a relatively great compliance for this material. It indicates the rubbery behavior. Comparatively, the glassy behavior is presented in the low temperature with small compliance.

So as to gain the compliance master curve of this sample, a reference relaxation curve with particular temperature should be chosen. For example, Figure C.9 shows that the reference temperature is the highest temperature (129.5 °C) in this testing. By

shifting the relaxation curves severally, the master curve over an extended frequency scale at the reference temperature can be generated.

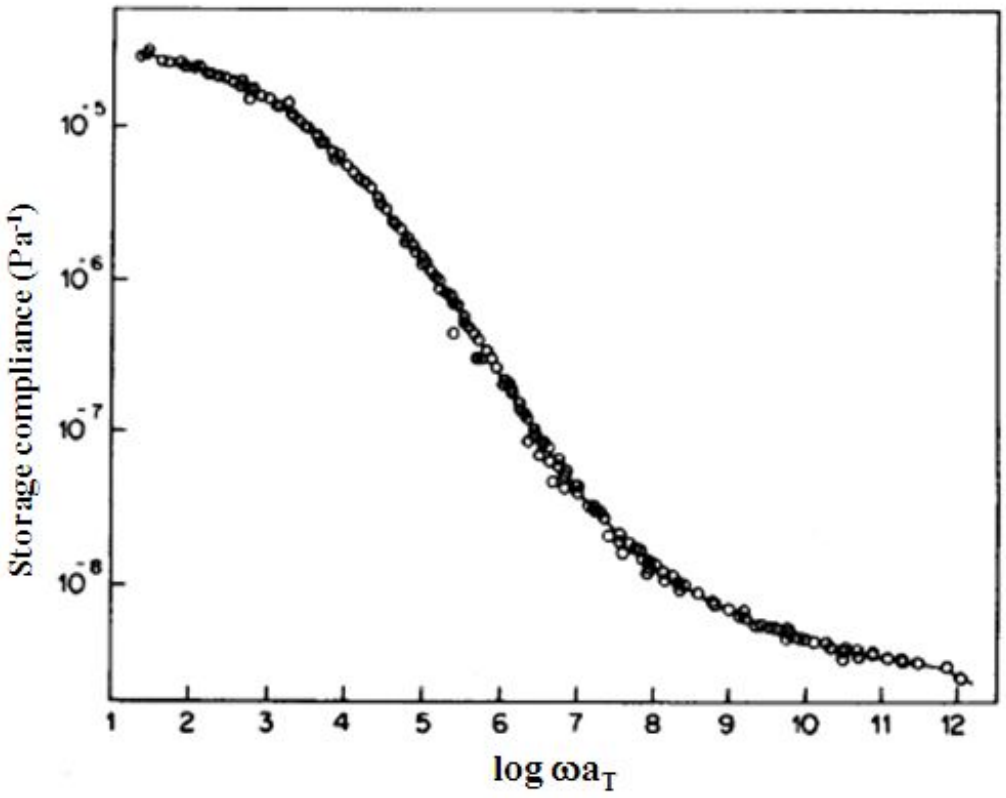


Figure C.9 Schematic of compliance master curve obtained by shifting the relaxation curves of Figure 3.27 [50].

Since every relaxation curve under a certain temperature has different shift values along the horizontal axis, the shift factor $a_T$ can be assessed by recording the change amounts. Figure C.10 shows the shift factor plotting on a logarithmic scale under different temperatures.

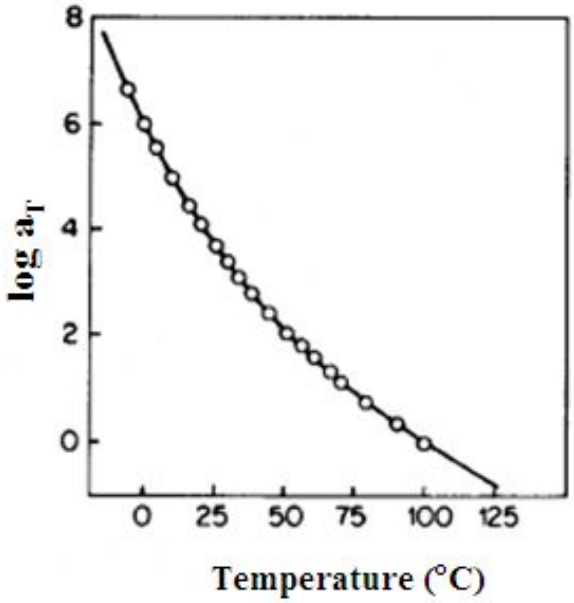


Figure C.10 Schematic of the shift factor $a_T$ plotting on a logarithmic scale under different temperatures [50].

As frequency defined as the inverse of time, the shift factor $a_T$ can be expressed as Equation (C.11). Here, F is the measurement frequency, and $F_{ref}$ is the reference frequency.

$$a_T = \frac{F}{F_{ref}} \tag{C.11}$$

In the case of frequency-based shift factor, the logarithmic shift value log $a_T$ is shown as Equation (C.12). Thus, the transform amounts between two curves of different temperature conditions can be adjusted to a variation on a logarithmic scale.

$$\log a_T = \log \frac{F}{F_{ref}} = \log F - \log F_{ref} \tag{C.12}$$

In addition, the correlation between an approximately identical shift factor and temperature to polymers is commonly described by two models. The first is established

by Williams, Landel and Ferry (WLF) equation [51]. The formula can be expressed as Equation (C.13).

$$\log a_T = \frac{C_a(T - T_{ref})}{C_b + (T - T_{ref})} \tag{C.13}$$

Where, $C_a$ and $C_b$ are empirical constants, T is the measurement temperature, and $T_{ref}$ is the reference temperature. The other commonly used model is the Arrhenius fit, which is reported by Kenner [52], as Equation (C.14) shown.

$$\log a_T = \frac{E_{act}}{2.303R}\left(\frac{1}{T} - \frac{1}{T_{ref}}\right) \tag{C.14}$$

Where, $E_{act}$ is the activation energy associated with the relaxation transition and R is the gas constant (R= 8.314 J/ mole °C).

So far, the using of TTS method is used to gauge long-time properties of polymers and generated the master curve by DMTA results. Thus, DMTA is one of the best thermal analysis techniques to detect the mechanical properties of polymeric materials.

# C.2 Results of DMTA

## C-3.1 Dynamic Frequency Sweep Data

Figure C.11 to Figure C.14 show the experimental results of dynamic frequency sweep tests for four PU samples (series 1). In each test, the frequency range is from 0.01 Hz to 70 Hz, strain is 0.01, and temperature is 0 °C. Transducer 1 is applied, which can control the force under 350 g. The blue, green, and red curves in the figures represent the storage modulus, loss modulus and damping factor tan δ, respectively. Before carrying out the dynamic temperature ramp testing, the dynamic frequency sweep testing is performed in order to find the suitable frequency value. Here, the storage modulus (blue symbols) is an indicator which is used to represent the frequency dependent behavior of a sample, i.e., a flat curve represents a suitable working region, and a curve which changes rapidly in a short time represents a bad working region. The storage modulus curves are a little noisy for the four samples, especially for PU-A1 and PU-B1. The modulus values of these two samples scatter slightly in the entire sweep (0.01 Hz to 70 Hz). The noise is most likely due to extra thin sample condition (thickness ~ 0.06 mm). For the extra thin sample, the force applied to the sample, which is correlated with the sample geometries, is extremely small during the tests. Therefore, measurement uncertainties are large and data scatter more. Although the storage modulus curves appear slightly noisy, the values didn't change a lot during the tests so that the frequency is chosen at 1 Hz for the following tests.

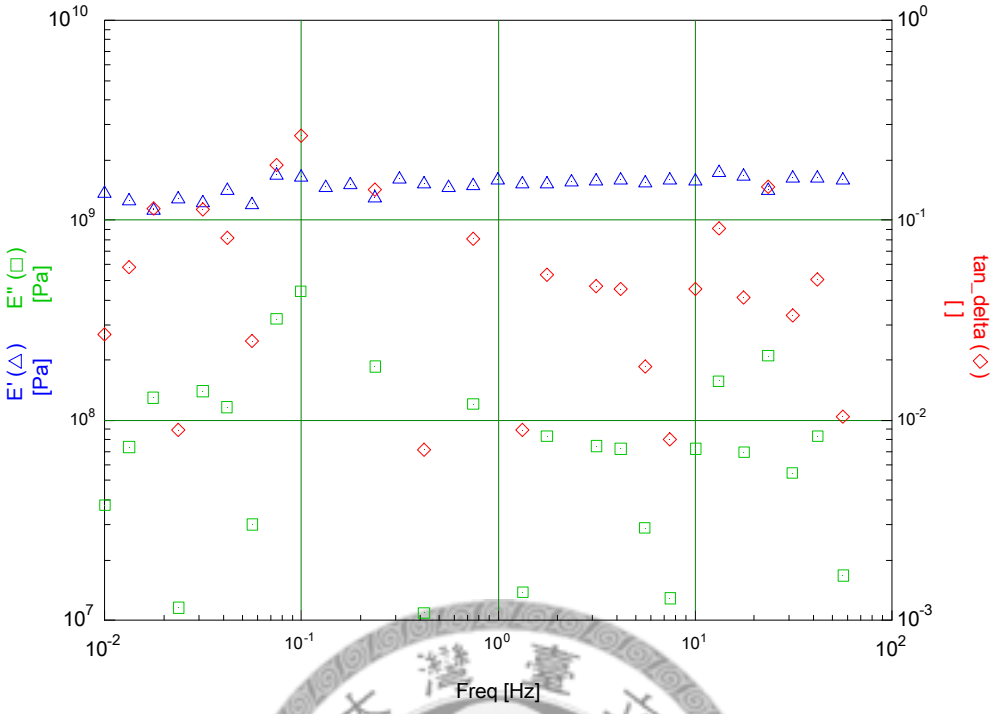


Figure C.11 The dynamic frequency sweep test (0.01 Hz ~ 70 Hz) result for PU-CTRL1.

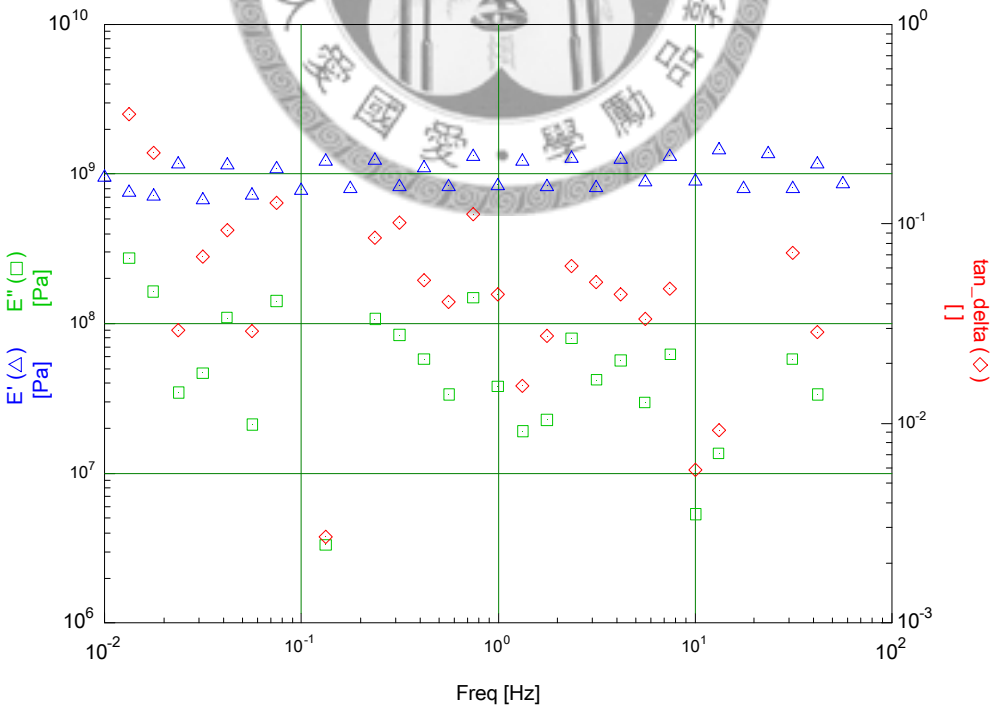


Figure C.12 The dynamic frequency sweep test (0.01 Hz ~ 70 Hz) result for PU-A1.

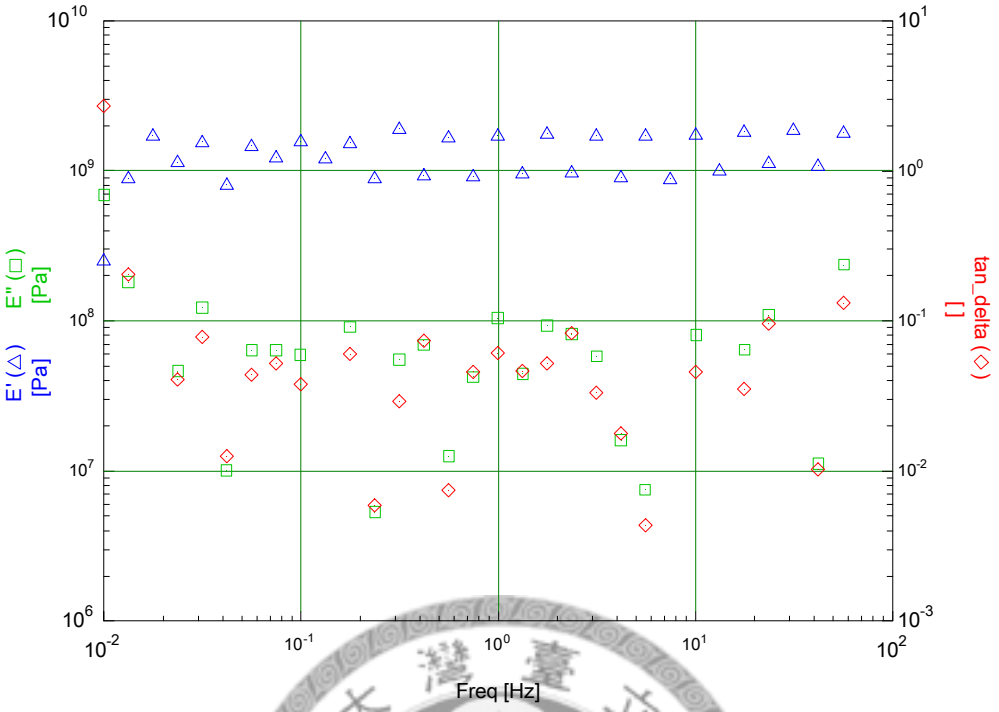


Figure C.13 The dynamic frequency sweep test (0.01 Hz ~ 70 Hz) result for PU-B1.

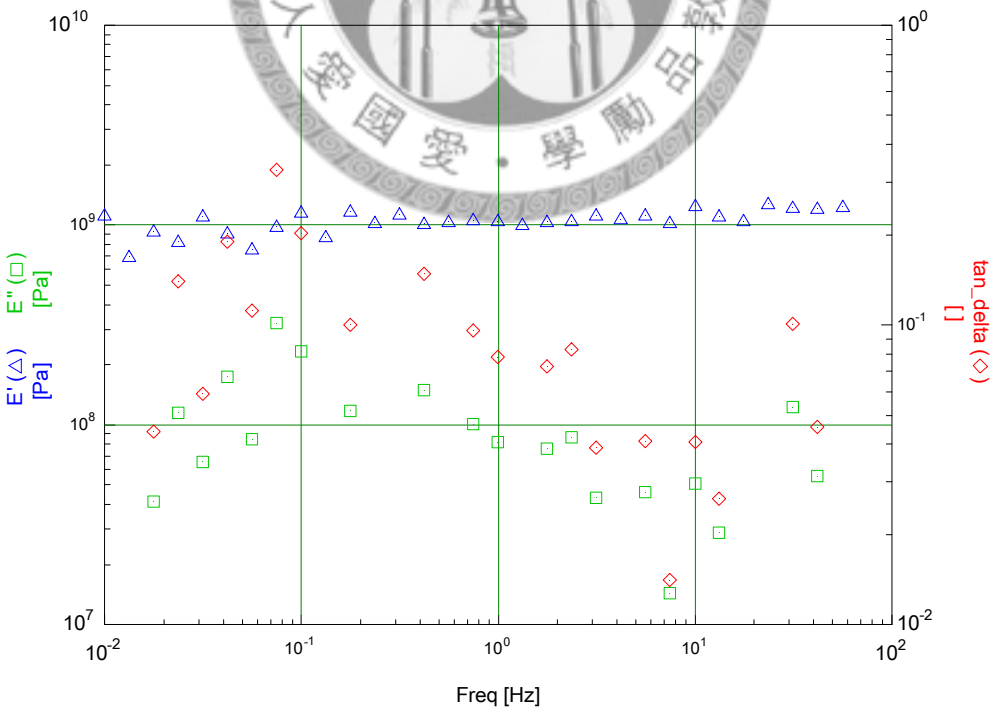


Figure C.14 The dynamic frequency sweep test (0.01 Hz ~ 70 Hz) result for PU-C1.

## C-3.2 Dynamic Strain Sweep Data

Figure C.15 to C.18 show the experimental results of dynamic strain sweep tests for four PU samples (series 1) at -125 °C, and Figure C.19 to Figure C.22 are at 23 °C (The room temperature). In each test, the strain range is from 0.001 to 10, and the frequency is 1 Hz. Transducer 2 is applied, which can control the force under 3500 g so as to cope with the greater strain changes. The blue, green, and red curves in the figures represent the storage modulus, loss modulus and damping factor tan δ, respectively. The star symbol (pale blue) is an indicator which represents the nonlinear behavior during the dynamic tests. The formulation of this function (star symbol) is not known so that it would not be discussed in this study. At -125 °C (see figures C.15 to C.18), the modulus curves are similar for four samples. The curves start with a little noisy and last until the strain around 0.08. After that, the curves increase slightly and reach a plateau. At 0 °C (see figures C.19 to C.22), PU-CTRL1 and PU-C1 have flatter curves in the whole tests. PU-A1 and PU-B1 samples show the same trend as present in the low temperature (-125 °C). It is similar to the dynamic frequency sweep results. Therefore, PU-CTRL1 and PU-C1 are found to have better responses as function of frequency and strain at 0 °C. Noticeably, all of the four samples always broke around strain = 3 ~ 5. As a result, all of the curves changed dramatically. Although the storage modulus curves appear slightly noisy in the beginning, the strain is chosen at 0.01 Hz for the following tests under the consideration of extra thin sample condition.

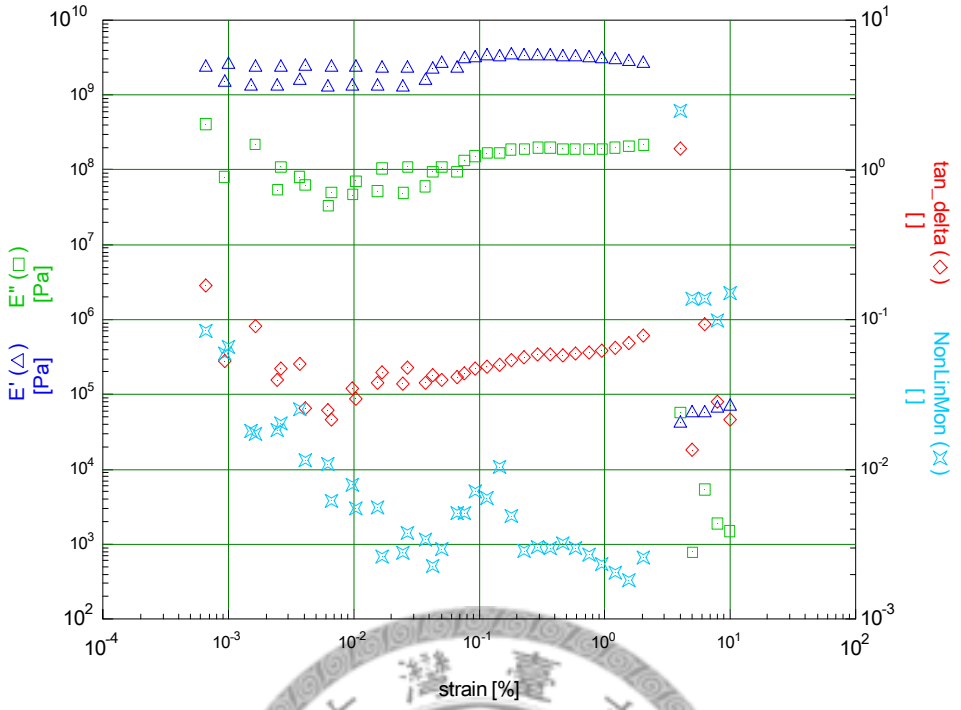


Figure C.15 The dynamic strain sweep test (0.001 ~ 10) result for PU-CTRL1 at -125 °C.

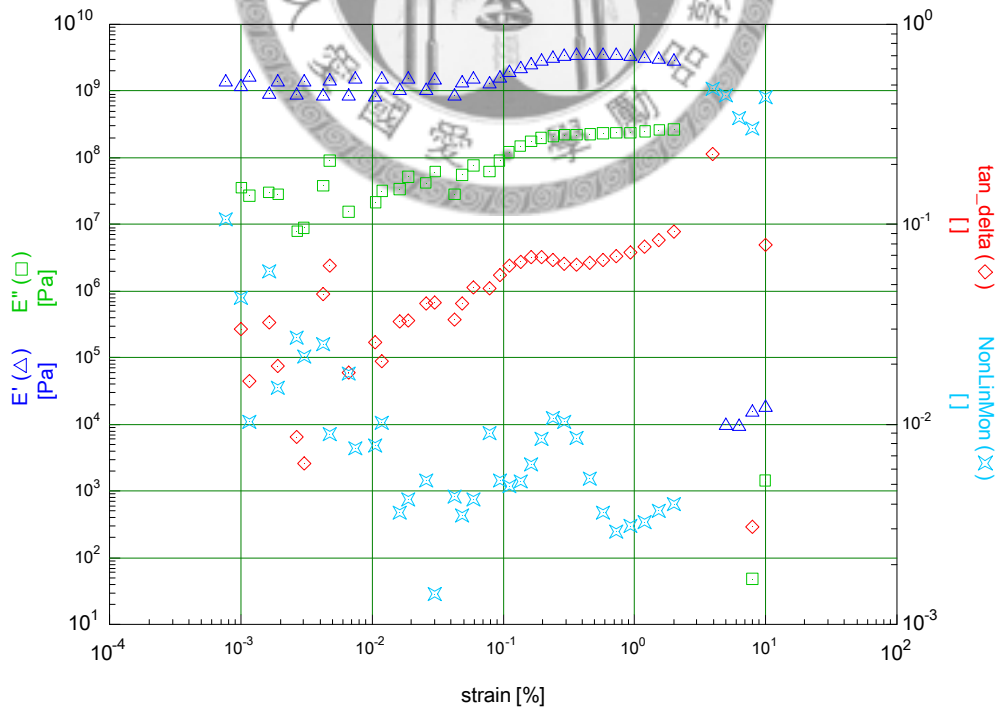


Figure C.16 The dynamic strain sweep test (0.001 ~ 10) result for PU-A1 at -125 °C.

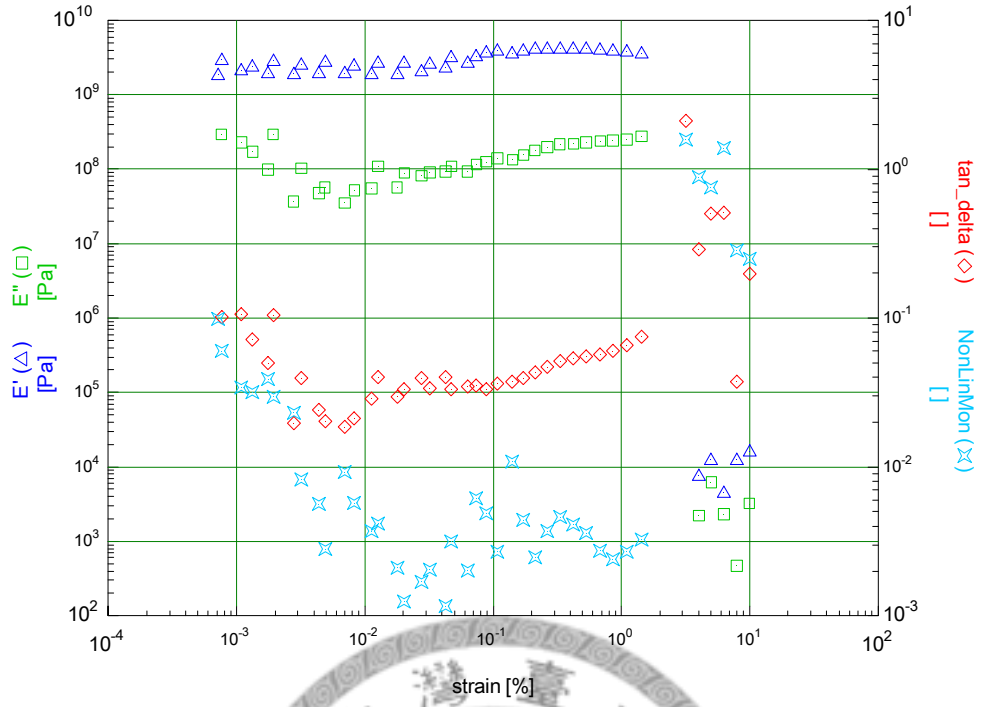


Figure C.17 The dynamic strain sweep test (0.001 ~ 10) result for PU-B1 at -125 °C.

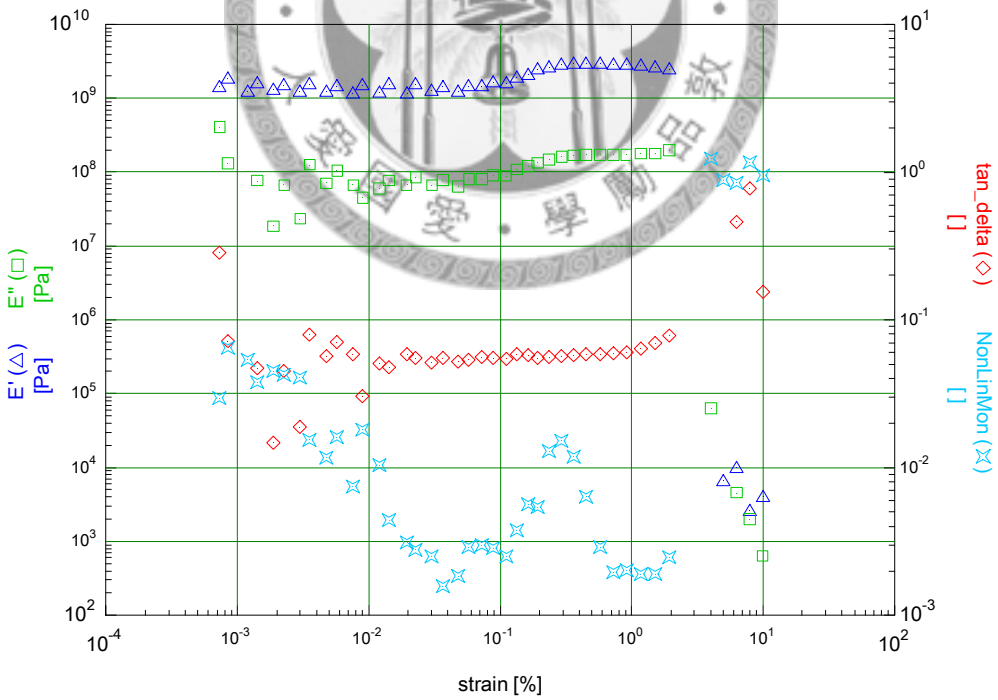


Figure C.18 The dynamic strain sweep test (0.001 ~ 10) result for PU-C1 at -125 °C.

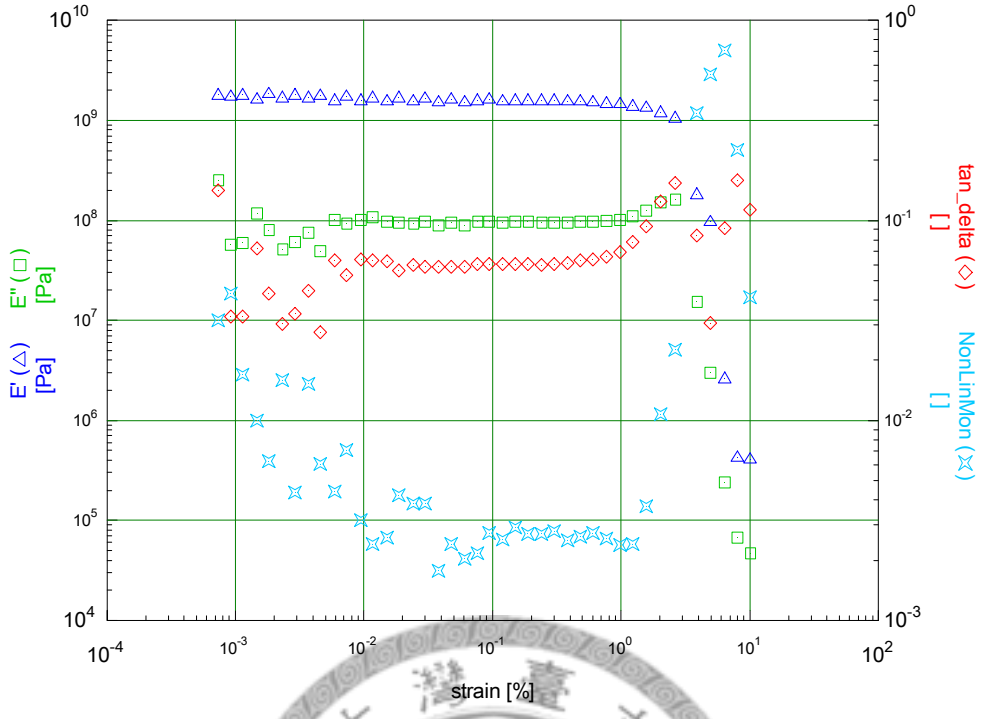


Figure C.19 The dynamic strain sweep test (0.001 ~ 10) result for PU-CTRL1 at 23 °C.

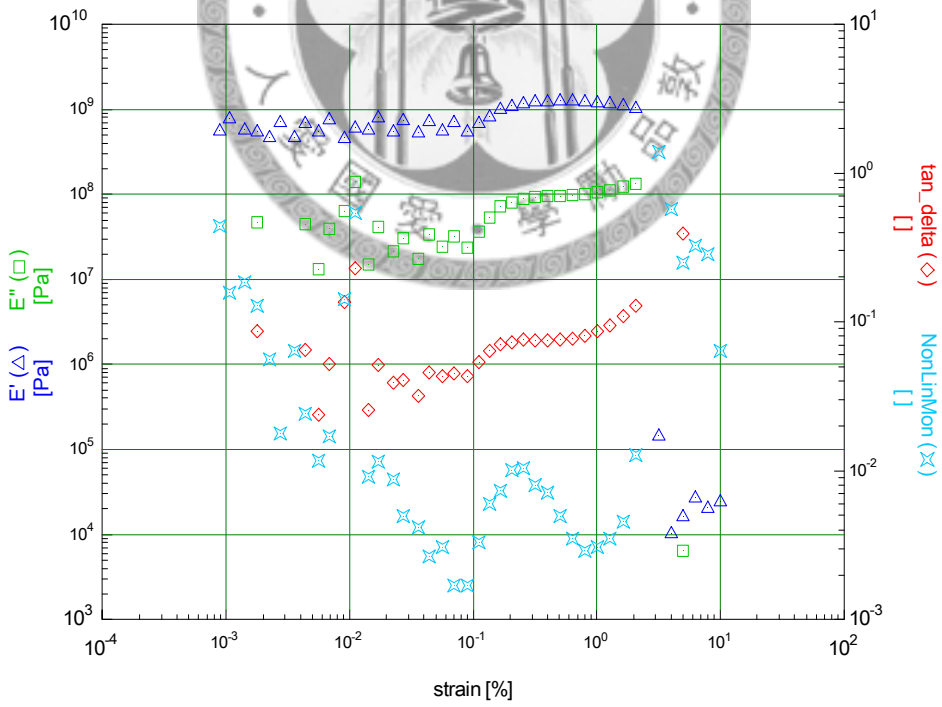


Figure C.20 The dynamic strain sweep test (0.001 ~ 10) result for PU-A1 at 23 °C.

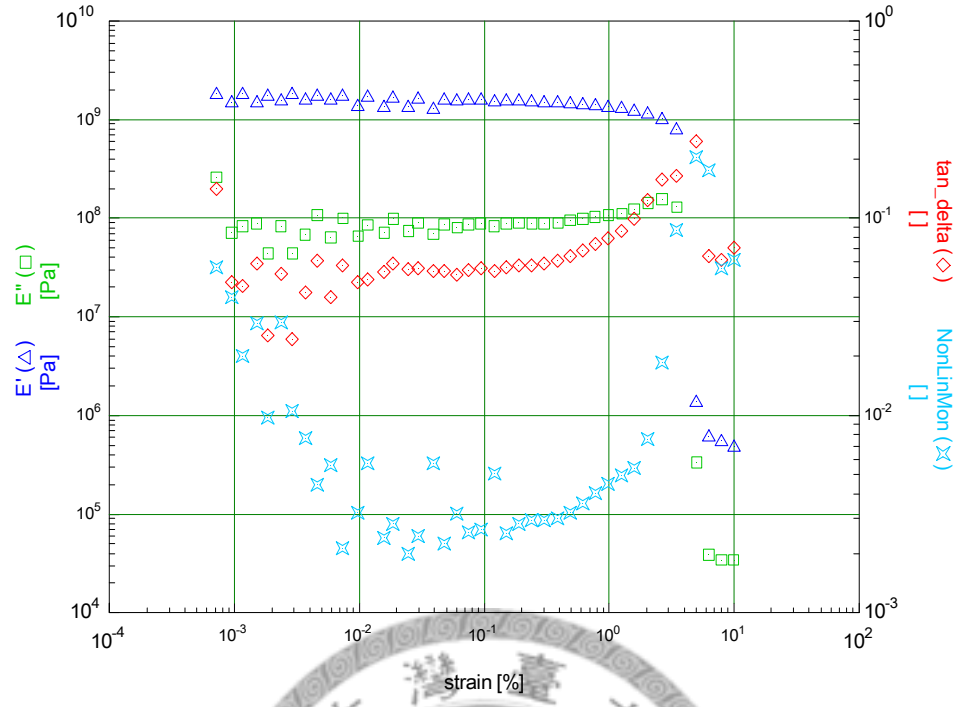


Figure C.21 The dynamic strain sweep test (0.001 ~ 10) result for PU-B1 at 23 °C.

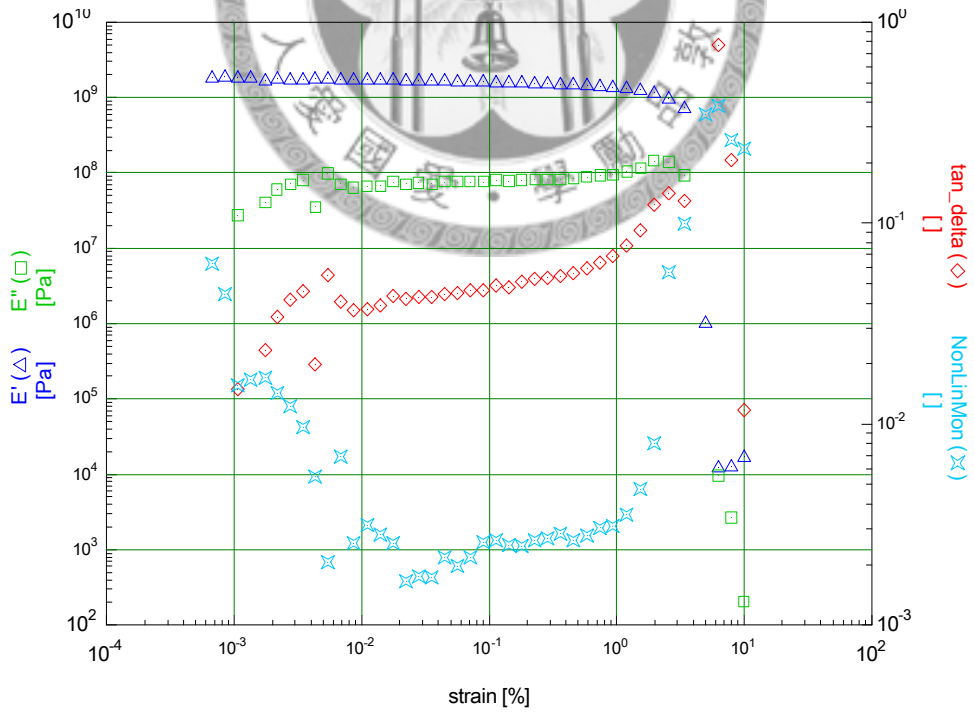


Figure C.22 The dynamic strain sweep test (0.001 ~ 10) result for PU-C1 at 23 °C.

## C-3.3 Dynamic Temperature Ramp Data

### *1. Polyurethane- series 1*

Figure C.23 to Figure C.26 show the experimental results of dynamic temperature ramp tests for four PU samples (series 1). In each test, the frequency is chosen to be 1 Hz and strain is 0.01 which are determined from the results of dynamic frequency and strain sweep tests. The temperature range is from -125 °C to 110 °C, and the ramp rate is 3 °C/ minute. The transducer 1 is applied, which can control the force under 350 g. The blue, green, and red curves in the figures represent the storage modulus, loss modulus and damping factor tan δ, respectively. The peaks of tan δ indicate the glass transition temperature $T_g$. In spite of the scatters in the tan δ data, the peak locations are found clearly around 90 °C for all samples. Similar, the noise of tan δ curve is most likely due to extra thin sample condition. When the temperature exceeds the $T_g$, the sample starts to reflow quickly and the problem to control small force becomes noticeable.

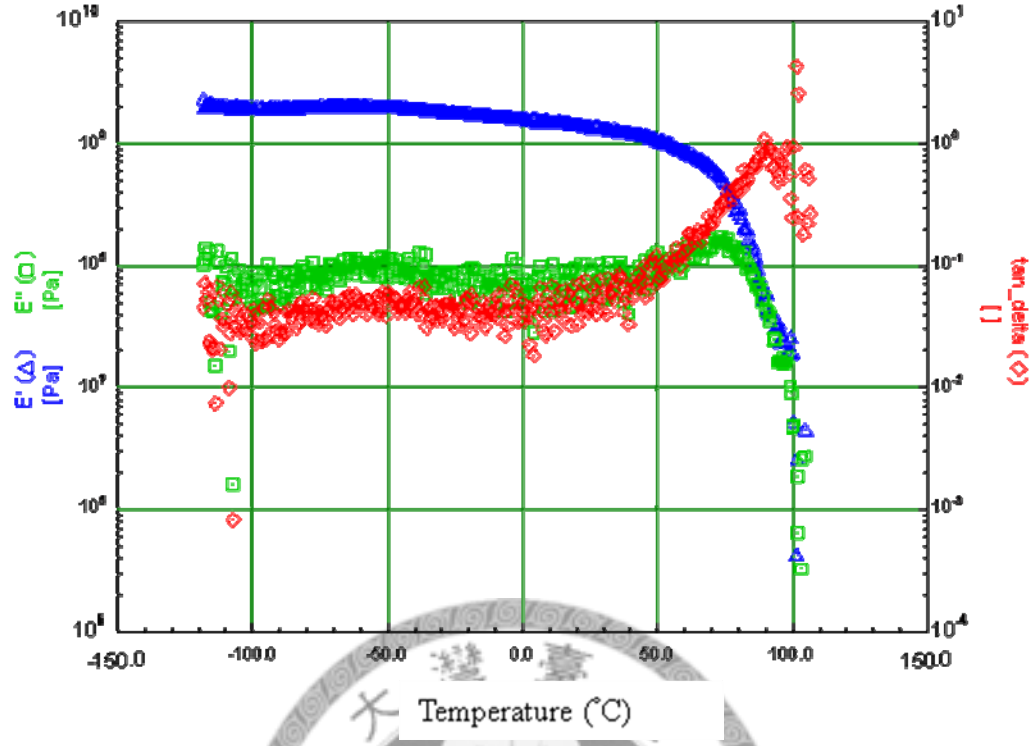


Figure C.23 The dynamic temperature ramp test (-125 °C ~ 110°C) result for PU-CTRL1.

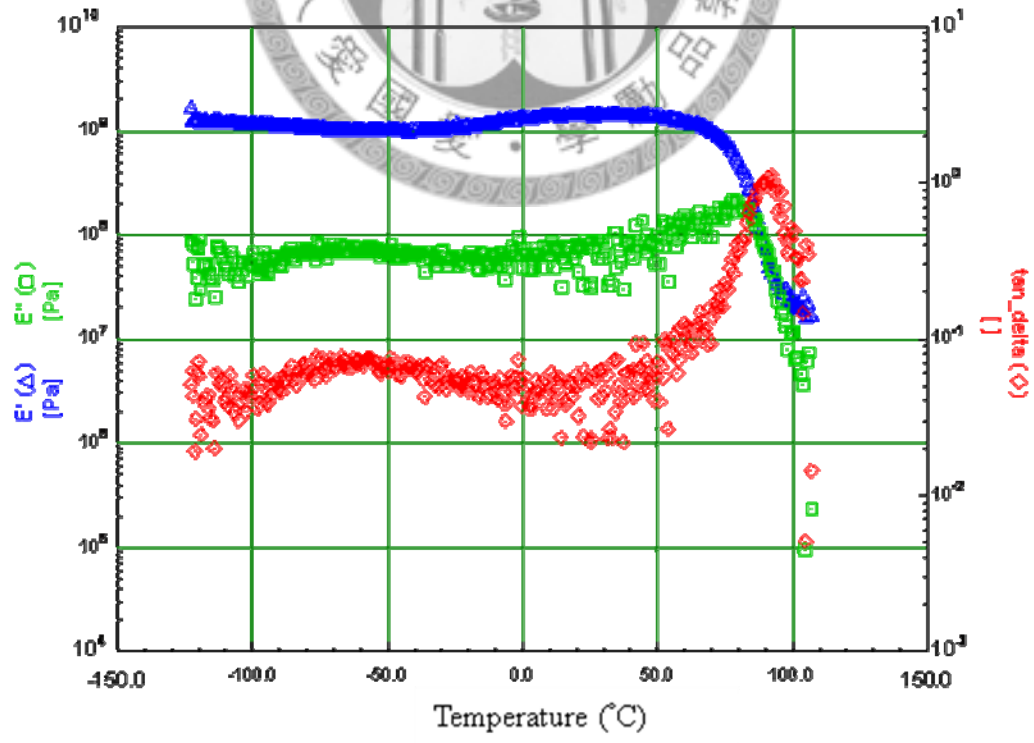


Figure C.24 The dynamic temperature ramp test (-125 °C ~ 110°C) result for PU-A1.

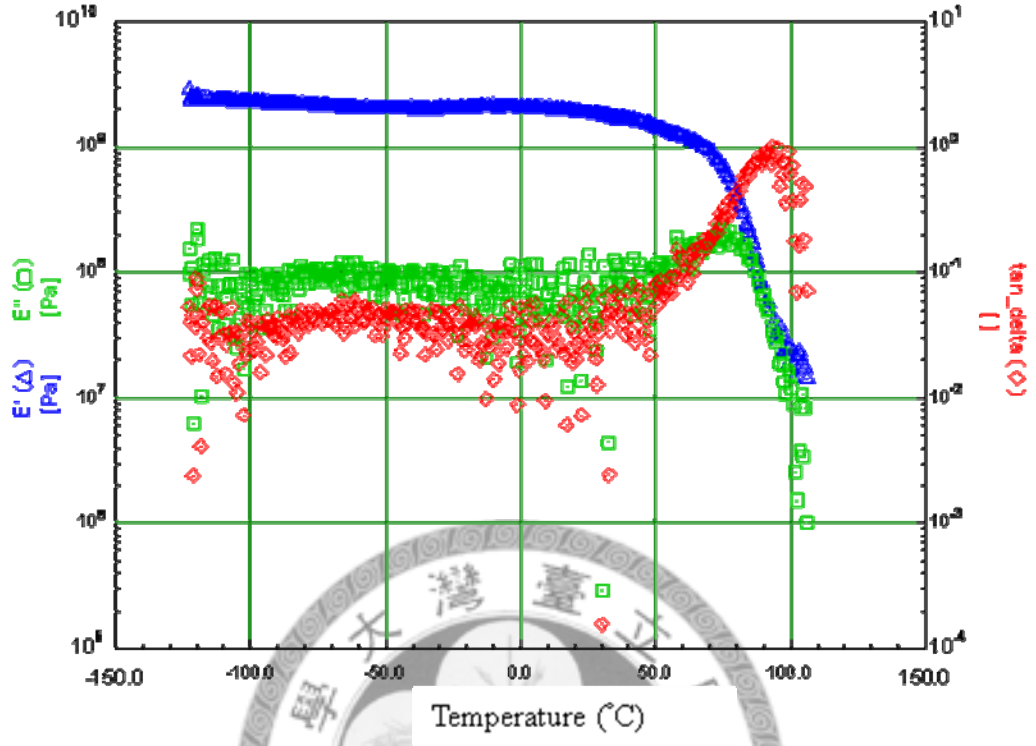


Figure C.25 The dynamic temperature ramp test (-125 °C ~ 110°C) result for PU-B1.

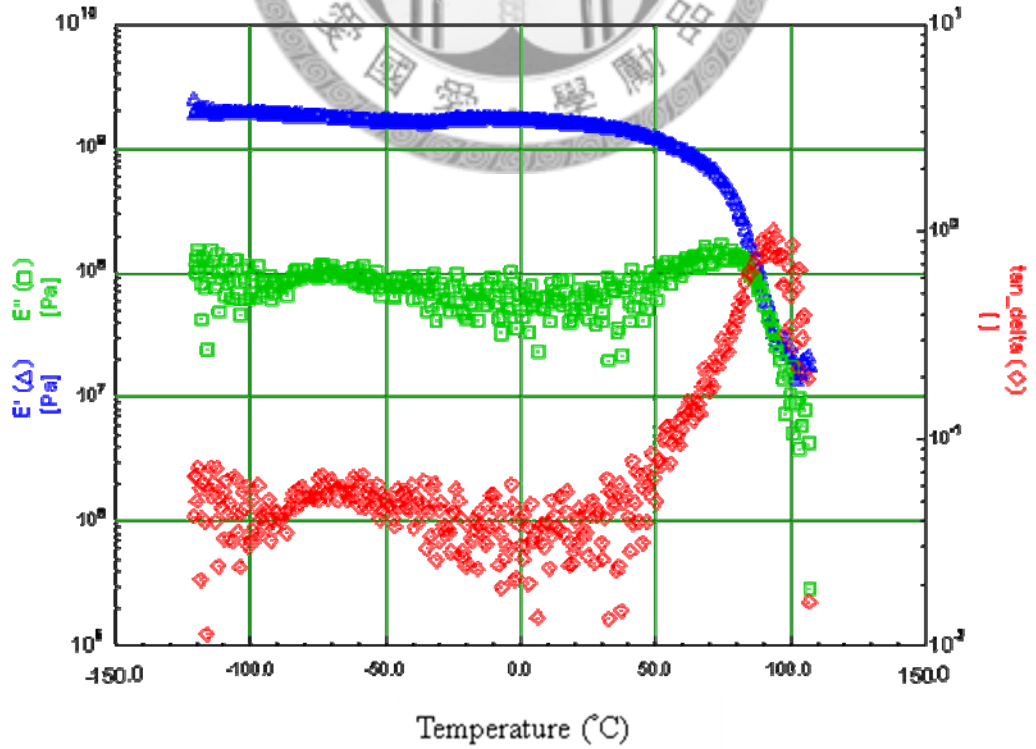


Figure C.26 The dynamic temperature ramp test (-125 °C ~ 110°C) result for PU-C1.

## 2. *Polyurethane- series 2*

Figure C.27 and Figure C.28 show the dynamic temperature ramp testing results for PU-CTRL2 and PU-A2. Transducer 1 is applied in the tests, which can provide the force control smaller than 350 g. The testing conditions are: frequency = 1 Hz, strain = 0.01, temperature range = 0 °C ~ 80 °C and ramp rate = 3 °C/ minute. The blue, green, and red curves represent the storage modulus, loss modulus and damping factor tan δ, respectively. The storage and loss modulus values are similar to the results obtained form series 1. From the tan δ curves, the $T_g$ is can be estimated around 55 °C in both two PU-2 samples, which is lower than the $T_g$ of series 1 samples ($T_g$ for series 1 is around 90 °C). Similar to the series 1 sample, the tan δ data scatter a lot. We have expected that series 2 will have less noise in the data due the increase in sample thickness (series 1 thickness = 0.06 mm and series 2 = 0.12 mm). Unfortunately, the low $T_g$ causes a more severe reflow behavior even if we double the sample thickness. Hence, no more DMTA tests were held to study this series of samples.

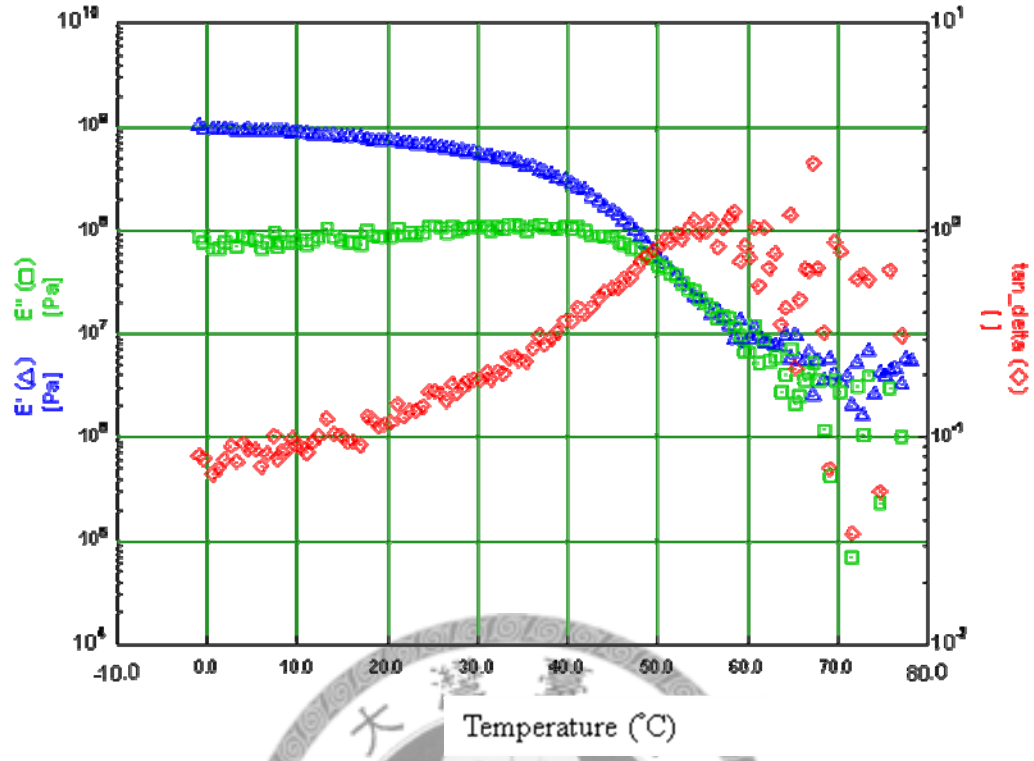


Figure C.27 The dynamic temperature ramp test (0 °C ~ 80°C) result for PU-CTRL2.

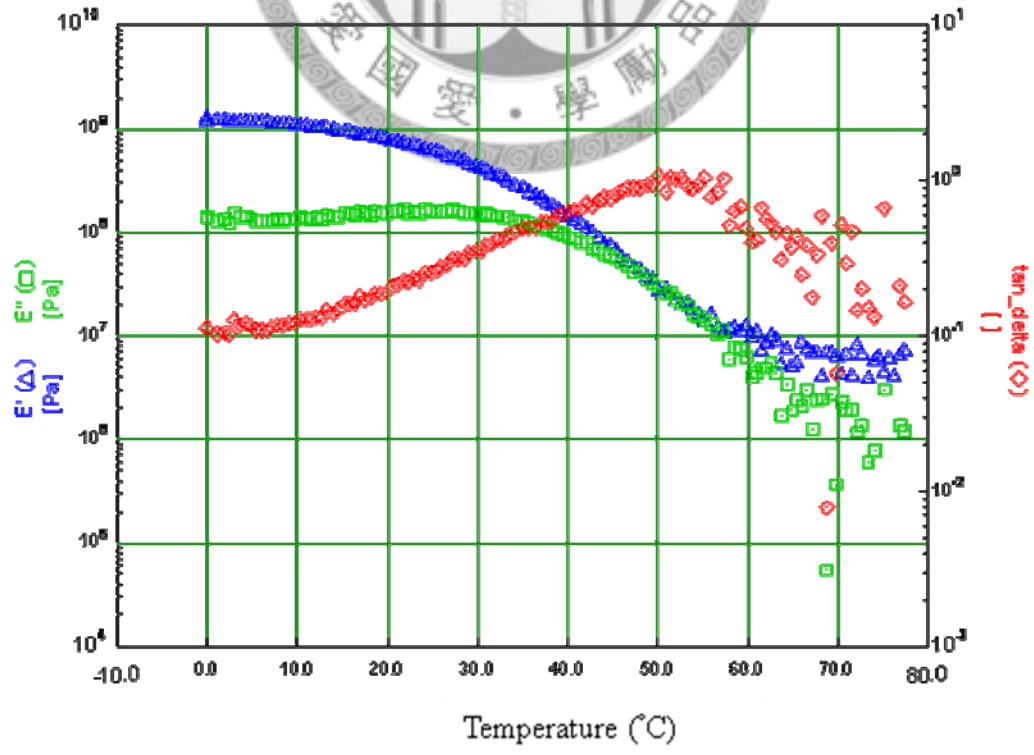


Figure C.28 The dynamic temperature ramp test (0 °C ~ 80°C) result for PU-A2.

## C-3.4 Master Curves

Figure C.29 to Figure C.36 show the master curves of storage modulus and shift factors for four samples (series 1), which are obtained from dynamic frequency/temperature sweep tests. The experimental setting are: strain= 0.001, frequency= 0.06~10, temperature= 0~80 °C, and temperature increment = 5 °C. Transducer 1 is also applied in the tests. The master curve presents the long time behavior of a sample, i.e., the reference temperature $T_{ref}$ is chosen around 0 °C so that the master curve represents the storage modulus change in 0 °C as a function of frequency. The master curves of storage modulus for four samples are not all the same. For example, the storage modulus decreases slowly in PU-CTRL1 comparing to the reference group while a smaller frequency is applied. However, the differences can be caused by the measurement or shifting uncertainties. All of the tests show that the storage modulus curves increase along with the increasing of frequency first, and then get flat in the high frequency region. The corresponding shift factors were assessed by recording the shift amounts as generated the master curve. However, the shift factor curves do not appear smoothly. The experimental results are noisy, and it is hard to overlap the data points precisely.

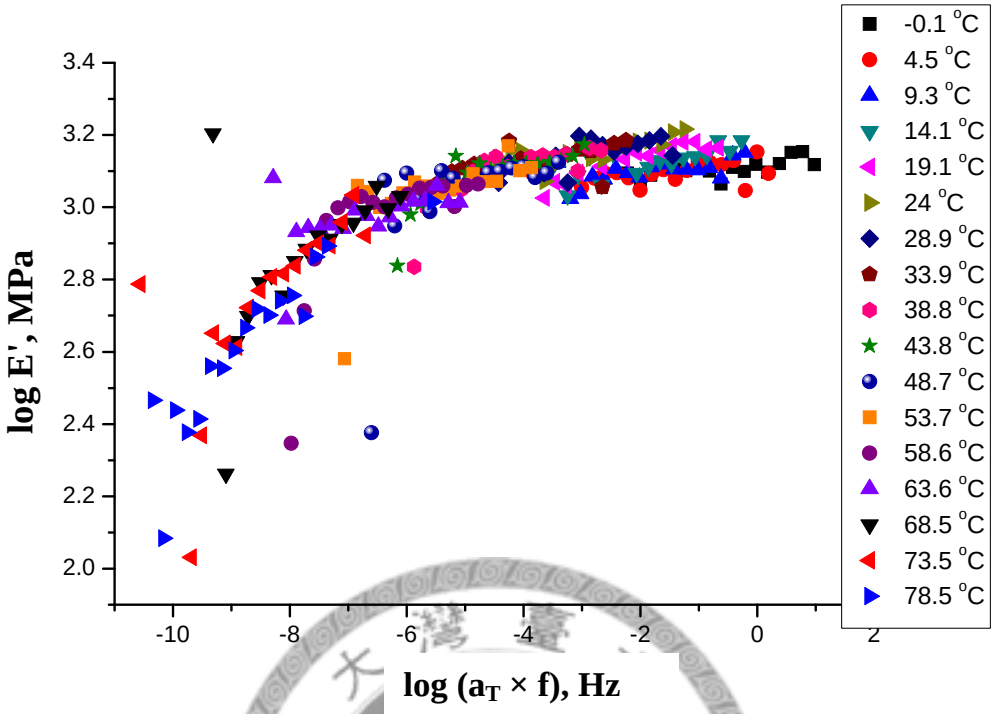


Figure C.29 Master curve of the storage modulus for PU-CTRL1 ($T_{ref}$ = -0.1 °C).

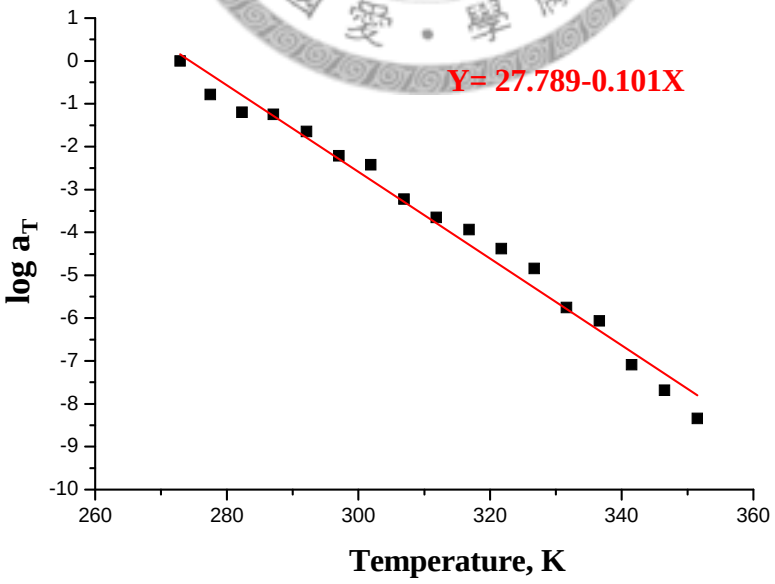


Figure C.30 The shift factors on a logarithmic scale with a linear fitting for PU-CTRL1.

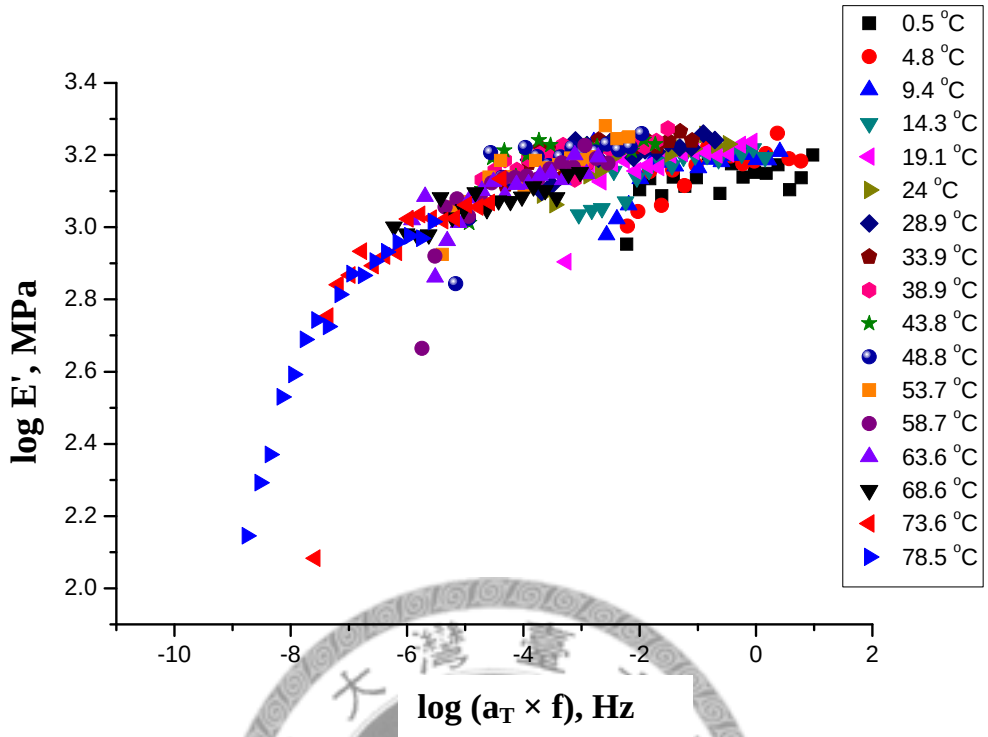


Figure C.31 Master curve of the storage modulus for PU-A1 ($T_{ref}$ = 0.5 °C).

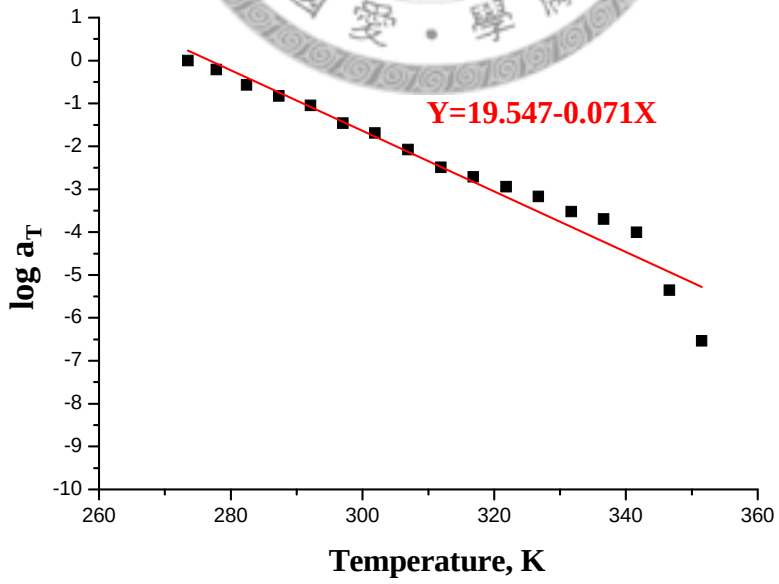


Figure C.32 The shift factors on a logarithmic scale with a linear fitting for PU-A1.

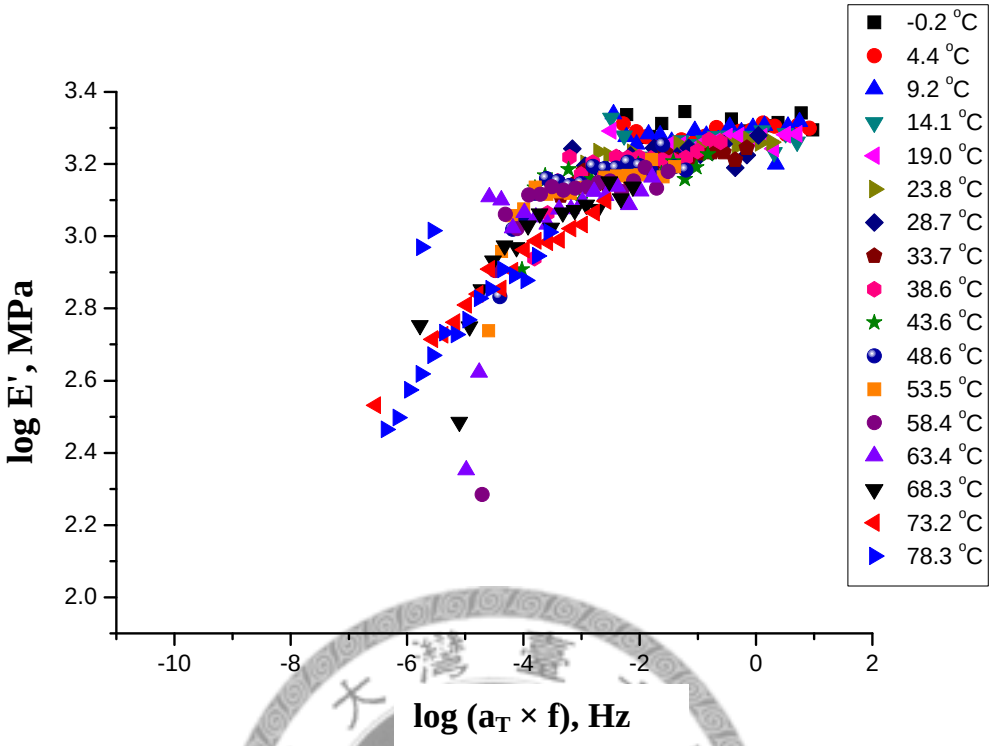


Figure C.33 Master curve of the storage modulus for PU-B1 ($T_{ref}$ = -0.2 °C).

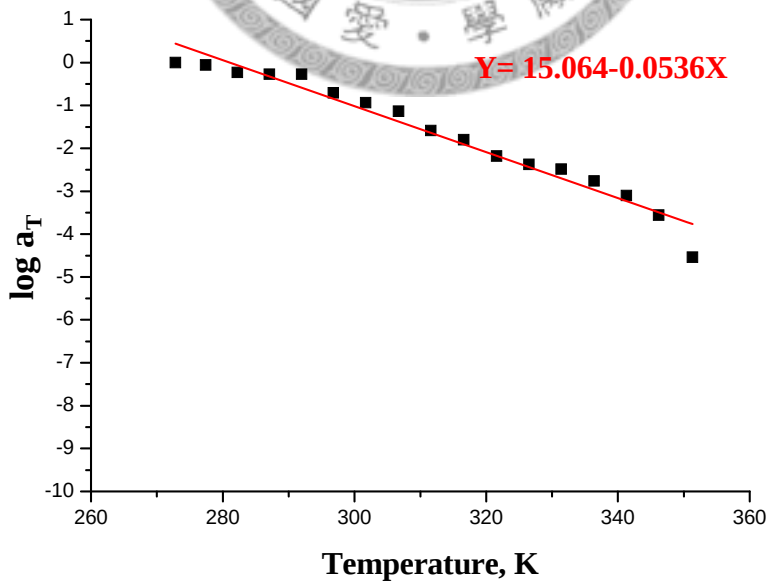


Figure C.34 The shift factors on a logarithmic scale with a linear fitting for PU-B1.

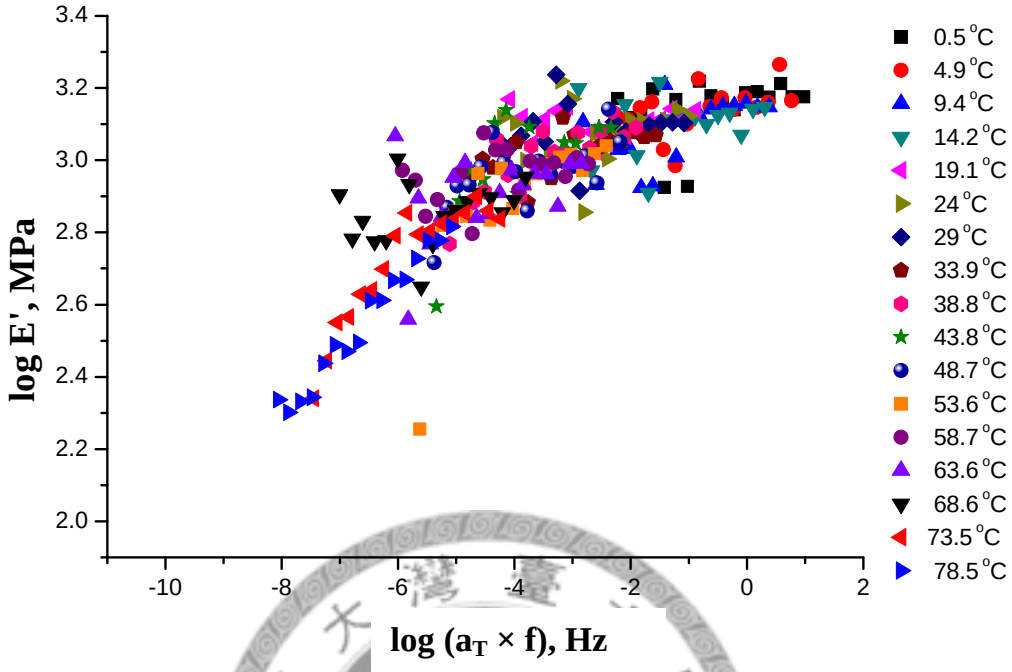


Figure C.35 Master curve of the storage modulus for PU-C1 ($T_{ref}$ = 0.5 °C).

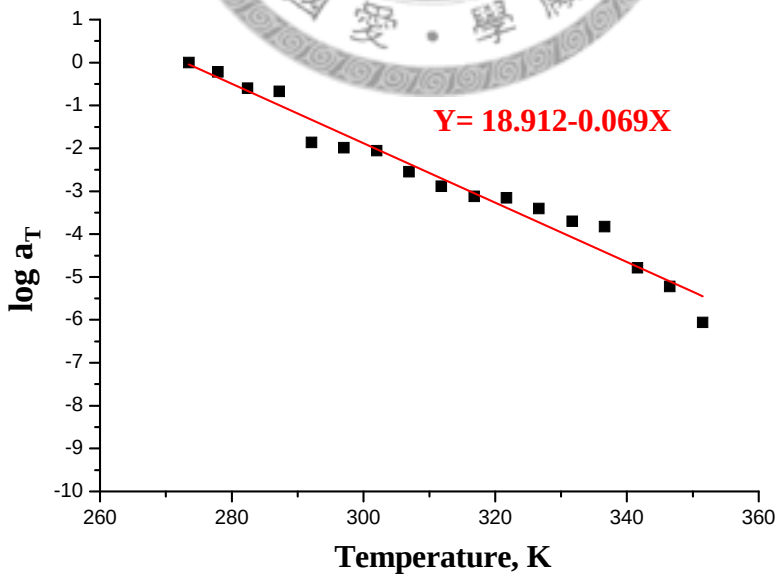


Figure C.36 The shift factors on a logarithmic scale with a linear fitting for PU-C1.

## C-3.5 Summary

For PU series 1 samples, the suitable frequency (1 Hz) and strain (0.01) values were determined by the dynamic frequency and strain sweep testing, respectively. $T_g$ were observed from dynamic temperature ramp tests. It is found that all of the samples have similar Tg around 90 °C. The master curves and corresponding shift factors can be obtained from the dynamic frequency/temperature sweep test. All of the samples have similar trends. The storage modulus enhances as increases the frequency in the low frequency region, and then stays almost the same in the high frequency region. The low and high frequency regions are different from samples. According to the extra thin sample condition (thickness ~ 0.06 mm), the modulus curves are noisy and the shift factor curves are not smooth. The measurement uncertainties cannot be ignored.

For PU series 2 samples, only two dynamic temperature ramp tests were performed and $T_g$ were observed around 55 °C. Due to the low $T_g$ effect, the more severe reflow behaviors occurred in this series of samples even if the samples are twice as thick as series 1. Therefore, the DMTA tests are not suitable for studying the viscoelastic behaviors for the PU series 2 samples.

# REFERENCE


[1] R. Ryntz and D. Britz, "Scratch resistance behavior of automotive plastic coatings," Journal of Coatings Technology, vol. 74, pp. 77-81, 2002.

[2] N. Tahmassebi and S. Moradian, "Predicting the performances of basecoat/clearcoat automotive paint systems by the use of adhesion, scratch and mar resistance measurements," Polymer Degradation and Stability, vol. 83, pp. 405-410, 2004.

[3] J. Lange, A. Luisier, and A. Hult, "Influence of crosslink density, glass transition temperature and addition of pigment and wax on the scratch resistance of an epoxy coating," Journal of Coatings Technology, vol. 69, pp. 77-82, 1997.

[4] J. M. Torres, C. M. Stafford, and B. D. Vogt, "Elastic modulus of amorphous polymer thin films: relationship to the glass transition temperature," Acs Nano, vol. 3, pp. 2677-2685, 2009.

[5] R. Fernando and L. Sung, Nanotechnology applications in coatings: ACS Symposium Series, Washington DC, 2009.

[6] N. Tahmassebi, S. Moradian, B. Ramezanzadeh, A. Khosravi, and S. Behdad, "Effect of addition of hydrophobic nano silica on viscoelastic properties and scratch resistance of an acrylic/melamine automotive clearcoat," Tribology International, vol. 43, pp. 685-693, 2010.

[7] J. W. Martin, R.A. Ryntz, and R.A. Dickie, Service life prediction: challenging the status quo Pennsylvania: Federation of Societies for Coatings Technology, Pennsylvania 2005.

[8] The Polymer Surface/Interface (PSI) scratch test method was developed under the research corporation agreement of the NIST/Industry Polymer Interphase Consortium (PIC, renamed as Polymer Surface/Interface, PSI in 2009). Brief description were in L. Sung, P. Drzal, M. VanLandingham, T. Wu, and S. Chang, "Metrology for characterizing scratch resistance of polymer coatings," Journal of Coatings Technology and Research, vol. 2, pp. 583-589, 2005.

[9] L. Sperling, Introduction to physical polymer science: John Wiley and sons, New Jersey, 2006.

[10] H. Eyring, "Viscosity, plasticity, and diffusion as examples of absolute reaction rates," The Journal of Chemical Physics, vol. 4, pp. 283-295, 1936.

[11] T. Fox Jr and P. Flory, "Intrinsic viscosity relationships for polystyrene1," Journal of the American Chemical Society, vol. 73, pp. 1915-1920, 1951.

[12] J. Gibbs and E. DiMarzio, "Nature of the glass transition and the glassy state," The Journal of Chemical Physics, vol. 28, pp. 373-383, 1958.

[13] M. Wolfgardt, J. Baschnagel, W. Paul, and K. Binder, "Entropy of glassy polymer melts: Comparison between Gibbs-DiMarzio theory and simulation," Physical Review E, vol. 54, pp. 1535-1543, 1996.

[14] S. Sinha, Scratching of materials and applications: Elsevier, London, 2006.

[15] P. Morel and V. Jardret, "Viscoelastic effects on the scratch resistance of polymers: relationship between mechanical properties and scratch properties at various temperatures," Proceeding of Materials Research Society Symposium, 2002.

[16] C. Gauthier, S. Lafaye, and R. Schirrer, "Elastic recovery of a scratch in a polymeric surface: experiments and analysis," Tribology International, vol. 34, pp. 469-479, 2001.

[17] S. Lafaye, C. Gauthier, and R. Schirrer, "A surface flow line model of a scratching tip: apparent and true local friction coefficients," Tribology International, vol. 38, pp. 113-127, 2005.

[18] X. Gu, T. Nguyen, L. Sung, M. VanLandingham, M. J. Fasolka, J. W. Martin, Y. C. Jean, D. Nguyen, N. Chang, and T. Wu, "Advanced techniques for nanocharacterization of polymeric coating surfaces," Journal of Coatings Technology and Research, vol. 1, pp. 191-200, 2004.

[19] B. Briscoe, "Isolated contact stress deformations of polymers: the basis for interpreting polymer tribology," Tribology International, vol. 31, pp. 121-126, 1998.

[20] B. Briscoe, E. Pelillo, and S. Sinha, "Scratch hardness and deformation maps for polycarbonate and polyethylene," Polymer engineering and science, vol. 36, pp. 2996-3005, 1996.

[21] R. Misra, R. Hadal, and S. Duncan, "Surface damage behavior during scratch deformation of mineral reinforced polymer composites," Acta Materialia, vol. 52, pp. 4363-4376, 2004.

[22] J. Chu, C. Xiang, H. Sue, and R. Hollis, "Scratch resistance of mineral-filled polypropylene materials," Polymer Engineering and Science, vol. 40, pp. 944-955, 2000.

[23] M. Wong, G. Lim, A. Moyse, J. Reddy, and H. Sue, "A new test methodology for evaluating scratch resistance of polymers," Wear, vol. 256, pp. 1214-1227, 2004.

[24] H. Jiang, R. Browning, and H. Sue, "Understanding of scratch-induced damage mechanisms in polymers," Polymer, vol. 50, pp. 4056-4065, 2009.

[25] http://www.zeiss.de/ ( link of software: LSM image browser rel. 4.2)

[26] T. Corle and G. Kino, Confocal scanning optical microscopy and related imaging systems: Academic Pr, California, 1996.

[27] V. Koinkar and B. Bhushan, "Effect of scan size and surface roughness on microscale friction measurements," Journal of Applied Physics, vol. 81, pp. 2472-2479, 1997.

[28] L. Sung, J. Jasmin, X. Gu, T. Nguyen, and J. W. Martin, "Use of laser scanning confocal microscopy for characterizing changes in film thickness and local surface morphology of UV-exposed polymer coatings," Journal of Coatings Technology and Research, vol. 1, pp. 267-276, 2004.

[29] J. Faucheu, K. Wood, L. Sung, and J. W. Martin, "Relating gloss loss to topographical features of a PVDF coating," Journal of Coatings Technology and Research, vol. 3, pp. 29-39, 2006.

[30] Y. Pang, S. S. Watson, A. M. Foster, and L. Sung, "Correlating nanoparticle dispersion to surface mechanical properties of $TiO_2$/polymer composites," Proceeding of Materials Research Society Symposium, 2009.

[31] J. Courter, "Mar resistance of automotive clearcoats: relationship to coating mechanical properties," Journal of Coating Technology, vol. 69, pp. 866-872, 1997.

[32] M. VanLandingham, L. Sung, N. Chang, T. Wu, S. Chang, and V. D. Jardret, "Measurement approaches to develop a fundamental understanding of scratch and mar resistance," Journal of Coatings Technology and Research, vol. 1, pp. 257-266, 2004.

[33] G. Pharr, W. Oliver, and F. Brotzen, "On the generality of the relationship among contact stiffness, contact area, and elastic modulus during indentation," Journal of Materials Research, vol. 7, pp. 613-617, 1992.

[34] W. C. Oliver and G. M. Pharr, "An improved technique for determining hardness and elastic modulus using load and displacement sensing indentation experiments," Journal of Materials Research, vol. 7, pp. 1564-1583, 1992.

[35] W. C. Oliver and G. M. Pharr, "Measurement of hardness and elastic modulus by instrumented indentation: Advances in understanding and refinements to methodology," Journal of Materials Research, vol. 19, pp. 3-20, 2004.

[36] I. Sneddon, "The relation between load and penetration in the axisymmetric Boussinesq problem for a punch of arbitrary profile," International Journal of Engineering Science, vol. 3, pp. 47-57, 1965.

[37] B. Lucas, W. Oliver, and J. Swindeman, "Dynamics of frequency-specific, depth-sensing indentation testing," Proceeding of Materials Research Society Symposium, 1998.

[38] A. Fischer-Cripps, Nanoindentation: Springer Verlag, New York, 2004.

[39] L. Sung, J. Comer, A. M. Forster, H. Hu, B. Floryancic, L. Brickweg, and R. H. Fernando, "Scratch behavior of nano-alumina/polyurethane coatings," Journal of Coatings Technology and Research, vol. 5, pp. 419-430, 2008.

[40] B. Beake and G. Leggett, "Nanoindentation and nanoscratch testing of uniaxially and biaxially drawn poly (ethylene terephthalate) film," Polymer, vol. 43, pp. 319-327, 2002.

[41] S. Wen, R. Zong, F. Zeng, S. Guo, and F. Pan, "Nanoindentation and nanoscratch behaviors of Ag/Ni multilayers," Applied Surface Science, vol. 255, pp. 4558-4562, 2009.

[42] A. Dasari, S. Sarang, and R. Misra, "Strain rate sensitivity of homopolymer polypropylenes and micrometric wollastonite-filled polypropylene composites," Materials Science and Engineering A, vol. 368, pp. 191-204, 2004.

[43] J. Wong, H. Sue, K. Zeng, R. Li, and Y. Mai, "Scratch damage of polymers in nanoscale," Acta Materialia, vol. 52, pp. 431-443, 2004.

[44] J. Swadener, E. George, and G. Pharr, "The correlation of the indentation size effect measured with indenters of various shapes," Journal of the Mechanics and Physics of Solids, vol. 50, pp. 681-694, 2002.

[45] W. Gerberich, N. Tymiak, J. Grunlan, M. Horstemeyer, and M. Baskes, "Interpretations of indentation size effects," Journal of applied mechanics, vol. 69, pp. 433-442, 2002.

[46] K. Menard, Dynamic mechanical analysis: a practical introduction: CRC Press, Boca Raton, 2008.

[47] H. Brinson and L. Brinson, Polymer engineering science and viscoelasticity: an introduction: Springer Verlag, New York, 2007.

[48] H. Leaderman and T. Foundation, Elastic and creep properties of filamentous materials and other high polymers: The Textile Foundation, Washington, DC, 1943.

[49] A. Tobolsky, Properties and structure of polymers: John Wiley and Sons, New Jersey, 1960.

[50] J. Ferry, Viscoelastic properties of polymers: John Wiley and Sons, New Jersey, 1980.

[51] M. Williams, R. Landel, and J. Ferry, "The temperature dependence of relaxation mechanisms in amorphous polymers and other glass-forming liquids," Journal of the American Chemical Society, vol. 77, pp. 3701-3707, 1955.

[52] V. Kenner, B. Harper, and V. Itkin, "Stress relaxation in molding compounds," Journal of Electronic Materials, vol. 26, pp. 821-826, 1997.

# 作者簡介

姓名：黃宇欣

性別：女

學歷：台北市立大湖國民小學

台北市立南門國民中學

台北市立中山女子高級中學

國立成功大學機械工程學系

國立台灣大學機械工程研究所

E-mail: r97522502@ntu.edu.tw

# National Institute of Standards and Technology (NIST)

Founded in 1901, NIST is a non-regulatory federal agency within the U.S. Department of Commerce. It's mission is to promote U.S. innovation and industrial competitiveness by advancing measurement science, standards, and technology in ways that enhance economic security and improve our quality of life.

## The NIST Laboratories

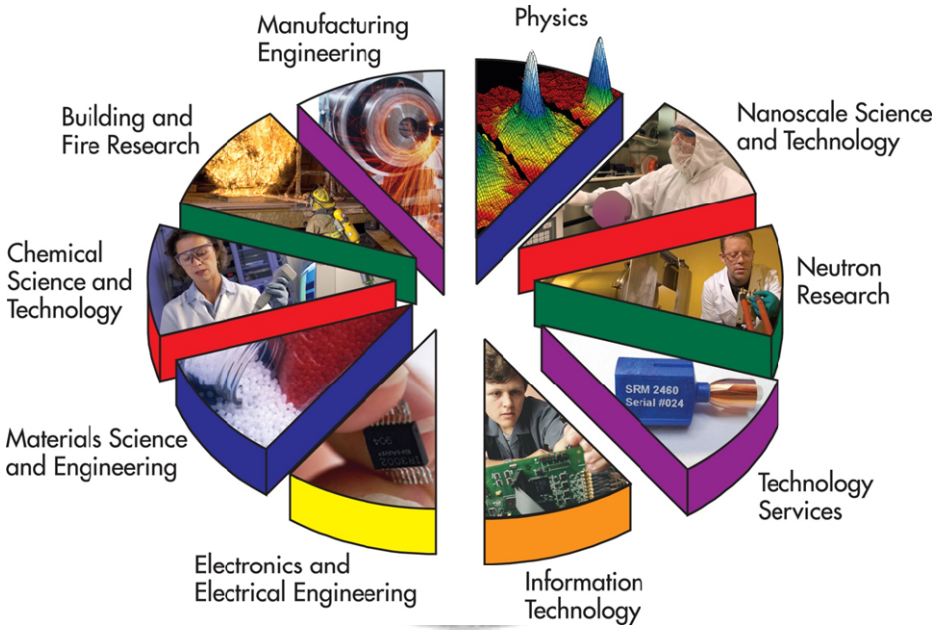


Major Assets

- ~ 2,800 employees
- ~ 2600 associates and facilities users
- ~ 1,600 field staff in partner organizations
- ~ 400 NIST staff serving on 1,000 national and international standards committees

# Building and Fire Research Laboratory (BFRL)